

Thermo-hydro-mechanical behavior of the Callovo-Oxfordian claystone : Effects of stress paths and temperature changes

Philipp Braun

▶ **To cite this version:**

Philipp Braun. Thermo-hydro-mechanical behavior of the Callovo-Oxfordian claystone : Effects of stress paths and temperature changes. Géotechnique. Université Paris-Est, 2019. English. NNT : 2019PESC1004 . tel-02483143

HAL Id: tel-02483143
https://pastel.hal.science/tel-02483143

Submitted on 18 Feb 2020

HAL is a multi-disciplinary open access archive for the deposit and dissemination of scientific research documents, whether they are published or not. The documents may come from teaching and research institutions in France or abroad, or from public or private research centers.

L'archive ouverte pluridisciplinaire **HAL**, est destinée au dépôt et à la diffusion de documents scientifiques de niveau recherche, publiés ou non, émanant des établissements d'enseignement et de recherche français ou étrangers, des laboratoires publics ou privés.

UNIVERSITÉ PARIS-EST

Thèse

soumise pour l'obtention du grade de
Docteur de l'Université Paris-Est
Ecole Doctorale Sciences, Ingénierie et Environnement (SIE)

par

Philipp Braun

Thermo-hydro-mechanical behaviour of the Callovo-Oxfordian claystone

Effects of stress paths and temperature changes

Spécialité : *Géotechnique*

Soutenue le 6 mai 2019 devant un jury composé de :

Prof. Chris Spiers	Utrecht University	Président du Jury
Prof. Philippe Cosenza	Université de Poitiers	Rapporteur
Prof. Antonio Gens	Universitat Politecnica de Catalunya	Rapporteur
Prof. Jianfu Shao	Université de Lille	Examinateur
Dr. Nathalie Conil	Andra R&D	Examinatrice
Prof. Pierre Delage	Ecole des Ponts ParisTech	Directeur de thèse
Dr. Siavash Ghabezloo	Ecole des Ponts ParisTech	Co-directeur de thèse

Abstract

Extensive research is carried out by the French National Radioactive Waste Management Agency (Andra), in order to characterize the Callovo-Oxfordian (COx) claystone, a candidate host rock for a deep geological radioactive waste repository in France. The hydromechanical behaviour of the rock due to the excavation of the galleries are studied, as well as the thermo-hydro-mechanical (THM) response arising from heat generated by the exothermic waste packages. A laboratory programme was carried out in this work to characterize the response of COx claystone to different THM loadings, within the framework of transversely isotropic thermo-poro-elasticity.

Due to the very low permeability of the COx claystone, laboratory experiments have to be adapted for long saturation and drainage durations. Analytical solutions are presented for describing the time dependent pore pressure field in a specimen, which is submitted to various loading paths and different rates. This provides a simple and efficient tool for the estimation of the conditions that must hold for reliable determination of material parameters. It allows as well an optimization of various testing conditions.

Based on this approach, a new transient step loading procedure was developed for isotropic tests in drained and undrained conditions, under both thermal and mechanical loading. These protocols render experiments on low permeable rocks more time efficient, giving access to several THM parameters and permeability measurements in a single test.

In isotropic compression tests, pore pressure tests, and deviatoric loading tests parallel and perpendicular to the bedding plane, poroelastic properties were investigated on saturated rock specimens. The performed experiments provide compatible material parameters at different stress levels, and evidencing a significant transverse isotropy. This had little effects on the anisotropy of back-calculated Biot's coefficients and more effects on the anisotropy of Skempton's coefficients.

Thermal loads were exerted on COx specimens along different heating and cooling paths. Drained and undrained thermal expansion coefficients along both the transverse isotropic directions were determined. The measurement of pore pressure changes yielded the thermal pressurization coefficient, with a stress and temperature dependency identified.

Thermo-hydro-mechanical loading paths corresponding to the paths expected *in situ*, were mimicked in the laboratory. Using a specially developed novel triaxial device, samples were heated with no radial strain allowed, until thermally induced pore pressures caused effective tensile stresses. We ultimately fractured the material at axial effective stresses around -3.0 MPa. Fracturing under different lateral total stresses allowed to a tensile failure

criterion. Using the THM properties evaluated earlier in the study, one is able to satisfactorily reproduce the observed deformations under tension.
Last of all, a thermo-poroelastic model was implemented in the finite element solver FreeFem++. The THM behaviour around parallel microtunnels in periodic layout is simulated in a 2D configuration. This helps to better understand the spatial arrangement of THM processes, heat and fluid transport, and the change of stress states with respect to the presented failure criterion.

Keywords: Thermo-poro-elasticity, Transverse isotropy, Callovo-Oxfordian claystone, Triaxial testing, Thermal pressurization, Tensile failure

Résumé

L'Agence nationale de gestion des déchets radioactifs (Andra) mène des recherches approfondies afin de caractériser l'argilite du Callovo-Oxfordien (COx) en France, roche hôte potentielle pour le stockage géologique profond des déchets radioactifs. Les études concernent le comportement hydromécanique de la roche dû à l'excavation des galeries ainsi que la réponse thermo-hydro-mécanique (THM) résultant de la chaleur produite par les colis de déchets exothermiques. Un programme expérimental a été mené dans ce travail pour caractériser la réponse de l'argilite du COx sous différentes sollicitations THM dans un cadre thermo-poro-élastique isotrope transverse. Comme l'argilite du COx a une très faible perméabilité, les expériences en laboratoire doivent être adaptées pour de longues durées de saturation et de drainage. Nous présentons des solutions analytiques pour le champ de pression interstitielle en fonction du temps dans un échantillon soumis à différents chemins de chargement et à différents taux. Il s'agit d'un outil simple et efficace pour estimer les conditions devant être réunies afin de déterminer avec fiabilité les paramètres du matériau. Cela permet également d'optimiser les différentes conditions d'essai.

À partir de cette approche, une nouvelle procédure de chargement transitoire par étapes a été mise au point pour les essais isotropes, dans des conditions drainées et non drainées, et sous charge thermique et mécanique. Ces protocoles rendent les expériences sur les roches à faible perméabilité plus efficaces en termes de temps, donnant accès à plusieurs paramètres THM et mesures de perméabilité en un seul essai.

A partir des données d'essais de compression isotrope, de pression interstitielle et de chargement déviatoriques selon des directions parallèles et perpendiculaires au litage, on a étudié les propriétés poroélastiques des échantillons de roche saturée. Ces essais ont fourni un jeu compatible de paramètres de matériaux, et ce sous différents niveaux de contrainte, mettant en évidence une anisotropie significative. Alors que l'anisotropie du coefficient de Biot calculé par analyse inverse était très faible, nous avons observé une anisotropie importante du coefficient de Skempton.

Des essais thermiques ont été réalisés selon différents chemins de chauffage et de refroidissement. Nous avons déterminé les coefficients de dilatation thermique drainée et non drainée dans les deux directions isotropes transverses. La mesure des variations de pression interstitielle a donné le coefficient de pressurisation thermique. Nous avons identifié une dépendance aux contraintes et à la température.

Nous avons reproduit des chemins de chargement thermo-hydro-mécaniques correspondant aux chemins in situ sur l'axe de symétrie entre deux alvéoles dans lesquels sont placés

les colis de déchets. À l'aide d'un système triaxial spécialement adapté et novateur, les échantillons ont été chauffés sous condition de déformation latérale nulle jusqu'à ce que les surpressions interstitielles thermiques provoquent des contraintes de traction qui ont fini par fracturer le matériau à des contraintes axiales effectives d'environ -3,0 MPa. Des essais sous différentes contraintes latérales totales a permis de décrire la rupture selon un critère de rupture en traction. En utilisant les propriétés des THM évaluées dans l'étude, nous sommes en mesure de reproduire de façon satisfaisante les déformations observées sous tension.
Enfin, un modèle thermo-poroélastique a été implanté dans un code de calcul d'éléments finis FreeFem++. Le comportement THM autour des alvéoles parallèles disposés à intervalles réguliers a été modélisé. Cela permet de mieux comprendre la disposition spatiale des processus THM, les transferts de chaleur et de fluides, ainsi que le changement des états de contrainte par rapport au critère de rupture présenté ici.

Mots-clés : Thermo-poro-élasticité, Isotropie transverse, Argilite du Callovo-Oxfordien, Essai triaxial, Pression thermique, Rupture en traction

Acknowledgement

This work was based on a collaboration between Andra and Laboratoire Navier at Ecole des Ponts ParisTech. Without their support, this work would not have been possible. I would like to express my gratitude to everybody who contributed to the accomplishment of this thesis.
First of all, I would like to thank my two supervisors, Prof. Pierre Delage and Dr. Siavash Ghabezloo. It was really a pleasure to work with them and learn from them. I feel privileged to have had them as advisors. Thanks to them for the time they invested and always having an open door. Thanks to Pierre for sharing his vast experience and supporting all our unconventional ideas. I would like to thank Siavash especially for not only introducing me to this field of science but also keeping me there and giving me the right directions. Thanks to both for their guidance throughout these three years.
I also want to express my gratitude towards Dr. Nathalie Conil. I appreciate all the important input she gave me during this thesis, in particular from her valuable field experience. Thanks to her for her warm reception in the Andra R&D team. I have to thank her also for introducing me to the underground lab and for managing the in situ measurements.
I owe my deep gratitude towards Prof. Jean Sulem for giving his support, valuable discussions and important advice. I also appreciate the guidance he provides for the geotechnical team at Laboratoire Navier. The working ambience at this Lab is really outstanding, with intensive exchange between the researchers and a great team spirit.
Here I also want to include the technical team of the laboratory. They made great efforts for the experimental studies contained in this work. I give my thanks to Emmanuel De Laure, for his support and guidance in the lab, to Baptiste Chabot for his design work, and to Marine Lemaire, Xavier Boulay and Loic Lesueur for offering their helping hands.
I would also like to thank the fluid and solid mechanics team around Dr. Gilles Armand, who provided valuable scientific input, allowed me to participate in their project and get insight in collaborations with other research teams. I want to thank Dr. Darius Seyedi and Dr. Minh-Ngoc Vu for fruitful discussions and contributions, especially in the numerical part of this study. I am grateful to the members of the jury, Prof. Philippe Cosenza, Prof. Antonio Gens, Prof. Jianfu Shao and Prof. Chris Spiers. I would like to thank them for accepting to participate in the committee and for offering their invaluable input to this work. I was also very lucky to have such great colleagues, doctoral students, postdocs and researchers included. Thank you for the fantastic time we spent together, for your solidarity and also for the activities outside of work.
To my family I express my deepest gratitude for their love and continuous and unconditional support. Most importantly, thank you Camille for giving me your love and for always backing me up.

Contents

1 Introduction **1**

1.1 Motivation 1

1.2 Problem Statement 4

1.3 Thesis Structure 7

2 Bibliographic study **9**

2.1 Fundamentals of thermo-poro-elasticity 9

2.1.1 Transverse isotropy 10

2.1.2 Equivalent isotropy 13

2.1.3 Thermal pressurization 15

2.1.4 Heat and fluid transport 16

2.2 Characteristics of the COx claystone 18

2.2.1 Geological context 18

2.2.2 Microstructure 18

2.2.3 Variability of measurements 20

2.2.4 Hydromechanical properties 22

2.2.5 Permeability 28

2.2.6 Heat transport 29

2.2.7 Thermal volume changes 30

3 Materials and Methods **33**

3.1 *In situ* suction measurements 33

3.2 Sample preparation and initial characterization 39

3.3 Experimental devices 40

3.3.1 Isotropic cell 40

3.3.2 Triaxial cell 40

3.3.3 Deformation measurement 41

3.3.4 Calibration of the effect of the drainage system 42

3.4 Development of a novel thermal extension apparatus 45

3.4.1 Control of cell pressure 45

3.4.2 Tension between piston and top cap 45

3.4.3 Tension between caps and sample 46

3.4.4 Design of the novel device 47

3.4.5 Preparation of specimens 49

3.5 Analytical solution for pore pressure dissipation . . . 51
3.5.1 Introduction . . . 51
3.5.2 Test conditions . . . 52
3.5.3 Analytical solutions for pore pressure controlled experiments . . . 56
3.5.4 Numerical analysis of undrained experiments . . . 62
3.5.5 Evaluation of optimal loading conditions . . . 63
3.5.6 Application example for COx claystone . . . 65
3.5.7 Conclusions . . . 72
3.6 Transient testing protocol . . . 73
3.6.1 Introduction . . . 73
3.6.2 Theoretical considerations . . . 74
3.6.3 Testing procedure . . . 76
3.6.4 Example results and analysis . . . 80
3.6.5 Conclusions . . . 83
3.7 Numerical modelling . . . 85
3.7.1 Constitutive equations . . . 86
3.7.2 Model Geometry . . . 87
3.7.3 Boundary conditions . . . 89
3.7.4 Time and space discretization . . . 90
3.8 Conclusions . . . 92

4 Poroelastic behaviour **95**
4.1 Testing Procedure . . . 96
4.2 Experimental Results . . . 99
4.2.1 Stress dependent properties under isotropic stress . . . 99
4.2.2 Stress dependent properties under deviatoric stress . . . 104
4.3 Regression analysis and discussion . . . 104
4.3.1 Equivalent isotropic parameters . . . 107
4.3.2 Anisotropic response to isotropic stresses . . . 109
4.3.3 Analysis of drained isotropic and deviatoric test results . . . 110
4.3.4 Analysis of undrained isotropic and deviatoric test results . . . 110
4.4 Application example in a numerical model . . . 111
4.4.1 Adopted material properties . . . 112
4.4.2 Temperature evolution . . . 114
4.4.3 Resulting THM response . . . 114
4.4.4 Effect of transverse isotropy . . . 119
4.4.5 Adoption of stress dependent anisotropic poroelasticity . . . 122
4.5 Conclusions . . . 124

5 Behaviour under thermal loads **127**
5.1 Testing programme . . . 127
5.2 Experimental results . . . 131

5.2.1 Drained thermal deformations . . . 131
5.2.2 Undrained thermal deformations . . . 134
5.2.3 Strain response to pore pressure change . . . 136
5.2.4 Thermally induced pore pressure . . . 136
5.3 Discussion . . . 139
5.3.1 Thermal strains of the solid matrix . . . 139
5.3.2 Parametric study of THM couplings . . . 140
5.3.3 Anomalous thermal behaviour of pore fluid . . . 140
5.3.4 Stress and temperature dependent thermal pressurization . . . 142
5.4 Application of properties in a numerical model . . . 144
5.4.1 Influence of the pore water thermal expansion coefficient . . . 144
5.4.2 Influence of the anisotropy of solid thermal expansion coefficients . . . 145
5.5 Conclusions . . . 147

6 Extension behaviour and tensile failure **149**
6.1 Testing Procedure . . . 149
6.2 Experimental results . . . 152
6.3 Discussion . . . 155
6.3.1 Thermo-poroelastic analysis . . . 157
6.3.2 Failure criterion . . . 158
6.3.3 Comparison with other shales . . . 160
6.4 Comparison with a numerical simulation . . . 161
6.5 Conclusions . . . 162

7 Concluding remarks and perspectives **165**
7.1 Conclusions . . . 165
7.2 Perspectives . . . 168

A Appendix **171**
A.1 Calculation of time dependent pore pressure distribution . . . 171
A.2 Alternative two-stage loading protocol . . . 174
A.2.1 Two-stage compression test . . . 175
A.2.2 Two-stage heating test . . . 175

Bibliography **179**

List of Figures **189**

List of Tables **197**

1 Introduction

1.1 Motivation

At the present time, feasibility studies of deep geological radioactive waste repositories are subject to worldwide research. Several countries (e.g. France, Switzerland, Belgium, Sweden, Canada, Japan) consider a deep geological repository as a possible disposal solution for high- and long lived radioactive wastes. Some among them, like France, Switzerland or Belgium, are investigating clay-based geomaterials as possible host formations.

Clays and clayrocks can represent the essential barrier of a deep geological repository, with its main required functions (Andra, 2005):

- Protecting the waste packages from natural erosion and human activities at an inaccessible location
- Limiting the diffusion of radionuclides emitted from the waste. A reducing environment, impeding water flow, has to be provided for very long timescales (up to several hundreds of thousands of years).
- Ensuring these properties during very long timescales, by withstanding thermo-chemo-mechancial exposure, even after the concrete and metal components are deteriorated.

In France, the Callovo-Oxfordian (COx) claystone, a rock formation at around 500 m depth located near the village of Bure (Fig. 1.1), is a candidate host rock for a potential repository (Cigéo project), with the French national agency for radioactive waste management (Andra) being in charge of this project. Andra confirmed, that the claystone has chemical retaining properties due to the clay particles, and that it provides a chemically stable environment and a very low permeability, limiting the transport of radionuclides dissolved in water. High temperatures around the exothermic waste packages are avoided due to the specific design of the repository and by a cooling phase of the waste before storing it. Furthermore, the COx claystone provides mechanically enough stability for the construction of galleries. The rock was observed to have a so-called self-sealing ability, through which fractures, induced during excavation, partially close themselves over time. These aspects demonstrated, that the COx claystone fulfils the requirements of a natural barrier (Andra, 2005).

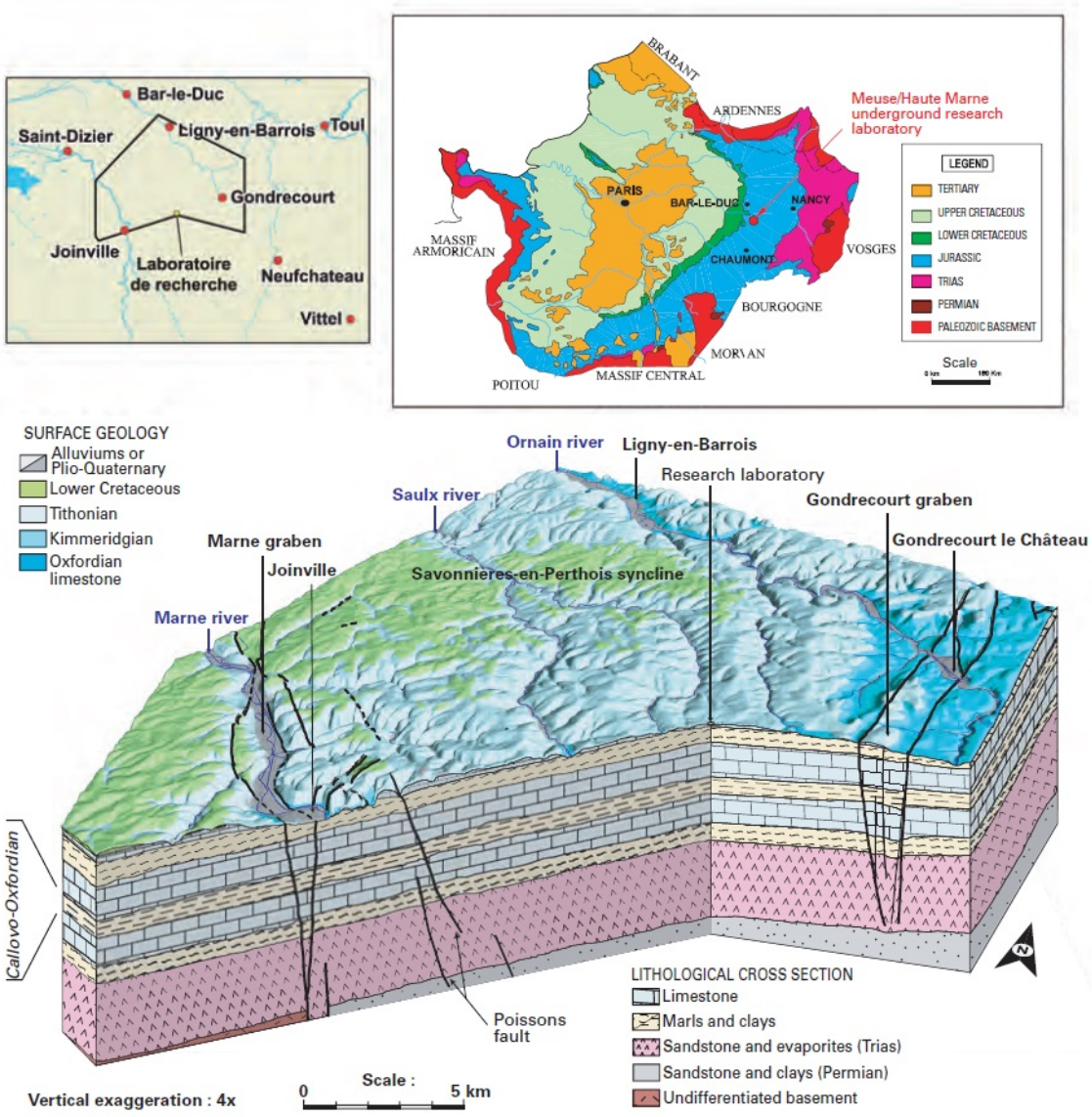


Fig. 1.1.: Geological map of the Meuse/Haute-Marne area in eastern France, where the Callovo-Oxfordian claystone is located in a layer at around 500 m depth. The Andra underground research laboratory is found near the village of Bure (Andra, 2005)

Within the concept proposed by Andra, different phases in the lifetime of the repository are described. Starting is the preparatory phase, in which the galleries and surface installations are constructed, followed by the operation and observation phase. In this phase, waste packages are placed, accompanied by comprehensive monitoring. The modules are closed progressively, while a freedom of choice for the management of the waste and the installations, and a reversibility is always ensured. After the operation phase, which has no fixed time scale, the post-closure phase begins by sealing the repository for containing radionuclides up to several hundreds of thousands of years. During all these stages, the aforementioned barrier properties have to be verified, in order to ensure short- and long term safety (Andra, 2005).

An underground research laboratory (URL) in the COx layer, close to the site of the potential repository, managed by Andra, allows extensive studies on the host formation. The key aspects of the URL facility are quoted by Armand et al. (2015), defined as:

- Verification and optimization of the design of the disposal facility, and development of construction methods and
- Verification of the ability to seal the vaults drifts and shafts, development of methods for the sealing of drifts and shafts
- Confirmation of the low impact of perturbations caused by the disposal facility, assessment of the behavior of the perturbed argillaceous rocks and materials at the interfaces.
- Confirmation of the confinement abilities of the Callovo-Oxfordian formation, characterization of the argillaceous rocks
- Assessment of the conditions of radionuclide transfer towards the biosphere, observation of the hydrogeological context and the environment over time
- Development of monitoring methods for the reversible management of the disposal facility

These investigations bring together different disciplines, with the fields of hydrogeology, structural geology, mineralogy, geochemistry and rock mechanics (Armand et al., 2017b). The present study is positioned in the latter discipline, contributing to the design of the repository, based on the thermo-hydro-mechanical response of the rock observed in the laboratory or during *in situ* experiments.

In particular, the galleries have to be designed for withstanding hydro-mechanical loads induced through excavation, and provide safety during operation. Once the exothermic waste packages are placed in the microtunnels, additional thermal effects have to be taken into account. In the long term, time dependent mechanical properties have to be considered. The transport of pore-fluid and heat has to be investigated, accounting for potential changes due to induced fractures. The generation of excessive fractures has to be avoided, as they can provide pathways for pore-water transport and therefore radionuclide migration.

1.2 Problem Statement

The main interest of this study lies within the behaviour of the claystone formation evoked by thermal loading, starting from the operational phase. The highest thermal charges are considered to be exerted by the high level, long-lived wastes, which represent about 1 % of the volume of total radioactive waste. They consist of material from spent fuel reprocessing and are planned to be vitrified and enclosed in packages of stainless steel cylinders (Fig. 1.2) (Andra, 2005).

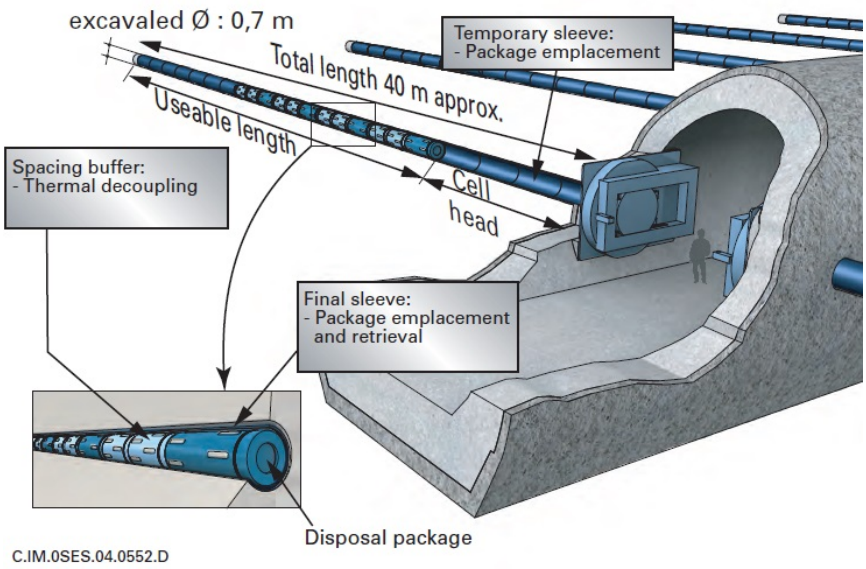


Fig. 1.2.: Concept of microtunnels, which incorporate high level radioactive waste packages (Andra, 2005)

Heat is expected to radiate from the cells, heating up the surrounding rock in consequence. The waste is planned to be stored after it cooled down for about 70 years, to reduce the thermal loading. The design of the repository ensures that a maximum temperature of 90°C at the wall of the disposal cell is not exceeded. The claystone, regarded as a porous medium, is composed of a solid matrix and pores. These pores are naturally fully saturated by water, consequently both solid and water phases undergo thermal volume changes.

Thermal strains of the solid phase have been evidenced to be of complex thermoplastic nature upon heating (Mohajerani et al., 2014; Belmokhtar et al., 2017b). A thermoplastic behaviour was also formerly discovered on the Opalinus clay (Monfared et al., 2011a), similar to that of stiff clays (Baldi et al., 1988, Sultan et al., 2002 on Boom clay, Abuel-Naga et al., 2007 on Bangkok clay).

Temperature induced pore pressure, the so-called thermal pressurization, occurs when saturated geomaterials are heated in undrained conditions (Ghabezloo and Sulem, 2009). Laboratory studies have evidenced this phenomenon on the COx claystone (Mohajerani

et al., 2012; Zhang et al., 2017) and on Opalinus clay (Monfared et al., 2011a). Thermal pressurization represents an interaction between solid and fluid phase, therefore the properties of the pore fluid play an important role, as shown by Baldi et al. (1988) on low porosity clays, by Ghabezloo et al. (2009b) on hardened cement paste and by Monfared et al. (2011a) on Opalinus clay. These authors stated, that their laboratory measurements of thermal pressurization could only be reproduced by adopting a thermal expansion coefficient of the pore fluid which is higher than that of free water. This aspect was not yet investigated on the COx claystone.

Also *in situ* heating tests have shown an important thermal pressurization in claystone formations, e.g. the TER and TED tests (Wileveau et al., 2007b; Conil et al., 2012; Armand et al., 2017a) in COx claystone at the Bure underground laboratory and the HE-D test (Thury and Bossart, 1999; Gens et al., 2007) in Opalinus clay at the Mont Terri rock laboratory. In the works of Gens et al. (2007) and Seyedi et al. (2017), THM processes observed *in situ* have been analysed by numerical simulation.

Similarly, thermal volume changes of the solid matrix can lead to induced stress changes, when strains are constrained due to some boundary conditions. Together with induced pore pressures, this can evoke complex stress paths, which have to be considered in the design of the repository.

Fig. 1.3a illustrates a concept for the tunnel layout in the Cigéo project, designed for the high level waste. The microtunnels, which incorporate the waste packages, are evenly spaced with enough distance, such as to keep the temperature around them below 90 °C (Fig. 1.3b). Given the relatively high length of the microtunnels and their periodic layout, thermo-hydro-mechanical processes around these drifts can be modelled and analysed in a plane strain model with some symmetry conditions between the tunnels. Peculiar boundary conditions are encountered at this symmetry axis, which are zero horizontal deformations and no horizontal heat nor fluid flux. This fact favours the accumulation of heat at the mid-distance between two microtunnels. Due to the thermal pressurization, the pore pressure rises with temperature, which would then dissipate gradually towards the far-field. At the symmetry axis however, we suspect a larger pore pressure build-up, as the horizontal fluid flow is limited. Regarding the mechanical conditions at the symmetry axis, one finds zero horizontal strains and a practically constant total vertical stress, given by the overburden of the formation.

The increasing pore pressure acts on the material creating vertical expansion, while the laterally constrained dilation increases most likely the lateral total stress in consequence. Heating the rock unlimitedly would rise the pore pressure up to a point, where it exceeds the vertical overburden stress. This would generate vertical effective tensile stresses, which might lead to a vertical tensile failure.

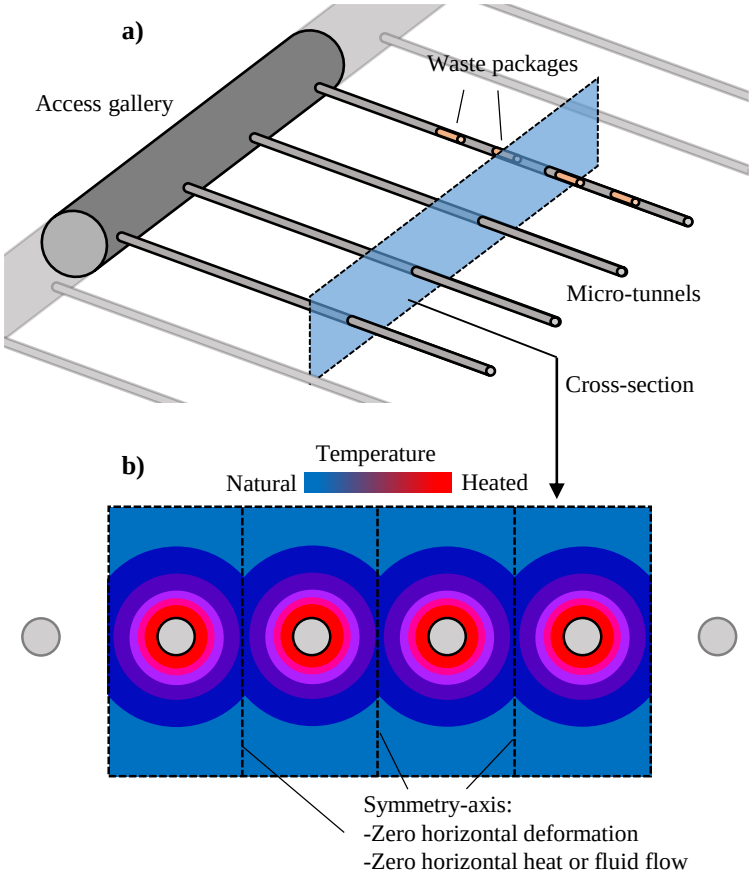


Fig. 1.3.: a) Schematic layout of the microtunnels containing high-level radioactive waste (adopted from Andra, 2005), with b) a cross-section where we can assume plane strain and zero heat/ temperature flux perpendicular to the image plane, illustrating the heat radiation from periodically constructed microtunnels

The possibility of fracturing shales through temperature induced pore pressure was recently proven in the laboratory by Li and Wong (2018) in unconfined heating tests. In absence of stress and strain measurements, they concluded that the fractures are supposedly created when the pore pressure exceeds the tensile strength. Fractures were observed to occur parallel to the bedding plane. However, to the authors best knowledge, the THM fracturing of geomaterials has hitherto not been achieved under controlled stresses, pore pressure and temperature.

This experimental study was carried out to investigate the thermo-hydro-mechanical behaviour of the COx claystone, including important interactions with the water contained in its pores. We characterized the material within the transversely isotropic thermo-poroelasticity, to be able to predict strains and pore pressure changes occurring under the expected *in situ* loading paths. A newly designed triaxial extension device was used to load specimens under extension paths until tensile failure. A tensile failure criterion accounting for THM fracturing could be established in consequence. Finally, the experimentally determined properties were applied in an finite element code to show their effect on the structural scale.

1.3 Thesis Structure

Chapter 2 is devoted to a bibliographic study. We first discuss the mathematical framework of transversely isotropic poroelasticity, coupled with thermal and hydraulic effects. Heat and fluid transport are taken into account with anisotropic conductive properties. Secondly, we recall findings from the literature on the COx claystone, concerning the properties within the thermo-poromechanical constitutive model. This includes laboratory investigations, supported by *in situ* experiments, commissioned or carried out by Andra.

In **Chapter 3**, the adopted experimental procedures, devices and methods are presented. An *in situ* investigation of the natural saturation state of COx helped to better estimate the pore fluid loss induced during specimen handling. We measured petrophysical properties of the cores, from which laboratory samples were taken, and describe the sampling procedure. The set-ups of a high pressure isotropic cell and a high pressure triaxial cell are explained in the following. Both systems are temperature controlled until 90 °C. A newly designed triaxial system is presented, which allows to maintain effective axial tension stresses on specimens, while servo-controlling the radial strains. This system was developed to investigate effective tensile deformations and failure. An analytical solution was derived, which allows to calculate the pore pressure field within specimens submitted to 1D drainage, under imposed pore pressure changes and isotropic thermo-mechanical loads. Consequently, we can simulate the measured strains in various basic isotopic rock mechanics tests, accounting for time and rate effects induced by a low material permeability. A procedure for evaluating the optimal loading durations, by reducing the induced error on the measured parameters is

given for basic experiments and demonstrated for a test on COx claystone. An optimized loading protocol, adapted for low permeable geomaterials, was developed. This procedure allows to determine multiple THM properties in a single transient test. In addition, the specimen permeability can be back-calculated from the time dependent strain response. A numerical thermo-poroelastic model with heat and fluid transport governed by Fourier's law and Darcy's law, respectively, is presented. This code was implemented in the free finite element solver Freefem++. We considered the parallel microtunnels in periodic layout in plane strain conditions, with geomechanical data provided by Andra. For the COx layer, we adopted the properties determined in this study. After each of the following chapters, we briefly discuss the application of the experimentally determined properties in the large scale scenario. These simulations allowed to better understand the impact of various parameters on the structural scale.

Chapter 4 presents experimental results of hydromechanical tests and their analysis. COx specimens were fully saturated under confining stress and tested in the aforementioned experimental devices and protocols. We start with a series of experiments on the poroelastic properties of the material. Transversely isotropic coefficients, determined from isotropic and triaxial tests at different stress levels, are presented as a set of stress dependent parameters.

In **Chapter 5**, thermal experiments were carried out in the isotropic cell under constant stress conditions, which provided interesting insight on thermal strains in drained and undrained conditions. The thermal pressurization coefficient was measured. The observed thermally induced pore pressures and strains in undrained conditions were analysed in the stress dependent, transversely isotropic thermo-poroelastic framework.

Chapter 6 discusses the behaviour of specimens under thermally induced pore pressures until failure, investigated with a novel triaxial device. Specimens were heated in undrained conditions, causing a pore pressure increase, while lateral deformations were constrained. In these tests, the lateral effective stress changed only little, whereas the axial effective stress decreased up to negative values until failure. Measured strains could be reproduced within the THM framework, based on evaluated parameters. The observed failure stresses perpendicular to the bedding plane, under different lateral stresses, enabled us to adopt a failure criterion for the tension region.

The conclusions of this work are given in **Chapter 7**, together with some perspectives for future research.

2 Bibliographic study

In this chapter, we recall the theoretical background of thermo-poroelasticity in Sec. 2.1. This is followed by a comprehensive literature study on various THM properties of the COx claystone, presented in Sec. 2.2.

2.1 Fundamentals of thermo-poro-elasticity

In this section, we present the theoretical framework of thermo-poroelasticity. This theory permits to describe the behaviour of a porous, fluid-saturated medium under thermal, hydraulic and mechanical loadings. The theoretical basis of the formulation has been presented in various earlier studies, where one can refer to the works of Biot and Willis (1957), Brown and Korringa (1975), Rice and Cleary (1976), Detournay and Cheng (1993), Vardoulakis and Sulem (1995) and Coussy (2004). In the following, the theory is recalled according to these authors.

In the poromechanics theory, a porous material of total volume V is assumed to consist of two distinct phases: a solid phase with a volume V_s and a fluid phase with a volume V_ϕ. The solid phase can be heterogeneous and anisotropic in the micro-scale (Zimmerman et al., 1986). Occluded pores do not contribute to the pore volume, but are counted to the solid volume. The thermo-poromechanical formulations are written for a Representative Elementary Volume (REV) of the porous material, submitted to strain ε, stress σ, pore fluid pressure p_f and temperature T. A stress-strain-temperature relationship is expressed within this framework as:

$$\mathrm{d}\sigma_i = M_{ij}\mathrm{d}\varepsilon_j + b_i \mathrm{d}p_f + M_{ij}\alpha_{d,j}\mathrm{d}T \tag{2.1}$$

$$\mathrm{d}\varepsilon_i = C_{ij}(\mathrm{d}\sigma_j - b_i \mathrm{d}p_f) - \alpha_{d,i}\mathrm{d}T \tag{2.2}$$

where p_f denotes the pore fluid pressure and σ_i the normal strains and shear strains in different directions:

$$\sigma_i = [\sigma_x, \sigma_y, \sigma_z, \sigma_{xy}, \sigma_{yz}, \sigma_{zx}]^\top \tag{2.3}$$

The strains ε in different direction are contained within the strain vector ε_i:

$$\varepsilon_i = [\varepsilon_x, \varepsilon_y, \varepsilon_z, \varepsilon_{xy}, \varepsilon_{yz}, \varepsilon_{zx}]^\top \tag{2.4}$$

The material properties in this framework are represented by the Biot effective stress coefficients b_i, the stiffness matrix M_{ij} with its inverse compliance matrix $C_{ij} = M_{ij}^{-1}$ and the drained thermal expansion coefficients $\alpha_{d,i}$.

$$b_i = [b_x, b_y, b_z, 0, 0, 0]^\top \tag{2.5}$$

$$\alpha_{d,i} = [\alpha_{d,x}, \alpha_{d,y}, \alpha_{d,z}, 0, 0, 0]^\top \tag{2.6}$$

2.1.1 Transverse isotropy

The material analysed in this study has been found to be transversely isotropic. Therefore, we can use a simplified set of coefficients for such case, where the properties in directions x and y are identical, denoted in the following with a subscript h. This plane of isotropy corresponds for the COx claystone, such as in many other sedimentary geomaterials, to the bedding plane. According to Cheng (1997), the coefficients in transverse isotropy are recalled here. The vector b_i represents the Biot effective stress coefficents in both directions of anisotropy:

$$b_i = [b_h, b_h, b_z, 0, 0, 0]^\top \tag{2.7}$$

We can also write down the stiffness matrix M_{ij} as follows:

$$M_{ij} = \begin{pmatrix} M_{11} & M_{12} & M_{13} & 0 & 0 & 0 \\ M_{12} & M_{11} & M_{13} & 0 & 0 & 0 \\ M_{13} & M_{13} & M_{33} & 0 & 0 & 0 \\ 0 & 0 & 0 & M_{11} - M_{12} & 0 & 0 \\ 0 & 0 & 0 & 0 & 2G & 0 \\ 0 & 0 & 0 & 0 & 0 & 2G \end{pmatrix} \tag{2.8}$$

with

$$\begin{aligned} M_{11} &= \frac{E_h\left(E_z - E_h {v_{zh}}^2\right)}{(1+v_{hh})(E_z - E_z v_{hh} - 2E_h {v_{zh}}^2)} \\ M_{12} &= \frac{E_h\left(E_z v_{hh} + E_h {v_{zh}}^2\right)}{(1+v_{hh})(E_z - E_z v_{hh} - 2E_h {v_{zh}}^2)} \\ M_{13} &= \frac{E_h E_z v_{zh}}{E_z - E_z v_{hh} - 2E_h {v_{zh}}^2} \\ M_{33} &= \frac{{E_z}^2(1-v_{hh})}{E_z - E_z v_{hh} - 2E_h {v_{zh}}^2} \end{aligned} \tag{2.9}$$

The compliance matrix C_{ij} is written as:

$$C_{ij} = \begin{pmatrix} C_{11} & C_{12} & C_{13} & 0 & 0 & 0 \\ C_{12} & C_{11} & C_{13} & 0 & 0 & 0 \\ C_{13} & C_{13} & C_{33} & 0 & 0 & 0 \\ 0 & 0 & 0 & 1/2G' & 0 & 0 \\ 0 & 0 & 0 & 0 & 1/2G & 0 \\ 0 & 0 & 0 & 0 & 0 & 1/2G \end{pmatrix} \tag{2.10}$$

with

$$\begin{aligned} C_{11} &= 1/E_h \\ C_{12} &= -\nu_{hh}/E_h \\ C_{13} &= -\nu_{zh}/E_z \\ C_{33} &= 1/E_z \\ G' &= E_h/(1+\nu_{hh}) \end{aligned} \tag{2.11}$$

where E_z and v_{zh} are the Young modulus and the Poisson ratio perpendicular to the bedding plane, and E_h and v_{hh} parallel to the bedding plane, respectively. G describes the independent shear modulus perpendicular to the isotropic plane.

In laboratory experiments, the Young moduli and Poisson ratios are generally measured in a triaxial cell under deviatoric loads. The properties E_z and ν_{zh} are determined on a specimen which is submitted to a deviatoric load perpendicular to the bedding plane σ_z, generating strains ε_z and $\varepsilon_x = \varepsilon_y$ (Fig. 2.1). We can then measure $E_z = \mathrm{d}\sigma_z/\mathrm{d}\varepsilon_z$ and $\nu_{zh} = -\mathrm{d}\varepsilon_x/\mathrm{d}\varepsilon_z$. A specimen which is loaded in parallel direction with respect to the bedding plane with σ_y is required for the remaining properties. Here one is able to observe an axial strain ε_y and two different radial strains ε_x and ε_z. This provides $E_h = \mathrm{d}\sigma_y/\mathrm{d}\varepsilon_y$, $\nu_{hh} = -\mathrm{d}\varepsilon_x/\mathrm{d}\varepsilon_y$. The measured parameter $\nu'_{zh} = -\mathrm{d}\varepsilon_z/\mathrm{d}\varepsilon_y$ allows a calculation of $\nu_{zh} = \nu'_{zh}E_z/E_h$. To be able to determine the shear modulus G perpendicular to the isotropic plane, a third triaxial test is required, where a deviatoric load is applied inclined with respect to the bedding plane. This shear modulus is, other than the shear modulus parallel to the isotropic plane, independent of other elastic parameters.

The thermal properties, represented by $\alpha_{d,i}$, can be simplified to two linear drained thermal expansion coefficients, perpendicular ($\alpha_{d,z}$) and parallel ($\alpha_{d,h}$) to the bedding orientation:

$$\alpha_{d,i} = [\alpha_{d,h}, \alpha_{d,h}, \alpha_{d,z}, 0, 0, 0]^\top \tag{2.12}$$

These properties can be determined in drained thermal tests. The change of the Lagrangian porosity ϕ is described by the expression (Aichi and Tokunaga, 2012):

$$\mathrm{d}\phi = -b_i \mathrm{d}\varepsilon_i + \frac{1}{N}\mathrm{d}p_f - (b_i\alpha_{d,i} - \phi\alpha_\phi)\,\mathrm{d}T \tag{2.13}$$

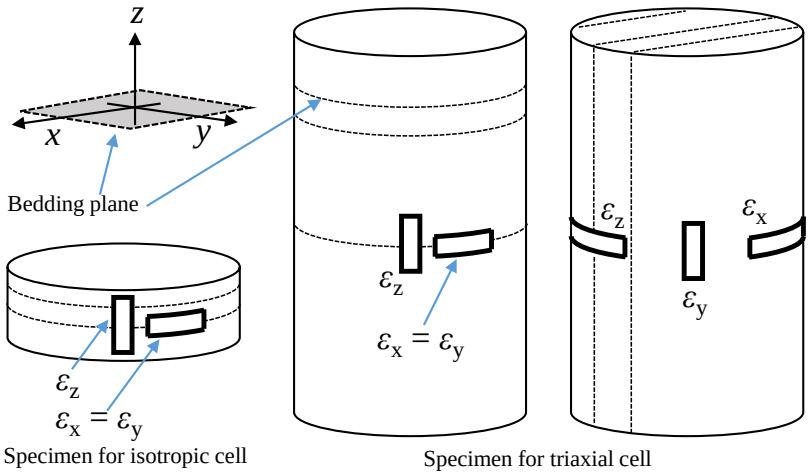


Fig. 2.1.: Strain gages and coordinate system oriented and attached with respect to the bedding plane of the COx specimens

with the modulus N depending on:

$$\frac{1}{N} = \frac{1}{M} - \frac{\phi}{K_f} \tag{2.14}$$

The parameter M is the Biot modulus, whereas K_f is the bulk modulus of the pore fluid. We can calculate the material property M acccording to the formula given by Aichi and Tokunaga (2012) for a saturated transversely isotropic material:

$$\frac{1}{M} = 2(1-b_h)\left[\frac{(1-\nu_{hh})\,b_h}{E_h} - \frac{\nu_{zh}b_z}{E_z}\right] + \frac{(1-b_z)}{E_z}\,(b_z - 2\nu_{zh}b_h) + \phi\left(\frac{1}{K_f} - \frac{1}{K_\phi}\right) \tag{2.15}$$

From this we can deduce the undrained case, where the pore fluid mass $m_f = \rho_f V_\phi$ remains constant. Here ρ_f stands for the fluid density. The change of pore pressure in undrained conditions and in function of strains writes then as:

$$\mathrm{d}p_f = M\left(b_i\alpha_{d,i} - \phi\alpha_\phi + \phi\alpha_f\right)\mathrm{d}T + Mb_i\mathrm{d}\varepsilon_i \tag{2.16}$$

A similar relationship, with respect to stress, provides:

$$\mathrm{d}p_f = \frac{\phi\,(\alpha_f - \alpha_\phi)\,\mathrm{d}T + b_i C_{ij}\mathrm{d}\sigma_j}{\frac{1}{M} + b_i C_{ij} b_j} \tag{2.17}$$

For this transversely isotropic relationship, heterogeneous at the micro-scale, 11 material coefficients (e.g. E_h, E_z, ν_{hh} ,ν_{zh}, b_h, b_z, G, K_ϕ,$\alpha_{d,h}$, $\alpha_{d,z}$, α_ϕ) are required for the solid-fluid composite, as well as the porosity ϕ, and the characteristics of the pore fluid K_f and α_f.

2.1.2 Equivalent isotropy

When analysing experiments under isotropic stress conditions, it can be helpful to utilize some poromechanical relationships for equivalent isotropy. Under isothermal conditions and isotropic stresses, the volumetric strain ε_v is described with respect to the changes in isotropic Terzaghi effective stress σ' ($\sigma' = \sigma - p_f$, where σ is the total isotropic stress and p_f the pore fluid pressure) and the temperature T as a sum of partial derivatives:

$$\mathrm{d}\varepsilon_v = \frac{1}{K_d}\mathrm{d}\sigma' + \frac{1}{K_s}\mathrm{d}p_f - \alpha_d \mathrm{d}T \tag{2.18}$$

in which K_d is the drained bulk modulus, K_s the unjacketed modulus and α_d the drained volumetric thermal expansion coefficient. α_d is related to the linear thermal expansion coefficients by:

$$\alpha_d = \alpha_{d,z} + 2\alpha_{d,h} \tag{2.19}$$

We are able to measure Biot's modulus H through a change of pore pressure under constant confining stress, defined as:

$$\frac{1}{H} = \frac{1}{V_0}\left(\frac{\partial V}{\partial p_f}\right)_{\mathrm{d}\sigma=0} = \frac{1}{K_d} - \frac{1}{K_s} \tag{2.20}$$

The equivalent isotropic Biot's coefficient b is defined as:

$$b = 1 - \frac{K_d}{K_s} = \frac{K_d}{H} \tag{2.21}$$

In undrained conditions, the mass of pore fluid remains constant, which results in a change in volumetric strain and pore pressure as follows:

$$\mathrm{d}\varepsilon_v = \frac{1}{K_u}\mathrm{d}\sigma, \quad \mathrm{d}p_f = B\mathrm{d}\sigma \tag{2.22}$$

Hereby K_u is the undrained bulk modulus and B the Skempton coefficient (Skempton, 1954). Following the approach of Belmokhtar et al. (2017a), the moduli D_i, U_i and H_i, which describe the anisotropic strain response to isotropic loads, are defined for a drained isotropic compression:

$$D_i = \left(\frac{\mathrm{d}\sigma}{\mathrm{d}\varepsilon_i}\right)_{\mathrm{d}p_f=0} \tag{2.23}$$

for an undrained isotropic compression:

$$U_i = \left(\frac{\mathrm{d}\sigma}{\mathrm{d}\varepsilon_i}\right)_{\mathrm{d}m_f=0} \tag{2.24}$$

and for a pore pressure loading:

$$H_i = \left(\frac{\mathrm{d}p_f}{\mathrm{d}\varepsilon_i}\right)_{\mathrm{d}\sigma=0} \tag{2.25}$$

We can also define the anisotropy ratios between deformations in h and in z-direction with $R_D = D_h/D_z$, $R_U = U_h/U_z$ and $R_H = H_h/H_z$, which provides:

$$D_h = K_d\left(2 + R_D\right), \quad D_z = K_d\left(1 + \frac{2}{R_D}\right) \tag{2.26}$$

$$H_h = H\left(2 + R_H\right), \quad H_z = H\left(1 + \frac{2}{R_H}\right) \tag{2.27}$$

The undrained moduli U_i are linked to the drained ones with the relationship:

$$\frac{1}{U_i} = \frac{1}{D_i} - B\frac{1}{H_i} \tag{2.28}$$

One is able to deduce a relationship between the parameters from isotropic and deviatoric experiments:

$$E_z = D_z\left(1 - 2\nu_{zh}\right), \quad E_h = \frac{1 - \nu_{hh}}{\frac{1}{D_h} + \frac{\nu_{zh}}{E_z}} \tag{2.29}$$

Also the parallel and perpendicular Biot's coefficients b_h and b_z can be calculated concurrently:

$$b_h = \frac{\nu_{zh}/H_z + 1/H_h}{\nu_{zh}/D_z + 1/D_h} \tag{2.30}$$

$$b_z = 2\nu_{zh}b_h + \left(1 - 2\nu_{zh}\right)\frac{D_z}{H_z} \tag{2.31}$$

For the two anisotropic Skempton's coefficients B_z and B_h one can find (Cheng, 1997):

$$B_i = \frac{3\sum_j C_{ij} - \frac{1}{K_s}}{\frac{1}{K_d} - \frac{1}{K_s}}B \tag{2.32}$$

This provides an alternative set of parameters (K_d, H, R_D, R_H, ν_{hh}, ν_{zh}, G, K_ϕ) for the transversely isotropic poroelasticity. The coefficients K_d, H, R_D and R_H are determined in drained isotropic test. The parameters ν_{hh}, ν_{zh} and G are measured in triaxial tests under deviatoric loading. K_ϕ can be determined separately in an unjacketed test by measuring the change in pore fluid mass during equal increments of pore pressure and total stress change. This fluid mass change is generally very small for common geomaterials, making the precise measurement a challenging task. For homogeneous materials at the micro-scale, one can assume $K_\phi = K_s$ (Cheng, 1997). If this is not known *a priori*, it is practical to use some poromechanical relationships for calculating K_ϕ, as given by Ghabezloo et al. (2008), which provide:

$$\frac{1}{K_\phi} = \frac{1}{K_f} - \frac{\left(1/K_u - 1/K_d + 1/H\right)}{\phi H\left(1/K_d - 1/K_u\right)} \tag{2.33}$$

The parameter K_ϕ can hence be replaced by K_u, which is less tedious to be determined in an undrained isotropic compression test. The porosity ϕ can be obtained by volume and mass measurements of oven-dried specimens, whereas the bulk modulus of the pore fluid K_f is

generally known for a specific fluid, such as for example water. If one is able to measure more than the minimum 8 coefficients (K_d, H, R_D, R_H, ν_{hh}, ν_{zh}, G, K_u) together with ϕ and K_f, an overdetermined set of parameters is obtained, which can help to check for a compatibility of these values.

2.1.3 Thermal pressurization

It is interesting to note, that under constant stresses and for isotropic materials, the expression of Eq. (2.17) becomes equivalent to the relationship presented by Ghabezloo et al. (2009b), which writes as:

$$\mathrm{d}p_f = \Lambda \mathrm{d}T + B\mathrm{d}\sigma, \qquad \Lambda = \frac{(\alpha_f - \alpha_\phi)}{\frac{1}{\phi H} + \left(\frac{1}{K_f} - \frac{1}{K_\phi}\right)} \tag{2.34}$$

where Λ represents the thermal pressurization coefficient. In undrained heating tests, where the fluid mass in a specimen remains constant, one obtains the following change in strains and pore pressure for constant stresses:

$$\mathrm{d}\varepsilon_i = -\alpha_{u,i}\mathrm{d}T \tag{2.35}$$

$$\mathrm{d}p_f = \Lambda \mathrm{d}T \tag{2.36}$$

where $\alpha_{u,i}$ includes the two linear undrained thermal expansion coefficients perpendicular and parallel to the bedding orientation:

$$\alpha_{u,i} = [\alpha_{u,h}, \alpha_{u,h}, \alpha_{u,z}, 0, 0, 0]^\top \tag{2.37}$$

The volumetric drained thermal expansion coefficient can be calculated as $\alpha_u = 2\alpha_{u,h} + \alpha_{u,z}$.

Eq. (2.34) evidences, that the thermal pressurization is mainly caused by the discrepancy between the bulk thermal expansion coefficients of the fluid α_f and that of the pore space α_ϕ. In geomechanical applications, when the material is micro-homogeneous, we can assume that α_ϕ is equal to the drained volumetric thermal expansion coefficient α_d. In the same manner, one can take the bulk modulus of the pore space K_ϕ equal to the unjacketed bulk modulus K_s. The porosity ϕ, the Biot's moduls H and the bulk modulus of the pore fluid are also involved in the thermal pressurization.

Comparing Eq. (2.2) with (2.35) and (2.36), one obtains the following relationship:

$$\alpha_{u,i} = \frac{\Lambda}{H_i} + \alpha_{d,i} \tag{2.38}$$

This can be simplified in terms of equivalent isotropy (Ghabezloo et al., 2009b) as follows:

$$\alpha_u = \frac{\Lambda}{H} + \alpha_d \tag{2.39}$$

We can hence evaluate $\alpha_{u,z}$, $\alpha_{u,h}$ and Λ in undrained heating tests, whereas $\alpha_{d,z}$ and $\alpha_{d,h}$ are determined in drained heating. The moduli H_z and H_h can then be calculated using Eq. (2.38). Alternatively, if H_i are measured, the parameter set ($\alpha_{u,i}$, Λ, H_i and $\alpha_{d,i}$) can be checked for its compatibility (Menke, 1989; Hart and Wang, 1995; Braun et al., 2019).

2.1.4 Heat and fluid transport

Assuming one dimensional fluid flow following Darcy's law, Ghabezloo and Sulem (2009) and Ghabezloo et al. (2009b) provided the following equation in terms of equivalent isotropic properties:

$$\frac{\mathrm{d}p_f}{\mathrm{d}t} = \frac{1}{\rho_f S}\frac{\partial}{\partial z}\left(k\frac{\rho_f}{\mu_f}\frac{\partial p_f}{\partial z}\right) + B\frac{\mathrm{d}\sigma}{\mathrm{d}t} + \Lambda\frac{\mathrm{d}T}{\mathrm{d}t} \tag{2.40}$$

where k is the intrinsic permeability, ρ_f the fluid density, μ_f the fluid dynamic viscosity. S is the storage coefficient, given by:

$$S = \frac{b}{K_d} + \phi_0\left(\frac{1}{K_f} - \frac{1}{K_\phi}\right) \tag{2.41}$$

This relationship can be extended for the framework of transverse isotropy, where parallel permeability k_h and perpendicular permeability k_z can differ, resulting in:

$$k_i = [k_h, k_h, k_z]^\top \tag{2.42}$$

Assuming a constant permeability and fluid density, one can write down for a three dimensional case:

$$\frac{\mathrm{d}p_f}{\mathrm{d}t} = \frac{1}{\mu_f S}k_i\nabla^2 p_f + \frac{1}{3}B_i\frac{\mathrm{d}\sigma_i}{\mathrm{d}t} + \Lambda\frac{\mathrm{d}T}{\mathrm{d}t} + q_p \tag{2.43}$$

where q_p is an additional volumetric pressure source.

The heat transport is considered with Fourier's heat equation, under the assumption of a constant thermal conductivity λ, simplified to:

$$\rho C\frac{\mathrm{d}T}{\mathrm{d}t} - \lambda_i\nabla^2 T = q_T \tag{2.44}$$

with C representing the specific bulk heat capacity, ρ the bulk density, q_T a volumetric heat source, and λ_i the transversely isotropic thermal conductivity:

$$\lambda_i = [\lambda_h, \lambda_h, \lambda_z]^\top \tag{2.45}$$

2.2 Characteristics of the COx claystone

2.2.1 Geological context

A lithostratigraphy in Fig. 2.2 presents a detailed vertical plan of the geological layers near the Bure URL, compared with the geological map in Fig. 1.1. The COx layer is grouped into different sub-layers (Armand et al., 2017b):

- The clay unit (UA) consists of about two-thirds of the total layer thickness. The URL is located within this layer, at around 490 m depth. Small mineralogical variations and a high clay fraction of 40 – 60 % were reported at the URL level.
- A transition unit (UT) is located between the clay unit (UA) and the silty carbonate-rich unit (USC). This layer shows a highest carbonate content (40 – 90 %).
- The silty carbonate-rich unit (USC) above the UT shows a high variability of the petrophysical parameters, due to lithological alterations (marl and carbonate siltstone), resulting also in a more heterogenous mineral composition.

At the level of the URL, the stress state was estimated as follows (Wileveau et al., 2007a; Conil et al., 2018): a total vertical stress $\sigma_v = 12.7$ MPa, a major horizontal stress $\sigma_H =$ 14 - 16 MPa, a minor horizontal stress $\sigma_h = 12.4$ MPa, and a pore pressure $p_f = 4.5$ MPa, resulting in a mean Terzaghi effective stress $\sigma' = (\sigma_v + \sigma_H + \sigma_h)/3 - p_f$ between 8.5 and 9.2 MPa.

2.2.2 Microstructure

Various studies were carried out to characterize the COx microstructure by means of X-ray diffraction (e.g. Gaucher et al., 2004; Andra, 2005; Yven et al., 2007; Robinet, 2008). Gaucher et al. (2004) reported a clay fraction of around 45 - 50 %, which itself is constituted of around 55 % I/S (illite–smectite interstratified minerals), 30 % illite and 15 % kaolinite and chlorite, illustrated in Fig. 2.3.

The fraction of smectite (50 - 70 % of I/S) is responsible for the swelling capacity of the claystone (e.g. Mohajerani et al., 2011; Delage et al., 2014) and the self-sealing phenomenon (e.g. Davy et al., 2007; Zhang, 2013; Menaceur et al., 2015; De La Vaissière et al., 2015; Auvray et al., 2015b; Giot et al., 2018).

Most of the porosity is located within the clay matrix (Robinet et al., 2015), with porosity estimates from 14 to 20 %, with around 18 % at the URL level (Yven et al., 2007). The natural water content was estimated with values between 5 to 8 % (Armand et al., 2017b), with 8 ± 1.2 % at URL level (Conil et al., 2018).

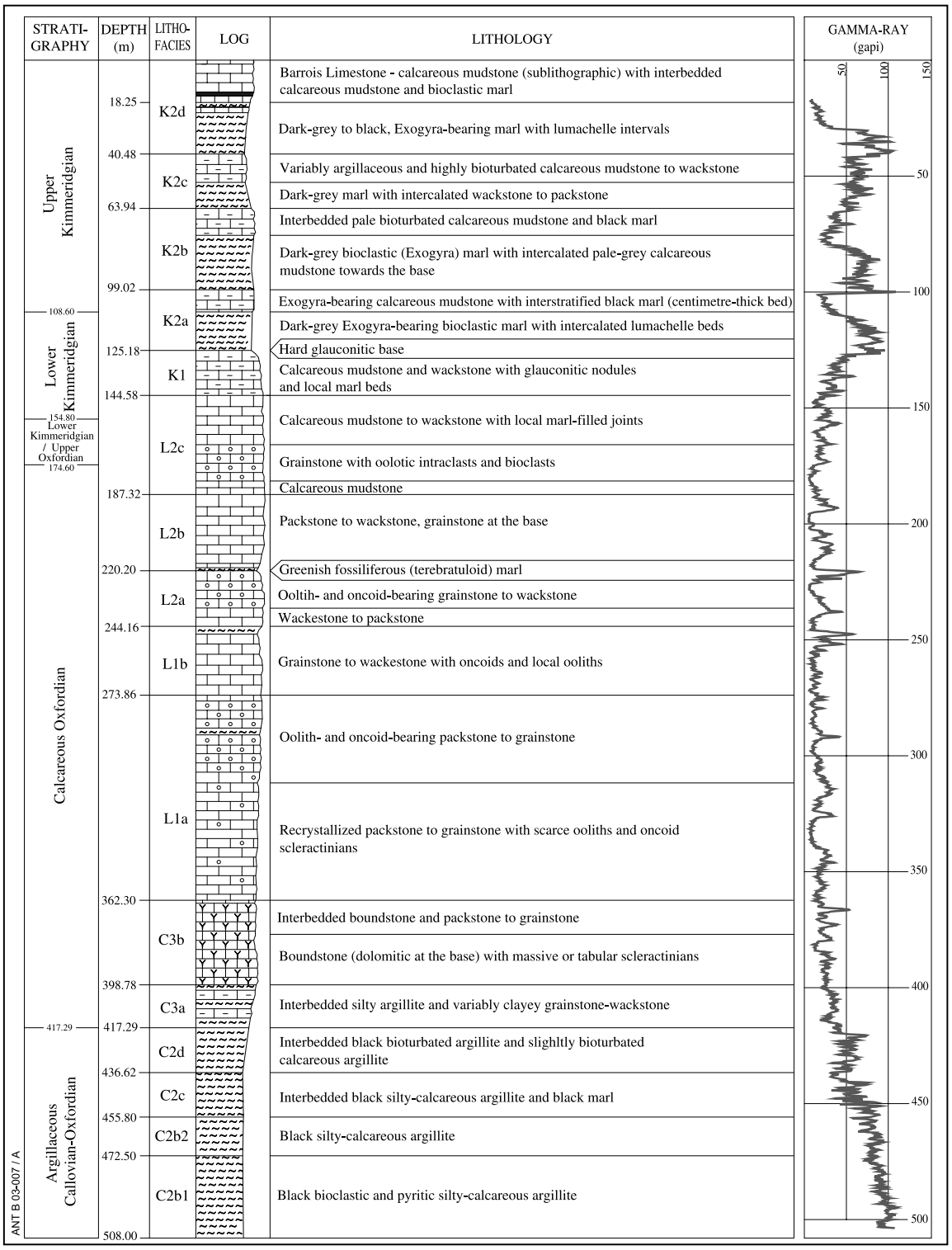


Fig. 2.2.: Lithostratigraphy of the borehole EST205, taken from Gaucher et al. (2004)

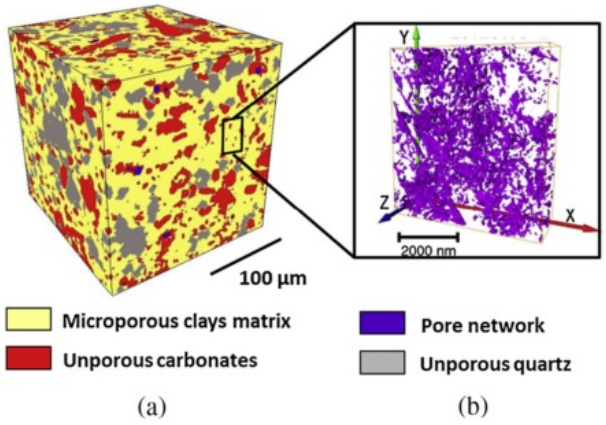


Fig. 2.3.: a) COx clay matrix obtained from synchrotron X-ray microtomography (Robinet et al., 2012), b) 3D reconstruction of the pore network from FIB/SEM images (Song et al., 2015), adopted from (Armand et al., 2017b)

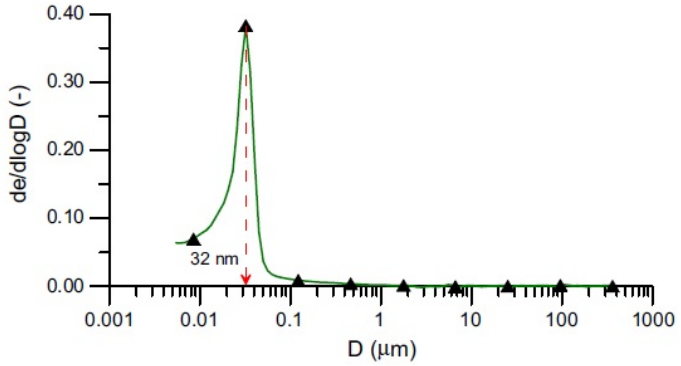


Fig. 2.4.: Cumulative pore size distribution measured by mercury intrusion porosimetry on a freeze dried sample (Menaceur et al., 2016)

The mean diameter of pores accessed by mercury intrusion, measured on freeze-dried specimens, was determined to 32 nm (Delage et al., 2014; Menaceur et al., 2016), with a cumulative pore size distribution curve presented in Fig. 2.4. Armand et al. (2017b) noted, that this small mean pore diameter is responsible for the low permeability of COx.

2.2.3 Variability of measurements

A rather large dispersion of the THM properties of the COx claystone, determined in previous laboratory investigations, showed a necessity for identifying and eliminating disturbing factors, from the core extraction up to testing procedures in the laboratory. The main factors described in the following section are:

- Varying mineralogy
- Coring methods/ location
- Damage through resaturation/swelling

- Effect of saturation on parameters
- Time dependent material behaviour
- Measurement methods

It is therefore important to have detailed information on the sample history and applied procedures, in order to be able to classify experimental results. The influence of rock mineralogy on mechanical and thermal parameters was described by Conil et al. (2018) and should be considered, especially when comparing samples from different depths. Over the years of research carried out at the Bure URL, the coring methods have changed. First, cores where extracted through vertical boreholes from the surface, whereas nowadays cores can be retrieved from the underground laboratory. The reduced core length from the galleries allows more precise spatial sample localization, less mechanical impact on the material and faster extraction to minimize drying. Monfared et al. (2011b) and Ewy (2015) stated that sample drying should be avoided as best as possible, as it can damage the material through drying cracks. Furthermore, the more desaturated a sample is, the more water has to be added in the resaturation process in the laboratory. Mohajerani et al. (2011), as well as Ewy (2015), observed, that with a lower saturation degree, the sample swelled more during resaturation, which can impair the mechanical properties. They stated therefore, that samples should always be resaturated under *in situ* effective stress.

Pham et al. (2007) observed, that desaturated samples had a higher mechanical resistance than fully saturated ones. This can be explained either by the capillary forces in an unsaturated material, acting as a confining mechanism, or by damage induced during the resaturation process. Efforts are made to define which samples represent best the *in situ* intact rock (Conil et al., 2018).

Another issue in experiments is the low permeability of COx claystone. This permits only slow drainage, which demands adopted testing protocols to ensure a homogeneous pore pressure field. Numerical and analytical methods allow estimating the effect of applied loading rates, durations and tested sample geometries. These have to be recorded and justified when presenting drained and undrained parameters.

When analysing measurements, corrections are necessary to eliminate some inevitable errors induced by the testing devices. As the deformations of the tested rock are rather small, the parasitic deformations of porous elements, drainage system, oedometer ring and LVDT or strain gage system cannot be neglected and have an influence on the measured response. Especially thermal deformations of the devices have to be considered, requiring a thorough selection and calibration of used equipment.

2.2.4 Hydromechanical properties

Oedometric compression

Various oedometric tests on COx claystone are described in the literature. By keeping the pore pressure constant and changing the axial stress, the oedometric modulus E_{oed} can be measured on specimens [Eq. (2.46)]. With the deformations of a test under constant axial stress and changing pore pressure, and by knowing the oedometric modulus, the Biot's coefficient can be calculated [Eq. (2.47)].

$$E_{oed} = K_d + \frac{4}{3}G = \left(\frac{\mathrm{d}\sigma_1}{\mathrm{d}\varepsilon_1}\right)_{p_f} \tag{2.46}$$

$$\frac{E_{oed}}{b} = \left(\frac{\mathrm{d}p_f}{\mathrm{d}\varepsilon_1}\right)_{\sigma_1} \tag{2.47}$$

Data on the oedometric modulus and Biot's coefficient from different authors is compared in Fig. 2.5 and explained in the following.

Vincké et al. (1998) performed six oedometric tests on samples, cored perpendicular and parallel to the bedding plane. The samples were tested in saturated conditions, however, the method for resaturation was not specified. The loading was carried out stepwise, in order to distinguish undrained and drained deformations. Biot's moduli determined on perpendicular and parallel samples showed no great difference, with the parallel values being slightly higher. Escoffier (2002) carried out 18 oedometric test with different samples under different stress levels and with loading perpendicular and parallel to bedding. The samples were saturated under 3 MPa Terzaghi effective stress and tested under loading steps and following equilibrium phases. In the first 9 tests, axial stress was changed under constant pore pressure. In addition, 9 complementary tests with changing pore pressure under constant axial stress were conducted. By doing so, the author evaluated 9 pairs of oedometric moduli and Biot's coefficients. Bemer et al. (2004) saturated 3 samples with water vapour. It was supposed, that the unconfined samples swelled during resaturation and tested in damaged condition. In addition to a drained test and a pore pressure test, also an undrained test was conducted for each sample and each stress level. However, the measured undrained parameters were not corrected for the deformability of the drainage system, and might therefore underestimate the true values. Mohajerani et al. (2011) observed during oedometric swelling tests, that the resaturation and hydration of COx samples under zero stress led to excessive swelling and damage. They found that the material swelled even under vertical stresses higher than the *in situ* stress, and suggested that samples should be hydrated under the *in situ* stress, in order to limit damage. This statement was later confirmed by Ewy (2015), to be the case for shales in general. Mohajerani et al. (2011) determined then the oedometric properties in two tests on two saturated samples.

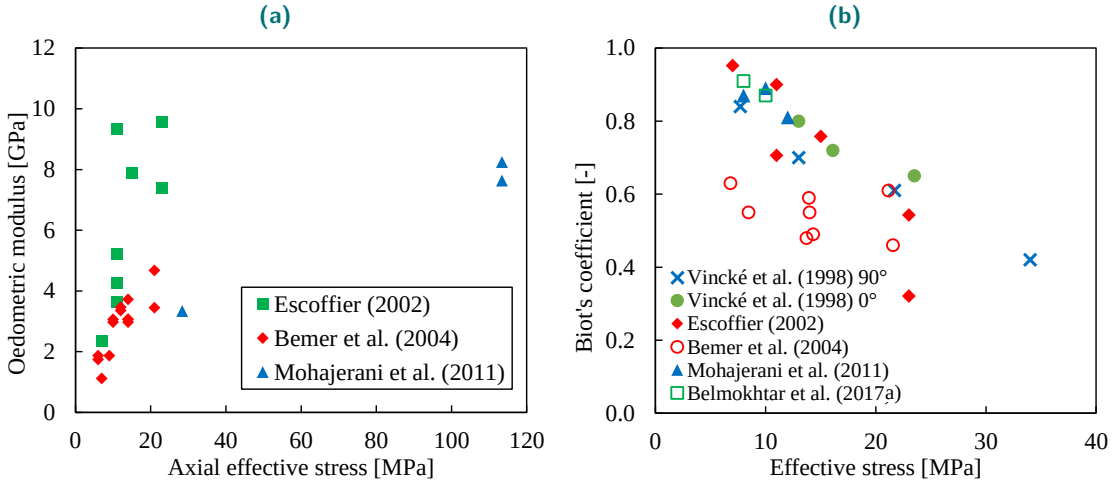


Fig. 2.5.: a) Oedometric modulus and b) Biot's coefficient under various effective axial stresses

Values for Biot's coefficient obtained by different authors show a dependency on the effective stress. The Biot's coefficient decreases with increasing effective stress starting from values around 0.9 at the *in situ* effective stress of around 9 MPa. A good coherence between b obtained in an isotropic cell by Belmokhtar et al. (2017a) and the other authors, who worked with oedometric devices, can be observed. Coefficients b determined by Bemer et al. (2004) appear to be lower than the common trend, however their oedometric moduli are in quite good accordance with Mohajerani et al. (2011).

Undrained isotropic compression

Among the authors who conducted undrained isotropic experiments on the COx claystone, only the more recent works mentioned here investigated fully saturated samples.

Escoffier (2002) recorded the undrained bulk modulus by measuring the instant deformation of a step unloading during a drained test. Samples were resaturated under 3 MPa Terzaghi effective stress. The step loading was repeated on one sample for 4 different stress levels. Mohajerani (2011) carried out one loading-unloading cycle on a hollow cylinder sample (60 mm inner diameter, 100 mm outer diameter), while the drainage system was closed. The error on the measurements caused by the dead volume of the drainage system was corrected and allowed to determine the undrained bulk modulus, as well as the Skempton coefficient. Belmokhtar et al. (2017a) measured in two tests the undrained bulk moduli of two samples (38 mm diameter, 10 mm height) for different stress levels. The measurements were corrected for the effects of the drainage system.

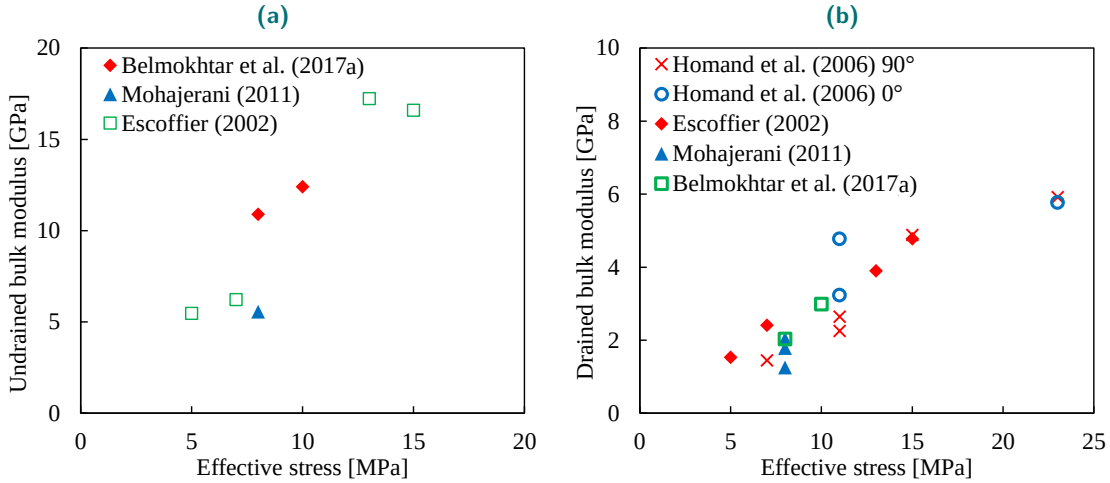


Fig. 2.6.: a) Undrained bulk modulus and b) drained bulk modulus with respect to effective stress

Comparing the different data on the undrained bulk modulus described in the literature, a rather large range of values is observed, and the parameter appears to be strongly dependent on the effective stress, as can be seen in Fig. 2.6a.

Drained isotropic compression

A comparison of laboratory data on the drained bulk modulus is given in Fig. 2.6b, showing a common trend of increasing modulus with increasing effective stress.

Escoffier (2002) tested one resaturated (under 3 MPa Terzaghi effective stress) sample under 4 different effective stresses. For each stress level, the confinement pressure was decreased in one step. When the sample stopped to deform, the measured total deformations were used to calculate the drained bulk modulus. Mohajerani (2011) tested 3 different samples under the *in situ* stress conditions. A disk-shaped sample of 38 mm diameter and 10 mm height was investigated in a loading-unloading cycle. Two tests were conducted on hollow cylinder samples, one with sudden change of confinement pressure and an equilibration phase, one under a slow, linear loading-unloading cycle. We can observe, that even for tests on the same stress level, the measured parameters can vary significantly between tests. Belmokhtar et al. (2017a) measured K_d on two samples tested at two different stress levels. The disk-shaped sample was loaded under constant rate of confining stress.

Unjacketed isotropic compression

Rather few and dispersed data is provided on the unjacketed modulus (Fig. 2.7), that is difficult to measure, given the small deformations generated through this kind of loading.

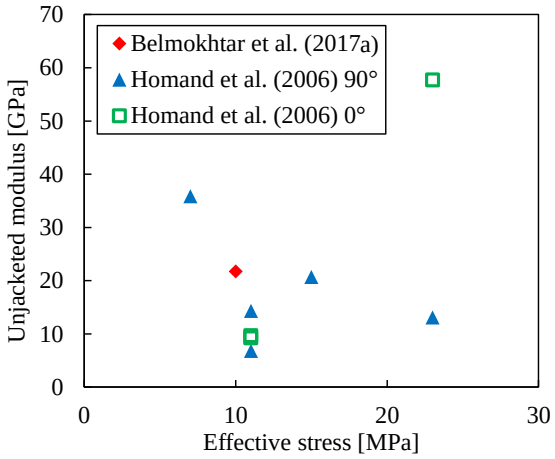


Fig. 2.7.: Unjacketed bulk modulus with respect to effective stress

Homand et al. (2006) used oedometric data, obtained from Vincké et al. (1998) and Escoffier (2002), to back calculate the drained bulk modulus K_d (see Fig. 2.6b) and the unjacketed modulus K_s. Only Belmokhtar et al. (2017a) carried out a direct measurement of K_s, following the previously described drained and undrained tests.

Deviatoric tests

Different deviatoric tests were carried out on COx samples using triaxial cells. In unconfined compression tests or triaxial tests under confinement, the drained Young's modulus E and the Poisson ratio ν can be measured, if the sample is in hydraulic equilibrium. Under fast loading or when the drainage is completely prevented, porous materials show an undrained response, characterized by the undrained Young's modulus E_u and the undrained Poisson ratio ν_u. When a sample is compressed until failure, the shear strength and the failure criterion can be determined. In Fig. 2.8, data on saturation dependent measurements is provided, whereas Fig. 2.9 shows compiled data from saturated specimens at different stress levels.

Chiarelli (2000) conducted a large number of triaxial test, under various confining stresses. The samples of 50 mm diameter and 100 mm height were compressed perpendicular to the bedding planes, with a rate of 6×10^{-6} s^{-1}. Compared to the loading rate in the order of 10^{-8} s^{-1}, determined by Belmokhtar et al. (2018) as necessary for full drainage of triaxial specimens, this loading rate seemed rather high. It is not clear if these experiments have satisfied drained conditions. Some samples were tested with their natural water content, others were resaturated under relative humidity (RH) of 100 %, 70 % and 60 %. Young's modulus and Poisson's ratio were determined in these tests (Fig. 2.8). One can observe, that the highest Young's moduli were obtained for samples with a natural water content, with a mean value of 92.7 %. The moduli for resaturated samples under RH 60 % appear

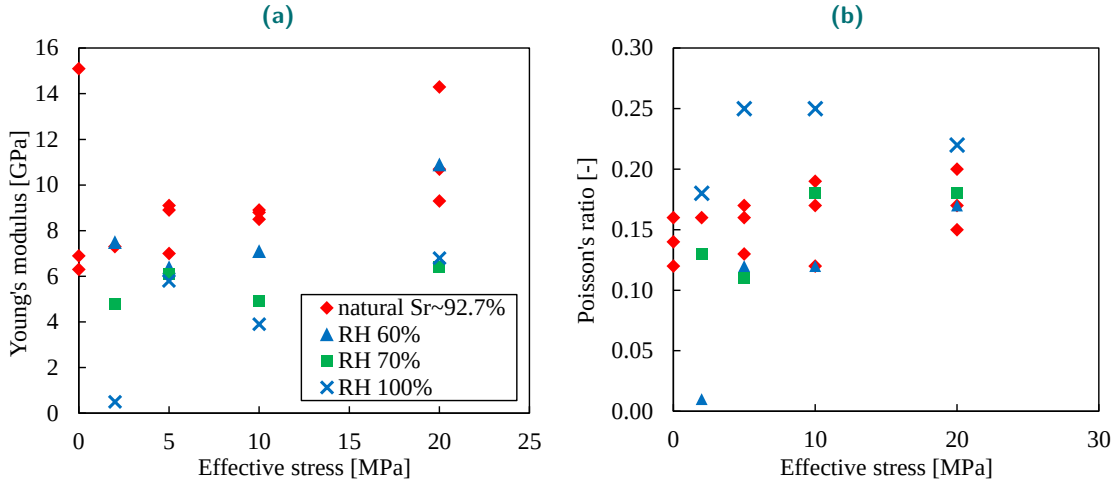


Fig. 2.8.: a) Young's modulus and b) Poisson's ratio with respect to effective stress, tested on specimen with different saturation degrees (Chiarelli, 2000)

slightly lower, and decrease as the relative humidity increases. For the Poisson ratio however, we can observe a direct dependency on the saturation degree, as the highest ratios were determined for the samples at RH 100 %, decreasing with saturation degree. For comparison reasons, only the completely resaturated test are plotted in Fig. 2.9. Homand (2000) tested samples in unconfined compression tests, perpendicular and parallel to the bedding plane. The samples were tested in saturated conditions. The measured parameters appear to be higher than values from other authors (Fig. 2.9). Menaceur et al. (2015) sheared saturated hollow cylinder samples in a triaxial apparatus, under rates in the order 10^{-10} s^{-1}. The loading direction was perpendicular to the bedding. Two tests were carried out under elevated temperatures of 80 °C, however the author found, that temperature had only a slight effect on the behaviour. Belmokhtar et al. (2018) carried out drained triaxial tests on two saturated samples, having improved the drainage conditions with lateral geotextiles and having confirmed the loading rate by numerical calculations. The specimens were sheared with a rate of 6.6×10^{-8} s^{-1} at two different stress levels. Mechanical properties obtained by Zhang et al. (2012), on unconfined specimens, saturated at RH 99 % are also shown in Fig. 2.9.

One can observe, that the supposedly fully resaturated samples of Chiarelli (2000) and Menaceur et al. (2015) show a quite good linear dependency of the Young's modulus perpendicular to the bedding on the Terzaghi effective stress (Fig. 2.9a). The data on the Poisson ratio however seems rather dispersed (Fig. 2.9b).

In the work of Belmokhtar et al. (2018), a compilation on the shear resistance, obtained in their experiments, together with data of Hu et al. (2014) and Menaceur et al. (2015), is presented (Fig. 2.10). Note that these experiments were carried out under various different testing conditions, as described before.

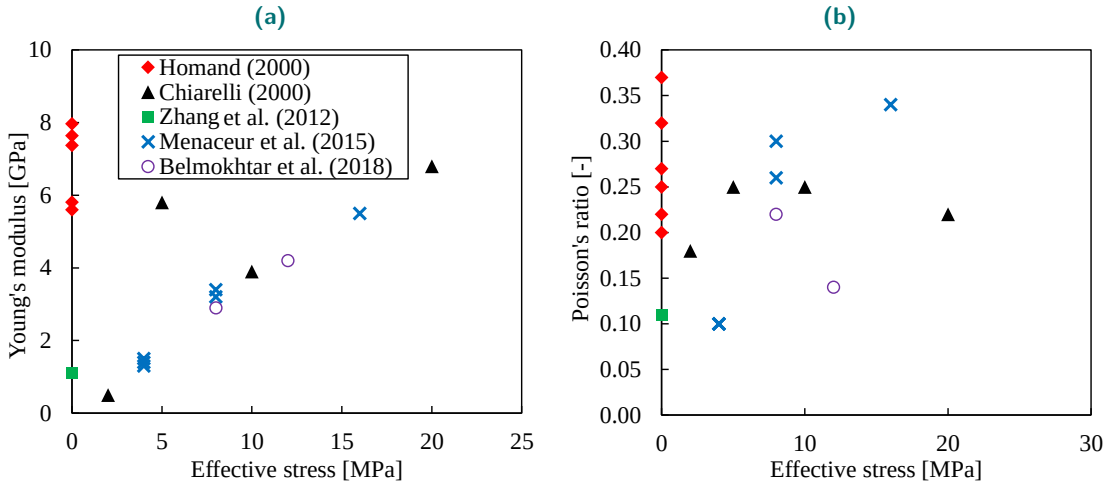


Fig. 2.9.: a) Young's modulus and b) Poisson's ratio with respect to effective stress tested on saturated specimens

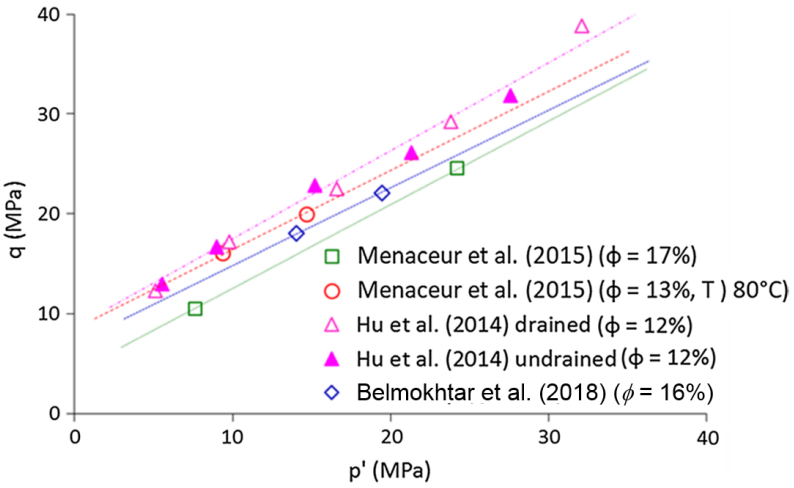


Fig. 2.10.: Comparison of the shear envelopes obtained from shear tests on saturated specimens, conducted by different authors, taken from Belmokhtar et al. (2018)

2.2.5 Permeability

In numerous *in situ* hydraulic permeability experiments, a mean permeability of 4.18 $\times$ 10^{-20} m^2 was determined through 399 tests (De La Vaissière et al., 2017). Within the UA layer, where the URL is situated, this data gave a mean permeability of 4.89 $\times$ 10^{-20} m^2. Laboratory investigations showed lower permeabilities, such as that determined by Davy et al. (2007) in the order of 10^{-21} m^2. Mohajerani et al. (2011) found values with k_z = 2 $\times 10^{-21}$ m^2 and 0.6 $\times 10^{-21}$ m^2 perpendicular to the bedding plane, using an inverse analysis of transient oedometric compression behaviour. In their pore pressure step tests, Harrington et al. (2017) measured similar values for the permeability perpendicular to the bedding plane (1.6 – 1.8 $\times 10^{-21}$ m^2). Recently, Giot et al. (2018) compared measurements from different laboratory testing methods. They observed a constant permeability of around 4.2 $\times 10^{-21}$ m^2 during steady state flow, while in transient pulse tests the permeability decreased with subsequent tests from 50.1 to 3.8 $\times 10^{-21}$ m^2. They suspected, that a swelling of the clay particles and gradual obstruction of pore connections caused this time dependent characteristics. Menaceur et al. (2015) and Harrington et al. (2017) found higher permeabilities parallel than perpendicular to bedding, with 0.9 - 2.9 $\times 10^{-20}$ m^2 and 4.5 - 7.0 $\times 10^{-21}$ m^2, respectively. *In situ* experiments confirmed this anisotropy of permeability, but values of about one order of magnitude higher were found there (4.1 $\times 10^{-20}$ m^2 perpendicular and 7.2 $\times 10^{-20}$ m^2 parallel to the bedding by Enssle et al. (2011), and around 1.0 $\times 10^{-20}$ m^2 parallel to the bedding plane by Vinsot et al. (2011)). In the analysis of the TED and TER *in situ* heating experiments, pore pressure measurements could be reproduced in a satisfactory manner, using permeability values of 3.0 and 6.0 $\times 10^{-20}$ m^2 for perpendicular and parallel directions to bedding, respectively (Armand et al., 2017a).

The rather high differences of observed values *in situ* and in the laboratory, as well as possible effects due to the resaturation of specimens (Conil et al., 2018; Giot et al., 2018), are still subject of ongoing investigations.

Yang et al. (2010) tested the gas permeability of COx samples that were resaturated or desaturated to different degrees of saturation (S_r). Using pulse tests conducted with argon gas, they evaluated an effective gas permeability under 5 MPa confining stress, in the order of 10^{-19} m^2. They noted that for a saturation degree S_r greater than 90 % the gas flow became discontinuous. No significant increase of the permeability through mechanical damage in deviatoric loading was reported, however the authors found that increase of isotropic confining stress decreased the permeability.

The gas permeability of intact COx samples, dried at 65 °C, was determined by M'Jahad et al. (2016), with values ranging between 1.35 $\times 10^{-19}$ m^2 and 6.42 $\times 10^{-17}$ m^2. For macro-cracked specimens, they found values between 6.6 $\times 10^{-19}$ m^2 and 3.36 $\times 10^{-16}$ m^2. Davy et al. (2007) found, that the steady state gas permeability of macro cracked COx

Tab. 2.1.: Laboratory data on the thermal conductivities λ (in W/m/K), provided by Conil et al. (2010) and Auvray et al. (2005) (table taken from Garitte et al., 2014)

	λ_{par}	λ_{per}	λ_0	λ_h/λ_v	n_{par}	n_{per}
TED area (DBE)						
Average	1.96	1.28	1.69	1.52	14	12
SD	0.08	0.07	0.06	0.08		
TED area (LAEGO)						
Average	1.89	1.26			5	3
SD	0.05	0.04				
TER area (LAEGO)						
Average	1.91	1.25			4	3

n_{par} and n_{per} are the number of measurements parallel and perpendicular to the bedding, respectively

samples was in the order of 10^{-14} m^2. The samples were preserved as best as possible from *in situ* conditions, with water contents between 7.4 and 8.3 %, but no explicit degrees of saturation given. The authors also observed a reduction of the gas permeability with increasing confining stress, which they explained by the crack closure through compression. Interestingly, for confining stress larger than *in situ*, the gas permeability remained nearly constant.

2.2.6 Heat transport

Garitte et al. (2014) analysed the thermal conduction experiments carried out *in situ* (Conil et al., 2010; Conil and Vitel, 2019) and in the laboratory (Auvray et al., 2005) (Tab. 2.1). They found a good agreement between *in situ* and laboratory measurements, taking into account various experimental uncertainties. These authors also noted that the uncertainty of specific heat of $\pm$100 J/kg/K had a minor influence on the thermal conductivity, resulting in a specific heat of the solid of about 800 - 820 J/kg/K and a bulk specific heat of 1000 J/kg/K, obtained from the data of Conil et al. (2010) and Auvray et al. (2005). However, a variation of the bulk phase composition could have a larger effect on the thermal conductivity. Based on their analysis, they proposed reference parameters of $\lambda_h = 1.88$ W/m/K and $\lambda_z = 1.26$ W/m/K.

It is also interesting to note, that during two years of *in situ* heating experiments, no variation of thermal conductivity with temperature could be observed (Conil, 2012).

2.2.7 Thermal volume changes

Drained thermal behaviour

In their drained heating tests on Opalinus clay, Monfared et al. (2011a) measured the thermal volume changes of the material. Under heating, up to 65 °C, the specimens expanded, and showed a thermo-plastic contraction at higher temperatures. Thermoplastic volume changes along the first heating path were evidenced after a subsequent cooling and reheating cycle, where the volume changes remained elastic. The temperature, at which plastic contraction occurred, was close to the maximum temperature at which the material was previously exposed to during their geological history. This thermoplastic behaviour is similar to that of clay, which thermal expansion properties depend on their degree of consolidation. Clays exhibit a thermoelastic expansion when in overconsolidated state, and thermoplastic contraction in normally consolidated state (e.g. Baldi et al., 1988; Sultan et al., 2002 on Boom clay, Abuel-Naga et al., 2007 on Bangkok clay). Recently, Belmokhtar et al. (2017b) reported a thermoplastic behaviour of COx claystone, similar to that of Opalinus clay. A thermoplastic contraction starting at 48 °C was found to correspond with the maximum burial temperature of the COx claystone of around 50 °C (Blaise et al., 2014). During cooling, they determined a drained volumetric thermoelastic expansion coefficient of 0.48×10^{-4} °C^{-1}. Mohajerani et al. (2014) observed an elastic drained expansion prior to a plastic contraction of heated COx samples in a hollow cylinder device. This phenomenon was compared to the behaviour of clays, that contract from normally consolidated state but expand elastically when they are overconsolidated. A drained thermal expansion coefficient of 0.43×10^{-4} °C^{-1} was estimated for a sample heated after mechanical compression cycles.

Undrained thermal behaviour

A rise of temperature in geomaterials does not only generate thermal strains, but can also induce an increase in pore pressure in undrained state, called thermal pressurization (Ghabezloo and Sulem, 2009). In this regard, various *in situ* heating tests haven been conducted and are currently ongoing in claystone formations. The TER test in COx claystone in the Bure underground laboratory and the HE-D test in Opalinus clay in the Mont Terri rock laboratory allowed to observe a significant thermal pressurization in both formations (see for instance Gens et al., 2007; Garitte et al., 2017; Seyedi et al., 2017; Conil and Vitel, 2019).

As quoted by Gens et al. (2007), the anisotropic nature of stiff clays has significant effects on coupled THM behaviour. They concluded in their sensitivity analysis, that the most

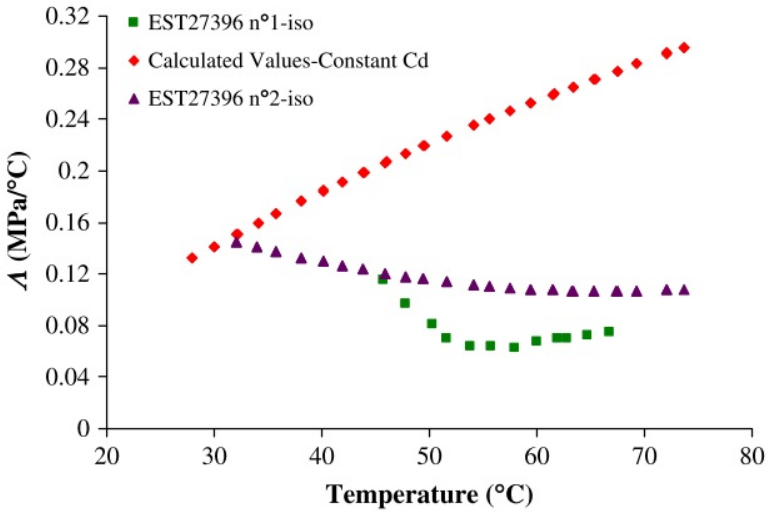


Fig. 2.11.: Thermal pressurization coefficient: experimental values and calculated values, assuming a constant drained compressibility (Mohajerani et al., 2012)

important coupling occurred between thermal and hydraulic behaviour, when the relatively high thermal expansion coefficient of water induces pore pressure increase. This is followed by the coupling between hydraulic and mechanical mechanisms, as the increasing pore pressure depends on the compliance of the rock matrix. Considering the importance of the thermal expansion properties of solid and fluid phases, they also found that a wide range of values from laboratory experiments exist in this regard. It has to be noted, that these authors could still satisfactorily reproduce the thermal strains and pore pressure changes of the HE-D test, by using a purely thermoelastic transversely isotropic constitutive model.

Mohajerani et al. (2012) investigated the undrained thermal behaviour of two COx samples in an isotropic cell. The samples were disk shaped (38 mm diameter, 10 mm height) and drained through a geotextile. It was reported, that the investigated samples were highly desaturated (S_r = 58 %, s = 29 MPa). The resaturated samples were kept at *in situ* stress state and were submitted to a stepwise increase of temperature, up to 80 °C. The pore pressure increase was measured by an external sensor and corrected for the deformation of the drainage system; sample deformations were not recorded. A thermal pressurization coefficient was recorded, decreasing with temperature from around 0.14 MPa/°C at 30 °C to 0.075 - 0.11 MPa/°C at 70 °C (Fig. 2.11). Trying to calculate the thermal pressurization coefficient, under assumption of a constant drained thermal expansion coefficient, its decrease was explained by a decrease of the drained bulk modulus due to the reduction of the effective stress. Concurrently, also values for the undrained thermal expansion coefficient were calculated and given in their work.

Monfared et al. (2011a) presented some data on the undrained thermal properties of Opalinus clay, that could only be reproduced by adopting a thermal expansion coefficient of

the pore fluid higher than that of free water. Similar observations were previously made by Baldi et al. (1988) on low porosity clays. Indeed, Derjaguin et al. (1992) and Xu et al. (2009) evidenced this phenomenon experimentally, on water contained in small pores of silica gel and silica glasses, respectively. This aspect was hitherto not revealed on the COx claystone.

3 Materials and Methods

This chapter explains in detail the different approaches used in this work. In Sec. 3.1, *in situ* measurements, carried out at the Bure URL, are presented. Sample preparation methods and their initial characterization are shown in Sec. 3.2. In Sec. 3.3, we describe the experimental devices, an isotropic and a triaxial compression cell, and the employed measurement techniques. Sec. 3.4 presents a novel device, developed in this study for performing specific stress paths in the laboratory. Sec. 3.4 points out some theoretical developments for analysing and improving the pore pressure conditions during experiments. These analytical findings allowed to establish improved testing procedures, discussed in Sec. 3.6. The framework of a numerical analysis on the COx THM behaviour around microtunnels is described in Sec. 3.7. The conclusions of this chapter are given in Sec. 3.8.

3.1 *In situ* suction measurements

The quality of shale/claystone specimens, extracted at great depth for laboratory testing, is an important concern, recently addressed in details by Ewy (2015). Claystone specimens are often unsaturated when trimmed in the laboratory, whereas their initial state in the rock mass is saturated. As commented by Monfared et al. (2011b), extracted cores are submitted to the successive effects of stress release, coring, storage, transportation and trimming in the laboratory, that may cause desaturation. To optimise the quality and conservation of cores of the Callovo-Oxfordian claystone, Andra specially developed the so-called T1 cell (Conil et al., 2018). In T1 cells, sections of cores are inserted in a latex membrane and placed in a PVC tube. A cement annulus is cast between tube and core, providing radial confinement once hardened. The top and bottom faces of are constrained by springs. Prior to being inserted in T1 cells, cores are transported from the core location to the surface facility in plastic boxes, to minimise evaporation. Given that partial saturation results in an increase of the mechanical parameters of claystones (Pham et al., 2007), the detailed characterisation of the initial state of claystone specimens is an important issue. Relevant parameters are the water content and the porosity (which permit to determine the initial degree of saturation S_r), and the suction s (Mohajerani et al., 2012; Ewy, 2015). S_r and s have opposite changes. In this section, these parameters were monitored on COx specimens just after coring, at 490 m depth in the underground research laboratory at Bure, and along the various subsequent handling stages. A 80 mm diameter horizontal core of the claystone was air drilled (borehole OHZ5015, 101 mm diameter) at the Bure URL, and

sections of about 1.5 m were retrieved (Fig. 3.1). Just after retrieval, fragments of claystone were broken and used to carry out suction measurements, by means of a chilled mirror dew point tensiometer (WP4C, Decagon brand) (Fig. 3.2). Other pieces were weighted, carefully wrapped into a mixture of 70 % paraffin and 30 % Vaseline oil and covered with aluminium foil, to allow further determination of water content, volume, porosity and degree of saturation one day after core extraction. Other suction measurements were carried out on a section, that was transported to the surface core storage facility. In parallel, Andra performed water content measurements, presented by Conil et al. (2018). The suction



Fig. 3.1.: Site at the underground laboratory with drilling machine (on the left)

measurements just after extraction, at various distances from the drift wall, are presented in Fig. 3.3. One can observe, that suctions are lower than 12 MPa at distances larger than 1.8 m, whereas a larger suction of 15.9 MPa is obtained close to the wall at 0.6 m, probably due to the proximity of the gallery and possible evaporation. The two smallest values between 6 and 8 MPa did not correspond to equilibrium in the WP4C. The measured suctions were generally smaller than the values around 20 MPa, often observed in the laboratory after storage and transportation in T1 cells (Menaceur et al., 2015).

Skempton (1961) and Skempton and Sowa (1963) showed that a suction close to the effective *in situ* mean stress was generated in extracted specimens, due to stress release (in shales, this suction was called "native activity" by Ewy, 2015). Its amount can be calculated by Skempton's formula, which describes the undrained unloading of the material. Ewy (2015) observed on shales, that this stress release could only explain about half of the native activity under zero stress. An important additional role in reducing the escaping tendency of pore water play the retaining properties of the clay molecules, and the solute concentration in the free pore water and in the clay interlayer space (Tarantino, 2010). Ewy (2015) stated also, that reconfining shales reduces the total suction, and positive pore pressures

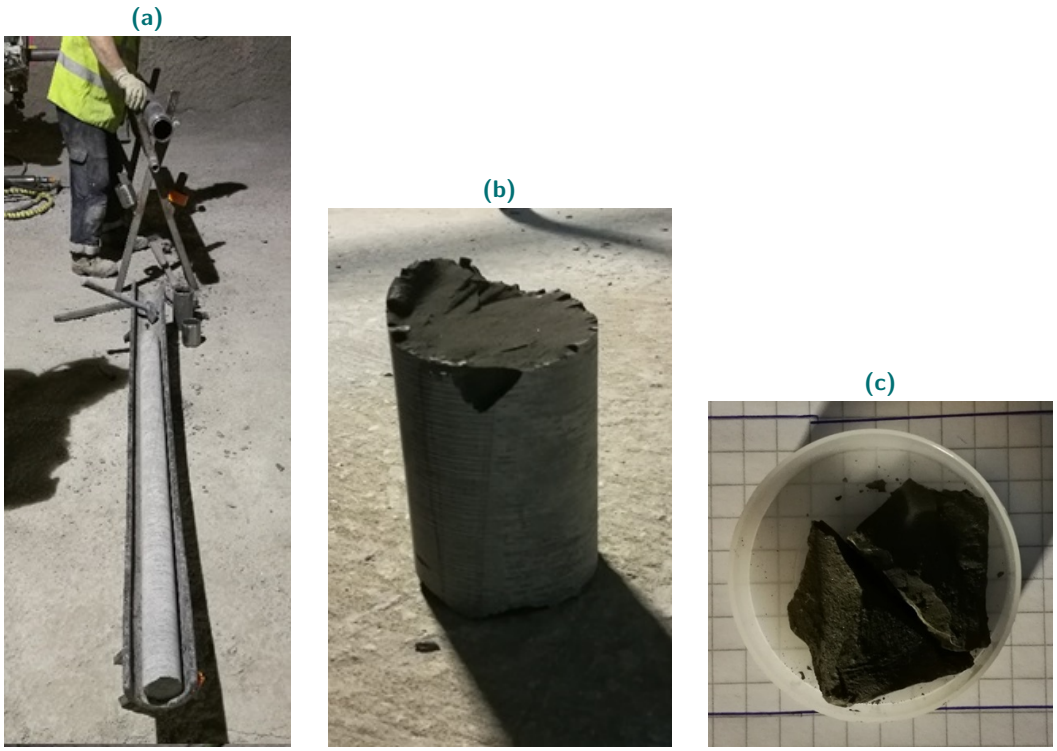


Fig. 3.2.: a) Extracted core section, b) core segment, c) core segment broken into fragments and placed in the WP4C tensiometer

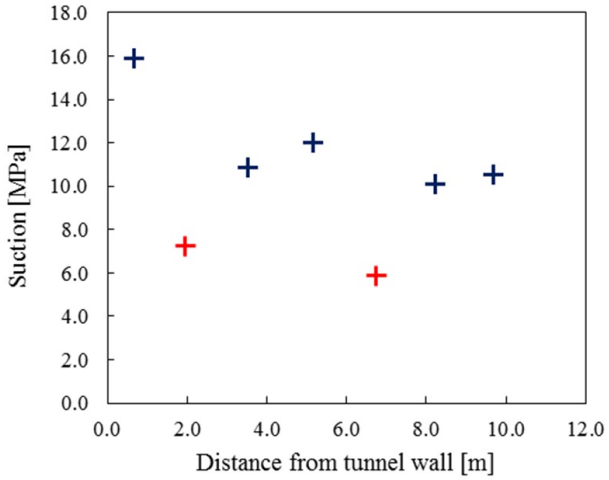


Fig. 3.3.: Suctions measured along the core, with measurements aborted before equilibrium in red

are generated, if enough stress is applied. In such case, the measured native activity is only governed by the clay particles and pore water solutes. Using *in situ* total stress and pore pressure of 12 and 4 MPa respectively, and a Skempton coefficient between 0.8 and 0.9 (Belmokhtar et al., 2017a), one can find a theoretically generated suction between 5.6 and 6.8 MPa under zero stress, about a half of the measurements.

At each distance, two measurements of the water content, volume and porosity were made on duplicates, with average water contents between 7.5 and 8.1 % and average porosities between 17.8 and 19 % (Fig. 3.4, 3.5). These values are both very close to the reference values of saturated COx (Conil et al., 2018). The water content appears to decrease slightly with distance. Interestingly, measurements on the same core, carried out by Conil et al. (2018) less than one hour after extraction at a surface facility, show already smaller values (Fig. 3.4). This indicates desaturation during this period. Average porosities between 15.5 and 19 % (Fig. 3.5b) and a resulting average saturation degree between 92 and 120 % were estimated (Fig. 3.5a). It was found, that this rather large uncertainty in the measured porosity and saturation degree was induced by the uncertainty of the paraffin density used. The density of the paraffin was checked by hydrostatic weighting of metal samples with applied layers of paraffin, which gave a relative density between 0.85 and 0.89. The observed variation was supposedly caused by the non-homogeneity of the layer, due to inclusion of air when applying it to the specimens. Hydrostatic weighting in hydrocarbon without paraffin was thereafter considered as a better method for volume determination. Regardless of the uncertainties, the measured values are close to the values of saturated COx presented by Conil et al. (2018).

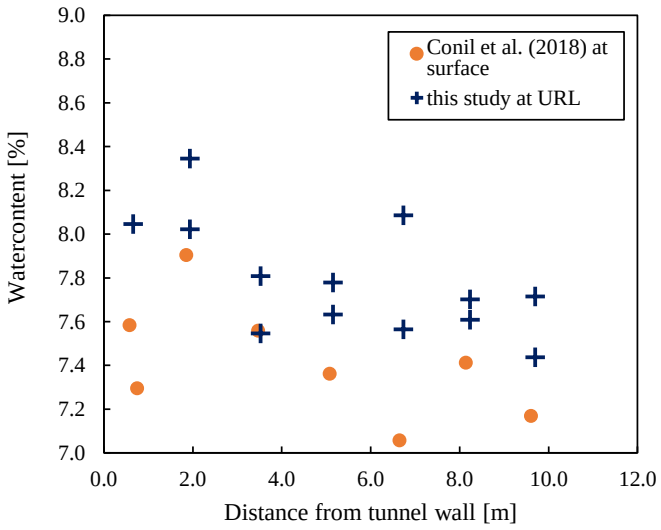


Fig. 3.4.: Watercontent measured along the core, directly after extraction (this study), and and at the surface (taken from Conil et al., 2018)

Fig. 3.6 shows the changes in suction with time, including the short-term measurements in the URL (around 10 MPa), a measurement at the surface, about 45 min after core extraction

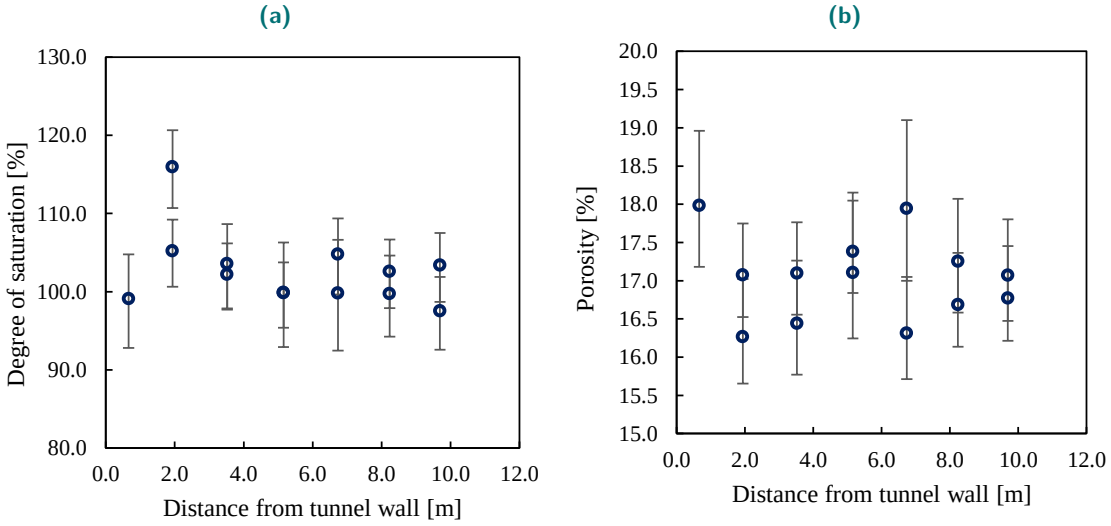


Fig. 3.5.: Porosity and saturation degree measured on extracted samples with a deviation caused by varying paraffin density

(14.9 MPa), and some measurements made on specimens trimmed after opening a T1 cell in our laboratory, after several months of storage (between 21 and 25 MPa, with average degree of saturation of 92 %). This data shows a constant increase in suction with respect to time, with, unsurprisingly, the lowest values obtained just after coring. Transportation to the surface resulted in an increase of 5 MPa, whereas conservation in T1 cell and sample trimming resulted in a further increase of 10 MPa, bringing the suction to the order of magnitude of what was measured in the laboratory. Suction measurements show that the

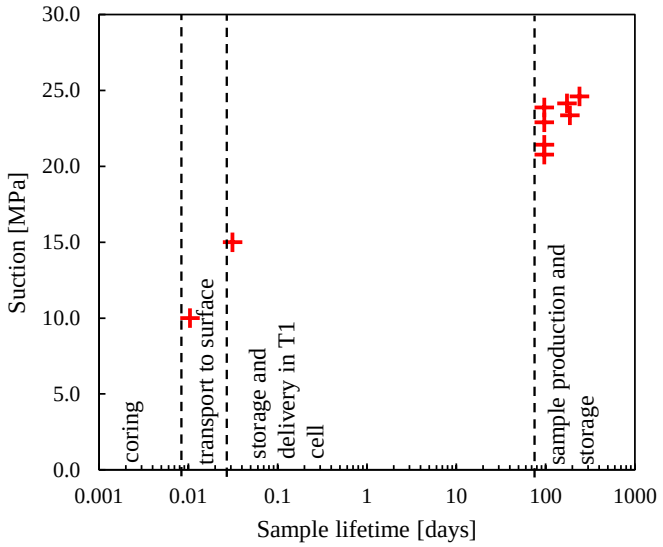


Fig. 3.6.: Measured suction changes during different handling phases

suction of COx samples increases (resulting in decrease in degree of saturation), while the material passes through the different stages, from the core extraction site to the laboratory, to which it has been shipped once conditioned in T1 cells. Relevant handling protocols,

adopted *in situ* and in the laboratory (Conil et al., 2018), can effectively minimize exposure to air, providing laboratory specimen with degrees of saturation higher than 90 %.

Tab. 3.1.: Mean and standard deviation (in brackets) of petrophysical measurements done on cuttings of three COx cores

Core	ρ [g/cm^3]	ρ_d [g/cm^3]	ϕ [%]	w [%]	S_r [%]	s [MPa]
EST 53650	2.37 (0.00)	2.22 (0.01)	17.9 (0.2)	7.5 (0.1)	92.5 (0.8)	24.2 (2.1)
EST 57185	2.38 (0.00)	2.21 (0.00)	18.2 (0.2)	7.9 (0.1)	95.3 (0.7)	17.4 (0.1)
EST 58132	2.39 (0.02)	2.22 (0.02)	17.9 (0.6)	7.8 (0.2)	96.3 (3.6)	22.8 (1.3)

Tab. 3.2.: Composition of synthetic pore fluid close to the *in situ* one, provided by Andra

	NaCl	$NaHCO_3$	KCl $2H_2O$	$CaSO_4$ $7H_20$	$MgSO_4$ $2H_2O$	$CaCl_2$	Na_2SO_4
Concentration [g/L(water)]	1.95	0.13	0.04	0.63	1.02	0.08	0.7

3.2 Sample preparation and initial characterization

In this laboratory study, we investigated specimens trimmed from COx cores, that were extracted at the URL from horizontal boreholes. To preserve the material *in situ* state as best as possible, that means to avoid desaturation (Monfared et al., 2011b; Ewy, 2015) and mechanical damage, cores were shipped and stored in T1 cells (Conil et al., 2018).

After receiving the cores, the T1 cells were removed and the cores were immediately covered by a layer of paraffin wax. This protection from drying remained during the following trimming process. Cylinders of 20 and 38 mm diameter were then cored using a diamond coring bit under air-cooling. These cylinders were also protected by a paraffin layer, before being cut into shorter cylinders for triaxial tests or discs for isotropic tests, using a diamond string saw. The specimens were enveloped by an aluminium-foil layer covered by a mixture of 70 % paraffin wax and 30 % Vaseline oil.

A petrophysical characterization, measured on cuttings of the cores, directly after the trimming and several months after protected storage, is presented in Table 3.1. The sample volume was determined by weighting submerged in unflavoured hydrocarbon, while the dry density was obtained after oven drying at 105 °C. A value for the solid density of 2.70 g/cm^3 was provided by Andra. The measurements of the suction s were carried out using a chilled mirror tensiometer (WP4, Decagon brand). We observe a relatively high degree of saturation with no decrease of the saturation degree during storage, which confirms the efficiency of the implemented protection methods.

3.3 Experimental devices

3.3.1 Isotropic cell

For the laboratory investigation, we used a high-pressure isotropic thermal compression cell, presented in Fig. 3.7 (Tang et al., 2008; Mohajerani et al., 2012; Belmokhtar et al., 2017a; Belmokhtar et al., 2017b). Specimens with 38 mm diameter and variable height, placed inside a neoprene membrane in the centre of the cell, were tested. A heating belt, coupled with a thermocouple next to the specimen, ensures temperature control. The cell is filled with silicone oil, which can be set under a pressure of up to 40 MPa by a pressure volume controller (PVC 1, GDS brand). The neoprene membrane isolates the specimen from the silicone oil, so that the pressure of the pore fluid can be controlled independently. The pore pressure is applied from the bottom of the specimen through a porous disk connected to the pressure volume controller PVC 2. Local strains were monitored using an axial and a radial strain gage (Kyowa brand), glued on the lateral surface of the specimen.

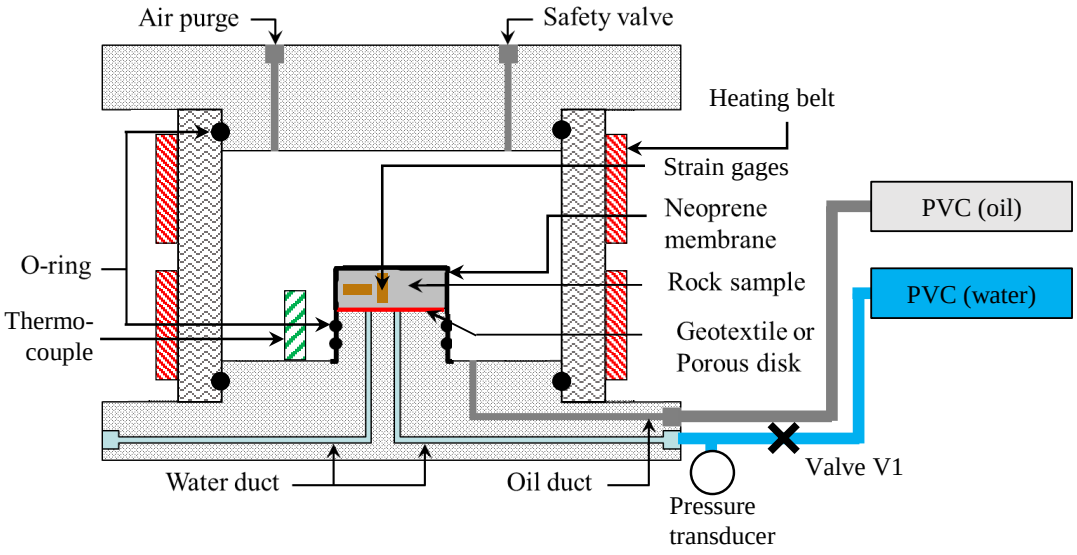


Fig. 3.7.: High pressure and temperature controlled isotropic cell

3.3.2 Triaxial cell

A conventional rock mechanics high pressure triaxial cell was used for experiments with deviatoric loading (Fig. 3.8). A triaxial cell is necessary for determining the Young moduli and Poisson ratios, needed for a complete transverse isotropic parameter set. The device is similar to the isotropic cell, with a pressurized cell (PVC 2), which applies confining pressure to the cylindrical specimen (38 mm diameter, variable height). The specimen, isolated by a neoprene membrane, is submitted to pore pressures through porous stones

on its top and bottom surfaces, controlled by PVC 3. Specimen deformations are detected by strain gages attached at specimen mid-height. A heating belt, connected to an internal thermocouple, regulates the cell temperature. The essential difference to the isotropic cell is the auto-compensated piston, which allows to apply axial loads. The auto-compensation keeps the piston in equilibrium, when the pressure applied by PVC 1 is zero, so that the specimen is in an isotropic stress state. Increasing the pressure of PVC 1 applies an additional deviatoric stress q.

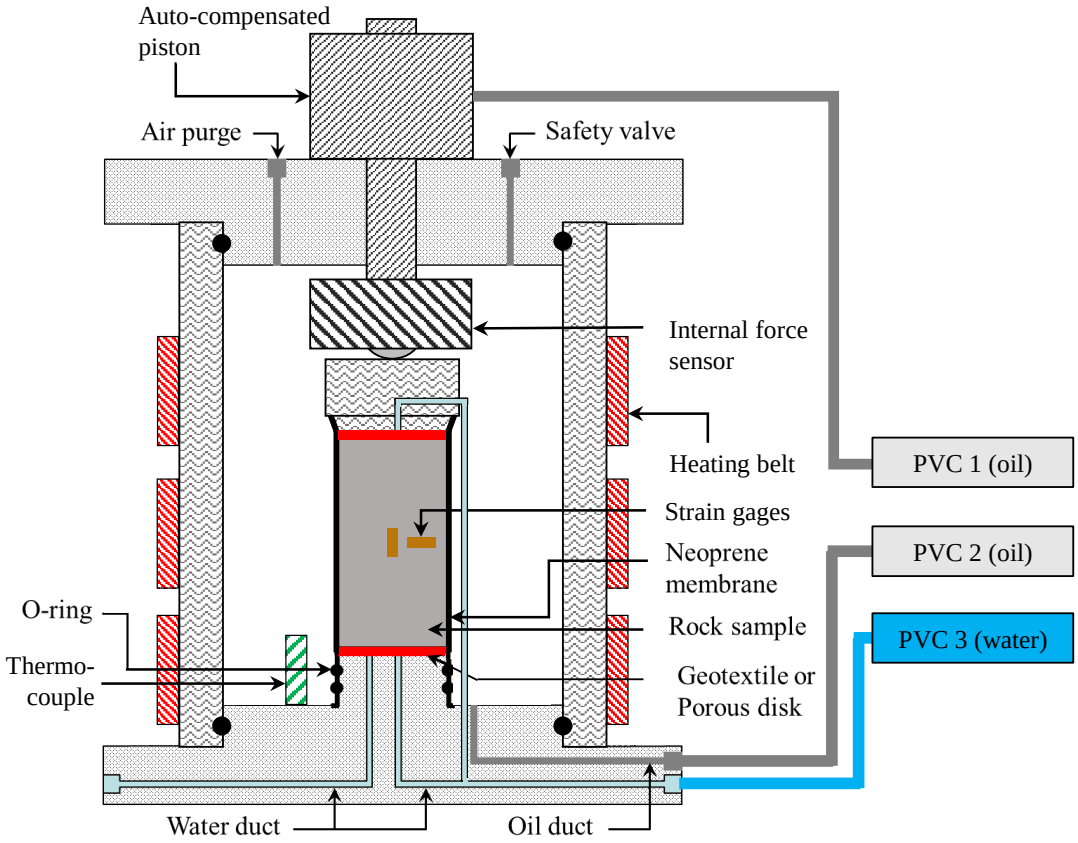


Fig. 3.8.: High pressure and temperature controlled triaxial cell

3.3.3 Deformation measurement

During the experiments, specimen deformations are detected by strain gages glued at specimen mid-height (Fig. 2.1). Measurements of strain gages can be altered by both temperature changes of the gage itself inside the cell and changes of the room temperature. To account for these effects, a reference gage, glued on a piece of steel 316L, was placed next to the tested specimen. Knowing the thermal expansion coefficient of steel 316L, the apparent thermal strains ε_T can be determined as a function of the variations of the cell temperature ΔT and the room temperature ΔT_{room}. During most of the experiments, a reference gage on steel 316L provided directly the apparent strains ε_T. In some cases a

reference gage was not available. The measured strains were then corrected *a posteriori* with the calculated value of $\varepsilon_T(\Delta T, \Delta T_{room})$. In Fig. 3.9a, an example of measured apparent strains during a thermal experiment, compared with the calculated values depending on cell temperature and room temperature, is presented. The importance of this correction is illustrated in Fig. 3.9b, where a clear difference is visible between measured and corrected deformations. Less noise was observed on the measurements corrected by the reference gage with respect to the calculated correction, making this the preferable method.

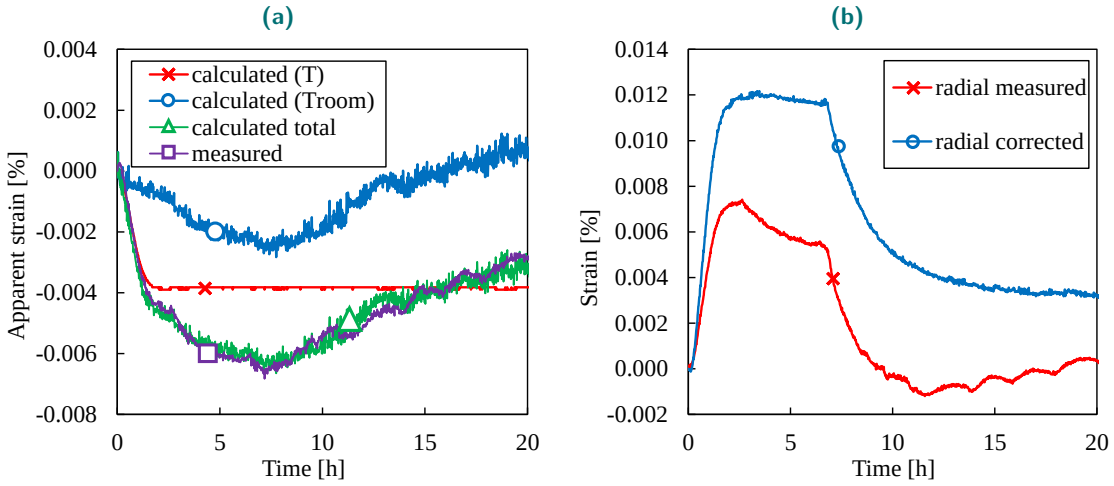


Fig. 3.9.: a) Apparent strains calculated in function of the cell temperature T, in function of the room temperature T_{room} and as total compared with the measured apparent strains during a thermal test; b) example horizontal strains in a thermal test, as measured by the strain gage on a COx specimen and after correction using apparent strains

To verify the thermal strain measurements, a specimen of aluminium 2011 was equipped with a strain gage and tested in the cell. The reference gage was placed next to the specimen. The cell was then heated in steps from 26 - 30 - 35 - 40 °C while the strains of the aluminium sample were recorded and corrected by ε_T. Fig. 3.10 shows the linear thermal expansion of the aluminium sample, with $\alpha_{linear} = 2.30 \times 10^{-5} °C^{-1}$. This value corresponds to the value given from the manufacturer.

3.3.4 Calibration of the effect of the drainage system

According to Wissa (1969), Bishop (1976), Ghabezloo and Sulem (2009), and Ghabezloo and Sulem (2010), closed drainage ducts might not always fulfil the requirement of a constant fluid mass inside the specimen. If there is some dead volume in the drainage system, such as in the ducts and porous disks, this volume changes due to the compressibility and thermal expansion of the drainage elements and of the fluid it contains. This allows fluid exchange between the system and the sample, changing the specimen fluid mass. The methods proposed by these authors account for these effects, and require a precise calibration of the testing device.

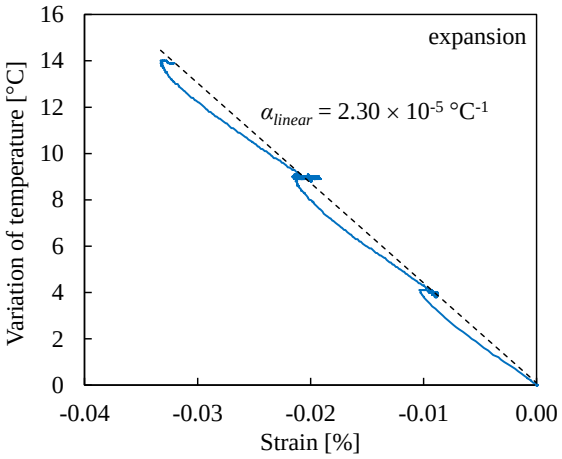


Fig. 3.10.: Linear thermal expansion of an aluminium 2011 specimen, heated from 26 °C

For isotropic tests, one can apply the following method, adapted from Ghabezloo and Sulem (2010). In their formulation, measured parameters are affected by volume changes of the drainage system (volume V_L, compressibility c_L and thermal expansion coefficient α_L). They distinguish between the pore fluid compressibility $c_f = 1/K_f$ and the compressibility of the fluid in the drainage system c_{fL}, and between the density of the pore fluid ρ_f and the drainage system fluid ρ_{fL}. The pore fluid compressibility $c_f = 1/K_f$ is taken equal to that of bulk water, taking into account its temperature and pressure dependency (IAPWS-IF97, 2008). For simplification reasons, we assume that $\rho_f = \rho_{fL}$ and $c_f = c_{fL}$, and we insert, considering an ideal porous material $c_s = c_\phi$ and $\alpha_\phi = \alpha_d$. The parameter β describes the ratio between the specimen and the drainage system temperature, while κ_L denotes the compressibility of the drainage system with respect to the confining pressure. The two latter parameters disappear however in the following notation, as they will be expressed through the newly introduced parameters B_L and Λ_L respectively. Using a calibration test on a dummy metal specimen with zero porosity ($\phi = 0$, $c_d = c_s$), submitted either to a mechanical or thermal loading, the drainage system can be characterised by a Skempton coefficient B_L and a thermal pressurization coefficient Λ_L:

$$B_L = \left(\frac{\partial p_f}{\partial \sigma}\right)_{m_f,T} = \frac{\kappa_L}{(c_f + c_L)}, \qquad \Lambda_L = \left(\frac{\partial p_f}{\partial T}\right)_{m_f,\sigma} = \frac{\beta\,(\alpha_f - \alpha_L)}{(c_f + c_L)} \tag{3.1}$$

The corrected coefficients B^{cor} and Λ^{cor} are obtained from the measured ones B^{mes} and Λ^{mes}:

$$B^{cor} = \frac{B^{mes}}{1 - \frac{V_L}{V}\,(c_f + c_L)\,H\,(B^{mes} - B_L)} \tag{3.2}$$

$$\Lambda^{cor} = \frac{\Lambda^{mes}}{1 - \frac{V_L(c_f + c_L)}{\phi V(\alpha_f - \alpha_d)}\,(\Lambda^{mes} - \Lambda_L)} \tag{3.3}$$

Similarly, we calculate a corrected undrained bulk modulus K_u^{cor} and an undrained thermal expansion coefficient α_u^{cor} with the measured K_u^{mes} and α_u^{mes}, which requires the Biot modulus H (Ghabezloo and Sulem, 2010):

$$\frac{1}{K_u^{cor}} = \frac{1}{K_d} - \frac{\left(\frac{1}{K_d} - \frac{1}{K_u^{mes}}\right)}{1 - \frac{V_L}{V}\left(c_f + c_L\right) H \left(\left(\frac{1}{K_d} - \frac{1}{K_u^{mes}}\right) H - B_L\right)} \tag{3.4}$$

$$\alpha_u^{cor} = \alpha_d + \frac{\left(\alpha_u^{mes} - \alpha_d\right)}{1 - \frac{V_L\left(c_f + c_L\right)}{\phi V\left(\alpha_f - \alpha_d\right)} \left[\left(\alpha_u^{mes} - \alpha_d\right) H - \Lambda_L\right]} \tag{3.5}$$

To calibrate the isotropic cell, a metal dummy specimen was mounted in the cell and submitted to undrained changes of confining pressure and temperature. The coefficient $B_L = 0.10$ was determined by increasing the confining pressure and measuring the pore pressure change. We assume B_L to be constant with respect to temperature. Applying step changes of temperature to the dummy specimen, the coefficient $\Lambda_L = (0.0039\ T + 0.2251)\ \mathrm{MPa^{\circ}C^{-1}}$ was determined for the experiments presented in this section. For the experiments in Sec. 5 the system was changed, which caused a slight change of $\Lambda_L = (0.0056\ T + 0.208)\ \mathrm{MPa^{\circ}C^{-1}}$. The temperature dependency of Λ_L can be attributed to the thermal expansion coefficient of the water filling the drainage system, which increases with temperature. The volume of the drainage system was measured to $V_L = 2000\ \mathrm{mm}^3$, whereas the compressibility of the drainage system $c_L = 0.30\ \mathrm{GPa}^{-1}$ was obtained by applying pressure changes to the tubing system and measuring its volume changes (Ghabezloo and Sulem, 2010).

3.4 Development of a novel thermal extension apparatus

A special interest of this thesis lies in investigating the material behaviour under undrained heating, while lateral deformations are constrained and the vertical confining stress remains constant. To generate such conditions in a triaxial cell, a novel testing device was developed.

3.4.1 Control of cell pressure

Within this device, lateral deformations of a cylindrical sample can be constrained by a servo-controlled system. During the laterally constrained heating tests, we evaluate the corrected lateral strains, which represent an error value for the implemented PID controller (Fig. 3.11). Using this error, a pressure increment is calculated by the routine and transmitted to the PVC, which changes the confining stress accordingly. The pressure applied by the axial PVC is controlled simultaneously, in order to apply a constant axial stress. Tuning of the PID controller parameters P (proportional), I (integral) and D (derivative) was carried out before the tests. It is possible to adapt them during the tests, as to allow a fast response of the confining PVC, while avoiding overshoot and oscillations. In the experiments presented in this study, the PID loop was executed in intervals of 30 seconds, which was sufficiently fast with respect to the heating rate of maximum 5 °C/h, and slow enough in order to avoid oscillations. The D (derivative) part was not necessary to achieve precise control.

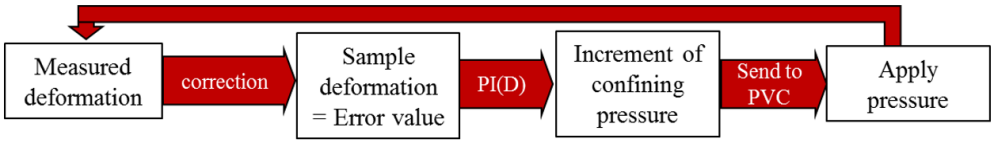


Fig. 3.11.: Schematic workflow of the controller loop

3.4.2 Tension between piston and top cap

When servo controlling the cell pressure to constrain lateral deformation, the cell pressure might become higher than the axial pressure. This will cause tension forces to occur between piston and cap. With the original piston, which applies a compression force through a ball contact (Fig. 3.8), no tension can be exerted. Therefore, the confining fluid with a higher pressure than the piston force will enter between piston and cap and push the piston up. The two elements will lose contact and the sample will be only under isotropic stress. Donaghe and Chaney (1988) presented a review over different system to avoid this, including screw connections and resin pot systems or a suction cap (Fig. 3.12). The former two methods

are difficult to implement, when the piston is not accessible after making contact with the top cap. A resin pot can not be applied, as the cell is filled with silicone oil, preventing bonding. The suction cap, however, allows closing the cell and then moving the piston downwards. Once in contact, a certain surface between top cap and piston is isolated by the means of a rubber membrane. By ensuring a lower pressure than the cell pressure within this surface, given that the isolated surface is larger than the specimen cross section, the confining pressure keeps the two pieces compressed together, allowing to transmit tension.

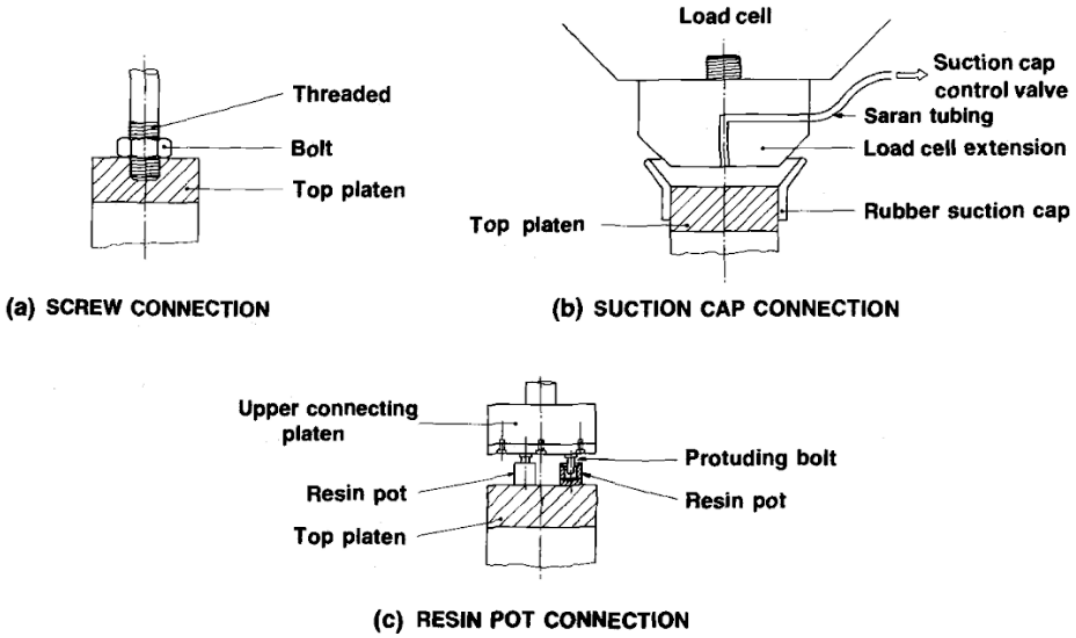


Fig. 3.12.: Different cap connections which allow for triaxial extension tests (Donaghe and Chaney, 1988)

3.4.3 Tension between caps and sample

In the laboratory tests, we aim to increase the pore pressure through thermal pressurization, which might eventually overcome the axial total stress. When that happens, the sample and the caps will detach, if they are not fixed together, terminating the test. To generate failure within the specimen through effective tension, one needs a tension-proof connection between the caps and the specimen. A comprehensive overview of different methods in tensile rock testing is given by Perras and Diederichs, 2014. They recall two principal techniques for direct tensile testing, which consist of attaching the ends of a specimen to a load frame by grips or glue (Fairhurst, 1961; Hawkes and Mellor, 1970), or in modifying the sample shape to a so-called dog-bone (Hoek, 1964; Brace, 1964). The latter method is not recommended for weak rocks such as claystone, as these materials would not withstand the required shaping process in lathe (Perras and Diederichs, 2014). Gluing or gripping the specimen has the advantage, that conventional cylindrical specimens can be used. In the

work of Hawkes and Mellor (1970), the strain localization with this connection method was investigated. The authors showed that with the so-called butt-joint method, where only the end surfaces are glued, almost no strain localization occured. A non-homogeneous stress field was observed in end connections, where also a part of the lateral surfaces was gripped or glued. Still, according to these authors experience, it was likely that failure occurred close to the glued the butt-joint end surface.

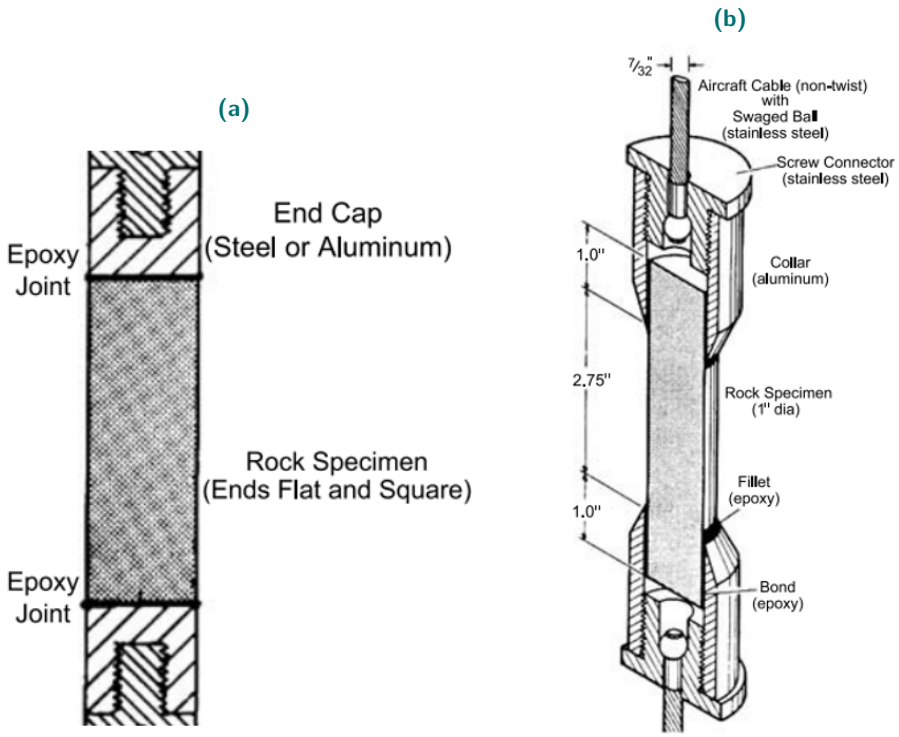


Fig. 3.13.: a) Glued end surfaces with a so-called butt-joint (Fairhurst, 1961), b) glued lateral surfaces (Hawkes and Mellor, 1970)

3.4.4 Design of the novel device

A connection between piston and top cap was implemented, based on the principle of a suction cap. We adapted the contact between piston and top cap, introducing an isolated surface by means of an O-ring (Fig. 3.15). This surface is connected to the outside of the cell, to ensure atmospheric pressure within it. Due to the isolated surface being larger than the specimen cross section, the confining pressure acting on the top cap pushes top cap and piston together. A protrusion of the modified piston ensures alignment of the two pieces.

Specially designed disk-shaped steel platens are glued with their flat surface to top and bottom end surfaces of the cylindrical specimen (Fig. 3.15). Both platens dispose of screw fittings. Once the adhesive hardened, the assembly can be screwed to the bottom cap, which is fixed to the triaxial cell. Also the top cap is fixed by screwing, which allows

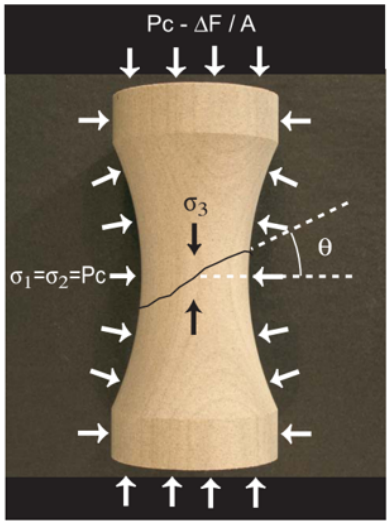


Fig. 3.14.: Dog-bone shaped sample (Bobich, 2005)

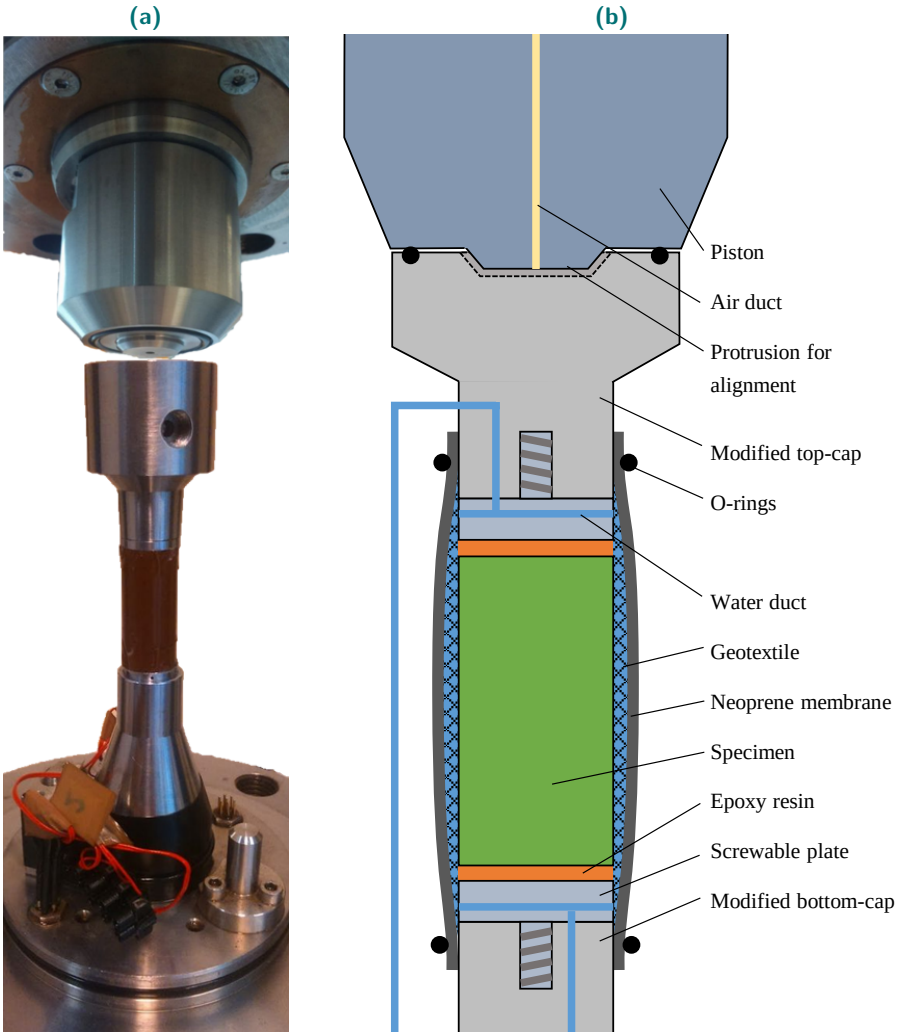


Fig. 3.15.: a) Photo and b) schema of the novel extension device, permitting to maintain pore pressures larger than the axial total stress through glued connection, while saturation and drainage is achieved through lateral geotextiles

to transmit tension forces. We integrated drainage lines into the platens, which connect via top and bottom cap to the pore pressure PVC. The drainage lines have access to a geotextile, wrapped around the specimen, which permits lateral saturation. Monfared (2011) confirmed, that these geotextiles remain permeable even under high confining pressure. A neoprene membrane is put over the specimen and the geotextile, providing isolation between the confining fluid and the pore fluid. The whole system was invented for specimens with a reduced diameter of 20 mm. This enables faster drainage and saturation, with a drainage length corresponding to the radius of 10 mm. Potential uncertainties of the applied axial stress arise from the friction of the piston, when the specimen stresses are estimated based on the stresses applied through the PVC. We implemented therefore a cylindrical aluminium (alloy 2011) element of 30 mm height and 20 mm diameter, connected in the same tension-proof manner as the specimen by epoxy adhesive, at the top of the specimen (Fig. 3.16). The aluminium element was equipped with two axial strain gages. By determining the stress-strain relationship of this element during prior calibration tests, we were able to use it in THM experiments, to estimate axial stresses.

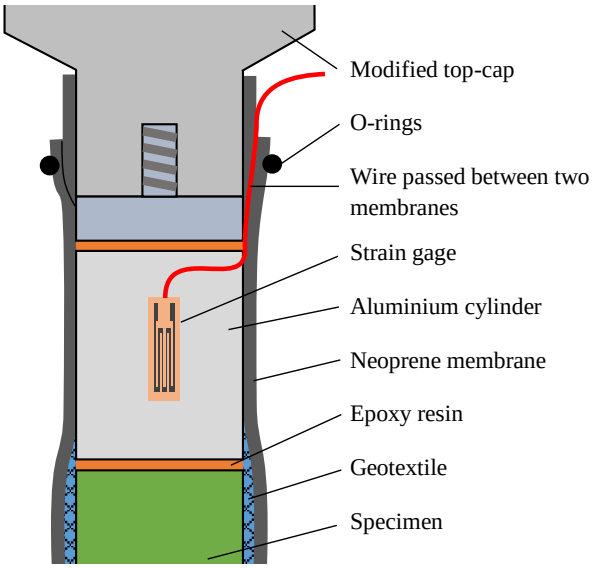


Fig. 3.16.: Aluminium cylinder equipped with strain gages for axial force measurement

3.4.5 Preparation of specimens

We chose here a two-component epoxy resin (Araldite 2014, Huntsman brand) with a tensile strength of 26 MPa, much larger than the expected strength of the specimens tested. The glass transition temperature of this adhesive is 80 °C, until which it maintains its original strength. This temperature was not exceeded in the laboratory tests. Special care had to be taken when preparing the bonding surfaces. To our experience, the epoxy resin bonded very well to the claystone, provided that the sample surface was cleaned from dust by wiping briefly with a paper towel. Bonding to the metal end cap surfaces required more caution,

here the surfaces were abraded with coarse sand paper and then wiped with acetone, to remove any dirt or grease.

After removing the specimens from storage and unwrapping the cover of aluminium foil and paraffin wax, the lateral surfaces of the specimen were protected from drying by adhesive tape. The specimen was placed in a V-block with clamp holders, and the epoxy was applied to the end surfaces. Top and bottom platens were affixed with the adhesive, and fastened with the clamp holders. The V-block ensured alignment of the specimen and the end platens (Fig. 3.17a).

To reach full bonding at room temperature, the epoxy resin had to cure for about 20 h. Afterwards, the assembly was removed from the V-block and the strain gages (one in each axial and radial direction) were attached to the specimen. A layer of geotextile was wrapped around the specimen, while ensuring contact between the geotextile and the outlets integrated in the platens. Two neoprene membranes were put over the geotextile, covering the whole specimen, in such configuration as to permit to pass-through the wires of the strain gages (Fig. 3.17b).

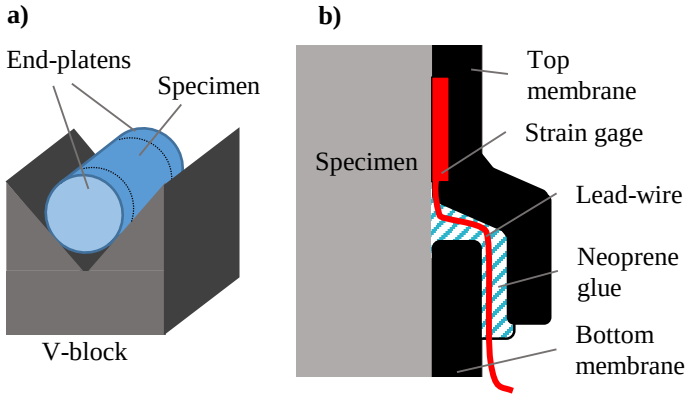


Fig. 3.17.: a) Attaching the end platens to the specimen using epoxy adhesive, placed in a V-block to ensure axial alignment; b) schematic cut to illustrate the layout of two overlapping membranes to pass through strain gage wires

Sample contact with water before applying confining stress, which would result in excessive swelling, has to be avoided. Therefore, we dried the drainage tubes prior to the test. Using the screw joints on the glued end platens, the specimen was installed in the triaxial cell, connected through top and bottom caps. O-rings were put around the membrane to avoid leaks between the membrane and the caps.

3.5 Analytical solution for pore pressure dissipation

Non-homogeneity of the pore pressure field in a specimen is an issue for characterization of the thermo-poro-mechanical behaviour of low permeability geomaterials, as in the case of the Callovo Oxfordian claystone. In tests with drained boundary conditions, excess pore pressure can result in significant errors in the measurement of material parameters. Analytical solutions are presented in this section, for the time evolution of the pore pressure field in a specimen, submitted to various loading paths and different rates. The pore pressure field in mechanical and thermal undrained tests is simulated with a 1D finite difference model, taking into account the dead volume of the drainage system of the triaxial cell connected to the specimen. These solutions provide a simple and efficient tool for the estimation of the conditions that must hold for reliable determination of material parameters. They permit an optimization of various test conditions to minimize the experiment duration, while keeping the measurement errors at an acceptable level.

This section has been published in: Braun, P. et al. (2018). „Theoretical Analysis of Pore Pressure Diffusion in Some Basic Rock Mechanics Experiments“. In: *Rock Mechanics and Rock Engineering* 51.5, pp. 1361–1378.

3.5.1 Introduction

When determining the basic linear thermo-poro-mechanical properties of porous materials, homogeneous stresses and strains throughout tested specimens are assumed. However, the pore-pressure generated in the centre of low permeability specimens during testing needs a certain time to diffuse and to equilibrate with the pressures imposed at the boundaries of the specimen. This might result in a non-homogeneous pore pressure distribution along the specimen and induce an error in the determination of the material poro-mechanical parameters. For example, a specimen loaded with a too high strain or stress rate during a drained compression test will exhibit an over-estimated drained compression modulus. These time dependent effects related to internal water flow have to be taken into account for a proper evaluation of the thermo-poro-mechanical parameters of porous materials, particularly for low permeability geomaterials such as clay rocks, shales, certain limestones or granites, that may have permeability values as low as 10^{-20} m^2, or even less.

The effects of pore-pressure diffusion during isotropic compression tests are studied in this section, in the context of the experimental characterization of the mechanical behaviour of the Callovo-Oxfordian claystone. Various authors (including Escoffier, 2002; Homand et al., 2004; Escoffier et al., 2005; Mohajerani et al., 2011; Mohajerani et al., 2012; Mohajerani et al., 2014; Menaceur et al., 2015; Belmokhtar et al., 2017a) have conducted thermo-hydro-mechanical experiments, mentioning that improper drainage could be a reason for the

rather large range of the measured poroelastic parameters found in the literature. Following the pioneering analysis provided by Gibson and Henkel (1954) on drained triaxial testing, Ghabezloo et al. (2009b) and Monfared et al. (2011b) and Belmokhtar et al. (2017a) conducted finite difference calculations of the one-dimensional diffusive flow equation, to determine a proper loading rate ensuring limited excess pore pressure in the specimen centre and satisfactory drainage. They, however, did not consider the dead volume of the drainage system in case of undrained experiments. Note that in undrained tests, the effect of the dead volume of the drainage system has to be taken into account to correct the measured undrained parameters, as done by Wissa (1969), Bishop (1976), Ghabezloo and Sulem (2009), and Ghabezloo and Sulem (2010) and Monfared et al. (2011b). Note that the expression "dead volume" is used in this work to mention the part of the testing device consisting of porous elements and drainage tubes in contact with the pore volume of the specimen (marked in blue colour in Fig. 3.18).

To improve drainage conditions, adapted specimen geometries with reduced drainage lengths have been proposed by different authors, including Monfared et al. (2011b) who developed a new hollow cylinder device with a lateral drainage length of 10 mm corresponding to half of the specimen thickness. Hu et al. (2014) who tested small specimens of 20 mm diameter and 40 mm height, established a radial drainage using lateral permeable geotextiles, resulting in a 10 mm drainage length equal to the specimen radius. The effectiveness of the hollow cylinder configuration compared to a standard cylindrical geometry for pore fluid dissipation has been confirmed by Monfared et al. (2011b) based on finite difference calculations. Mohajerani et al. (2012) utilized an isotropic cell with 10 mm thick disk-shaped specimens drained at the bottom, resulting in a drainage length of 10 mm. Makhnenko et al. (2017) determined poroelastic properties of Opalinus shale on unjacketed prismatic specimens with a minimum side length of 35 mm, giving a drainage length of 17.5 mm.

In this section, the effect of time and loading rate on the generated excess pore pressures and on the resulting strains in standard thermo-poro-mechanical experiments with one-dimensional drainage is investigated. To do so, an analytical and a numerical approach are developed to simulate laboratory experiments. The effect of material properties and of the testing device parameters are investigated in a parameter study. The results of this section can be used to improve testing procedures for low permeability rock specimens.

3.5.2 Test conditions

Fig. 3.19 schematically represents the boundary conditions of a half specimen submitted to an isotropic compression or thermal loading with axial drainage at the bottom. In this device, the drainage length H_d is equal to half the height of the specimen. The dimensionless length Z is equal to 0 at the lower boundary $(z = 0)$ and equal to 1 at the symmetry axis

($z = H_d$). It is important to note, that in the following section we consider only isotropic loads, the material can therefore be characterized with equivalent isotropic properties. The permeability involved in the equations is the one along the flow path of a respective specimen, in our case perpendicular to the bedding plane, if not specified differently.

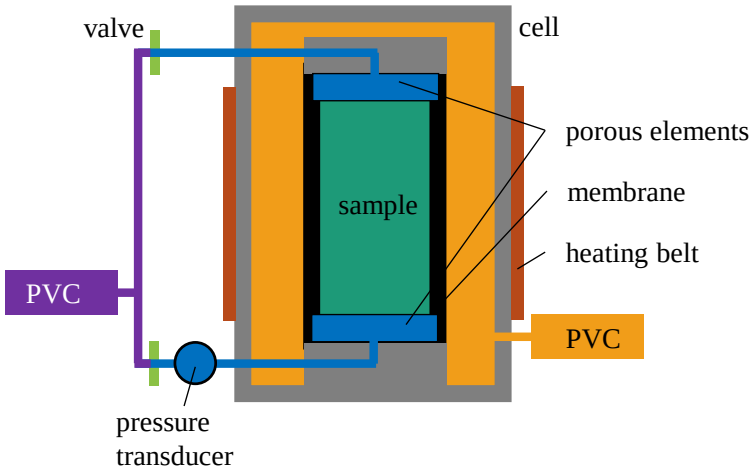


Fig. 3.18.: Schematic set-up of an isotropic cell, dead volume of drainage system coloured in blue

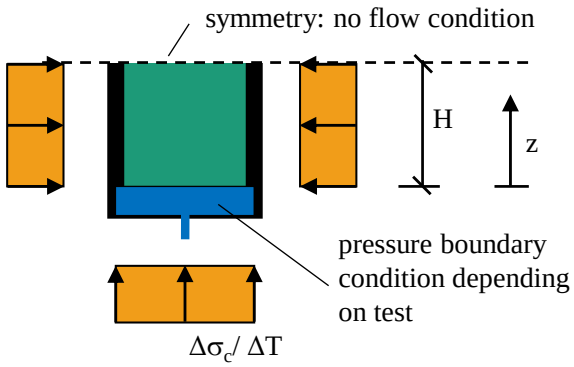


Fig. 3.19.: Geometry of model drainage conditions

In general THM processes, the time dependent diffusion of heat and of pore fluid through the specimen have to be considered. Heat diffuses both in the radial and axial directions with a heat conduction coefficient much larger than that for pore pressure diffusion (see for instance Delage et al., 2000 and Ghabezloo et al., 2009b). To demonstrate this, one can calculate the diffusion coefficients of fluid mass c_{fluid} and heat c_{heat}, as it is done here for the COx claystone. For the diffusion of fluid mass, we used $k = 10^{-20}\mathrm{m}^2$ (Escoffier, 2002; Davy et al., 2007; Zhang, 2011; Menaceur et al., 2015), $S = 0.36\mathrm{GPa}^{-1}$ (with $K_d = 3$ GPa, $K_\phi = 21$ GPa, $\phi = 0.17$ and $b = 0.87$ from Belmokhtar et al., 2017a) and $\mu_f = 10^{-9}$ MPa s (IAPWS-IF97, 2008; Spang, 2002). Using a thermal conductivity $\lambda = 1.88$ W/m/K (Garitte et al., 2014), a bulk density $\rho = 2.4$ g/cm^3 (Belmokhtar et al., 2017a), a bulk specific

heat $C = 1.0$ kJ/kg/K (Conil et al., 2010), one can also calculate the thermal diffusion coefficient:

$$c_{\text{fluid}} = \frac{k}{S\mu_f}, \quad c_{\text{heat}} = \frac{\lambda}{\rho C} \tag{3.6}$$

The calculated diffusion coefficients of heat ($7.8 \times 10^{-7}\text{m}^2/\text{s}$) is about 28 times larger than that of the fluid mass ($2.8 \times 10^{-8}\text{m}^2/\text{s}$). To get an estimation of the geometry effect of radial and axial drainage or heat diffusion, one can apply the method presented by Gibson and Henkel (1954), which was originally proposed for a fluid diffusion problem, but can be used analogously for a heat diffusion problem. This method allows one to calculate the degree of consolidation U at a given time t, for a standard triaxial specimen with a height (equal $2H_d$) equal four times the radius. Here η is the geometry factor for the drainage condition, which is equal to 3.0 for a axial diffusion from both ends, corresponding to the fluid drainage path, and equal to 35.0 for a combined radial and axial diffusion.

$$U = 1 - \frac{{H_d}^2}{\eta c t} \tag{3.7}$$

By introducing the geometry factor and the evaluated diffusion coefficients, one finds a ratio of 325 for the expression η_c between the heat and the fluid diffusion, showing a much faster heat diffusion. Therefore, we assume, that heat conduction occurs instantaneously, in such a way that the temperature throughout the specimen remains equal to that imposed along the boundaries. Similar conclusions have been made also by Ghabezloo et al. (2009b). At the symmetry axis, radial and axial strains are measured by strain gages or LVDTs. The internal pressure is initially equal to p_{init} over the whole specimen length [Eq. (3.8)] and changes according to Eq. (2.40) as time progresses. At the symmetry axis ($z = H_d$), there is no flow, resulting in the boundary condition defined in Eq. (3.9):

$$p_f\,(z, t = 0) = p_{init} \qquad \text{for} \quad 0 \leq z \leq H_d \tag{3.8}$$

$$\frac{\mathrm{d}p_f\,(z = H_d, t)}{\mathrm{d}z} = 0 \qquad \text{for} \quad t > 0 \tag{3.9}$$

Depending on the pore pressure conditions applied to the lower boundary and on the type of loading, a drained compression, undrained compression, unjacketed compression, pore pressure test or drained and undrained heating tests can be carried out. To better understand these tests, we now investigate the effects of applied constant gradients of confinement stress (v_σ), temperature (v_T) and pore pressure (v_p), respectively defined by $v_\sigma = \mathrm{d}\sigma/\mathrm{d}t$, $v_T = \mathrm{d}T/\mathrm{d}t$ and $v_p = \mathrm{d}p_f/\mathrm{d}t$. The corresponding tests are described in Tab. 3.3 and in Fig. 3.20. Note that gradients are often applied in cycles, as further discussed in section 3.5.3.

A drained isotropic compression or a drained heating test is carried out by increasing the confining pressure at a rate $v_\sigma = \mathrm{d}\sigma/\mathrm{d}t$ under constant temperature or by increasing

Tab. 3.3.: Applied loading rates and measured tangent parameters for different tests

Test type	Loading rate v	Measured tangent parameter $\beta = v\mathrm{d}t/\mathrm{d}\varepsilon$
Drained and undrained compression	v_σ	K_d, K_u
Unjacketed compression	$v_\sigma = v_p$	K_s
Pore pressure test	v_p	$-H$
Drained and undrained heating	v_T	$-1/\alpha_d$, $-1/\alpha_u$

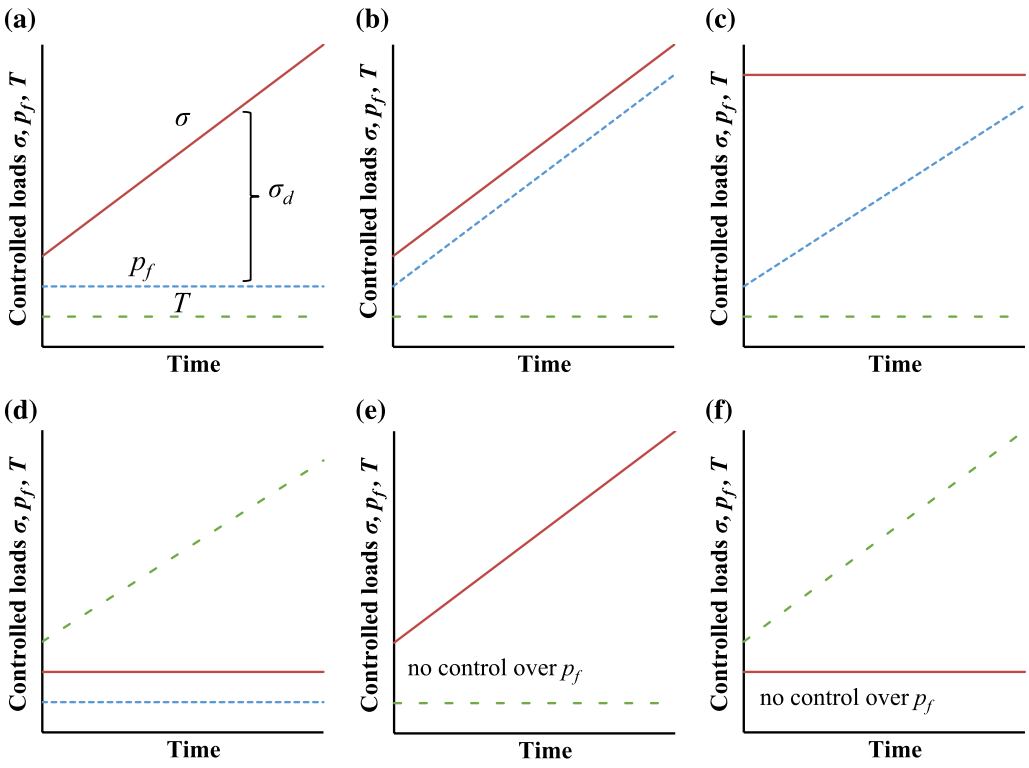


Fig. 3.20.: Applied pressure and temperature gradients during different test types, with confining stress in red solid lines, pore pressure in blue dashed lines and temperature in green dash dotted lines. a) Represents a drained compression test, b) an unjacketed test, c) a pore pressure test, d) a drained heating test, e) a undrained compression test and f) a undrained heating test

temperature at a rate $v_T = \mathrm{d}T/\mathrm{d}t$ under constant confining pressure (Fig. 3.20a,d), respectively, while keeping constant the pore pressure at the specimen boundary.

$$\mathrm{d}p_f\,(z=0,t)=0 \qquad \text{for} \quad t>0 \tag{3.10}$$

Unjacketed tests are carried out under constant temperature, while changing both the confining stress and the boundary pore pressure at a same rate $v_p = \mathrm{d}p_f/\mathrm{d}t$ (Fig. 3.20b):

$$\mathrm{d}p_f\,(z=0,t)=v_p t = v_\sigma t \qquad \text{for} \quad t>0 \tag{3.11}$$

In a pore pressure test, both the confining stress and temperature are held constant while pore pressure is changed at the boundary, at a rate $v_p = \mathrm{d}p_f/\mathrm{d}t$ (Fig. 3.20c):

$$\mathrm{d}p_f\,(z=0,t)=v_p t \qquad \text{for} \quad t>0 \tag{3.12}$$

In undrained tests, either the confining stress or temperature is changed at rate v_σ or v_T, respectively (Fig. 3.20e,f). In these tests, the pore pressure at boundary is not controlled, but the mass conservation of the pore fluid in the specimen and the drainage system connected to the pressure gage can be formulated as a boundary condition [Eq. (3.13)]. In other words, the change of the total fluid mass in the reservoir m_R is equal to the fluid mass expelled from the specimen pores through the surface A (Fig. 3.19). This area is the boundary surface of the specimen in contact with the porous element, through which the fluid flows in perpendicular direction.

$$\frac{\mathrm{d}M_R}{\mathrm{d}t} = \frac{k\rho_f}{\mu_f} A \nabla p_f\,(z=0,t) \qquad \text{for} \quad t>0 \tag{3.13}$$

3.5.3 Analytical solutions for pore pressure controlled experiments

We assume that permeability, fluid density and viscosity are constant over z and t. This is however only true for small temperature changes, as the fluid density and viscosity change significantly with temperature. Eq. (2.40) can be simplified by introducing a dimensionless time θ and a dimensionless length Z, where H_d is the drainage length, defined as the longest distance between the boundary where pore pressure is imposed and the point where no flow occurs:

$$\theta = \frac{t}{\tau_v}, \qquad \tau_v = \frac{\mu_f {H_d}^2}{k} S \tag{3.14}$$

$$Z = \frac{z}{H_d} \tag{3.15}$$

We define also a characteristic time τ_v, as it is done commonly for consolidation analysis. With dimensionless variables, Eq. (2.40) becomes:

$$\frac{\mathrm{d}p_f}{\mathrm{d}\theta} = \frac{\partial^2 p_f}{\partial Z^2} + B\frac{\mathrm{d}\sigma}{\mathrm{d}\theta} + \Lambda\frac{\mathrm{d}T}{\mathrm{d}\theta} \tag{3.16}$$

Monotonic loading

To solve the partial differential Eq. (3.16) for pore pressure controlled tests, that is i) isothermal drained compression, ii) drained heating test under constant confining stress, iii) unjacketed compression and iv) pore pressure tests, one can apply the method of separation of variables (see Sec. A.1). The analytical solution for the pressure field under one-dimensional drainage can be provided by expressing the pore pressure $p_f(z,t)$ with respect to the rates v (Tab. 3.3):

$$p_f\left(z,t\right) = \frac{1}{2}(v_\sigma B - v_p + v_T\Lambda)\tau_v F_1(z,t) + v_p t \tag{3.17}$$

with

$$F_1(z,t) = 4\sum_{n=1}^{\infty}\left[\left(1 - e^{\frac{-m^2 t}{\tau_v}}\right)\frac{1}{m^3}\sin\left(\frac{mz}{H_d}\right)\right] \tag{3.18}$$

$$m = \frac{(2n-1)\,\pi}{2} \tag{3.19}$$

The distribution of excess pore pressure inside the specimen can thus be expressed as the difference between the total pore pressure at z and the imposed pore pressure at the specimen boundary:

$$p_f^{ex}\left(z,t\right) = p_f\left(z,t\right) - v_p t = \frac{1}{2}(v_\sigma B - v_p + v_T\Lambda)\tau_v F_1(z,t) \tag{3.20}$$

The function F_1 varies between 0 and 1 and is the only term depending on time. At any time F_1 is equal to zero at the specimen boundary ($F_1(z=0,t)=0$) and increases going towards the specimen centre. It reaches its maximum value at the specimen centre for sufficiently long time ($F_1(z=H_d, t=\infty)=1$). The evolution of F_1 at $z=H_d$ as a function of dimensionless time and its evolution as a function of z for various dimensionless times are presented in Fig. 3.21.

One can see that for large dimensionless times ($\theta > 2.0$), F_1 comes close to 1 and the excess pressure in the specimen centre ($z=H_d$) remains constant. Therefore, the maximum

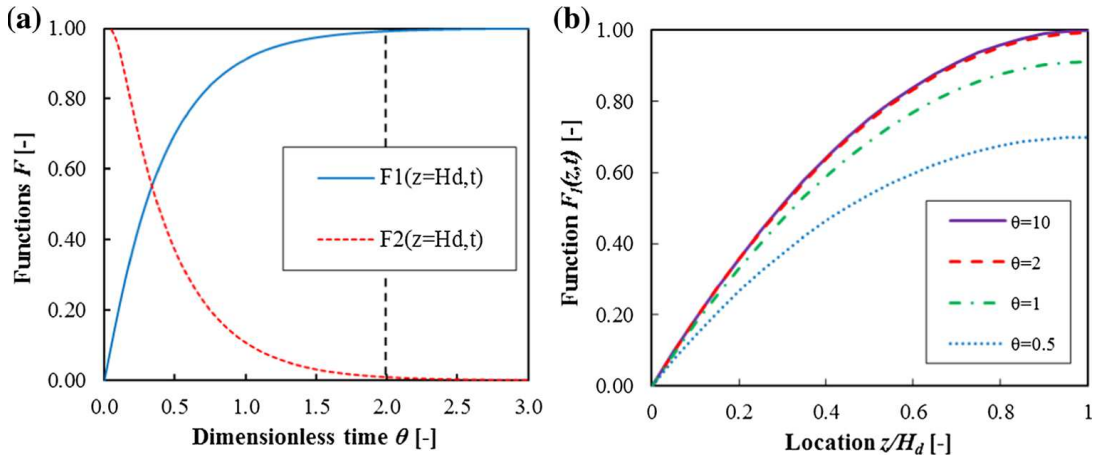


Fig. 3.21.: a) F_1 [Eq. (3.18)] and F_2 [Eq. (3.24)] for $z = H_d$ as functions of dimensionless time, b) change of $F_1(z)$ with time

potential excess pore pressure during a sufficiently long test (at $z = H_d$ and $t = \infty$) is obtained by inserting the maximum of $F_1(H_d, \infty) = 1$ into Eq. (3.20):

$$p_f^{ex-\infty} = \frac{1}{2}(v_\sigma B - v_p + v_T \Lambda)\tau_v \tag{3.21}$$

Function F_1 can be used to describe the evolution in time of the pressure distribution, and to investigate the effects of insufficient drainage. At the beginning of loading, F_1 is equal to zero and there is no excess pore pressure in the specimen. As time progresses, a maximum excess pore pressure is generated as F_1 becomes larger. The function F_1 is plotted in Fig. 3.21 as a function of dimensionless time. Under constant rates, the pore pressure field for $t > 0$ is always inhomogeneous and the magnitude of pressure difference between the boundary and the specimen centre is governed by the applied rates. In isothermal conditions, Eq. (3.21) allows one to compare the maximum excess pore pressure obtained during drained compression, unjacketed and pore pressure tests (note that the excess pore pressure in the case of a pore pressure loading test has a negative sign). Assuming equal rates $v_\sigma = v_p = 1$ for drained, unjacketed compression and pore pressure tests, respectively, one obtains a maximum excess pore pressure of $0.5B\tau_v$ for drained compression, $0.5(B-1)\tau_v$ for unjacketed tests and $-0.5\tau_v$ for the pore pressure test. Since Skempton's coefficient takes values between 0 and 1, the largest absolute excess pore pressure occurs in pore pressure tests. In addition, materials with a Skempton's coefficient $B > 0.5$ exhibit the smallest absolute excess pore pressure in unjacketed tests. By knowing the pore pressure profile in the specimen during the experiment, the volumetric strain in the specimen can be calculated by using Eq. (2.18).

$$\frac{\mathrm{d}\varepsilon\,(z,t)}{\mathrm{d}t} = \frac{1}{K_d} v_\sigma - \frac{b}{K_d} \frac{\mathrm{d}p_f\,(z,t)}{\mathrm{d}t} - \alpha_d v_T \tag{3.22}$$

with the time derivative of the pore pressure that can be evaluated from Eq. (3.17):

$$\frac{\mathrm{d}p_f\,(z,t)}{\mathrm{d}t} = (v_\sigma B - v_p + v_T \Lambda)\, F_2(z,t) + v_p \tag{3.23}$$

with

$$F_2(z,t) = 2\left[\sum_{n=1}^{\infty} e^{\frac{-m^2 t}{\tau_v}} \frac{1}{m} \sin\left(\frac{mz}{H_d}\right)\right] \tag{3.24}$$

Substituting Eq. (3.23) and (3.24) in Eq. (3.22), one can see that the effect of time on the evolution of the volumetric strain is represented by the time evolution of the term F_2, which varies between 1 and 0 (Fig. 3.21). The time derivative of the volumetric strain is thus given by:

$$\frac{\mathrm{d}\varepsilon\left(z,t\right)}{\mathrm{d}t} = \frac{1 - bBF_2(z,t)}{K_d} v_\sigma - \frac{b}{K_d}\left(1 - F_2(z,t)\right) v_p - \left(\alpha_d + \frac{b}{K_d}\Lambda F_2(z,t)\right) v_T \tag{3.25}$$

The tangent material parameters in various experiments (e.g. the tangent drained bulk modulus K_d, in a drained compression test or the drained thermal expansion coefficient α_d in a drained heating test) can be obtained as the derivative of the varied state variable (e.g. confining pressure in a drained compression test) with respect to the volumetric strain evaluated at the specimen centre. It is clear that the evaluated tangent thermo-poromechanical properties change somehow during the transient loading phase, as the material is subject to pore pressure diffusion processes, and reach constant values when the pore pressure in the specimen is in equilibrium. Evaluated tangent parameters at the specimen centre are therefore described as a function of time:

$$\frac{1}{\beta\left(t\right)} = \frac{1}{v}\frac{\mathrm{d}\varepsilon\left(H_d,t\right)}{\mathrm{d}t} \tag{3.26}$$

This value β corresponds to the bulk modulus in the different compression tests and to the inverse of the thermal expansion coefficient in heating tests, respectively. Knowing that $F_2(H_d,0) = 1$, the measured strain rate at the beginning of an experiment ($t = 0$) is given by:

$$\frac{\mathrm{d}\varepsilon\left(H_d,0\right)}{\mathrm{d}t} = \frac{1}{K_u} v_\sigma - \alpha_u v_T \tag{3.27}$$

showing that the evaluated bulk modulus (thermal expansion coefficient) in the middle of the specimen in the very beginning of a drained compression (heating) test corresponds to the undrained bulk modulus (undrained thermal expansion coefficient). In a similar way, knowing that $F_2(z,\infty) = 0$, the measured strain rate for sufficiently long times is given by:

$$\frac{\mathrm{d}\varepsilon\left(z,\infty\right)}{\mathrm{d}t} = \frac{1}{K_d} v_\sigma - \frac{1}{H} v_p - \alpha_d v_T \tag{3.28}$$

showing that the measured parameter β for sufficiently long times in a drained compression test, in a drained heating test, and in a pore pressure loading test corresponds to, respectively, the drained bulk modulus, the drained thermal expansion coefficient, or Biot's modulus H. These observations are summarized in Tab. 3.4.

Tab. 3.4.: Measured tangent parameter according to Eq. (3.26) for different tests

Test type	Measured tangent parameter $\beta = v\mathrm{d}t/\mathrm{d}\varepsilon$ for $t = 0$	for $t \to \infty$
Drained compression	K_u	K_d
Unjacketed compression	K_u	K_s
Pore pressure test	$\to \infty$	$-H$
Drained heating	$-1/\alpha_u$	$-1/\alpha_d$

An interesting observation can be made concerning the effect of the loading rate on the time evolution of the measured tangent parameter in any of the explored experiments. Consider for example an isothermal drained compression test. The evaluated tangent bulk modulus can be obtained from Eq. (3.25):

$$\frac{1}{K_d^{\mathrm{mes}}(z,t)} = \frac{\mathrm{d}\varepsilon(z,t)}{v_\sigma \mathrm{d}t} = \frac{1 - bBF_2(z,t)}{K_d} \tag{3.29}$$

One can see that the time evolution of the measured tangent bulk modulus is independent of the loading rate. Of course, for a given time the stress level at which the modulus is measured is different for different loading rates.

Cyclic loading

The time dependent behaviour caused by the pore pressure diffusion has an important effect also in cyclic loading. The presented solution in the previous section yields the generated pore pressure in a given experiment for a linear loading. In the elastic domain, these basic solutions can be superposed to obtain the pore pressure generated under a more complex loading history, by subdividing the load path into several linear loading paths (Cheng, 2016; chapter 7.3.3). The material has initially a homogeneous pore pressure p_{init} and is loaded through sequences i of different loading rates v_i (Fig. 3.22). The loading starts in section $i = 0$ up to section $i = N$ at the current time t. In each loading section, different loading rates v_i (which can be gradients of confining pressure $v_{\sigma,i}$, pore pressure $v_{p,i}$ or temperature $v_{T,i}$) are applied. It has to be noted that loading rates v_i have different signs for loading and unloading. For example in Fig. 3.22, the rate v_0 is positive, followed by v_1 with a negative value.

The total pore pressure can hence be written as a superposition of Eq. (3.17):

$$p_f(z,t) = p_{init} + p_0 + \sum_{i=1}^{N} \mathrm{H}\,[t - t_i] p_i \tag{3.30}$$

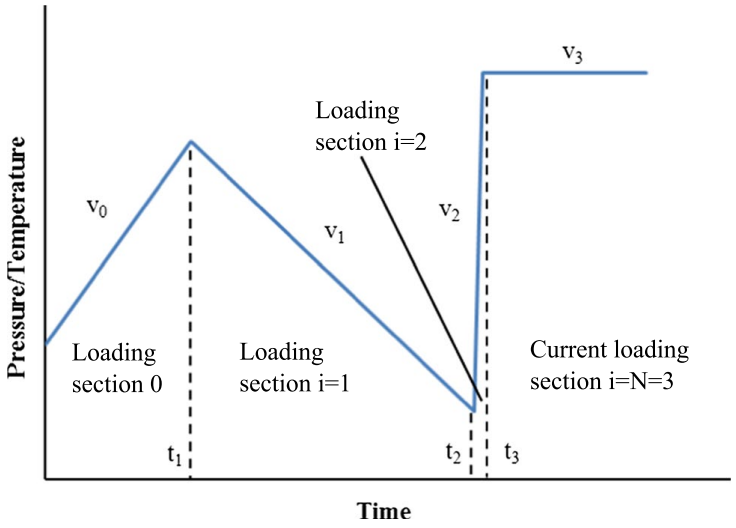


Fig. 3.22.: Arbitrary loading sequence

with

$$p_0 = \frac{1}{2}\left(v_{\sigma,0}B - v_{p,0} + v_{T,0}\Lambda\right)\tau_v F_1(z,t) + v_{p,0}t \tag{3.31}$$

$$p_i = \frac{1}{2}\left[\left(-v_{\sigma,i-1} + v_{\sigma,i}\right)B - \left(-v_{p,i-1} + v_{p,i}\right) + \left(-v_{T,i-1} + v_{T,i}\right)\Lambda\right] \times \tau_v F_1(z, t-t_i) + \left(-v_{p,i-1} + v_{p,i}\right)(t-t_i) \tag{3.32}$$

Again, the measured tangent parameters in various experiments can be obtained as the derivative of the varied state variable (e.g. confining pressure in a drained compression test) at each moment with respect to the volumetric strain. This means, that the tangent is initially governed by an undrained response and changes through a transient phase as the material goes into drained equilibrium. Concurrently, the time derivative of the varied state variable is given by the loading rate $v_{i=N}$ at the current time t in the current loading section number N (see Fig. 3.22). The time derivative of the volumetric strain is obtained by:

$$\frac{\mathrm{d}\varepsilon\left(z,t\right)}{\mathrm{d}t} = \frac{1}{K_d}v_{\sigma,i=N} - \frac{b}{K_d}\frac{\mathrm{d}p_f\left(z,t\right)}{\mathrm{d}t} - \alpha_d v_{T,i=N} \tag{3.33}$$

The change of pore pressure is also obtained by superposition:

$$\frac{\mathrm{d}p_f\left(z,t\right)}{\mathrm{d}t} = \frac{\mathrm{d}p_0\left(z,t\right)}{\mathrm{d}t} + \sum_{i=1}^{N} H\left[t-t_i\right]\frac{\mathrm{d}p_i\left(z,t\right)}{\mathrm{d}t} \tag{3.34}$$

where we define

$$\frac{\mathrm{d}p_0\left(z,t\right)}{\mathrm{d}t} = \left(v_{\sigma,0}B - v_{p,0} + v_{T,0}\Lambda\right)F_2(z,t) + v_{p,0} \tag{3.35}$$

$$\frac{\mathrm{d}p_i\,(z,t)}{\mathrm{d}t} = \left[\left(-v_{\sigma,i-1}+v_{\sigma,i}\right)B - \left(-v_{p,i-1}+v_{p,i}\right) + \left(-v_{T,i-1}+v_{T,i}\right)\Lambda\right] \times F_2(z,t-t_i) + \left(-v_{p,i-1}+v_{p,i}\right) \quad (3.36)$$

3.5.4 Numerical analysis of undrained experiments

Numerical finite difference calculations were used to describe the pressure diffusion with the more complex undrained boundary conditions. For this reason, we introduce the specimen surface A (Fig. 3.19) in contact with the reservoir, which has a volume V_L, an initial volume $V_{L,0}$, a modulus K_L, and a thermal expansion coefficient α_L.

$$\frac{1}{K_L} = -\frac{1}{V_{L,0}}\left(\frac{\partial V_L}{\partial p_f}\right)_T, \qquad \alpha_L = \frac{1}{V_{L,0}}\left(\frac{\partial V_L}{\partial T}\right)_{p_f} \quad (3.37)$$

Note that we assume that the reservoir is not influenced by the confining pressure and always has the same temperature as the specimen. Based on the fluid mass conservation explained in Eq. (3.13), we formulate the boundary conditions in undrained tests:

$$\frac{\mathrm{d}p_f\,(z=0,t)}{\mathrm{d}t} = \frac{kA}{\mu_f V_L\left(\frac{1}{K_f}+\frac{1}{K_L}\right)}\frac{\partial p_f(z=0,t)}{\partial z} + v_T\frac{(\alpha_f-\alpha_L)}{\left(\frac{1}{K_f}+\frac{1}{K_L}\right)} \qquad \text{for} \quad t>0 \quad (3.38)$$

This equation can be rewritten as a function of dimensionless parameters Z and θ:

$$\frac{\mathrm{d}p_f\,(Z=0,t)}{\mathrm{d}\theta} = RS\frac{\partial p_f(Z=0,\theta)}{\partial Z} + v_T\Lambda_L\tau_v \qquad \text{for} \quad t>0 \quad (3.39)$$

with

$$R = \frac{H_d A}{V_L S_L}, \quad S_L = \frac{1}{K_f}+\frac{1}{K_L}, \quad \Lambda_L = \frac{(\alpha_f-\alpha_L)}{\left(\frac{1}{K_f}+\frac{1}{K_L}\right)} \quad (3.40)$$

Eq. (3.39) shows that the boundary condition depends on a factor RS [Eq. (3.40)]. This includes a reservoir factor R depending on the geometry of the experimental setup and the material storage coefficient S. Furthermore we introduce a reservoir storage coefficient S_R and reservoir thermal pressurization coefficient Λ_L as defined in Eq. (3.40). Numerical calculations were carried out using the finite difference method, with an explicit scheme in time and second order space derivative in z. The problem was discretized in 150 elements over the length H_d and with 5×10^4 steps over a dimensionless time of 1.0θ. For each time step, the load was increased according to the applied loading rate, and pore pressures and deformations were calculated by Eq. (2.18) and (2.40) respectively. The pressure at the specimen boundary was updated according to Eq. (3.39). Some example results of numerical calculations in Tab. 3.5 show that the initial strains give a tangent parameter, which corresponds to the true undrained parameter K_u or $-\alpha_u^{-1}$. In undrained tests, we

Tab. 3.5.: Calculated time evolution of measurements during undrained tests. Parameters with an exponent "mes" correspond to the parameters defined by Ghabezloo and Sulem (2009)

	Measured tangent parameter $\beta = v\mathrm{d}t/\mathrm{d}\varepsilon$		Measured pore pressure change $\chi = \mathrm{d}p_f/(v\mathrm{d}t)$	
Test type	for $t = 0$	for $t \to \infty$	for $t = 0$	for $t \to \infty$
Undrained compression	K_u	K_u^{mes}	0	B^{mes}
Undrained heating	$-1/\alpha_u$	$-1/\alpha_u^{mes}$	0	Λ^{mes}

evaluate also the pore pressure coefficient (Skempton's coefficient or thermal pressurization coefficient) in the reservoir, given by:

$$\chi\left(t\right) = \frac{1}{v}\frac{\mathrm{d}p_f\left(0,t\right)}{\mathrm{d}t} \tag{3.41}$$

The simulation results show that no pressure change in the reservoir occurs at the beginning of the loading. At the very beginning of the test, no instantaneous exchange of fluid mass takes place, generating true undrained conditions. However, as there is no fluid expelled at the boundary, the pressure in the fluid reservoir does not change. The measured initial deformation related parameters (bulk modulus and thermal expansion coefficient) correspond thus to the true undrained parameters. For larger times, a certain quantity of fluid is expelled from the specimen to the reservoir and a change of pressure in the reservoir can be measured. As the specimen is not anymore in true undrained conditions, one obtains the tangent strain related and pore pressure related parameters (K_u^{mes}, α_u^{mes}, B^{mes} and Λ^{mes}, see also Ghabezloo and Sulem, 2010), which include an error caused by the deformability of the drainage system and the fluid filling it (Fig. 3.23). The true values of tangent parameters can be obtained by application of the correction methods presented by Wissa (1969), Bishop (1976), Ghabezloo and Sulem (2009), and Ghabezloo and Sulem (2010).

3.5.5 Evaluation of optimal loading conditions

We use hereafter the described analytical solutions and numerical calculations to make laboratory experiments more time efficient under optimal loading conditions by keeping the measurement errors at an acceptable level. As discussed before (see for an example Eq. (3.29)), measured tangent parameters are independent of the applied loading rate. Hence, to obtain drained parameters, one has to estimate a critical total loading duration needed for the pore pressure to reach steady state conditions. Afterwards an optimal loading rate can be determined from this minimum loading time.

$$t_{crit} = \theta_{crit}\tau_v = \theta_{crit}\frac{\mu_f {H_d}^2}{k}S \tag{3.42}$$

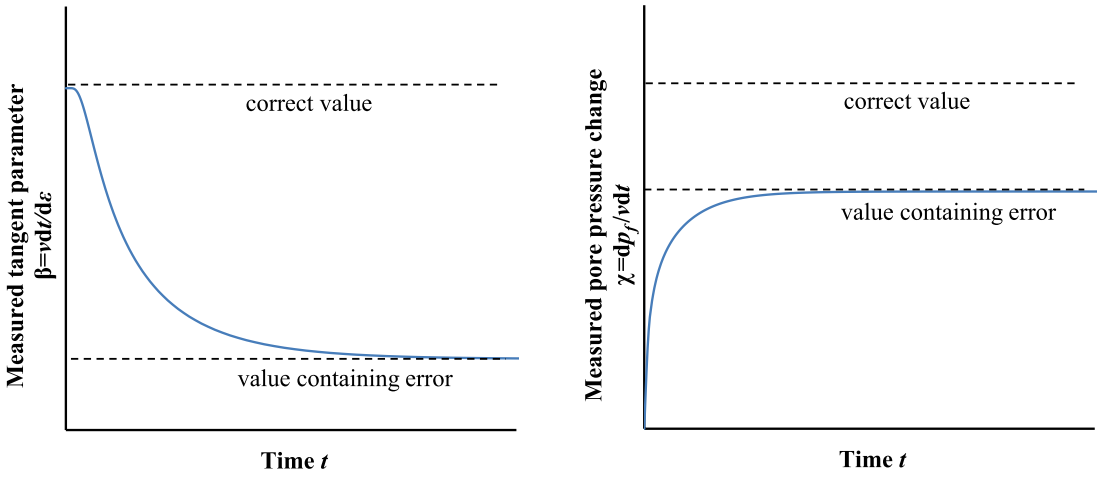


Fig. 3.23.: Numerical simulation of measured tangent parameter and pore pressure change in an undrained test

Therefore, it is desired to evaluate a critical dimensionless time, for which the measured tangent parameter $\beta(\theta)$ comes sufficiently close to its final value $\beta(\theta = \infty)$ in a steady state pore pressure field. We introduce hence a time dependent error:

$$\epsilon_\beta(\theta) = \left| \frac{\beta(\theta) - \beta(\infty)}{\beta(\infty)} \right| \tag{3.43}$$

The value of $\epsilon_\beta(\theta)$ is used to quantify the error of parameter evaluation, which decreases progressively with testing time and reaches 0 at a large enough time. We can then define an acceptable error of $\epsilon_\beta(\theta_{crit})$ small enough so that $\beta(\theta_{crit})$ is close enough to $\beta(\infty)$. For undrained tests we can quantify in a similar way the error in the measured pore pressure coefficient:

$$\epsilon_\chi(\theta) = \left| \frac{\chi(\theta) - \chi(\infty)}{\chi(\infty)} \right| \tag{3.44}$$

Initial and final values for $\beta(\theta)$ and $\chi(\theta)$ are listed in Tab. 3.4 and Tab. 3.5. To analyse the pore pressure controlled tests, we use the analytical solutions stated before. We calculate the error in the measured tangent parameter ϵ_β over dimensionless time with Eq. (3.43), (3.26) and (3.25). Looking at Eq. (3.25), one can see that $\epsilon_\beta(\theta)$ must be independent of permeability and drainage length, as the effects of these parameters are taken into account

by introducing dimensionless parameters of Eq. (3.14) and (3.15). We can reformulate $\epsilon_\beta(\theta)$ for different tests and solve for F_2:

$$F_2(H_d,\theta) = \frac{1}{bB}\left(\frac{\epsilon_\beta(\theta)}{\epsilon_\beta(\theta)+1}\right) \qquad \text{drained compression test} \tag{3.45}$$

$$F_2(H_d,\theta) = \frac{(1-b)}{b(1-B)}\left(\frac{\epsilon_\beta(\theta)}{1-\epsilon_\beta(\theta)}\right) \qquad \text{unjacketed test} \tag{3.46}$$

$$F_2(H_d,\theta) = \frac{\epsilon_\beta(\theta)}{\epsilon_\beta(\theta)+1} \qquad \text{pore pressure test} \tag{3.47}$$

$$F_2(H_d,\theta) = \frac{K_d\alpha_d}{b\Lambda}\left(\frac{\epsilon_\beta(\theta)}{1-\epsilon_\beta(\theta)}\right) \qquad \text{drained heating test} \tag{3.48}$$

This allows us to calculate F_2 for a given test, with a defined error of $\epsilon_\beta(\theta_{crit})$ and poroelastic material parameters (except for the pore pressure test). The value of $F_2(H_d,\theta_{crit})$ can then be used in Fig. 3.21. to evaluate the critical dimensionless time θ_{crit}, which is necessary for the test to reach steady state. Due to the different boundary conditions in undrained tests, the diffusion processes depend also on the reservoir properties. The undrained tangent parameter can be evaluated from the measured strain starting from the beginning of the loading and does not have to be corrected at $t = 0$. To be able to measure a pore pressure coefficient, the specimen needs a certain time to exchange the pore fluid with the reservoir and the pore pressure measurement system. A parametric study using the numerical approach explained in Sec. 3.5.4 can be carried out to determine this critical time θ_{crit} for undrained compression and undrained heating tests. An example for the COx claystone will be given in the next section. After determining the critical dimensionless time depending on the test type, we multiply it by the characteristic time to obtain the critical loading time [Eq. (3.42)]. Concurrently, the applied loading rate has to be calculated from a predefined level of stresses $\Delta\sigma$, Δp_f or temperature ΔT, which the material should be submitted to [Eq. (3.49)].

$$v_\sigma = \frac{\Delta\sigma}{t_{crit}}, \quad v_p = \frac{\Delta p_f}{t_{crit}}, \quad v_T = \frac{\Delta T}{t_{crit}} \tag{3.49}$$

This loading level should be chosen carefully depending on measurement accuracy of the devices or the linear elastic range of the material. In the discussed methods we assume a linear elastic material behaviour. Therefore, the proposed analysis is no longer applicable if the material undergoes non-elastic deformations when loaded beyond its elastic limit. As a lower bound of loading level, one can define the loading necessary to generate sufficient deformations to be measurable by the used experimental equipment.

3.5.6 Application example for COx claystone

In the following we take the example of the COx claystone and evaluate the optimal loading conditions as described in the previous section. The dominant parameters are identified. In

Tab. 3.6.: Combinations of expected reservoir properties for parametric study

		mean	range	R min	R max
V_L	[mm^3]	1000	(500 - 2000)	2000	500
K_L	[GPa]	5	(0.5 - 10)	0.5	10
V_H	[mm^3]	43096			
R	[GPa]	65.8		8.8	155.4

Tab. 3.7.: Expected elastic parameters for COx claystone

	average	range	S max	S min
b [-]	0.75	(0.6 - 0.9)		
B [-]	0.85	(0.8 - 0.9)		
K_d [GPa]	4	(2 - 6)	2	6
K_s [GPa]	25	(20 - 30)	30	20
ϕ [-]	0.15	(0.10 - 0.20)	0.20	0.10
S [GPa^{-1}]	0.27		0.55	0.16

doing so, possible optimization methods of the experimental set-up can be proposed, as for example adapting the specimen geometry, implementing additional drains, reducing the volume or the deformability of the drainage system.

Monotonic loading experiment

Elastic parameters typical for the COx claystone are shown in Tab. 3.7, representing the parameter range found in the data of Andra (2005), Belmokhtar et al. (2017b), Belmokhtar et al. (2017a), and Guayacán-Carrillo et al. (2017). Considered thermal properties for the COx claystone are given in Tab. 3.8, adopted from values found by Mohajerani et al. (2012) and Mohajerani et al. (2014). In our example calculation we define a maximum acceptable error of $\epsilon_\beta(\theta_{crit}) = 1.0\%$. To take into account uncertainties in the material properties we use the least favourable parameter set, which results in the lowest values of F_2 calculated from Eq. (3.48). Hence, in drained compression tests with $b = 0.9$ and $B = 0.9$, we obtain $F_2 = 0.012$. F_2 is equal to 0.006 for unjacketed tests using $b = 0.9$ and $B = 0.8$, and equal to 0.010 for pore pressure tests. For drained heating tests with $K_d = 2$ GPa, $\alpha_d = 10^{-5\circ}\mathrm{C}^{-1}$, $b = 0.9$ and $\Lambda = 0.2$ MPa/$\circ$C we evaluate $F_2 = 0.001$. The necessary critical dimensionless time can then be obtained from Eq. (3.24) or graphically from Fig. 3.21. A zoom of Fig. 3.21 is presented in Fig. 3.24, including the example results for F_2. In this example one can find θ_{crit} of about 1.9 for drained compression, 2.2 for unjacketed compression, 2.0 for pore pressure test, and 2.9 for drained heating.

The necessary time θ_{crit} can also be evaluated from a plot of ϵ_β versus the dimensionless time. Example calculations with a variation of the storage coefficient (Tab. 3.7) are displayed in Fig. 3.25, where we graphically determine θ_{crit} with $\epsilon_\beta(\theta_{crit}) = 1.0$ % under a maximum

Tab. 3.8.: Expected thermal characteristics of tests on COx claystone

		mean	range	Reference
v_T	[°C/min]	0.01	(0.1 - 0.001)	
α_d	[1/°C]	5 $\times 10^{-5}$	(10^{-5} - 10^{-4})	Mohajerani et al. (2014)
Λ_L/Λ	[MPa/°C]	2.0	(0.5 - 3.0)	Mohajerani et al. (2012), Ghabezloo and Sulem (2009)

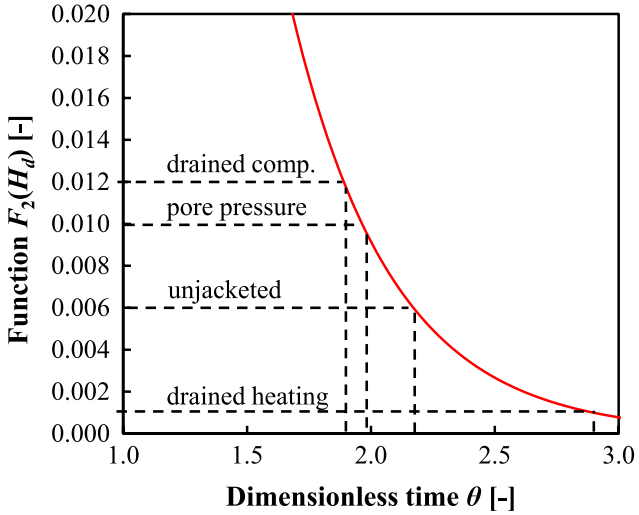


Fig. 3.24.: Zoom on F_2 [Eq. (32)] for $z = H_d$, used to evaluate θ, for example values of F_2

assumed storage coefficient. In the parametric study for undrained tests, a range of possible reservoir properties was chosen based on Mohajerani et al. (2012) and Ghabezloo and Sulem (2009), which are summarized in Tab. 3.6. In addition, the influence of the storage coefficient of the material was studied based on Tab. 3.7. For undrained heating, the thermal expansion of the fluid and the reservoir play an additional role in the boundary conditions. A range of thermal parameters for claystone and the reservoir was taken from Mohajerani et al. (2012), Mohajerani et al. (2014), and Ghabezloo and Sulem (2009) (Tab. 3.8). Results of calculations of ϵ_χ under variation of the storage coefficient, the reservoir coefficient and the ratio of Λ_L/Λ with example values equal to 3, 2 and 0.5 are presented in Fig. 3.26. A variation of the reservoir coefficient R with a constant S_{mean} has the most significant effect on the measured error of the pore pressure coefficient. For large R, a constant pore pressure change coefficient can be observed after a short time $\theta_{crit} = 0.35$. For small R (i.e. a very big or very deformable reservoir), $\theta_{crit} = 0.75$ is necessary for exact measurements, which more than doubles the critical loading time. Parameters such as the heating rate or the drained expansion coefficient do not change the calculation results of ϵ_χ. In conclusion, for the considered material tested in a standard device with the properties R_{mean}, $\theta_{crit} = 0.35$ is necessary to obtain an error smaller than 0.01 (Fig. 3.26). This leads to critical testing durations for undrained tests, which are equal to about 1/5 of the testing durations evaluated for a drained compression tests, for which we evaluated previously $\theta_{crit} = 1.9$ (Fig. 3.24). Using a reservoir with a too large volume or high compressibility

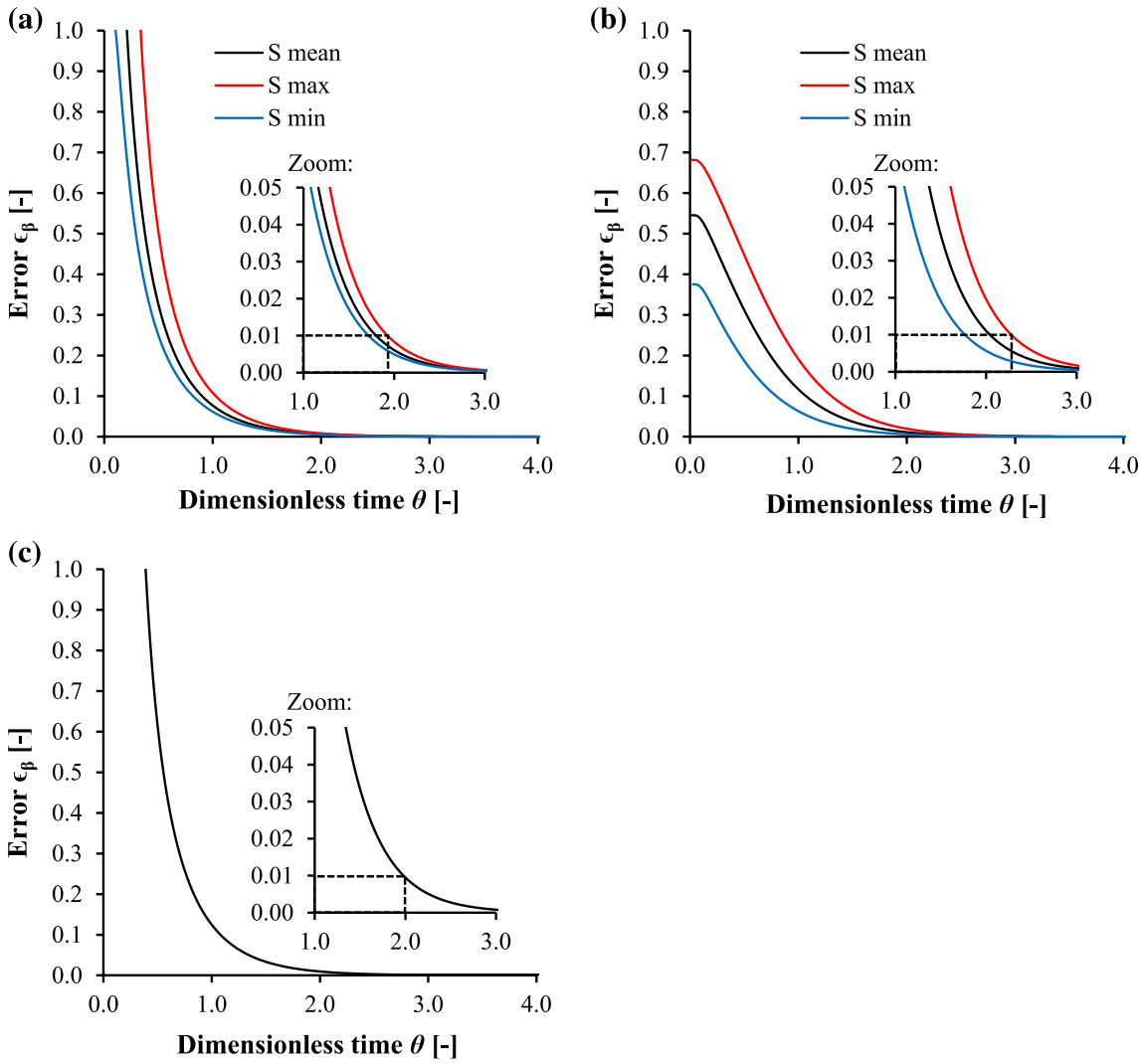


Fig. 3.25.: Error ϵ_β as a function of dimensionless time with a zoom indicating $\epsilon_\beta = 0.01$ under variation of the storage coefficient, for a) drained compression, b) unjacketed compression and c) pore pressure test. In c), the parameter variation has no effect on the result

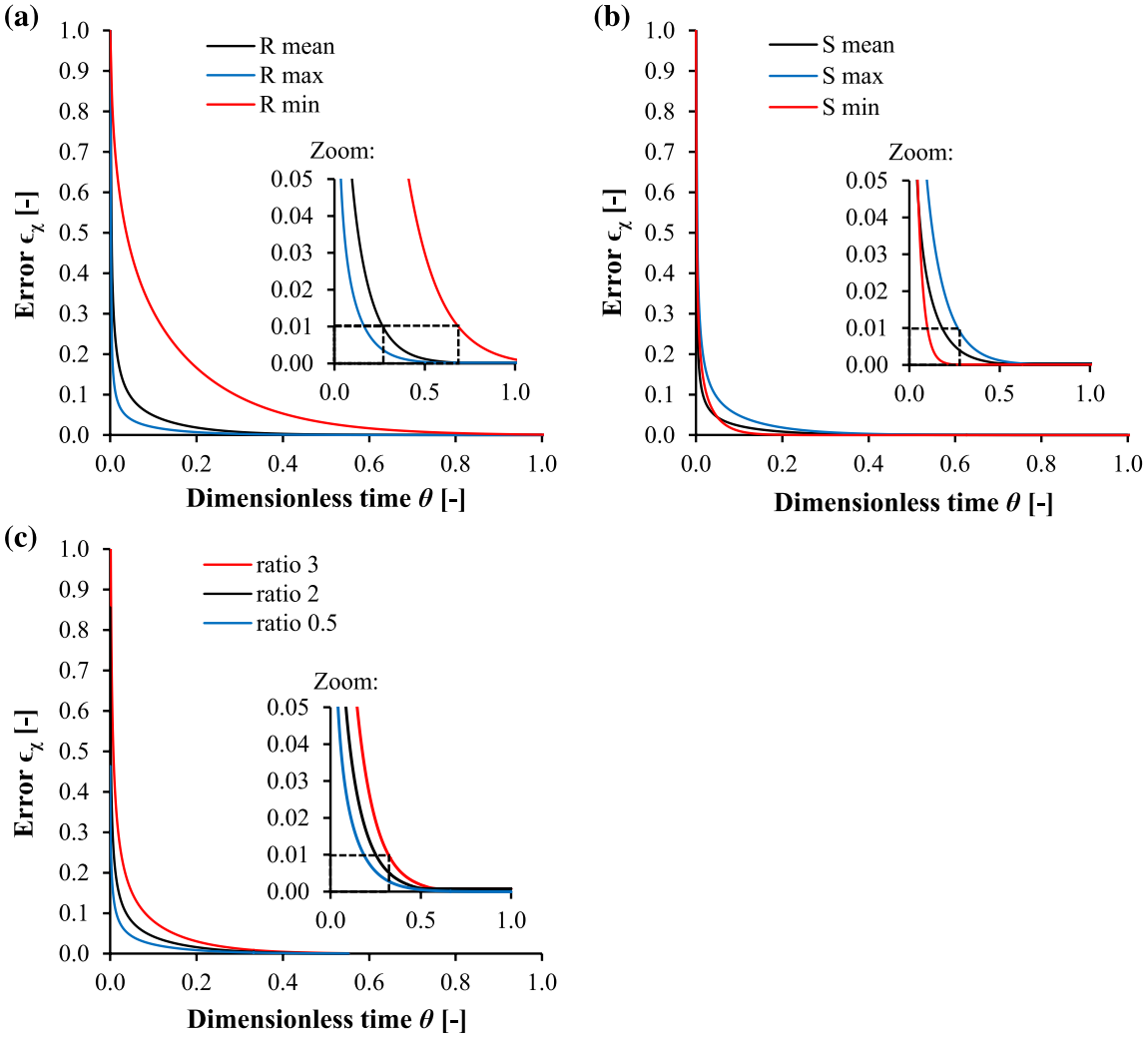


Fig. 3.26.: Error on measurement of undrained pore pressure-related parameters with a) variation of reservoir coefficient R according to Tab. 3.8; b) variation of storage coefficient S according to Tab. 3.7; c) variation of the ratio Λ_L/Λ

Tab. 3.9.: Influence of parameters on the characteristic time

	(a)	(b)	(c)	(d)
S [GPa^{-1}]	0.27	0.55	0.55	0.55
H [mm]	38.0	38.0	38.0	10.0
k [m^2]	1.0 $\times 10^{-20}$	1.0 $\times 10^{-20}$	1.0 $\times 10^{-21}$	1.0 $\times 10^{-21}$
μ [GPa s]		1.0 $\times 10^{-12}$		
τ_v [h]	10.9	22.1	220.6	15.3

increases necessary loading times. As we can imagine, for infinitesimally small R, the fluid mass is not prevented to drain and the material approaches drained conditions, for which the critical dimensionless time is $\theta_{crit} = 1.9$. It is of course interesting to evaluate the undrained tangent parameter from the measured strain at the very beginning of the test, where it corresponds to the true material parameter, without any correction of drainage system effects necessary.

To convert the evaluated critical dimensionless time into real time units, we have to determine the characteristic time. In Tab. 3.9, the effects of different parameters on the estimation of the characteristic time of the claystone are displayed. In (a) the material is characterized with the mean storage coefficient and with specimen dimension of 38 mm height. In (b) we use the maximum assumed storage coefficient (Tab. 3.7) to remain on the safe side, increasing the characteristic time. The permeability has a strong effect on the characteristic time, described in (c), where we insert the lower limit of permeability expected for the material. The long loading duration of (c) can be efficiently optimized by reducing the specimen geometry, which can be seen in column (d). For example, the critical dimensionless time for a pore pressure test with less than 1 % error was found to be $\theta_{crit} =$ 2.0, which gives a loading time of 30.6 h. If one conducts undrained experiments with a sufficiently incompressible and small reservoir, $\theta_{crit} = 0.35$ is necessary. Therefore, these tests can be conducted with a loading duration of 5.3 h.

One can then obtain an optimum loading rate from the critical time and the desired loading level of the experiment. For testing the example material, one could imagine the following scenario: A test with total confining stress change of 1 MPa is conducted. The loading is chosen relatively small to limit non-linearity effects of material parameters. Therefore, one can estimate the loading rate with the critical time estimated in Tab. 3.9d for the COx claystone. For pore pressure tests, one would have to load the specimen for 30.6 hours up to 1 MPa, giving a rate of 0.54 kPa/min. A drained compression test with the same loading should be carried out in a minimum of 29.1 h with a rate of 0.57 kPa/min, whereas unjacketed compression demands 33.7 h loading with 0.44 kPa/min. In undrained compression experiments, the critical time is 5.3 h, therefore the loading rate increased to 3.14 kPa/min. When heating from 25 to 30 ° C, 0.11 and 0.94 ° C/h are the maximum rates allowed for drained and undrained conditions, respectively.

Experiments with loading cycles

In the following, the calculations of two drained cyclic compression tests based on the parameters of the COx claystone with different loading rates (Fig. 3.27) are presented. In Fig. 3.28, analytical calculations of the resulting pore pressures and deformations at the specimen centre are plotted.

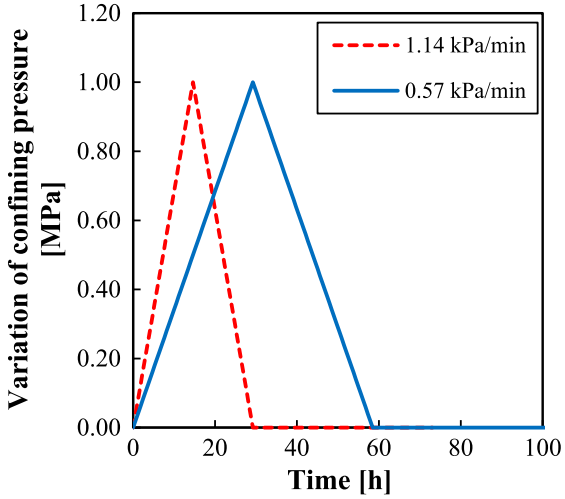


Fig. 3.27.: Cyclic drained loading paths with different rates

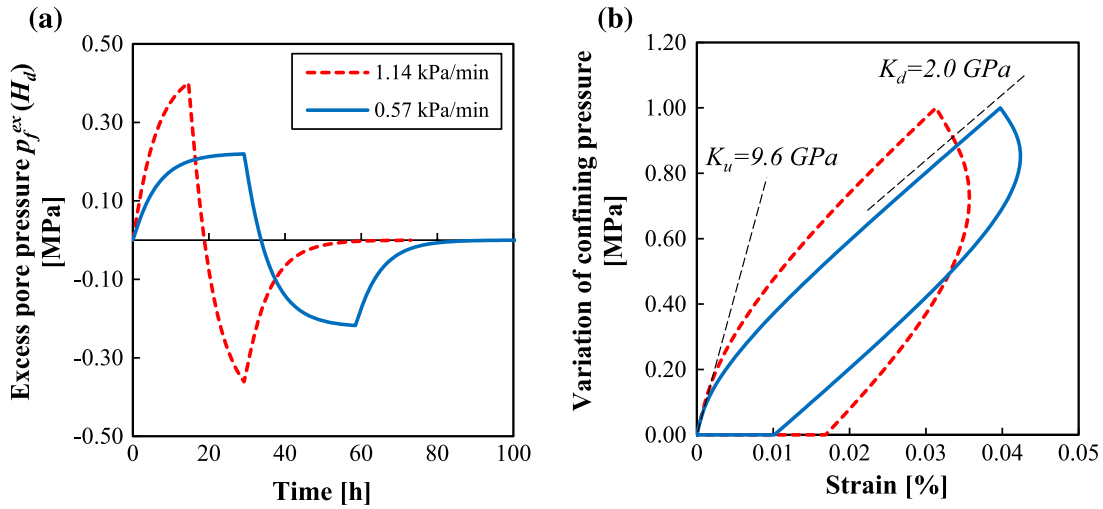


Fig. 3.28.: a) Calculated pore pressures in the specimen centre and b) measured volumetric strains for the fast loading path (red dotted line) and the slow loading path (blue solid line)

One can observe in Eq. (3.17) that the generated excess pore pressures are linearly dependent on the loading rate, therefore twice as much pressure is generated through the fast loading test plotted in red (Fig. 3.28a). Attention has to be paid to the fact that the effective stress state in the middle of the specimen is different from the one at the boundary. In this example, the generated excess pore pressure p_f^{ex} during loading results

in a lower the effective stress at the specimen mid-height compared to the boundary. A higher effective stress at the specimen mid-height caused by a negative p_f^{ex} is observed during unloading. Noting that p_f^{ex} can become negative for unloading in drained tests, the boundary pore pressure should be large enough in order to ensure to always have a positive total pore pressure and to avoid cavitation and desaturation of the material. Fig. 3.28b shows that the higher pore pressure generated through fast loading causes less deformation, which leads to an overestimation of the drained modulus. The loading duration of the blue path (continuous curve) is long enough in order to reach a constant tangent modulus, that corresponds to the desired material parameter K_d. When the elapsed time for each loading rate is large enough, equilibrium between generated and dissipated pore pressures is reached. This time corresponds to the critical loading time evaluated previously for single rates. When analysing laboratory results, the modulus should be determined as the tangent of the slope after the longest possible loading duration, as indicated with K_d in Fig. 3.28b. After the loading cycles, a certain time is required for the pore pressure field to come back to its initial state.

3.5.7 Conclusions

Analytical solutions for the pore pressure distribution and its time evolution inside a specimen were presented for various thermo-poro-mechanical experiments. By superposing these analytical solutions, the pore pressures generated through combined loading and unloading paths of different rates can be calculated. Concurrently, the time evolution of the measurable tangent material parameters during each experiment was described through analytical functions. A critical dimensionless loading time was found, describing the time after which the influence of drainage effects on the experimentally measured parameters becomes small. For undrained compression and undrained heating experiments, numerical solutions were proposed to describe the change of undrained parameters with time, accounting for the deformable dead volume of the drainage system. For undrained experiments, the critical dimensionless time depends only on the storage coefficient of the material and on the reservoir properties. The presented theoretical analysis makes it possible to propose a simple method for evaluation of the necessary loading conditions for experimental measurement of various thermo-poro-elastic material parameters. The loading conditions (loading rate or loading level), specimen geometry or drainage conditions can be optimized to reduce the experiments duration while keeping the measurement errors at an acceptable level. This is particularly important for characterization of low permeability geomaterials for which the experiments are generally very time consuming. An application of the proposed method has been provided by evaluating the optimal loading conditions for various thermo-poro-mechanical experiments on the Callovo-Oxfordian claystone.

3.6 Transient testing protocol

The experimental determination of the thermo-poro-elastic parameters of low permeability geomaterials is difficult because particular care has to be taken with respect to the homogeneity of the pore pressure field during the tests. A new transient step loading procedure is presented for isotropic rock tests in drained and undrained conditions, and under thermal and mechanical loading. Two different proposed protocols allow to measure various drained and undrained parameters in one single test. The observed specimen deformations are analysed based on analytical solutions for the pore pressure diffusion, which enables to back calculate the material permeability. This provides more information in less time, compared to conventional monotonic loading experiments. A demonstration is given on the Callovo-Oxfordian claystone.

This section has been published in: Braun, P. et al. (2019). „Determination of Multiple Thermo-Hydro-Mechanical Rock Properties in a Single Transient Experiment: Application to Shales“. In: *Rock Mechanics and Rock Engineering*. in press.

3.6.1 Introduction

The experimental determination of the thermo-poro-elastic parameters of low permeability geomaterials through drained tests is a challenging task because particular care has to be taken with respect to the homogeneity of the pore pressure field within the specimen. As a result, the test duration that depends on the permeability and the drainage length can be very long. Conversely, undrained tests require shorter durations, but measurements have most often to be corrected for the artefacts due to the deformability of the drainage system (Wissa, 1969; Bishop, 1976; Ghabezloo and Sulem, 2009; Ghabezloo and Sulem, 2010). Note however that some special devices allowing for the direct measurements with pore pressure gages placed in direct contact with the specimen do not need such corrections (Ewy et al., 2001; Giger et al., 2018). Thermal experiments also require careful calibrations to account for both the artefacts due to the drainage system (Ghabezloo and Sulem, 2009; Ghabezloo et al., 2009b; Mohajerani et al., 2012) and due to the thermal strains of the used strain measurement device (Belmokhtar et al., 2017b). Here we present a more time efficient loading protocol for laboratory experiments carried out under isotropic mechanical and thermal loads. Multiple isotropic elastic or thermal parameters can be evaluated directly in a single test by generating a transient deformation between undrained and drained state. The observed transient strains can be analysed using analytical functions described by Braun et al. (2018), Sec. 3.5, and provide the permeability. This loading protocol is inspired by that presented by Hart and Wang (1995) and by Ghabezloo et al. (2009a). Hart and Wang (1995) described a transient mechanical loading method, consisting also of an undrained and a drained phase, while the connected pore fluid ducts provided a constant fluid mass. Here

we impose a constant pore pressure, and we extend the protocol for thermal experiments. Ghabezloo et al. (2009a), as well as Hart and Wang (1995) used the transient behaviour generated through mechanical load to evaluate the permeability. In this work we also apply this method in thermal tests.

The proposed loading protocols are demonstrated on experiments on the COx claystone, allowing to evaluate the numerical values of material parameters in the framework of the thermo-poro-elasticity theory. The parameters are necessary to perform numerical simulations of the response of the COx claystone and more generally the waste disposal system during different phases, from the excavation process to the long-term behaviour. The low material permeability causes significantly long durations for the dissipation and equilibration of pore pressure in laboratory tests. Notably on such low permeable geomaterials, optimized protocols permit less time intensive experiments.

3.6.2 Theoretical considerations

In an isotropic testing device (see Fig. 3.18 and 3.19), confining pressure and temperature are applied uniformly on a cylindrical specimen. The pore pressure and strains are uniform in radial direction, but change along the axial direction z. The drainage length H_d of the specimen is equal to the specimen height, with the pore pressure at the contact with the bottom porous stone at $z = 0$ controlled by a pressure-volume-controller (PVC). The axial and radial strains of the specimen are measured at a certain height h_g (through LVDTs, strain gages, etc., generally at the specimen mid-height). We assume that water flow is governed by Darcy's law in axial direction. Within the thermo-poroelastic framework (Ghabezloo and Sulem, 2009; Ghabezloo et al., 2009b), the change of fluid pressure with time can be described using the following expression:

$$\frac{\mathrm{d}p_f}{\mathrm{d}t} = \frac{BK_d}{\rho_f b}\frac{\partial}{\partial z}\left(k\frac{\rho_f}{\mu_f}\frac{\partial p_f}{\partial z}\right) + B\frac{\mathrm{d}\sigma}{\mathrm{d}t} + \Lambda\frac{\mathrm{d}T}{\mathrm{d}t} \tag{3.50}$$

where k is the intrinsic permeability, ρ_f the fluid density and μ_f the fluid dynamic viscosity, which are assumed to be constant. An analytical solution (3.51) was developed in Sec. 3.5 (Braun et al., 2018), describing the pore pressure field $p_f(z,t)$ under a one-dimensional drainage and under changes in stress and temperature:

$$p_f\,(z,t) = \frac{1}{2}(v_\sigma B - v_p + v_T\Lambda)\tau_v F_1(z,t) + v_p t \tag{3.51}$$

$$F_1(z,t) = 4\sum_{n=1}^{\infty}\left[\left(1 - e^{\frac{-m^2 t}{\tau_v}}\right)\frac{1}{m^3}\sin\left(\frac{mz}{H_d}\right)\right], \quad \text{with} \quad m = \frac{(2n-1)\,\pi}{2} \tag{3.52}$$

in which the parameters $v_\sigma = \mathrm{d}\sigma\mathrm{d}t$, $v_T = \mathrm{d}T/\mathrm{d}t$ and $v_p = \mathrm{d}p_f/\mathrm{d}t$ are constant gradients of stress, temperature and pore pressure, respectively. In an isotropic compression test, we use a loading rate v_σ while keeping $v_T = v_p = 0$. A drained thermal loading test under constant

confining stress is governed by $v_T = \mathrm{d}T/\mathrm{d}t$, while keeping $v_\sigma = v_p = 0$. When changing only the pore pressure, imposed at the specimen boundary, we apply $v_p = \mathrm{d}p_f/\mathrm{d}t$ while keeping $v_\sigma = v_T = 0$. The characteristic time τ_v is defined as:

$$\tau_v = \frac{\mu_f {H_d}^2}{k} \frac{b}{BK_d} \tag{3.53}$$

Alternatively, we can write:

$$\tau_v = \frac{\mu_f {H_d}^2}{k} \frac{(K_u - K_d)}{K_u K_d} \tag{3.54}$$

For the time derivative of the pore pressure, we obtain:

$$\frac{\mathrm{d}p_f(z,t)}{\mathrm{d}t} = (v_\sigma B - v_p + v_T \Lambda) F_2(z,t) + v_p \tag{3.55}$$

$$F_2(z,t) = 2 \left[\sum_{n=1}^{\infty} e^{\frac{-m^2 t}{\tau_v}} \frac{1}{m} \sin\left(\frac{mz}{H_d}\right) \right] \tag{3.56}$$

When remaining within the elastic domain, these solutions can be superposed to simulate more complex loading histories, and a complex loading path can be calculated as the sum of several linear loading paths i (Cheng, 2016; chapter 7.3.3). This is done here by introducing the loading rates $v_{\sigma,i}$, $v_{p,i}$ and $v_{T,i}$, which change at t_i. The current loading phase, at which the pore pressure is evaluated at time t, has the number $i = N$.

$$p_f(z,t) = p_{init} + p_0 + \sum_{i=1}^{N} \mathrm{H}\left[t - t_i\right] p_i \tag{3.57}$$

$$p_0 = \frac{1}{2} \left(v_{\sigma,0} B - v_{p,0} + v_{T,0} \Lambda\right) \tau_v F_1(z,t) + v_{p,0} t \tag{3.58}$$

$$p_i = \frac{1}{2} \left[\left(-v_{\sigma,i-1} + v_{\sigma,i}\right) B - \left(-v_{p,i-1} + v_{p,i}\right) + \left(-v_{T,i-1} + v_{T,i}\right) \Lambda\right] \tau_v F_1(z, t - t_i) + \left(-v_{p,i-1} + v_{p,i}\right) (t - t_i) \tag{3.59}$$

These solutions will be used to back-analyse the material permeability. For a material with an anisotropic permeability, the parameter k in this calculation corresponds to the permeability in the axial direction z, which depends on the values of permeability in principal directions (e.g. parallel and perpendicular to the bedding), and the orientation of the specimen axis with respect to material anisotropy.

3.6.3 Testing procedure

Thermo-hydro-mechanical (THM) laboratory tests on low permeability geomaterials in isotropic or triaxial cells show some interfering effects related to the size and geometry of the specimen and to the imposed drainage conditions: i) in drained tests, the pore pressure field generated through THM loading needs a certain time to equilibrate with the pore pressure controlled through the drainage system; ii) the parameters measured in undrained tests have to be corrected for the volume change of the drainage system (Wissa, 1969; Bishop, 1976; Ghabezloo and Sulem, 2009; Ghabezloo and Sulem, 2010). To cope with these complications, loading protocols consisting of three or two thermo-hydro-mechanical loading stages are presented in this work. We take advantage of the low permeability to generate true undrained conditions under rapid loading, followed by a transient drainage phase. This procedure enables to determine multiple material parameters in one single test. The three-stage loading protocol, which provides 4 material parameters and enables a permeability analysis, is presented in the following section. An alternative simplified testing protocol consisting of two load phases, allowing for a permeability analysis and the measurement of 2 material parameters, is explained in Sec. A.2.

Three-stage protocol

The three-stage test is schematically described in Fig. 3.29, in which the coupled changes in load (stress or temperature), volumetric strain and pore pressure are presented with respect to elapsed time (note that the magnitude and directions of loading and resulting strains and pore pressure changes are only indicative). The three loading phases are applied in a certain order:

- Stage 1: Application of rapid mechanical or thermal loading, while the drainage system is closed
- Stage 2: Confining stress and temperature are held constant with a closed drainage system, until measured strains and pore pressure stabilize
- Stage 3: The drainage system is opened and the initial pore pressure is imposed until measured strains stabilize.

A more detailed description of each stage is given in the following:

Stage 1: Valve V1 (see Fig. 3.18) is closed before and during Stage 1, which keeps the fluid mass filling the sample and drainage system constant. The experiment is then started with a rapid application of a mechanical or thermal load. During fast mechanical loading or heating of low permeable geomaterials, the pore fluid cannot escape the pores, resulting in an instantaneous generation of pore pressure that is not yet altered by the dissipation

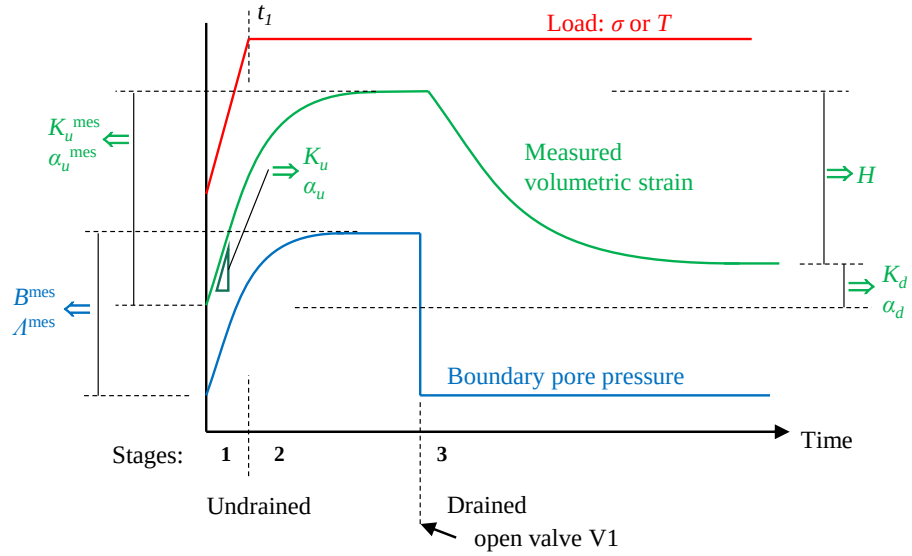


Fig. 3.29.: Three-stage loading protocol and schematic volumetric response for mechanical or thermal tests. Note that annotated parameters are only indicative and need always a pair of stress-strain, temperature-strain, pore pressure-temperature or pore pressure-stress values for their determination

process. This permits to measure true undrained strains that do not need to be corrected for the effects of any dead volume of the drainage system. The loading rate has to be chosen as fast as technically possible, or based on preliminary estimations prior to testing, and verified by back-analysis afterwards. At the same time, the rate should not be too fast to allow for an accurate monitoring of the strains. During the rapid loading, the undrained parameters K_u (undrained compression modulus) or α_u (undrained thermal expansion coefficient) can be determined from the tangent at the origin of the stress-strain or temperature-strain curves, respectively.

Stage 2: Since valve V1 is closed, the pore fluid pressure generated during the first undrained stage will equilibrate through the porous disk with the dead fluid volume of the drainage system. This results in a pseudo-undrained condition that will stabilise at a certain constant pore pressure and volume change values. Once specimen strains stabilise at the end of stage 2, one can then determine parameters K_u^{mes} and B^{mes}, or α_u^{mes} and Λ^{mes}, by comparing the initial strains with the equilibrated strains. These material parameters measured in pseudo-undrained conditions have to be corrected with respect to the effects of the drainage system (Wissa, 1969; Bishop, 1976; Ghabezloo and Sulem, 2009; Ghabezloo and Sulem, 2010).

Stage 3: Valve V1 is now opened, which results in a dissipation of the generated (mechanically or thermally induced) pore pressure. The pore pressure field inside the specimen comes back progressively to its initial homogeneous state, with pore pressure dissipation governed by the material THM properties, particularly its permeability. We suppose that the specimen reaches equilibrium once the monitored strains stabilise. The difference in

strain between the pseudo-undrained and the drained states provides the Biot modulus H, whereas the difference of strains between initial state and drained state provides either the drained compression modulus K_d (mechanical loading) or the drained thermal expansion coefficient α_d (thermal loading). At the end of Stage 3, the specimen is brought back to equilibrium, and any further testing phase can easily be carried out.

In a mechanical test, we obtain therefore an overdetermined parameter set, having measured all 4 unknowns K_d, K_u, B and H, where only 3 independent parameters are necessary, providing also the Biot coefficient b. These experimentally determined parameter sets are often not perfectly consistent, meaning that theoretically calculated and measured values show some differences. We can however find a consistent theoretical parameter set, which approaches as best as possible the measured values, following the approach of Menke (1989) and Hart and Wang (2001). In this approach we consider the experimentally determined dataset **d** and an optimized theoretical dataset **x** with

$$\mathbf{d} = \begin{bmatrix} K_d \\ K_u \\ H \\ B \end{bmatrix}, \quad \mathbf{x} = \begin{bmatrix} K_d^{\mathrm{opt}} \\ K_u^{\mathrm{opt}} \\ H^{\mathrm{opt}} \\ B^{\mathrm{opt}} = \left(\frac{1}{K_d^{\mathrm{opt}}} - \frac{1}{K_u^{\mathrm{opt}}} \right) H^{\mathrm{opt}} \end{bmatrix} \tag{3.60}$$

In a thermal test we can proceed analogously, using the measured dataset **a** and the optimized dataset **y**:

$$\mathbf{a} = \begin{bmatrix} \alpha_d \\ \alpha_u \\ H \\ \Lambda \end{bmatrix}, \quad \mathbf{y} = \begin{bmatrix} \alpha_d^{\mathrm{opt}} \\ \alpha_u^{\mathrm{opt}} \\ H^{\mathrm{opt}} \\ \Lambda^{\mathrm{opt}} = \left(\alpha_u^{\mathrm{opt}} - \alpha_d^{\mathrm{opt}} \right) H^{\mathrm{opt}} \end{bmatrix} \tag{3.61}$$

The optimized dataset, which is compatible in the poroelastic formulation, is obtained by varying the entries of **x** or **y**, respectively, to minimize the sum of the squared residuals between the entries of **d** and **x** or between the entries of **a** and **y**, respectively. Small differences between experimental and optimized values indicate consistent measured material parameters. For certain materials these determined parameters might be a function of stress, pore pressure or temperature. In this case, a variation of the THM properties with the mentioned state variables should be taken into account, if the step change of a state variable in one experiment is significantly large. Carrying out small steps at different levels of total stress, pore pressure or temperature permits to characterize the dependency of THM parameters on the state variables. For example increasing the confining stress in subsequent step-tests of small increments of confining stress can permit to identify the stress-dependency of the material parameters.

Permeability analysis

The analytical solution described in Sec. 3.6.2 permits to simulate the transient loading path (phase 3) between pseudo-undrained and drained state. We insert the imposed testing conditions with the initial pore pressure p_{init}, the specimen height H_d and the location of the strain measurement $z = h_g$. For simulating an instantaneous pore pressure change Δp_f, a simplified analytical solution can be deduced from the general solution described in Eq. (3.57). When we use a series of Heaviside functions to describe the pore pressure distribution, we insert a change of the imposed pore pressure $\Delta p_f = v_{p,0} t_1$ ($v_{\sigma,i} = v_{T,i} = v_{p,1} = 0$). Eq. (3.57) for $t \geq t_1$ is simplified to:

$$p_f(z,t) = p_{init} + \frac{1}{2} v_{p,0} \tau_v \left(F_1(z, t - t_1) - F_1(z,t) \right) + \Delta p_f \tag{3.62}$$

For t_1 approaching 0, corresponding to the instantaneous change of imposed pore pressure, we have to calculate the limit of Eq. (3.62):

$$\lim_{t_1 \to 0} p_f(z,t) = p_{init} + \Delta p_f + \frac{1}{2} \Delta p_f \tau_v \frac{\lim\limits_{t_1 \to 0} \left[\left(F_1(z, t - t_1) - F_1(z,t) \right) \right]}{\lim\limits_{t_1 \to 0} t_1} \tag{3.63}$$

This limit can be found using L'Hopital's rule, and by inserting Eq. (3.56) we obtain:

$$p_f(z,t) = p_{init} + \Delta p_f \left(1 - F_2 \left(z, t \right) \right) \tag{3.64}$$

The volumetric strain can then be evaluated by inserting Eq. (3.64) in Eq. (2.18).

The mechanical three-stage test allows us to directly measure all necessary parameters (K_d, K_u, B and H) to obtain a full set of poroelastic constants. A simulation of the transient response of the specimen in phase 3 of the experiment requires the knowledge of 3 poroelastic material parameters (among the 4 evaluated parameters) and the permeability k. As the poroelastic parameters have already been evaluated, the simulation of the transient response can be used for a back analysis of the permeability, which remains the only unknown parameter. The transient volumetric strains due to pore pressure diffusion are calculated for different values of permeability, varied in a reasonable range, and compared with the experimentally evaluated response. The best fit value of the permeability is found using the least square method, similar to Ghabezloo et al. (2009a). In a thermal test we measure the parameter H directly, whereas 2 additional poroelastic parameters are necessary for a simulation of transient behaviour. We propose therefore to carry out a sequence of a mechanical and a thermal three-stage test, which provides K_d and K_u in the mechanical experiments to be used in the analysis of thermal experiments. With three poroelastic parameters and a variable permeability, we are able to calculate a best fit strain response for thermal tests. Directly measured parameters and parameters necessary for the permeability analysis are presented in Tab. 3.10. As described in the previous section for

Tab. 3.10.: Input material parameters for the analytical simulation of three-stage THM tests

Load type:	Mechanical	Thermal
Measured parameters:	K_u	α_u
	K_d	α_d
	B	Λ
	H	H
Unknown parameters for permeability back-analysis:	k	k
		K_d
		K_u

mechanical and thermal parameters, the permeability of a material may also have some dependency on stresses, pore pressure or temperature. A variation of permeability with total stress, pore pressure or temperature can be captured by carrying out separate three-stage tests, by applying small increments at different levels of the mentioned state variables. When the permeability variation is significant, this permeability evolution during the experiment should be taken into account directly in the back analysis of the results. One can assume a certain mathematical expression for the permeability as a function of a state variable (e.g. a permeability-stress relationship) and fit its parameters in the back-analysis of the experiment. This method has been used by Ghabezloo et al. (2009a) who fitted a permeability-porosity relationship based on the results of a transient experiment.

3.6.4 Example results and analysis

The THM testing programme carried out in this work is composed of four tests on the four specimens coming from two COx cores. Specimens 1 and 2 come from core EST57185 and specimens 3 and 4 from core EST53650 (Tab. 3.1), which both showed a high degree of saturation of at least 90 %. The high-pressure isotropic thermal compression cell, discussed in detail in Sec. 3.3.1, was used to test the specimens equipped with strain gages. The specimens were initially submitted to isotropic stresses close to the *in situ* Terzaghi effective mean stress: specimens 1 and 2 were brought to an isotropic stress of 10 MPa, and specimens 3 and 4 were put under 8 MPa isotropic stress. The ducts of the cell were previously flushed under vacuum, and the COx specimens were mounted in the isotropic cell in their initial state. The specimens were compressed at constant water content under a loading rate of 0.1 MPa/min, while the drainage system was kept dry. Once the specimens were brought to the desired effective stress state, they were saturated with the synthetic pore water (Tab.3.2). Saturation was performed by applying a small water pressure of 0.1 MPa through the porous disk at the bottom of the specimens. Swelling that stabilized after about 5 days was observed during this phase (0.61 % for specimen 1, 0.71 % for specimen 2, 0.72 % for specimen 3 and 0.86 % for specimen 4). The pore pressure and the confining pressure were then simultaneously increased to 4 MPa and 14 MPa respectively for specimens 1 and 2, and to 4 MPa and 12 MPa respectively for specimens 3 and 4.

Tab. 3.11.: Directly measured and optimized poroelastic parameters

Parameter		Experiment	Optimized	Deviation [%]
K_d	[GPa]	2.18	2.21	1.3
H	[GPa]	2.37	2.35	-1.0
K_u	[GPa]	10.30	10.48	1.8
K_u^{cor}	[GPa]	10.71		-2.1
B^{cor}	[-]	0.83	0.84	1.0
b (calculated)	[-]	0.92	0.94	2.4

Three-stage compression test

Before starting this experiment on specimen 1, valve V1 was closed. The confining pressure was then rapidly increased for 10 MPa under a rate $v_{\sigma,0}$ = 6 MPa/h, resulting in a loading time of t_1 = 1.7 h. This rate has to be fast enough to generate a true undrained material response unaffected by fluid dissipation. This condition can be verified using the analytical solutions (Sec. 3.5), which require the parameter τ_v, approximated if not known beforehand. As it can be seen in Eq. (3.56), for a certain z and depending on τ_v, we can find a time t small enough for which F_2 has a value equal or close to 1.0. Eq. (3.55) becomes then $\mathrm{d}p_f = B\mathrm{d}\sigma + \Lambda\mathrm{d}T$, satisfying undrained conditions [Eq. (2.22)]. For our configuration, with a specimen height H_d = 10 mm and a measurement height of $z = h_g$ = 6 mm, one obtains $F_2 >$ 0.90, which appears to be close enough to 1.0, for $t/\tau_v <$ 0.06. We can observe in the experiment, that generated pore pressures need about 20 h to dissipate. In the analytical solution the time of complete pressure dissipation corresponds to $t \approx 2\tau_v$. True undrained conditions are therefore fulfilled after starting the loading for about $t <$ 40 min. In this period we measure K_u = 10.30 GPa. The applied load was kept constant after the rapid loading. Pore pressure and strain measurements stabilized after about 6 h, providing K_u^{mes} = 6.30 GPa and B^{mes} = 0.67 (Fig. 3.30a,b). Valve V1 was then opened to impose the initial pore pressure of 4 MPa (Fig. 3.30a). We assume a total drainage after 25 h, when measured strains stabilized again, which provides K_d = 2.18 GPa and H = 2.37 GPa (Fig. 3.30a,b). This results in a Biot coefficient of b = 0.92. Belmokhtar et al. (2017a) recently found b between 0.87 and 0.91 for the same material. We carry out the correction of undrained parameters as presented in Sec. 3.3.4, which provides K_u^{cor} = 10.71 GPa and B^{cor} = 0.83. An optimization scheme, described in Sec. 3.6.3, provides a compatible parameter set presented in Tab. 3.11. The small deviation of optimized from experimental values gives confidence in the measured parameters.

For the permeability evaluation, we use the third stage of the test, starting with the opening of valve V1, which corresponds to a pore pressure test (change of pore pressure under isostatic temperature and confining pressure). This can be simulated as described in Sec. 3.6.3, using Eq. (3.64) with the optimized input parameters (K_d = 2.21 GPa, H = 2.35 GPa, K_u = 10.48 GPa) and the specimen geometry (H_d = 10 mm and $z = h_g$ = 6 mm). This leaves only the permeability k as an unknown, which was determined to 2.03 $\times 10^{-21}$ m^2

with the best fit shown in Fig. 3.31. Note that this value represents the material permeability perpendicular to the bedding plane, as the specimen geometry effects a flow only in this direction.

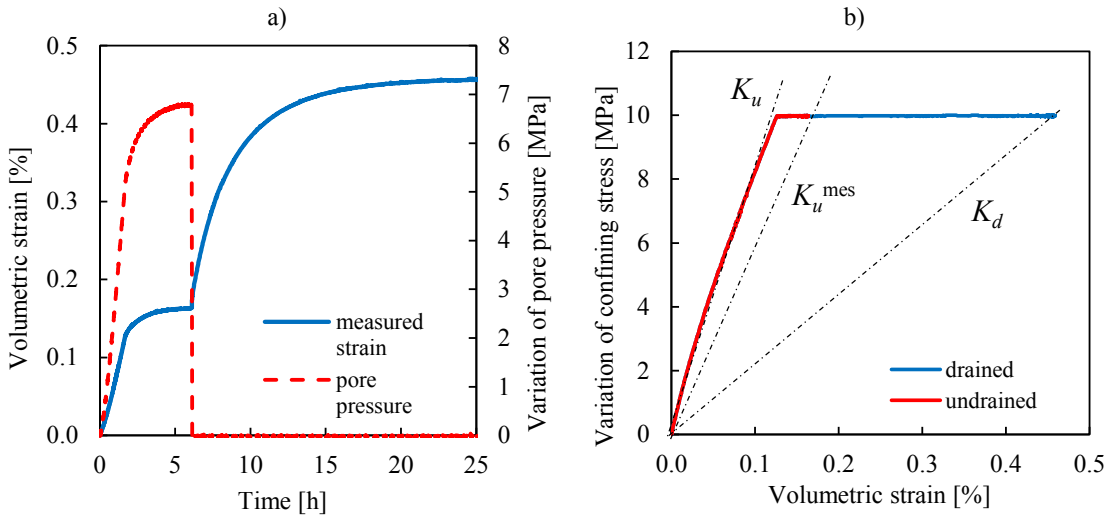


Fig. 3.30.: Three-stage compression test with a) measured specimen strain and pore pressure over time, b) stress-strain curve

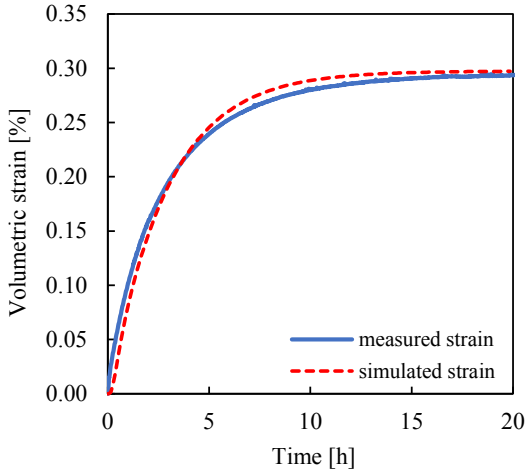


Fig. 3.31.: Drainage phase from Fig. 3.30a with measured and simulated strains

Three-stage thermal test

Before starting this thermal test on specimen 2, valve V1 was closed. The cell and the specimen inside it were cooled rapidly from 50 to 45 °C (Fig. 3.32a). Under a constant temperature, strains and pore pressure stabilized after about 7 h. The valve V1 was then opened, imposing the initial pore pressure of 4 MPa (Fig. 3.32b). Full drainage was assumed after 24 h when measured strains stabilized. In the rapid cooling phase we measure a tangent

Tab. 3.12.: Directly measured and optimized THM parameters

Parameter		Experiment	Optimized	Deviation [%]
α_d	[10^{-4} °C^{-1}]	0.17	0.17	0.3
H	[GPa]	2.37	2.33	-1.6
α_u	[10^{-4} °C^{-1}]	1.16	1.17	1.1
α_u^{cor}	[10^{-4} °C^{-1}]	1.21		-3.1
Λ^{cor}	[MPa °C^{-1}]	0.23	0.23	1.6

α_u = 1.16 $\times 10^{-4}$ °C^{-1}, while the secant moduli in the undrained and drained equilibrium phases provide α_u^{mes} = 1.43 $\times 10^{-4}$ °C^{-1} and α_d = 0.17 $\times 10^{-4}$ °C^{-1} respectively (Fig. 3.32c). Λ^{mes} = 0.29 MPa/°C was determined from the pore pressure change in undrained equilibrium. After opening valve V1 we can determine H = 2.37 GPa in the third stage. All direct measurements are presented in Tab. 3.12. The undrained equilibrium was reached after about 6 h, including 1 h necessary to reach the imposed temperature change. The drained equilibrium required an additional 13 h to reach. The correction of undrained parameters provides α_u^{cor} = 1.21 $\times 10^{-4}$ °C^{-1} and Λ^{cor} = 0.23 MPa/°C, which corresponds well with the direct measurements (Tab. 3.12). The optimized and compatible parameter set presented in Tab. 3.12 shows only little deviation from the measurements.

We simulate the third stage of the test, starting with the opening of valve V1, which consists of a change of imposed pore pressure under isostatic temperature and confining pressure. Some input parameters are given by the specimen geometry (H_d = 10 mm and $z = h_g$ = 6 mm) and we measured H = 2.33 GPa, whereas K_d, K_u and k are unknown. To be able to back-calculate the permeability, we need to adopt parameters measured in a separate mechanical test. In Eq. (3.64) we insert optimized values for K_d and K_u from the three-stage mechanical test. The best fit of the calculated strains obtained with k = 1.61 $\times 10^{-21}$ m^2 is shown in Fig. 3.33.

3.6.5 Conclusions

Thermo-hydro-mechanical laboratory tests on low permeability geomaterials in isotropic or triaxial cells show some interfering effects related to the size and geometry of the specimen and to the imposed drainage conditions: i) in drained tests, the pore pressure field generated through THM loading needs a certain time to equilibrate with the pore pressure controlled through the drainage system; ii) the parameters measured in undrained tests have to be corrected for the volume change of the drainage system (Wissa, 1969; Bishop, 1976; Ghabezloo and Sulem, 2009; Ghabezloo and Sulem, 2010).

To cope with these complications, loading protocols consisting of three or two thermo-hydro-mechanical loading stages are presented in this work. We take advantage of the low permeability to generate true undrained conditions under rapid loading, followed by a

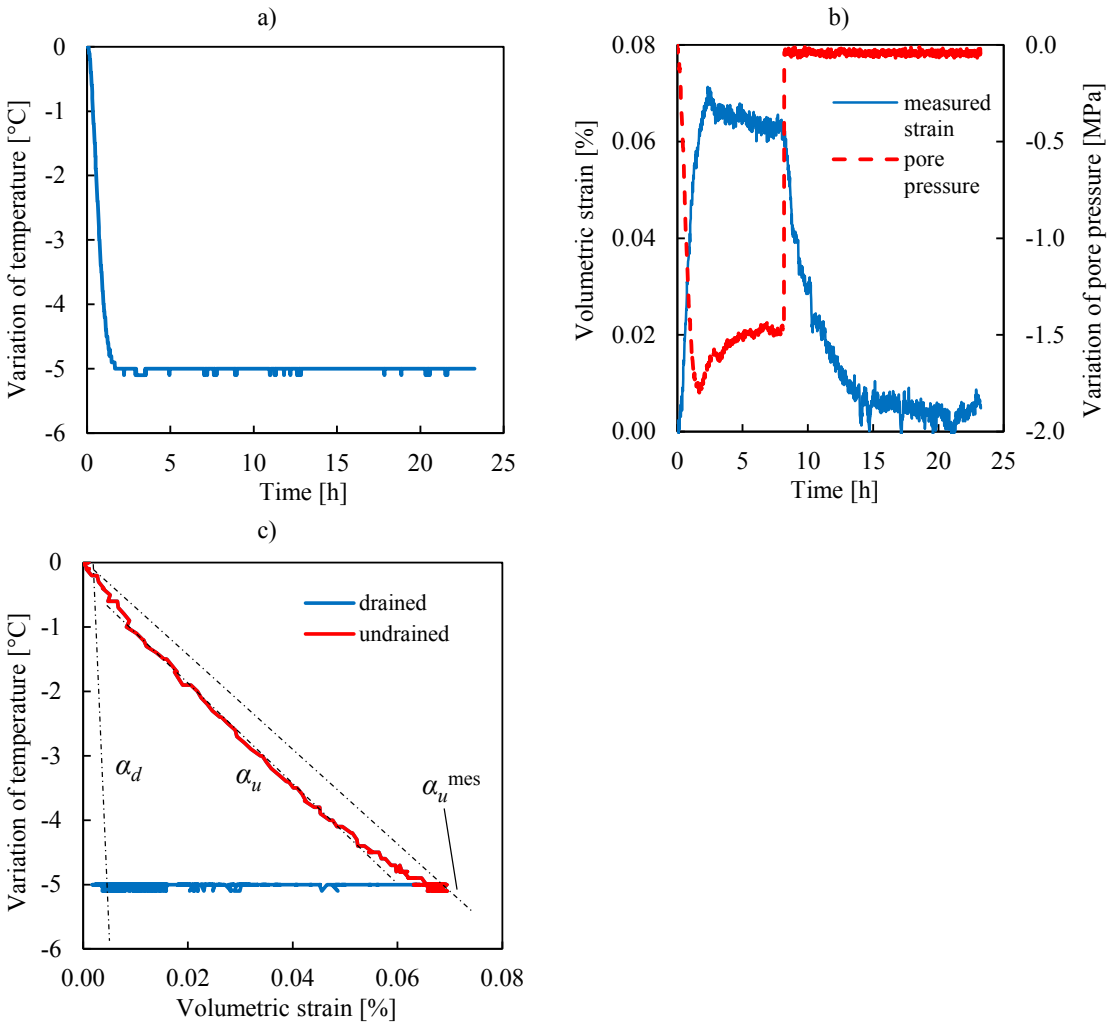


Fig. 3.32.: Three-stage thermal test with a) applied temperature change, b) specimen strains and pore pressure over time, c) temperature-strain curve

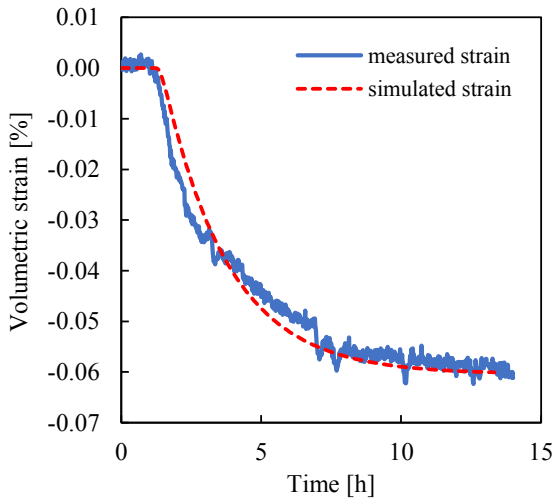


Fig. 3.33.: Drainage phase from Fig. 3.32b with measured and simulated strains

transient drainage phase. This procedure enables to determine multiple material parameters in one single test. The three-stage loading protocol, which provides 4 material parameters and enables a permeability analysis is presented in the following section. An alternative simplified testing protocol consisting of two load phases, allowing for a permeability analysis and the measurement of 2 material parameters, is explained in Sec. A.2.

A new loading procedure for mechanical and thermal rock tests is presented, which takes advantage of the low permeability of geomaterials. In this procedure consisting of three stages, the confining stress or the temperature respectively is first changed in a short time. If this rate is fast enough, the pore fluid inside the specimen has no time to drain and an undrained material behaviour is measured (K_u or α_u respectively) which does not have to be corrected for the deformability of the drainage system. Concurrently, the applied load is held constant, so that generated pore pressure stabilize in a second undrained stage. The perturbation on measured parameters in this stage (K_u and B or α_u and Λ respectively), caused by the deformability of the drainage system, can be corrected with a calibration of the testing system. In the third stage, the pore pressure is controlled again and brought back to its initial value, effecting a gradual drainage. When specimen strains stabilize, we suppose a completely drained state and the parameters K_d or α_d, respectively, can be determined. We simulate these laboratory test using analytical solutions of a diffusion equation. The permeability of the specimen is back-calculated from the transient behaviour between undrained and drained state. Application examples on COx claystone show this procedure in practice. In the mechanical three-stage test, one obtains an overdetermined set of 4 isotropic elastic parameters and the permeability, allowing to describe the hydro-mechanical coupling. The thermal three-stage test provides the same number of parameters and permits to characterize the THM coupling. A conventional drained test under monotonic loading would require about 24 h for the loading path and another 24 h to bring the specimen back to hydraulic equilibrium. Such monotonic loading tests provide only one material parameter. The presented procedure for evaluating 5 parameters in one single test took about 24 h on the COx claystone, which demonstrates its time-efficiency.

3.7 Numerical modelling

In this section, we provide some information on the approach adopted for a numerical analysis of the thermo-hydro-mechanical behaviour around heated microtunnels in COx claystone. To this end, the geological layers with the microtunnels, at a certain depth and with a certain distance to each other, are modelled. Note that the dimensions used in this study does not reflect the dimensions planned for the real structure. The aim here is not to give recommendations for the dimensioning of the microtunnels. The simulations presented in this work are carried out using a simple thermo-poroelastic model. We do not consider time dependent properties, non-elastic deformations, nor damage. The purpose of this

analysis is to understand the basic thermo-hydro-mechanical couplings in a transversely isotropic framework. We emphasize the application of the properties evaluated in the present experimental studies and their impact on simulated THM phenomena. Note also, that the focus lies here in observations on the far field, where one supposes that the rock is unaffected by the excavation damage zone (EDZ) around the drifts. Within the EDZ, where the elastic limit is attained due to excavation, an elastic model is not capable to model the material behaviour. In the following discussions, we therefore exclude stresses and strains of the zone within 2.5 times the microtunnel diameter. The temperature evolution, which is believed to be less influenced by the EDZ, is however studied in this zone.

Material parameters, presented in the literature (Sec. 2.2), with the contributions of this study (Sec. 4 and 5), are applied in the numerical model, which is based on the theoretical framework discussed in Sec. 2.1.

Numerical analysis of thermal pressurization in COx claystone has been addressed by various authors (e.g. Gens et al., 2007; Seyedi et al., 2017). Recently Seyedi et al. (2018), investigated the rock behaviour around microtunnels in a periodical disposition, by adopting a thermo-poroelastic model.

3.7.1 Constitutive equations

One can write down the basic momentum balance as:

$$\nabla \sigma_{ij} + \mathrm{f} = 0 \tag{3.65}$$

where σ_{ij} is the stress tensor, defined positive in compression, and f a body force. The stress tensor can be expressed in function of strain, pore pressure and temperature [Eq. (2.1)], explained in detail in Sec. 2.1.1. In terms of material parameters, two Young's moduli and Poisson's ratios E_h, ν_h and E_z, ν_z in horizontal (parallel to bedding) and vertical (perpendicular to bedding) direction, respectively, are involved. We also require a shear modulus G perpendicular to bedding to compose the stiffness tensor. Two Biot's coefficients b_i, and two drained thermal expansion coefficients $\alpha_{d,i}$, are needed for the THM model.

The conservation of fluid mass m_f is expressed by the following equation:

$$\frac{\mathrm{d}m_f}{dt} + \nabla q_{f,i} = 0 \tag{3.66}$$

where the fluid flow $q_{f,i}$ follows Darcy's law, which includes the intrinsic permeability k_i in both anisotropy directions, the fluid dynamic viscosity μ_f, the fluid density ρ_f and the earth gravitational acceleration g:

$$q_{f,i} = \rho_f \frac{-k_i}{\mu_f} \left(\nabla p_f - \rho_f g\right) \tag{3.67}$$

The fluid mass change can be rewritten in terms of $\mathrm{d}m_f = \rho_f \mathrm{d}\phi + \phi \mathrm{d}\rho_f$, in which we insert Eq. (2.13), to obtain:

$$-b_i \frac{\mathrm{d}\varepsilon_i}{\mathrm{d}t} + \frac{1}{M}\frac{\mathrm{d}p_f}{\mathrm{d}t} - \left(b_i\alpha_i - \phi\alpha_\phi + \phi\alpha_f\right)\frac{\mathrm{d}T}{\mathrm{d}t} + \frac{1}{\rho_f}\nabla\left(\rho_f \frac{-k_i}{\mu_f}\left(\nabla p_f - \rho_f g\right)\right) = 0 \tag{3.68}$$

We consider heat transport governed by Fourier's heat equation [Eq. (3.69)], under the assumption that heat transport occurs only by conduction. As stated by Gens et al. (2007), heat convection in the COx claystone can be neglected due to its low permeability. This causes a decoupling of the heat equation, given that it can be solved independently of the fluid mass and momentum balance equations.

$$\rho C \frac{\mathrm{d}T}{\mathrm{d}t} - \nabla\left(\lambda_i \nabla T\right) = q_T \tag{3.69}$$

with C representing the specific bulk heat capacity, ρ the bulk density, q_T a volumetric heat source, and λ_i the transversely isotropic thermal conductivities.

To carry out a numerical THM analysis, one has to solve first the heat equation (3.69), which provides a temperature field. Afterwards the coupled equations (3.65) and (3.68) are solved. This was done in the present study, within the finite element solver FreeFem++ (Hecht, 2012). This free software, written in C++, is highly adaptive and optimized for solving multiphysics problems. The constitutive equations were implemented in FreeFem++ in their weak form, and solved by the program, using meshes created with the integrated mesh generator. The code was validated on analytical solutions of the heat equation, combined with the analytical solutions for THM coupling from Sec. 3.5.

3.7.2 Model Geometry

Due to symmetry conditions, we are able to represent the parallel microtunnels and the surrounding rock by modelling only half of the gallery, and a formation extending to the vertical mid axis between two tunnels (Fig. 3.34a). Given their important length, a cross section is in the following analysed in a simplified plane strain 2D model. The circular microtunnel with a diameter of 0.70 m is located at a depth of -549 m, enclosed by the Callovo-Oxfordian claystone. The COx layer is divided into subunits, with a high carbonate

content layer (USC, from -471.7 to -501.8 m), a transition layer (UT, from -501.8 to -517.1 m), and three high clay content layers (UA1-3, from -517.1 to -624 m). Above the COx layer, we encounter the Oxfordian layer from -201 to -471.7 m and the Kimmeridgian from the surface at 0 m to -201 m. Below the COx layer there is the Dogger, which extends to larger depth than the model, designed up to -1100 m. The extend of the modelled region below and above the microtunnel was chosen *a priori* large enough in order not to induce boundary effect through the imposed pore pressure and temperature conditions at top and bottom borders.

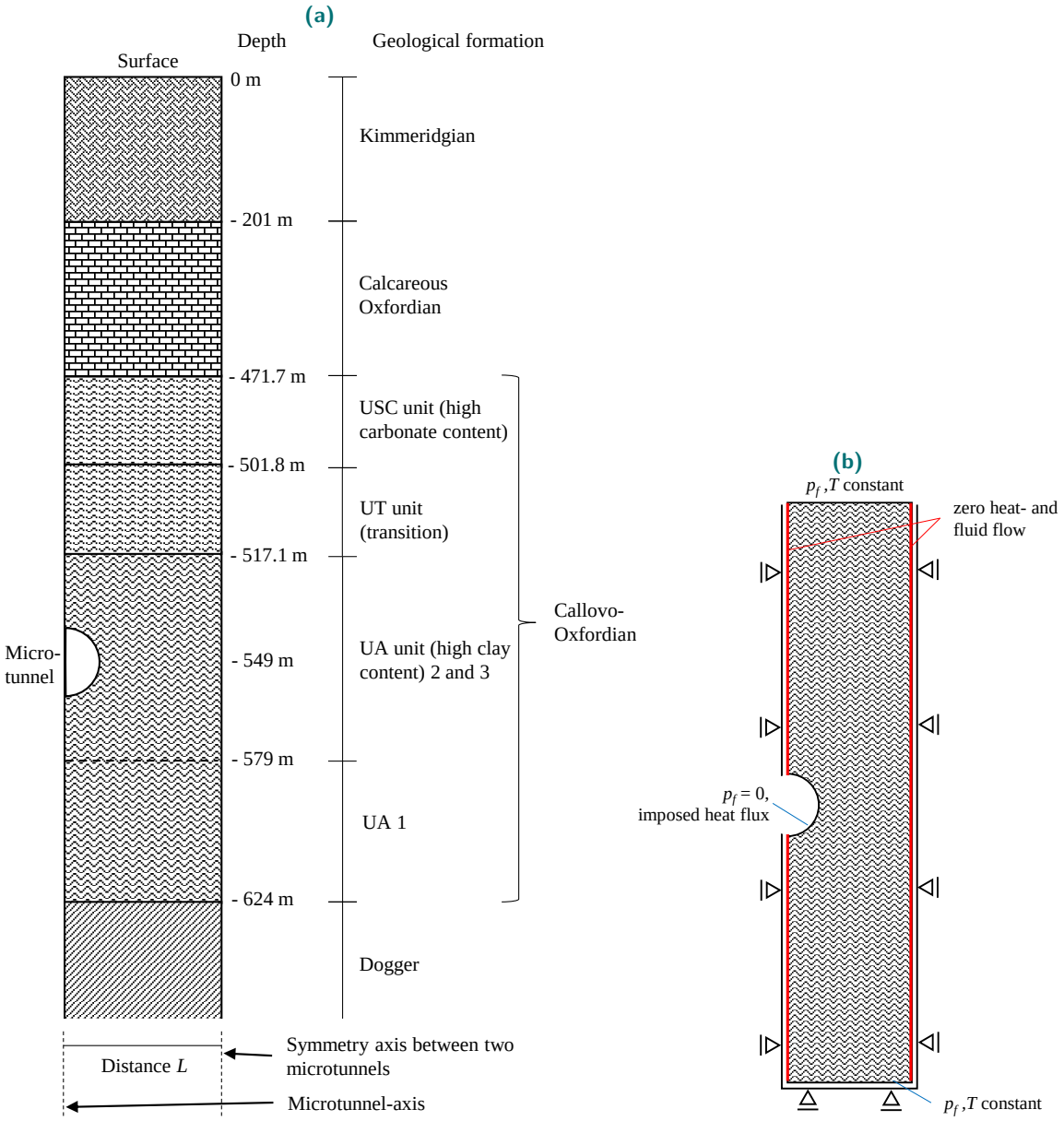


Fig. 3.34.: Schematic illustration of a) the geometry of the finite element model and b) the displacement, temperature and pore pressure boundary conditions applied to the finite element model. The dimensions are not to scale

3.7.3 Boundary conditions

Displacement

We assume plane strain conditions, therefore deformations perpendicular to the 2D plane are prohibited. The symmetric layout causes also zero horizontal deformation along both vertical boundaries, displayed in Fig. 3.34b. At the horizontal boundary at the bottom, the vertical deformations are kept to zero, whereas surface deformations are unrestricted. For the wall of the microtunnel we assume free deformations. This is a simplifying assumption, as in reality the possible instalment of a lining could provide some support. Moreover, the convergence of the microtunnel might at some point fill the spaces between rock and waste packages, which would influence this boundary condition.

Stress

Data from extensive studies on the natural stress conditions is provided by Andra. In this model, we consider a vertical stress σ_z calculated from the lithostatic pressure of the rock formations, with constant densities for each respective geological layer. This weight of the rock mass remained as a constant body force during the time integration. The minor horizontal stress σ_h, in this case acting in the modelled plane, is equal to the vertical stress. The major horizontal stress σ_H is equal to the vertical stress within the Kimmeridgian layer, and increased with $\sigma_H = 1.3\ \sigma_h$ starting from the Callovo-Oxfordian layer downwards. In the Oxfordian layer, a linear interpolation between the major horizontal stresses of the surrounding upper and lower layers is used. At the level of the microtunnel we obtain hence stresses of $\sigma_z = \sigma_h = 13.3$ MPa and $\sigma_H = 17.2$ MPa. To find an initial stress field which is in equilibrium, a separate first calculation step had to be carried out. The model included initially no excavation and the circular hole was filled with material, which had a zero horizontal deformation and zero flow condition on the left boundary. The material properties of the whole model were modified, such as to obtain the stress field observed *in situ*. After this step the deformations were set to zero, and the real material parameters applied. The gallery excavation was simulated by removing the half-circle region of the mesh, using the FreeFem++ function “trunc”.

Pore pressure

The initial pore pressure corresponds to the hydrostatic pressure of water. The weight of the water is also considered during the time integration steps. Constant pore pressures are imposed at the surface, equal to zero, and at the bottom of the model, equal to the initial

hydrostatic pressure. Around the microtunnel, one finds an initial pore pressure of 5.5 MPa. Due to the symmetry in horizontal direction, a zero flux condition is set at both left and right vertical boundaries and in horizontal direction perpendicular to the model plane. At the wall of the microtunnels, we assume constant zero pore pressure. In reality however, this surface might be sealed by a tunnel lining, which would result in zero flow boundary conditions. These conditions are not investigated in the present work.

Temperature

An initial temperature distribution over all geological layers is given by Andra through data on the geothermal gradient. The temperature increases with depth, with around 7 °C on the surface and constant gradients for each respective layer. At the repository level, the initial temperature is 23 °C. For $t > 0$, the temperature at the surface and at the bottom depth are kept constant, equal to their respective initial value. Horizontal heat flux is set to zero at both left and right vertical boundaries and in direction perpendicular to the model plane.

The radioactive waste packages emit heat, which is represented in the model by a heat flux boundary condition. A heat flux density q_T, is imposed at the wall of the microtunnel and gradually decreases with time. The magnitude of q_T and its variation with time is given by data from Andra, depicted in Fig. 3.35.

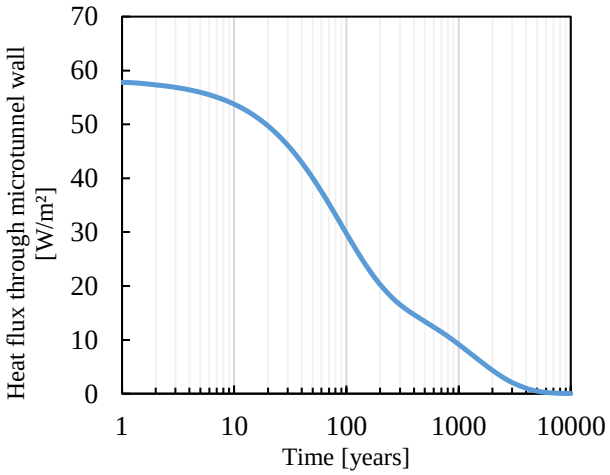


Fig. 3.35.: Heat flux density through the microtunnel wall, exerted by the radioactive waste packages (from the Andra database)

3.7.4 Time and space discretization

A finite element mesh with triangular elements was created using the integrated mesh-generator of FreeFem++. A simplified preliminary thermal calculation was carried out. The

temperature field was used as an argument for the integrated mesh optimization function "adaptmesh". This function refines the mesh based on the thermal field, giving a finer mesh around the microtunnel where stress, temperature and pore pressure gradients are expected to be important, and a coarser mesh far away from the gallery. This mesh adaptation is important for saving calculation time, especially for such a relatively large mesh with a localized problem. Fig. 3.36 shows the generated mesh (3868 triangles) used for the later calculations. A convergence of results was verified with a coarser mesh (800 triangles) and a finer mesh (13694 triangles).

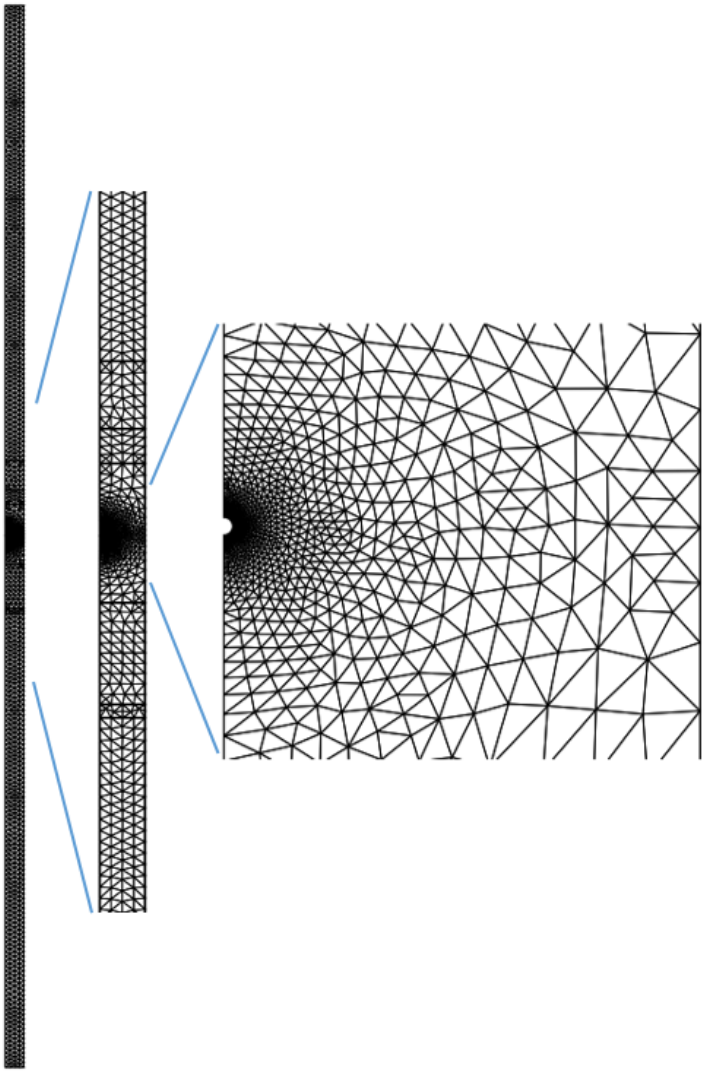


Fig. 3.36.: Complete mesh displayed on the left, with zooms on the microtunnel. The mesh was generated using the FreeFem++ mesh builder, and utilized in the presented analysis

The problem was solved with an implicit time integration. During the ventilation phase in the first two years after excavation, a timestep of $\mathrm{d}t = 14.6$ d was sufficient for minimizing integration errors. This timestep was hence adopted for the following calculations of the ventilation phase.

Due to the large timescales in the thermal phase, an automatic time step optimization was implemented in the code. We chose the following method in this work: Given the solution u_0 at $t = 0$ and an initial timestep of $\mathrm{d}t$,

- one large timestep $n \times \mathrm{d}t$ is used to calculate $u'_{1(n\mathrm{d}t)}$
- n timesteps of $\mathrm{d}t$ are carried out to calculate $u_{1(n\mathrm{d}t)}$
- if the difference between $u'_{1(n\mathrm{d}t)}$ and $u_{1(n\mathrm{d}t)}$ is smaller than a defined acceptable error ϵ, the increased timestep $n \times \mathrm{d}t$ is used for the following steps.

Smaller timesteps for reducing calculation errors are predominantly required for the thermal problem, as the heat conduction is faster than the hydraulic conduction. Therefore we chose temperature values as an error criteria ϵ, calculated at the gallery wall, 4 m above the gallery and at the mid distance between two galleries. An initial timestep of 6 seconds, a factor $n = 10$ and $\epsilon = 0.01$ °C were chosen in this context. A maximum timestep of 1/10 year was allowed. Due to uncoupling of the thermal problem, the additional calculation for the timestep $n\mathrm{d}t$ had to be carried out only for the relatively time efficient thermal calculation, hence did not significantly increase the computation time.

The presented model is employed in Sec. 4.4, where we first analyse the uncoupled temperature evolution. A reference THM calculation is conducted using transversely isotropic, stress independent, parameters. We carry out further calculations by modifying the anisotropy ratio of poroelastic properties and by adopting stress dependent parameters. Simulations under a variation of the thermal properties of solid and fluid phase are presented in Sec. 5.4. In Sec. 6.4, we compare simulated stress paths with the ones created in laboratory experiments.

3.8 Conclusions

We presented some *in situ* measurements, carried out at the Bure URL, which gave new insight on the natural state of the COx claystone. Cores retrieved from some distance of the drift walls, considerably fully saturated, showed suctions of around 10 MPa. These values helped in the evaluation of employed handling protocols and could give some useful information for potential future characterization of the undrained behaviour of the material.

In this regard, we observed that samples trimmed from cores in the laboratory had a very high saturation degree, larger than 92 %, confirming well preserved specimens. Additional petrophysical data was evaluated for the different cores, showing comparable characteristics with the Andra database, such as for instance a porosity around 18 % and a water content around 8 %.

We presented in detail the experimental devices, an isotropic and a triaxial cell, allowing testing under high stresses, pore pressures and controlled temperature. The implemented strain gage system had to be precisely calibrated for measurement perturbations due to temperature changes. Furthermore, the properties of the drainage system were assessed, necessary for correcting measured undrained material parameters.

We also detailed the developments made for a novel triaxial apparatus, which can recreate unconventional stress paths in the laboratory. In this device, the pore pressure (controlled by a PVC or thermally induced in undrained conditions) can exceed the axial total stress, which generates effective tension within the specimen. The radial stress can be controlled independently, with the option of imposing zero radial deformation by a servo-controlled confining pressure. Consequently, tensile behaviour and tensile strength of geomaterials can be explored with this device.

Due to the low permeability of the COx claystone, laboratory experiments require generally long durations for saturation and pore pressure equilibration. We presented some analytical solutions to describe the time dependent 1D pore pressure field in a specimen, submitted to various THM loading paths under different rates. These solutions allow a fast estimation of testing conditions, that must hold for reliable determination of material parameters. Potential errors due to non-homogeneous pore pressures within the specimen can be assessed, and testing conditions improved accordingly.

Based on this approach, we developed a new transient step loading procedure for isotropic THM test. With this procedure, several THM parameters can be measured in one single step test. Moreover, conditions of hydraulic equilibrium can be easily confirmed when transient deformations stabilize. The back analysis of transient deformations also provides permeability values. The efficiency of these protocols was demonstrated on application examples of laboratory experiments.

Finally, a numerical model for a large scale THM problem was discussed. We implemented a plane strain thermo-poroelastic model, for simulating the rock behaviour around parallel microtunnels in simplified repository conditions. A model with 20 m width and 1100 m depth was created, including a microtunnel located at about mid-height. The microtunnel is submitted to a ventilation phase, followed by the application of a heat source up to 200 years. In consequence, this model allows to analyse the material behaviour with respect to different adopted THM parameters.

4 Poroelastic behaviour

In this chapter, we present the data of a series of tests, carried out to investigate the hydromechanical response of the COx claystone. We conducted isotropic compression tests, pore pressure tests and triaxial shear tests and measured the specimen strains parallel and perpendicular to bedding. For this purpose, a high pressure isotropic and a deviatoric cell (Sec. 3.3) were utilized, adopting the optimized loading protocols discussed in Sec. 3.6. This enabled us to determine a large number of material coefficients, to characterize the COx claystone within a transversely isotropic material model. The conducted testing program and followed protocols are presented in Sec. 4.1, with their outcomes given in Sec. 4.2. These observations are discussed in and analysed in Sec. 4.3. In Sec. 4.4 we show a simplified numerical application of determined parameters. The conclusions of this chapter are given in Sec. 4.5.

The experimental findings of this chapter are included in the publication: Braun, P., Ghabezloo, S., Delage, P., Conil, N., and Sulem, J. (2019) "Transversely isotropic poroelastic behaviour of the Callovo-Oxfordian claystone: A set of stress-dependent parameters ". in preparation.

Tab. 4.1.: Overview of tested specimens with their initial saturation phase under stress and their respective subsequent loading paths; the inclined arrows (↘,↗) indicate that several load steps were carried out between mentioned effective stresses. σ denotes the total isotopic confining stress, σ'_{ax} and σ'_{rad} the axial and radial effective stresses, respectively, while ε_{hyd} denotes the swelling strains observed during saturation

Sample	Core	Saturation phase		Loading path	
		σ	ε_{hyd}	Isotropic tests:	Deviatoric tests:
#	EST	[MPa]	[%]	$\sigma'_{rad} = \sigma'_{ax}$ [MPa]	q [MPa]
ISO1	57185	10	0.71	10↘1↗18	-
ISO2	53650	8	0.86	-	-
ISO3	53650	8	0.80	-	-
ISO4	53650	8	0.72	8↗15↘2	-
ISO5	53650	10	0.61	10↗36↘0.5	-
ISO6	53650	14	0.57	14↔16	-
ISO7	53650	10	0.66	-	-
ISO8	53650	8	0.95	-	-
ISO9	53650	30	0.15	-	-
ISO10	58132	20	0.33	20↔18	-
DEV1	57185	10	0.55	30→20→10	0↔5 (@σ'_{rad} = 30/20/10)
DEV2	57185	10	0.62	-	0↔10 (@σ'_{rad} = 11)
DEV3	57185	20	0.42	-	0↔10 (@σ'_{rad} = 10)

4.1 Testing Procedure

The COx specimens were mounted in the isotropic and triaxial cells in their initial state at 25 °C. The specimens were first consolidated at constant water content under isotropic stress with a loading rate of 0.1 MPa/min, while the drainage system was kept dry.

Most of the specimens were brought to a confining pressure close to the *in situ* effective stress between 8 MPa and 10 MPa. 3 Specimens were saturated at higher confining stress to investigate the effect of confining on swelling strains during hydration. An overview of all tested specimens with their respective initial confining stress is given in Tab. 4.1.

When specimen deformations remained stable after application of confining stress, the air in the dry drainage ducts was evacuated by vacuum. The ducts were then filled with synthetic pore water under a pressure of 100 kPa. To prepare synthetic water, salts were mixed to water according to a recipe provided by Andra (Tab. 3.2), to obtain a fluid composition close to the *in situ* one. The initial applied pore water pressure was chosen small enough, in order to limit poromechanical effects. Hydration resulted in swelling strains, that stabilized after about 5 days on all samples, showing similar transient characteristics. Tab. 4.1 lists the measured volumetric swelling strains, which decrease with increasing confining stress. The volumetric swelling for each specimen with respect to the applied confining stress is plotted in Fig. 4.1 and follows a function of the form $y = a/x$, with $a = 6.58$, fitted by a least square optimization. This trend highlights, as previously mentioned by various authors (e.g. Mohajerani, 2011; Menaceur et al., 2015; Belmokhtar et al., 2017a), the

necessity to saturate the claystone under confined conditions, in order to limit swelling and corresponding potential damage.

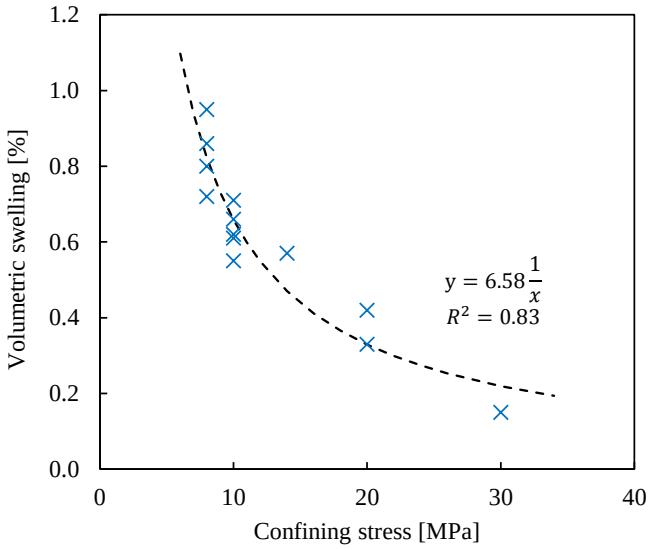


Fig. 4.1.: Measured swelling strains of specimens during hydration under various confining stresses, with a proposed power-law regression

After hydration, pore pressure and confining pressure were increased simultaneously of 4 MPa, keeping a constant Terzaghi effective stress. The applied pressures were increased until the pore pressure reached 4 MPa. Consequently, the samples reached Terzaghi effective stresses, which were equal to the initial confining stress described in Tab. 4.1. A step testing procedure, presented by Braun et al. (2019), Sec. 3.6, was then utilized to determine the poroelastic parameters of the material in isotropic tests. This procedure consists of increasing or decreasing the confining pressure rapidly at a rate of 0.1 MPa/min, and of keeping it then constant at a certain level. This generates first an undrained response, which permits to evaluate the undrained bulk modulus K_u as a tangent modulus, together with the anisotropic moduli U_h and U_z. During a constant load phase, the pore pressures generated in the first phase are allowed to drain. A drained response can be observed, when all pore pressures dissipated and the deformations stabilize, providing the drained bulk modulus K_d with D_h and D_z. When the confining pressure is held constant and the imposed pore pressure is changed instantly by the PVC, a transient deformation can be observed. After stabilization of these deformations, the Biot modulus H with H_h and H_z can be evaluated. Deviatoric tests on specimens DEV1 and DEV3 were conducted perpendicular to the bedding plane, providing E_z, ν_{zh} $E_{u,z}$ and $\nu_{u,zh}$, whereas the test parallel to the bedding plane on DEV2 provided E_h, ν_{hh}, ν'_{zh}, $E_{u,h}$, $\nu_{u,hh}$ and $\nu'_{u,zh}$ (compare Fig. 2.1). Here we proceeded similar as in isotropic loading tests, by applying the deviatoric load q in a relatively rapid loading of 0.1 MPa/min. The stress-strain path during the rapid initial loading was confirmed to be undrained by conducting a quick unloading/reloading cycle on specimen DEV2, which displayed a continuous slope (Fig. 4.2 and 4.3). Once the target deviatoric stress was reached, we kept it constant, causing a fluid dissipation and equilibration of the pore pressure field inside the specimen. We supposed competed

drainage when measured strains stabilized. The strains in drained state permit to evaluate the drained Young moduli and Poisson ratios as secant parameters.

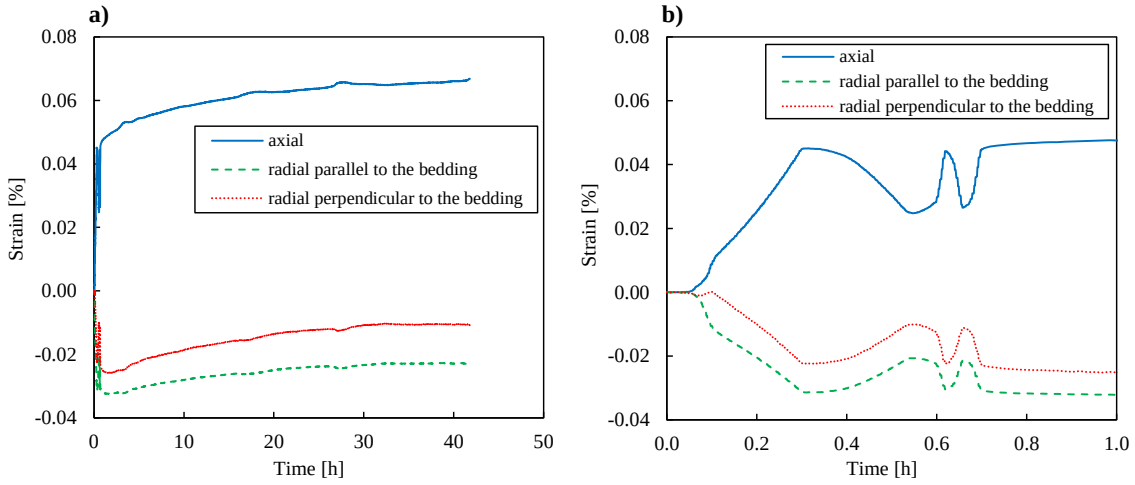


Fig. 4.2.: Measured deformations during a deviatoric test on sample DEV2 loaded parallel to the bedding plane in a) function of time, with b) zoom on the first hour of a). One observes the time dependent deformations due to fluid dissipation, and the anisotropic radial strain response

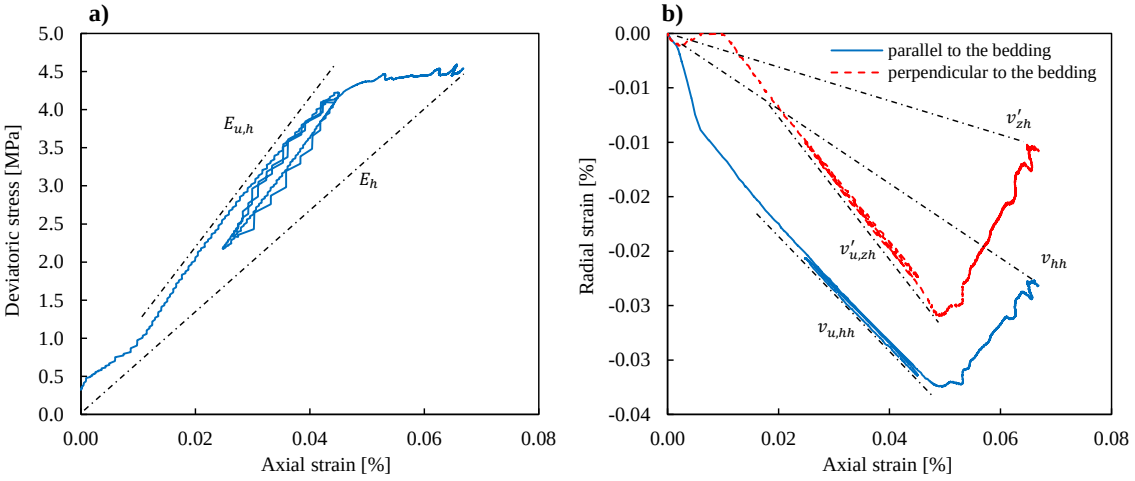


Fig. 4.3.: Measured deformations during a deviatoric test on sample DEV2 loaded parallel to the bedding plane in a) function of deviatoric stress q highlighting the determination of the Young moduli, and in b) radial strains with respect to axial strains indicating the Poisson ratios

For isotropic tests, the measured parameters are presented in function of the mean between initial and final effective stress applied during each step test ($\sigma' = \sigma'_{\mathrm{ax}} = \sigma'_{\mathrm{rad}}$). All discussed coefficients were measured under unloading or reloading and are therefore supposed to be elastic. Several subsequent step tests were carried out, starting from the initial stress level and then gradually increasing or decreasing the effective stress in each step with an increment of between 1.0 and 5.0 MPa stress. These ramps are indicated in Tab. 4.1 with inclined arrow symbols ($\searrow$,$\nearrow$). Horizontal arrows ($\rightarrow$) characterise only one step between the indicated effective stresses, which was repeated in the case of a double arrow ($\leftrightarrow$). The same applies for the deviatoric tests on specimens DEV1 - DEV3. Specimen DEV1 was loaded and unloaded by applying a devatoric load q between 0 and 5 MPa, which was

repeated at effective radial stresses σ'_{rad} of 30, 20 and 10 MPa. Samples DEV2 and DEV3 were only tested at 10 MPa and 20 MPa effective radial stress, respectively. The resulting parameters are plotted with respect to the average of the inital and final mean effective stress σ' at each step loading. Specimens without any loading part given were not tested under hydro-mechanical experiments; they were either only tested in thermal tests (not discussed here) or had to be abandoned due to technical problems.

4.2 Experimental Results

4.2.1 Stress dependent properties under isotropic stress

A large number of isotropic hydromechanical tests provided measurements of the moduli K_d and H with a strong dependency on the effective stress, coherent for all tested specimens (Fig. 4.4 and 4.5). Zimmerman et al. (1986) showed, that under the condition of a constant modulus K_s, a stress dependency of the tangent bulk moduli of an isotropic material can be expressed in function of the Terzaghi effective stress. In Section 4.3.1 we demonstrate, that assuming a constant K_s, we are indeed able to reproduce the measured COx properties. Even though the COx claystone is not isotropic, we decided here to present the following measurements with respect to the mean Terzaghi effective stress.

The isotropic moduli are smaller than 1.0 GPa for low Terzaghi effective stresses and increase with an increasing effective stress. With an effective stress larger than about 20 MPa, the moduli appear to remain constant. For K_d under effective stresses around 10 MPa, we can observe a good accordance with the findings of Mohajerani (2011) and Belmokhtar et al. (2017a). The modulus H was previously measured by Belmokhtar et al. (2017a) at around 10 MPa effective stress with 3.47 and 2.24 GPa.

Interestingly, the reduction of stiffness appears to be reversible, as it can be seen if Fig. 4.6. Here we compare the drained bulk modulus, measured on sample ISO1 after subsequent unloading steps, starting from the initial under stress saturated state. The bulk modulus decreases through unloading. After reloading, the drained bulk modulus came back to the same level as before unloading, comparable also to the values on ISO6 and ISO10, for which the effective stress level was not significantly reduced after saturation.

The undrained bulk modulus K_u shows also a stress-dependency, although less pronounced than for K_d and H (Fig. 4.7). Note here the rather large dispersion of observed values, which was also evidenced in the works of Escoffier (2002), Mohajerani (2011), and Belmokhtar et al. (2017a).

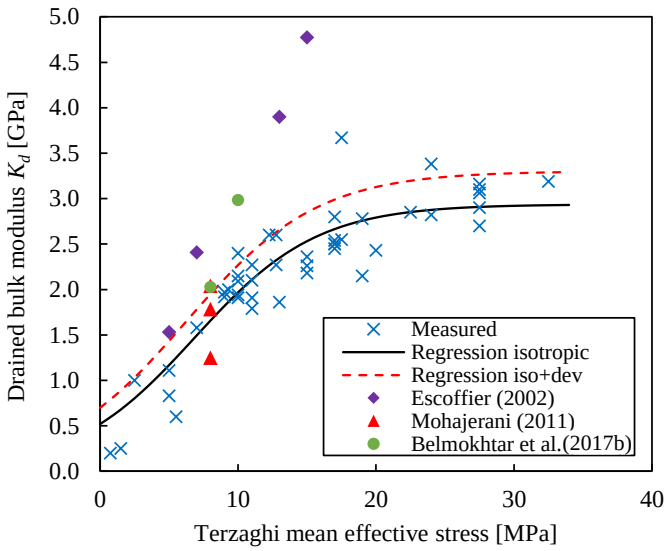


Fig. 4.4.: Measured stress dependent drained bulk modulus K_d for equivalent isotropy, with a fitted model based on isotropic tests (Tab. 4.3) and a fitting based on all isotropic and deviatoric test results (Tab. 4.5).

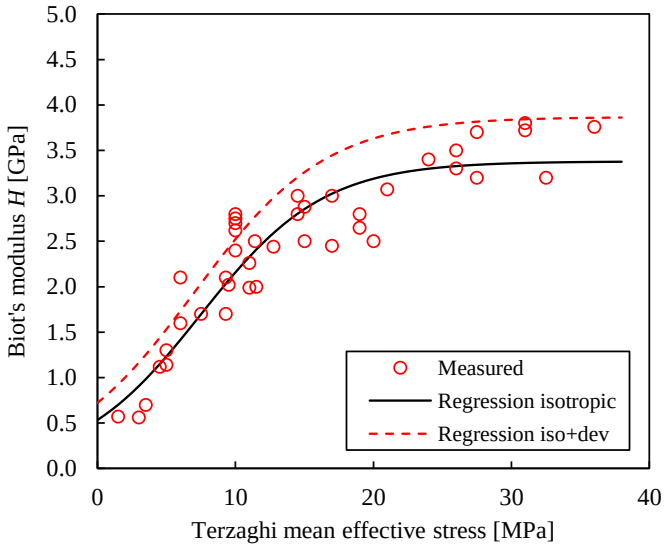


Fig. 4.5.: Measured stress dependent Biot's modulus H for equivalent isotropy, with a fitted model based on isotropic tests (Tab. 4.3) and a fitting based on all isotropic and deviatoric test results (Tab. 4.5).

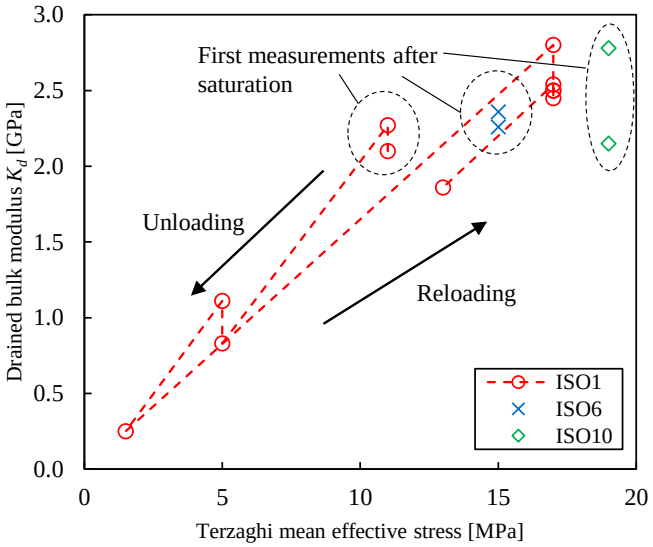


Fig. 4.6.: Measured stress dependent drained bulk modulus K_d on samples ISO1, ISO6 and ISO10, illustrating the reversible reduction of stiffness with decreasing effective stress

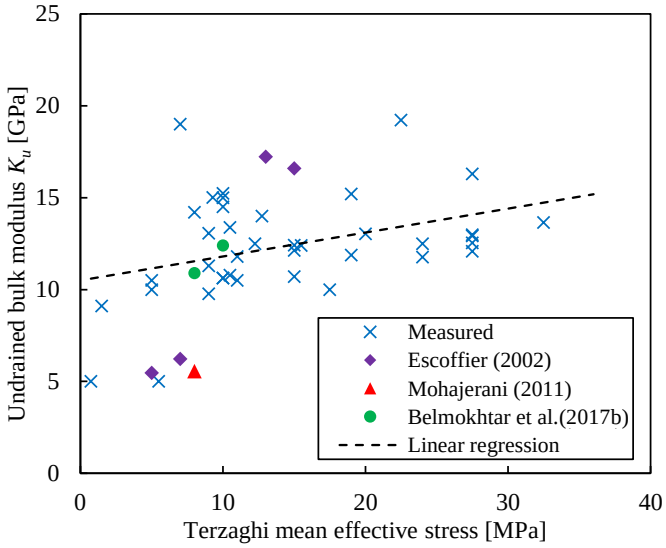


Fig. 4.7.: Measured stress dependent undrained bulk modulus K_u for equivalent isotropy, with fitted linear relationship (Eq. (4.2), Tab. 4.3).

The transversely isotropic strain response was recorded simultaneously with K_d, H and K_u in all tests (Fig. 4.8, 4.9 and 4.10). For drained tests (K_d, H), one observes axial strains perpendicular to the bedding plane about three times larger than radial ones. For Terzaghi effective stresses lower than 15 MPa, this ratio showed values of around 4.0. In undrained tests, the ratio of anisotropy varied more importantly with effective stress, with values around 1.5 for low effective stress and values around 2.0 for 30 MPa effective stress. The ratios of anisotropy are summarized in Fig. 4.11 for all three isotropic test types.

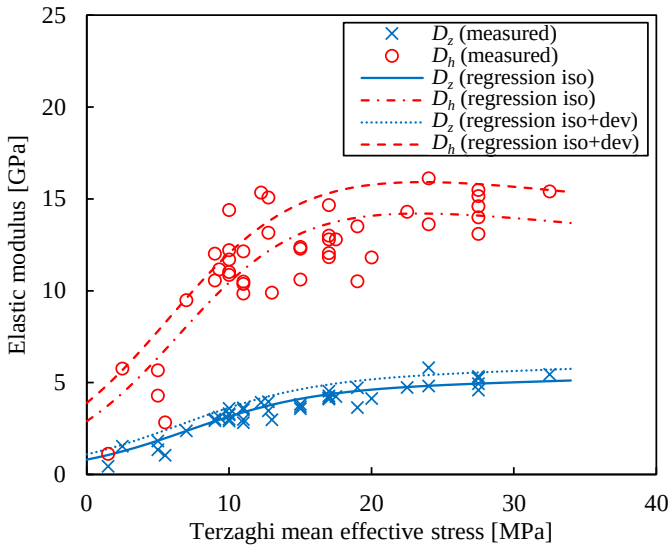


Fig. 4.8.: Measured anisotropic responses D_i during drained compression, with a fitted model based on isotropic tests (Tab. 4.3, 4.4) and a fitting based on all isotropic and deviatoric test results (Tab. 4.4, 4.5).

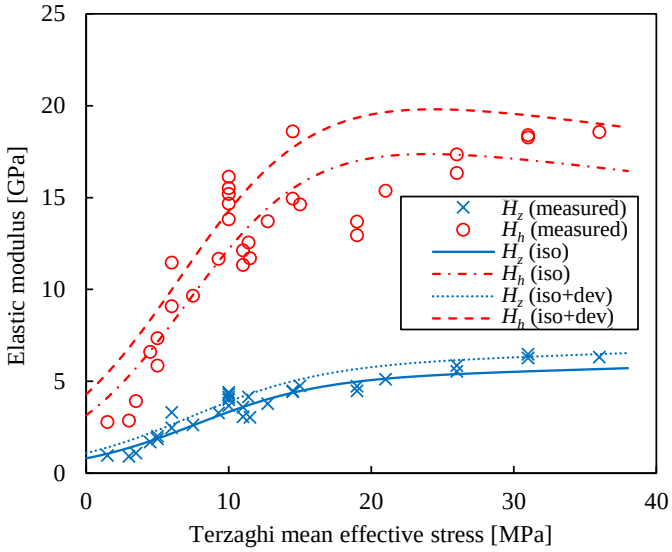


Fig. 4.9.: Measured anisotropic responses H_i during pore pressure tests, with a fitted model based on isotropic tests (Tab. 4.3, 4.4) and a fitting based on all isotropic and deviatoric test results (Tab. 4.4, 4.5).

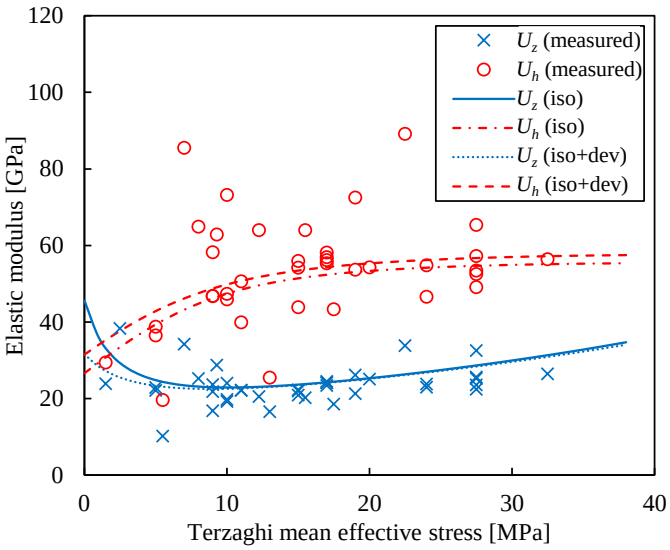


Fig. 4.10.: Measured anisotropic responses U_i during undrained compression, with a fitted model based on isotropic tests (Tab. 4.3, 4.4) and a fitting based on all isotropic and deviatoric test results (Tab. 4.4, 4.5).

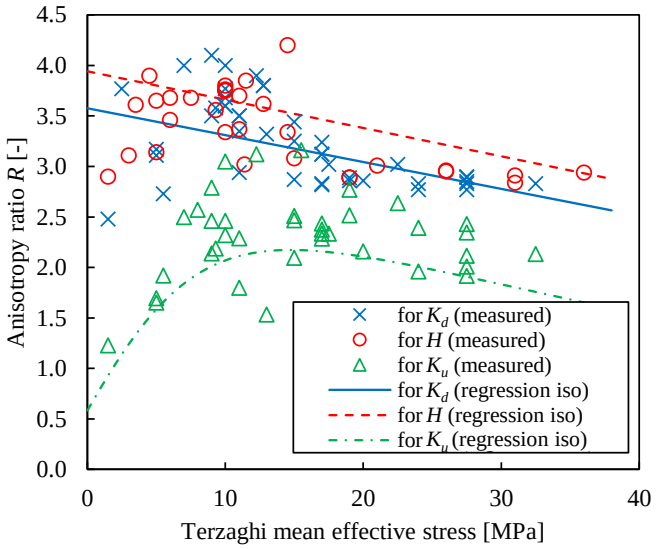


Fig. 4.11.: Measured ratio of anisotropic strain response R_i during drained and undrained compression and pore pressure tests, with a fitted model based on isotropic tests (Tab. 4.3, 4.4).

4.2.2 Stress dependent properties under deviatoric stress

In the triaxial tests, we measured E_z and ν_{zh} on specimens DEV1 and DEV3 for effective confining stresses from 10 to 30 MPa. Whereas the Poisson ratio remained more or less constant, with values between 0.10 and 0.17, the Young's modulus E_z increased with increasing confining stress from 3.4 to 6.7 GPa. The parameters E_h and ν_{hh} on sample DEV2 were measured only for 10 MPa mean effective stress, with values for E_h between 6.4 and 8.0 GPa and ν_{hh} between 0.30 and 0.34 (Fig. 4.12, 4.13). Compared with the values of E_z from Zhang et al. (2012), Belmokhtar et al. (2017a) and Belmokhtar et al. (2018), a coherent stress dependency can be observed. As expected, the undrained response during these tests provided higher moduli than the drained ones. The parameter $E_{u,z}$ was found between 6.4 and 8.6 GPa and $E_{u,h}$ between 9.8 and 10.8 GPa. The anisotropy of the undrained moduli shows a ratio $E_{u,h}/E_{u,z}$ around 1.4, whereas the drained moduli show a ratio E_h/E_z of around 1.75 (Fig. 4.14, 4.15).

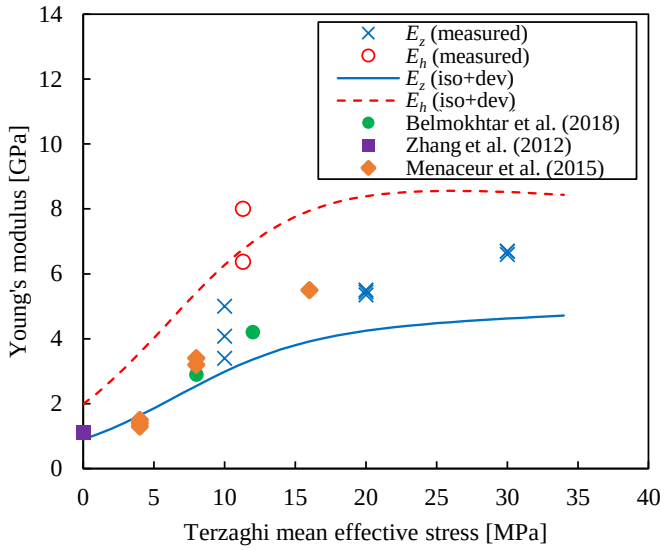


Fig. 4.12.: Measured stress dependent drained Young's modulus E_z perpendicular and E_h parallel to the bedding plane, with a fitted model using isotropic experimental results (Tab. 4.3) and a fitting based on all isotropic and deviatoric test results (Tab. 4.5)

4.3 Regression analysis and discussion

The obtained data evidences a significant stress dependency of the COx transversely isotropic poromechanical parameters. We aim therefore to establish a set of coefficients, which can reproduce the observed measurements and captures at the same time the stress dependency.

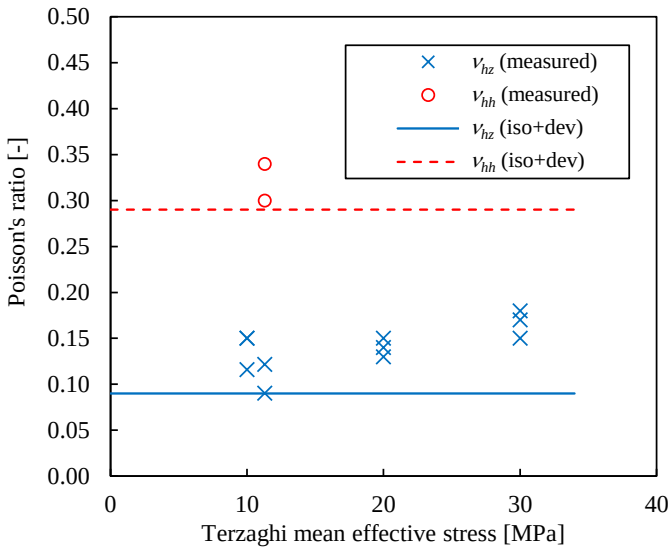


Fig. 4.13.: Measured drained Poisson's ratio ν_{zh} perpendicular and ν_{hh} parallel to the bedding planes with respect to effective stress, with a fitted model using isotropic experimental results (Tab. 4.3) and a fitting based on all isotropic and deviatoric test results (Tab. 4.5)

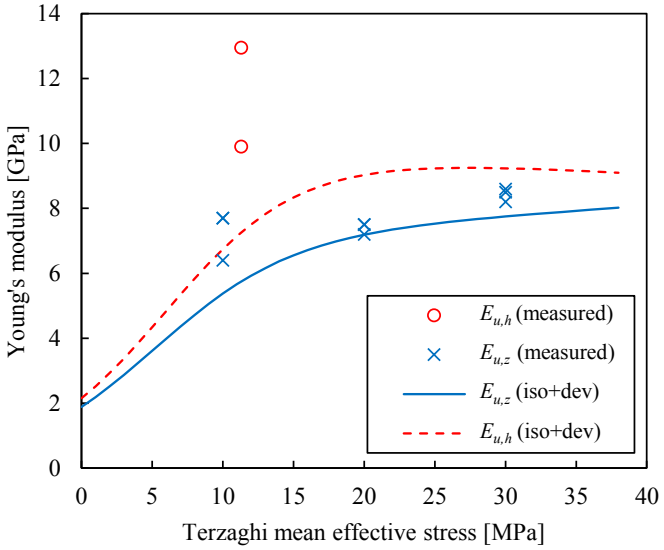


Fig. 4.14.: Measured stress dependent undrained Young's modulus $E_{u,z}$ perpendicular and $E_{u,h}$ parallel to the bedding plane, with a fitted model using isotropic experimental results (Tab. 4.3) and a fitting based on all isotropic and deviatoric test results (Tab. 4.5)

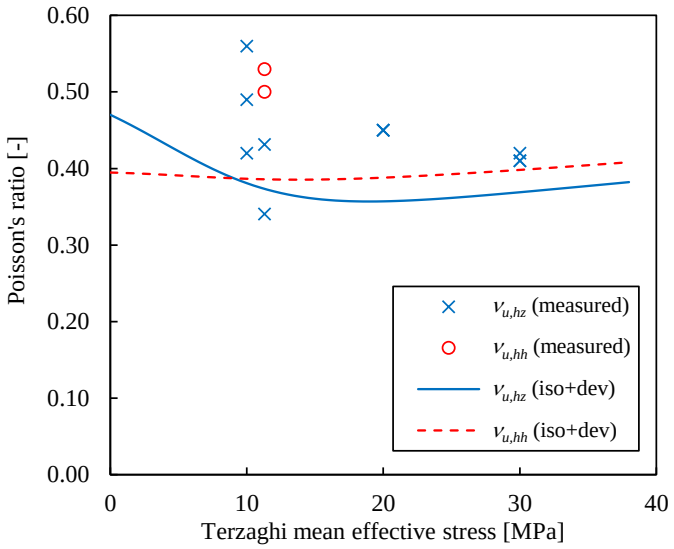


Fig. 4.15.: Measured undrained Poisson's ratio $\nu_{u,zh}$ perpendicular and $\nu_{u,hh}$ parallel to the bedding planes with respect to effective stress, with a fitted model using isotropic experimental results (Tab. 4.3) and a fitting based on all isotropic and deviatoric test results (Tab. 4.5)

In the following, we first analyse only laboratory results obtained from isotropic tests, which represent a determined set of isotropic poroelastic parameters:

- We establish some mathematical expressions for the parameters K_d and H with respect to the effective stress using 4 variables. This relationship provides the unjacketed modulus K_s.

- A linear function for K_u with 2 variables was fitted to the measurements, allowing then to calculate b and B.

- The anisotropic strain response, measured through D_i, H_i and U_i, is characterized by introducing the anisotropy ratios R_D and R_H with 4 additional variables.

Due to the fact that parameters with different units were fitted here, we used the mean of squared relative errors in all calculations presented. The behaviour under deviatoric stress, applied parallel and perpendicular to the bedding plane, provided also values for the 8 parameters E_i, $E_{u,i}$, ν_i and $\nu_{u,i}$. Together with the 6 parameters from isotropic tests D_i, H_i and U_i, we dispose of an overdetermined set of parameters. If these are compatible, it allows us to describe a set of transversely isotropic poroelastic coefficients. Adapting the model we established in the previous step, we fit now some mathematical functions by reducing the error between model and both isotropic and deviatoric results:

- The drained behaviour was modelled by simultaneously fitting some functions with 7 variables to the stress dependent measurements of E_i, ν_i and D_i.

Tab. 4.2.: Summary of best-fit model parameters determined using a regression analysis, with some properties depending on the mean Terzaghi effective stress σ' (in MPa)

K_d(iso)	$(\frac{1}{2.94} + (\frac{1}{0.52} - \frac{1}{2.94})\exp(-0.22\sigma'))^{-1}$GPa
K_d(iso+dev)	$(\frac{1}{3.30} + (\frac{1}{0.70} - \frac{1}{3.30})\exp(-0.21\sigma'))^{-1}$GPa
K_s	22.5 GPa
K_u	$(13.4 \times 10^{-3}\sigma' + 10.3)$GPa
R_D	$-26.6 \times 10^{-3}\sigma' + 3.58$
R_H	$-28.1 \times 10^{-3}\sigma' + 3.94$
ν_z	0.09
ν_h	0.29
ϕ	0.18
K_f	2.2 GPa

- 5 additional variables allowed to calculate H, K_u, U_i, H_i, $E_{u,i}$ and $\nu_{u,i}$. The variables were optimized by reducing the mean of the squared relative errors between measured and calculated H, K_u, U_i and H_i. Doing so, we obtain a stress dependent set of poroelastic parameters, allowing also to calculate K_s, B_z, B_h and the transversely isotropic Biot's coefficients b_z and b_h. A summary of the determined independent parameters is given in Tab. 4.2.

4.3.1 Equivalent isotropic parameters

The experimental results evidence an increase of the drained bulk modulus K_d with increasing Terzaghi effective stress (Fig. 4.4), starting from a certain value at zero effective stress and reaching a plateau at a given effective stress. To describe this trend, we chose a sigmoid function, used regularly in rock mechanics literature (e.g. Zimmerman, 1991; Hassanzadegan et al., 2014; Ghabezloo, 2015):

$$\frac{1}{K_d} = \frac{1}{K_d^\infty} + \left(\frac{1}{K_d^0} - \frac{1}{K_d^\infty}\right) \exp\left(-\beta_1 \sigma'\right) \tag{4.1}$$

where K_d increases with σ' from a lower limit K_d^0 to an upper limit K_d^∞. The shape of transition is governed by a parameter β_1. The function can be seen in Fig. 4.4.

The Biot modulus H can then be calculated with the unjacketed modulus K_s as a fitting parameter, using Eq. (2.20). We observed that satisfactory results are achieved with a stress independent K_s (Fig. 4.5).

We fitted simultaneously the results of the model [Eq. (4.1) and (2.20] to the experimental data, using the least square method. This provided values for the unknowns K_d^0, K_d^∞, β_1 and for the constant K_s, as presented in Tab. 4.3. The best-fit curves, together with experimental results, are shown in Fig. 4.4 and 4.5.

Tab. 4.3.: Best-fit model parameters resulting from a simultaneous fit of K_d and H and an independent linear fit for K_u.

Fitted with K_d and H				Fitted with K_u	
K_d^0 [GPa]	K_d^∞ [GPa]	β_1 [MPa^{-1}]	K_s [GPa]	β_2 [-]	β_3 [GPa]
0.52	2.94	0.22	22.5	13.4	10.30

An independent linear relationship between the observed values for K_u and σ' is proposed with:

$$K_u = \beta_2 \sigma' + \beta_3 \tag{4.2}$$

The best fit parameters for this relationship, found by the least square method, are presented in Tab. 4.3, with the stress evolution of K_u shown in Fig. 4.7. Using Eq. (2.21) with the previously determined stress dependent equivalent isotropic moduli, one can calculate b (Fig. 4.16a). This parameter is close to 1.0 for zero effective stress, and decreases with increasing effective stress. Starting from around $\sigma' = 20$ MPa, b remains fairly constant with a value of around 0.86. This is comparable with the values presented by Escoffier (2002), Mohajerani (2011), and Belmokhtar et al. (2017a) up to 10 MPa effective stress.

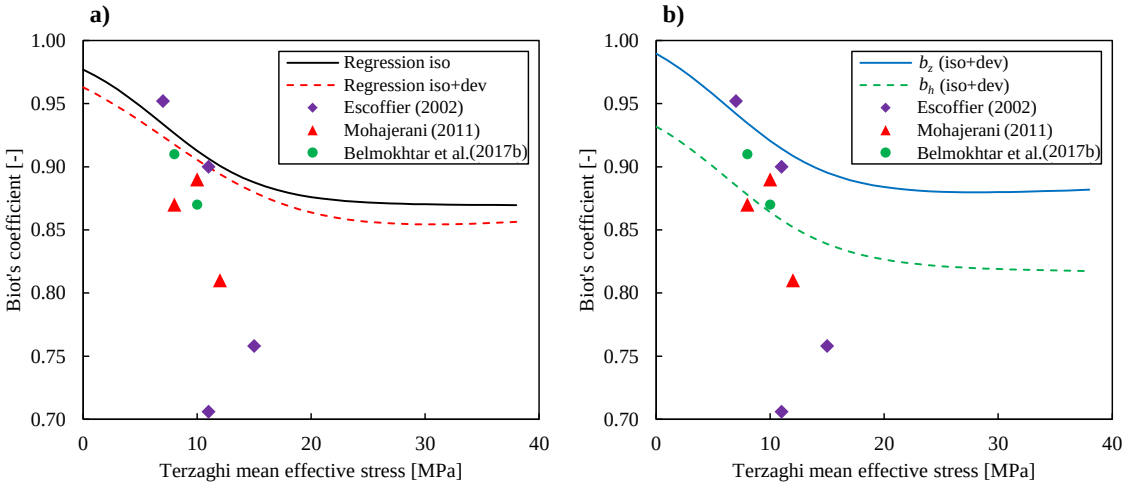


Fig. 4.16.: Biot's effective stress coefficient b for a) equivalent isotropy and b) transverse isotropy; calculated with Eq. (2.21) using the regression based on isotropic tests (Tab. 4.3, 4.4) and the regression based on isotropic and deviatoric tests (Tab. 4.4, 4.5).

By knowing K_u (Eq. (4.2), Tab. 4.3), we can also compute the Skempton coefficient B as a function of effective stress (Fig. 4.17a), using the relationship of Eq. (2.21). The maximum value of the calculated parameter B is close to 0.97 for zero effective stress. It decreases slightly with increasing effective stress, and a re-increase is observed starting from $\sigma' = 18$ MPa. Generally, the parameter B remains around a mean value of 0.90 for effective stresses observed up to 35 MPa. Belmokhtar et al. (2017a), Mohajerani et al. (2012), and Mohajerani et al. (2014) also determined rather high B coefficients with values of 0.87 and 0.84, respectively.

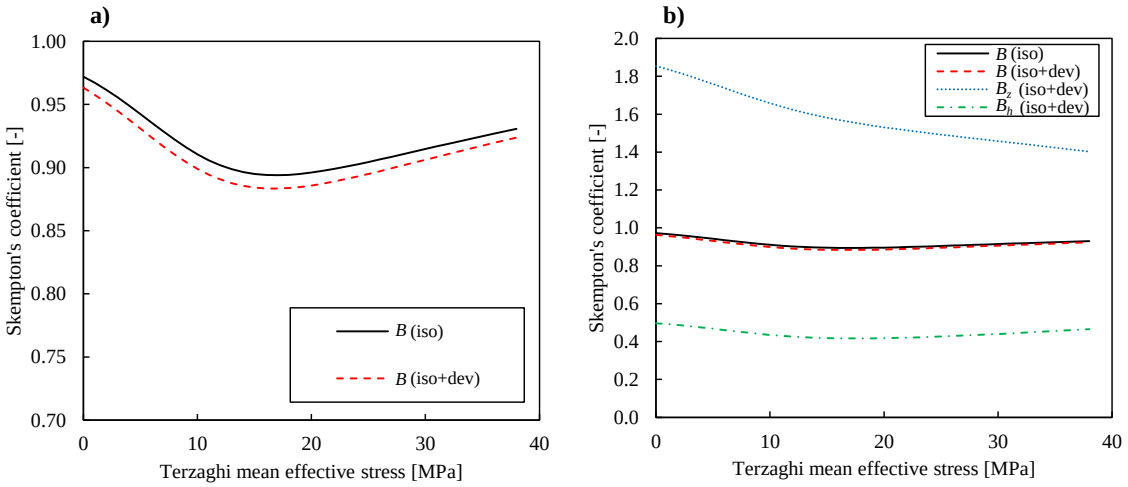


Fig. 4.17.: Skempton's coefficient B for equivalent isotropy, calculated with Eq. (2.32) and (4.1) using the regression based on isotropic tests (Tab. 4.3, 4.4) and the regression based on isotropic and deviatoric tests (Tab. 4.4, 4.5).

Tab. 4.4.: Best-fit model parameters resulting from a simultaneous fit of D_i, H_i and U_i.

Fitted with D_i, H_i and U_i			
β_4 [GPa^{-1}]	β_5 [-]	β_6 [GPa^{-1}]	β_7 [-]
-26.6	3.58	-28.1	3.94

4.3.2 Anisotropic response to isotropic stresses

Having determined the stress dependent equivalent isotropic parameters K_d, H and K_u, the two anisotropy ratios R_D and R_H are required to calculate the transversely isotropic parameters D_h, D_z, H_h, H_z, U_h and U_z using Eq. (2.26), (2.27) and (2.28). We allowed here linear relationships for R_D and R_H with respect to the effective stress:

$$R_D = \beta_4 \sigma' + \beta_5 \tag{4.3}$$

$$R_H = \beta_6 \sigma' + \beta_7 \tag{4.4}$$

We then carried out a least square error optimization of all 6 transversely isotropic parameters. The best fit was obtained with values shown in Tab. 4.4, evidencing that the anisotropy of the strain response to isotropic loads decreases slightly with effective stress. The optimized calculated parameters are presented in Fig. 4.8, 4.9 and 4.10, with the anisotropy ratios plotted in Fig. 4.11.

Tab. 4.5.: Best-fit model parameters resulting from a simultaneous fit of E_i, ν_i and D_i.

K_d^0 [GPa]	K_d^∞ [GPa]	β_1 [MPa^{-1}]	ν_{zh} [-]	ν_{hh} [-]
0.7	3.3	0.21	0.09	0.29

4.3.3 Analysis of drained isotropic and deviatoric test results

To take into account the compatibility relationships between deviatoric and isotropic responses, we established a new set of parameters which aims to find a compatible optimum for all measured values. First, the drained behaviour was modeled by attributing the function of Eq. (4.1) to K_d. R_D was described with a linear stress dependent relationship [Eq. (4.3)] with the values taken from Tab. 4.4, as evaluated before. The Poisson ratios ν_{hh} and ν_{zh} were assumed to be stress independent. The 5 variables (K_d^0, K_d^∞, β_1, ν_{zh}, ν_{hh}) were varied, in order to minimize the sum of squared relative errors between measured and calculated E_i, ν_i and D_i. The best fit values can be seen in Tab. 4.5, and the calculated stress dependent parameters are presented in Fig. 4.4, 4.10, 4.12 and 4.13.

4.3.4 Analysis of undrained isotropic and deviatoric test results

We used then 5 additional variables, evaluated in the isotropic tests, which include a linear function for K_u, a constant unjacketed modulus K_s and a linear stress dependent R_H. The values from from Tab. 4.3 and 4.4 were applied, which, together with the drained properties from Tab. 4.5, provide K_u, U_i, H and H_i. This determined set of parameters allows now to calculate $E_{u,i}$, $\nu_{u,i}$, b_i, B and B_i. The resulting fully compatible poroelastic coefficients are shown in Fig. 4.5, 4.7, 4.9, 4.10, 4.14 and 4.15.

One can observe, that the optimized set of parameters satisfactorily reproduces the measured characteristics in a compatible poroelastic framework. Some compatibility issues were encountered in the response to deviatoric loads, where the model slightly underestimated the measured moduli E_i and $E_{u,i}$. This could be due to the fact that we express the moduli in function of effective mean stress, while the measured moduli might be predominantly influenced by the deviatoric stress q applied. Cariou et al. (2012) and recently Zhang et al. (2019), reported an increase of the Young's modulus in function of q during test under partially saturated conditions.

The Biot coefficients b_h and b_z can be calculated using Eq. (2.30) and (2.31). We obtain stress dependent Biot's coefficients (Fig. 4.16), with less pronounced anisotropy, originating from small differences between K_d and H and between R_D and R_H.

The equivalent isotropic Skempton's coefficient B, back calculated from isotropic and deviatoric results, differs very little from the one calculated from isotropic results, showing values close to 1.0. Using Eq. (2.32), one is able to calculate the anisotropic Skempton's coefficients, presented in Fig. 4.17b. One observes a large difference between B_z and B_h, with values of 1.66 and 0.44, respectively, at 10 MPa Terzaghi effective stress. Whereas B_h remains reasonably constant, B_z decreases with effective stress. The anisotropy of this parameters is induced by the significant anisotropy of poromechanical properties, which was observed to decrease slightly with increasing effective stress. Such important anisotropy effects on the Skempton coefficient have been addressed by Holt et al. (2018). They noted, that B_i can be related to the Skempton parameter A (Skempton, 1954) by the relationship $A_i = B_i/(3B)$. Skempton reported values for A between -0.5 and +1.5 (corresponding to B_i equal to -0.17 and +0.5, respectively, with $B = 1.0$). High values were attributed to compaction processes. Holt et al. (2018) tested soft shales with B values close to 1.0, A_z around 0.5 and A_h around 0.2. This corresponds to a value of B_z around 1.5 and of B_h around 0.6, similar to the findings of this study. Their measurements could be explained by adopting a transversely isotropic poroelastic model, and they pointed out its important effect on pore pressure increase due to subsurface drilling, injection or depletion. In the numerical study of Guayacán-Carrillo et al. (2017), transversely isotropic material parameters provided the best results to model the *in situ* measurements of induced pore pressures during excavation of galleries in the COx claystone. Although not discussed explicitly, the material properties used in their study most likely resulted in anisotropic Skempton's parameters, responsible for the non-uniform pore pressure field observed around the galleries.

4.4 Application example in a numerical model

In the following, we discuss the observed THM processes through a numerical simulation, using the model discussed in Sec. 3.7. The simulation was run until around 200 years, with the adopted material properties presented in the following section. Due the uncoupling of thermal transport we obtained a temperature evolution, which remained unchanged during all calculations. A THM simulation was carried out with constant material properties, except for the pore fluid. This first calculation serves as a reference case for comparisons with further simulations. We show the impact of transversely isotropic poroelastic properties, by comparing with results assuming an isotropic material. Afterwards, we implemented the stress dependency of poroelastic properties, discussed in Sec. 4, and we examine the resulting effects.

4.4.1 Adopted material properties

In Tab. 4.6, the material properties adopted in the finite element model are displayed. The information about the different layers was provided by the Andra database. Note that values for the shear modulus and the unjacketed modulus were not explicitly given, but back calculated from other elastic properties. Some properties of the COx layer, excluding the USC unit, were adapted based on the findings of this study. These parameters are shown in bold in Tab. 4.6 and are briefly explained in the following.

The Young moduli, Poisson ratios, Biot coefficients and unjacketed modulus for a transversely isotropic model were investigated in Sec. 4. We provided a set of parameters, which is dependent on the mean effective stress. In the case of the first reference calculation with stress independent properties, values calculated for the initial effective stress level at the depth of the microtunnel (9.5 MPa) were used (Tab. 4.6). Due to lack of experimental data on the shear modulus G, a value of 1.7 GPa is taken from Guayacán-Carrillo et al. (2017). The thermal expansion coefficients were measured experimentally in this study, detailed in Sec. 5. For the numerical simulations, we adopted a permeability value of 1.6 $\times 10^{-21}$ m^2 in vertical direction, close to the measurements presented in Sec. 3.6 and provided by Harrington et al. (2017). Data from Harrington et al. (2017) and Enssle et al. (2011) shows an average anisotropy factor of 2.2, resulting in a horizontal permeability of 3.5 $\times 10^{-21}$ m^2 adopted here. Note that these laboratory results were found to be about one order of magnitude lower than values determined from *in situ* experiments (Enssle et al., 2011; Vinsot et al., 2011). All of these studies confirm an anisotropic permeability. The significant difference between laboratory and *in situ* experiments, potentially induced due to the resaturation of specimens (Conil et al., 2018) is still under ongoing investigation. As shown by Seyedi et al. (2018), the permeability is one of the most influencing parameters in this THM problem, but shall not be subject of the present study. A stress and temperature dependent compressibility and a thermal expansion coefficient, both corresponding to bulk water (Spang, 2002; IAPWS-IF97, 2008) were attributed to the pore fluid.

Tab. 4.6.: Material properties, taken from the Andra database, with modified values indicated in bold

	λ_i [W/m/K]		C_p [J/kg/K]	ρ [g/cm3]	E_i [GPa]		ν_i [-]		b_i [-]		G [GPa]	K_s [GPa]	$\alpha_{d,i}$ [10^{-5}/K]		k_i [m^2]		ϕ [%]
	z	h			z	h	zh	hh	z	h			z	h	z	h	
Kimmeridgian	1.1	1.4	1024	2.45	3.6		0.3		0.6		1.4	7.5	2.2		1.0E-19		13
Calc. Oxfordian	2.3		925	2.47	30		0.3		0.6		11.5	25.0	0.45		1.0E-16		13
USC	1.8	1.8		2.48	12.8		0.3		0.6		4.9	26.7	1.28		4.1E-21		15
UT	1.4	2.1	978														
UA2-3	1.25	1.875		2.45	**2.81**	**5.95**	**0.09**	**0.29**	**0.93**	**0.87**	**1.7**	**22.5**	**0.21**	**0.51**	**1.6E-21**	**3.5E-21**	18
UA1	1.6	2.4															
Dogger	2.3		925	2.47	30		0.3		0.6		11.5	62.5	0.45		1.0E-18		10

4.4.2 Temperature evolution

In this context of uncoupled heat conduction, the temperature field is independent of the THM mechanisms. The temperature evolution hence depends solely on the thermal conductivity and the heat capacity of the saturated rock. These properties have been previously evaluated, based on laboratory studies and *in situ* measurements, showing very good accordance and giving confidence in the values (Gens et al., 2007; Jia et al., 2009; Conil et al., 2012; Garitte et al., 2014). The resulting temperature field and its evolution with time is displayed in Fig. 4.18. Due to the instantly imposed thermal flux at the microtunnel, the temperature increases in the beginning with a high gradient around the microtunnel. Heat is flowing in radial direction away from the microtunnel, with higher rate in horizontal direction, due to the anisotropic thermal conductivity. At a time of around 2.7 years, including 2 years ventilation, the temperature front reaches the right symmetry boundary. The zero heat flux condition causes an accumulation of heat at this location. In Fig. 4.19, different points are indicated, for which the temperature and pore pressure values are shown in Fig. 4.20. The points close to the top and bottom boundaries (VT and VB) were used to control if the pore pressure and temperature gradient remained constant there. The values at VT and VB did not change over the investigated timespan, which confirmed a sufficiently large model. Over time, the temperature reaches its maximum near the gallery wall (positions V0 and H0), with 80.7 °C after around 24.7 years (Fig. 4.20a,c). Afterwards, the temperature around the gallery decreases. In Fig. 4.20a,c, one can observe, that the the rock mass farther away reaches lower temperature levels. As the thermal output of the waste packages decreases with time, the localized temperature around the microtunnel equilibrates with the the overall rock mass. At points farther away than 5 m from the microtunnel, the temperature converges to a value of approximately 60 °C after 200 years. Also in 3D simulations at the structure scale, presented by Bauer et al. (2004) and Andra (2005), it was confirmed that the temperature in the rock did not exceed 90 °C, with a thermal peak after around 10 - 20 years.

4.4.3 Resulting THM response

Pore pressure

Fig. 4.22 shows the evolution of the pore pressure distribution in the formation. The increasing pore pressures, induced by thermal pressurization, follow the thermal field. The pore pressure rises first in radial direction around the microtunnel. Due to the zero pore pressure condition at the gallery wall, pore pressures are allowed to drain towards the microtunnel. This generates a high pressure gradient around the microtunnel. With respect to the distance, it is followed by a pressure peak (Fig. 4.21). Behind the peak, at larger distances, the pore pressure comes back to the natural value, under a less pronounced

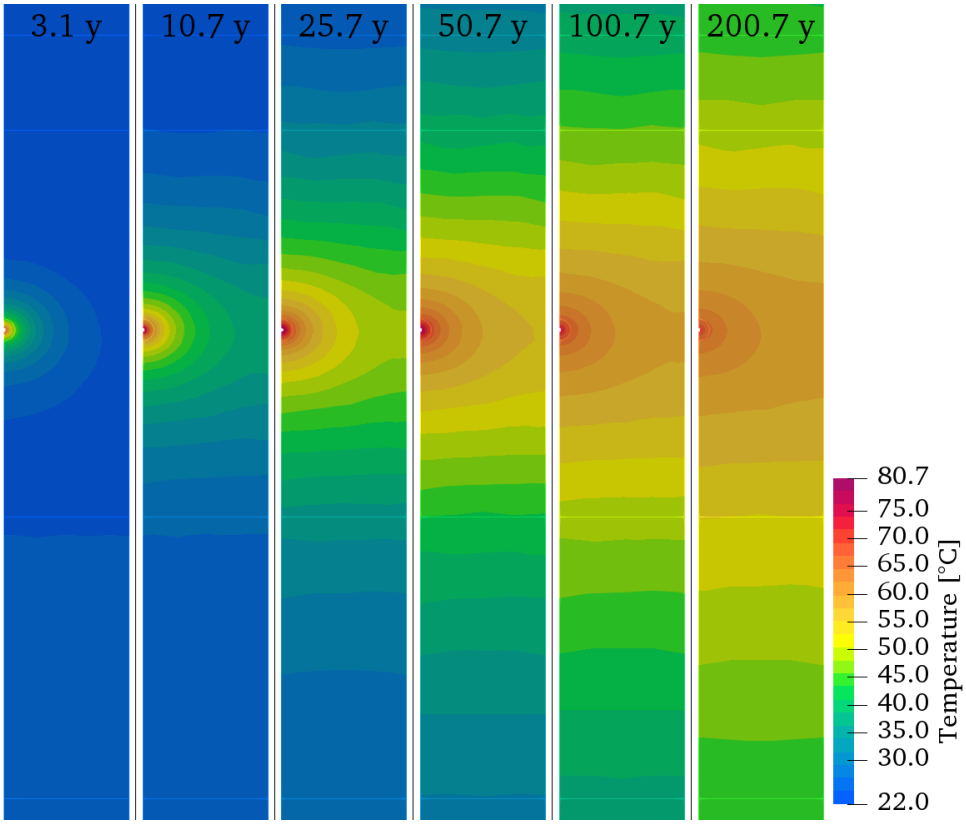


Fig. 4.18.: Temperature field and its evolution with time, calculated for a model with 20 m width

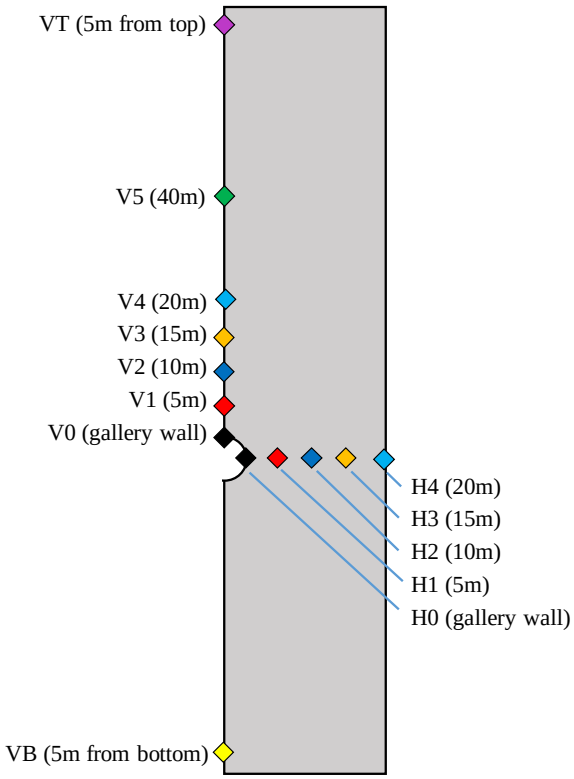


Fig. 4.19.: Locations of the extracted point data, with their horizontal and vertical distance to the microtunnel center, respectively. The dimensions are not to scale

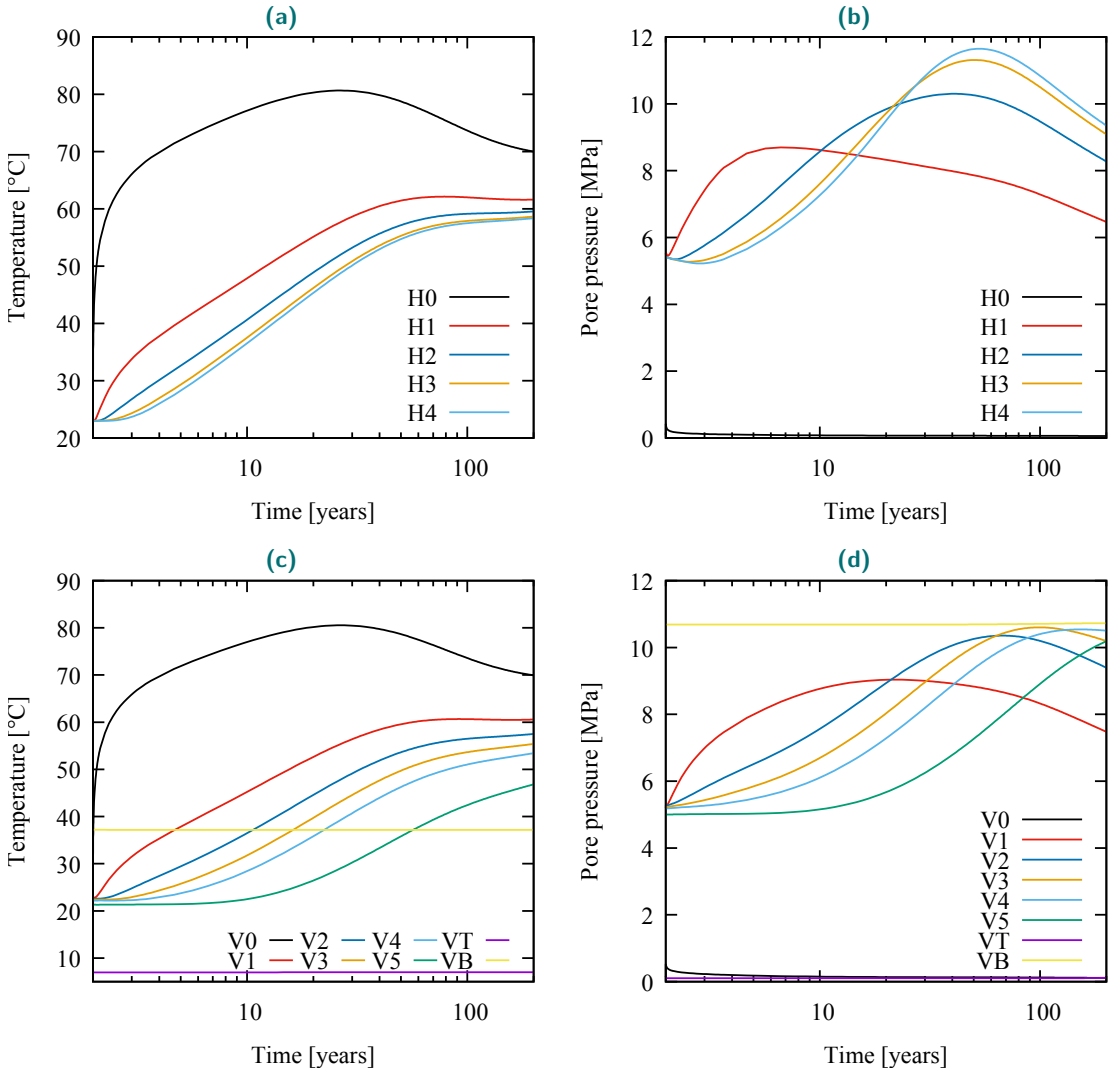


Fig. 4.20.: Time evolution of a) temperature and b) pore pressure at different horizontal distances form the microtunnel. Values for points in vertical distance are shown for c) temperature and d) pore pressure. The exact locations of these points are indicated in Fig. 4.19

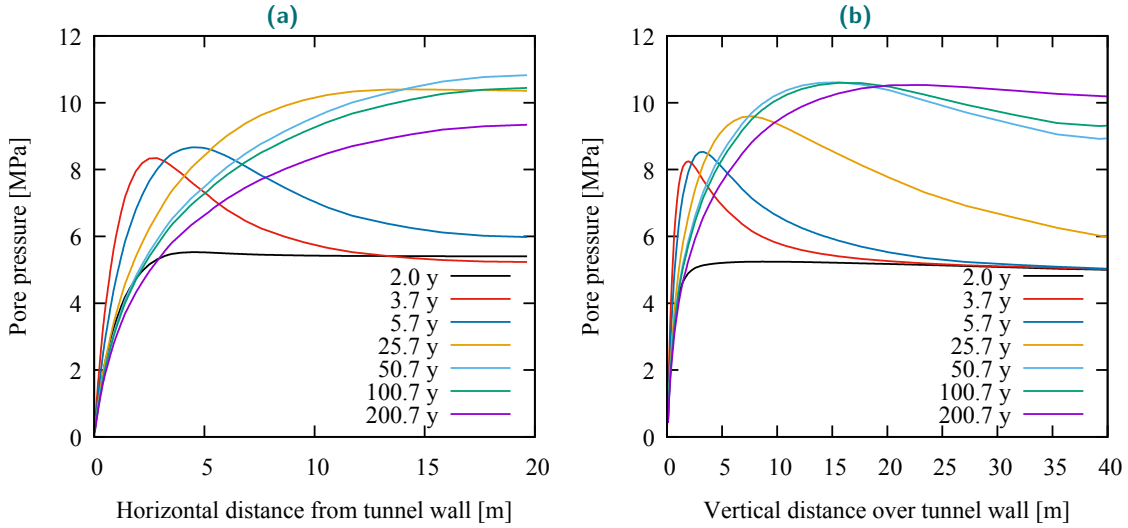


Fig. 4.21.: Pore pressure with respect to distance from the tunnel wall, changing with time, in a) horizontal direction and b) vertical direction from the microtunnel

gradient. The high near-field gradient results from a superposition of a high initial pore pressure gradient (see Fig. 4.21 for $t = 2$ years, which already decreased during the ventilation phase), and a high thermal gradient.

The pore pressure peak moves with time, until reaching the right symmetry boundary. One observes a higher increase rate in horizontal direction, governed by the anisotropic thermal field and the higher permeability in this direction. Similar to the temperature evolution, the zero horizontal flow condition at the boundary causes an accumulation of pore pressure at the location between two microtunnels, starting from around 22 years. The zone of maximum pore pressure is indicated in Fig. 4.22 with a blue circle. Note that for times larger than 50 years, the highest pore pressure is found below the microtunnel level, even though the fluid and temperature transport occurs fairly symmetrical around the tunnel in vertical directions. Due to the initially higher values at higher depth (given the geothermal gradient and hydrostatic pressure), one observes the pressure maximum in this zone. Fig. 4.20b,d show the pressure evolution with respect to time at selected points. One can identify a maximum pore pressure at point H4 at the vertical symmetry boundary. This peak of 11.7 MPa, attained after around 50 years, represents the overall pressure peak for the COx formation, as seen in Fig. 4.23. The behaviour at larger timescales was not in the scope of this work and not further investigated here.

Stresses

The stresses calculated during the analysis are presented in the following in terms of principal effective stresses. In Fig. 4.24, the calculated major and minor principal effective

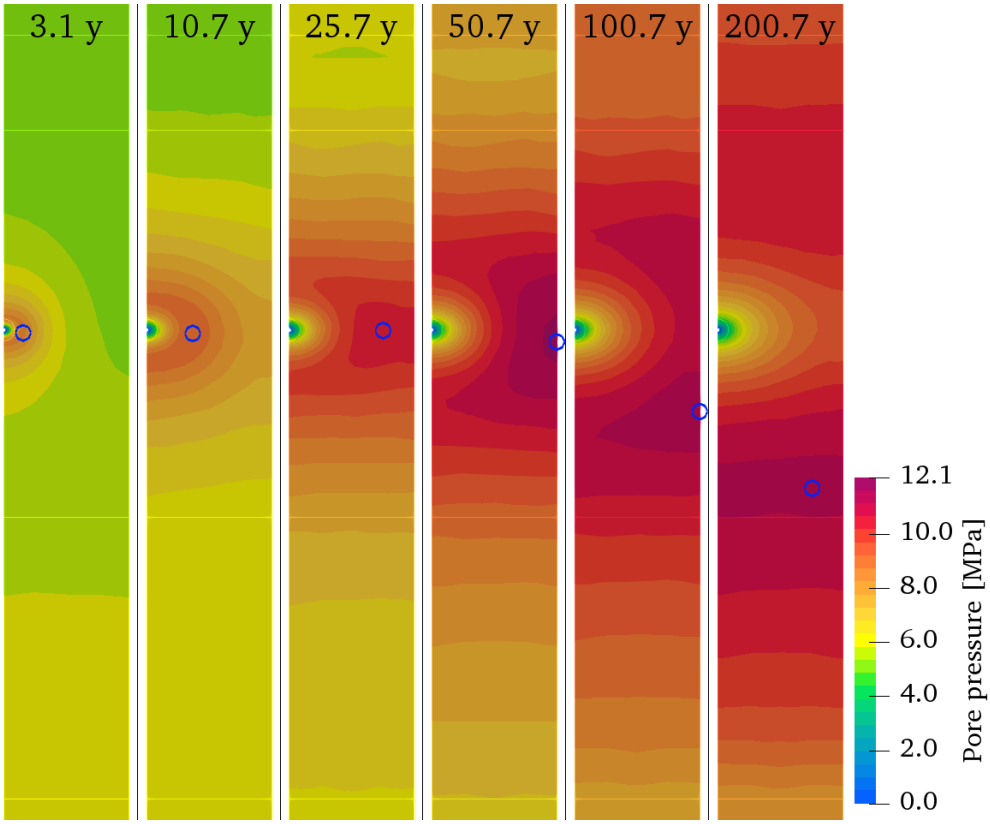


Fig. 4.22.: Pore pressure field with respect to time, calculated for a model with 20 m width. Blue circles indicate the location of maximum pore pressure

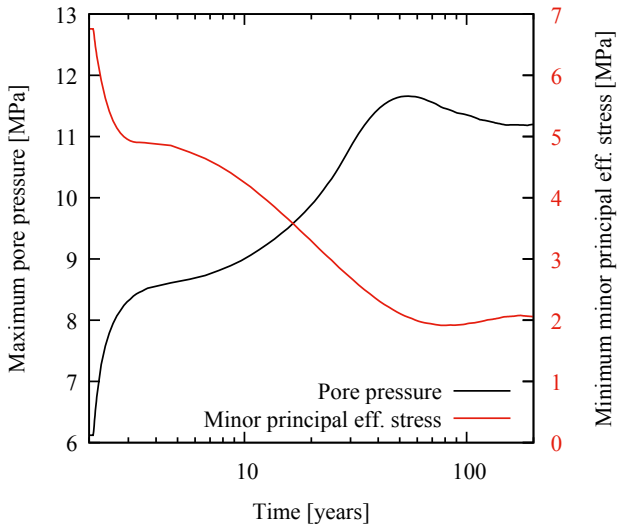


Fig. 4.23.: Maximum value of the pore pressure field and minimum value of the minor principal effective stress (disregarding the zone close to the tunnel wall), evaluated for a 20 m wide model

stresses, parallel to the model plane, are depicted. One can observe that, disregarding the excavation induced stress changes in the vicinity of the microtunnel, σ'_1 remains fairly constant over time. A slight increase is due to the volume increase caused by temperature and pore pressure increase, which is constrained in horizontal direction. Computed stress directions show, that σ'_1 remains fairly constantly horizontal, corresponding therefore to the horizontal effective stress σ'_x. More important changes are evaluated in terms of the minor principal effective stress σ'_3, depicted in Fig. 4.24. With the vertical load governed by the lithostatic weight, the overall vertical total stress remains constant. Hence, σ'_3 decreases gradually from its initial value in quasi-isotropic conditions, following the temperature induced pore pressure increase. Due to the fluid drainage near the microtunnel, σ'_3 is higher in this zone. The observed minimum values are in the order of a few MPa, similar to the values presented by Seyedi et al. (2018). Higher temperatures would result in higher pore pressures, resulting in lower σ'_3. Stresses of σ'_3 lower that the tensile strength could induce damage or create fractures. The minor effective stress σ'_3 represents therefore an important design parameter for the microtunnel layout. To account for tensile failure, a failure criterion is established and discussed in Sec. 6.

Comparing in detail the different THM fields in their spatial evolution with time, one can make another interesting observation: Zones of maximum pore pressure and minimum minor principal effective stress do not coincide. Whereas the area of maximum pore pressure moves away from the microtunnel in horizontal direction, the area of minimum σ'_3 remains on the vertical microtunnel axis. Looking closer at the time evolution of the maxima of pore pressure and temperature, a shift between the two peaks is observed. This shows, that the minimum effective stress is not only related to the maximum pore pressure, but also influenced by some stress redistributions. These stress redistributions are influenced by the material parameters adopted and the assumed model conditions.

Looking at the stress paths for the far field in Fig. 4.25, depicted for selected points in the model (Fig. 4.19), one can observe a movement of the stress state to the left. The stress paths for these elements are similar to that of confined tension perpendicular to bedding. The minor effective stress decreases through pore pressure increase, while there are only small changes in the major effective stress.

4.4.4 Effect of transverse isotropy

In the previous experimental investigations, we determined poroelastic properties with a significant anisotropy. To illustrate the effects of anisotropy in the discussed numerical simulation, we replace the transversely isotropic properties by their equivalent isotropic parameters (Tab. 4.7). Thermal properties are left as before. Fig. 4.26 evidences important effects due due to the adaptation of a equivalent isotropic parameter set. We observe that the maximum pore pressure increases up to around 14 MPa, decreasing in consequence the

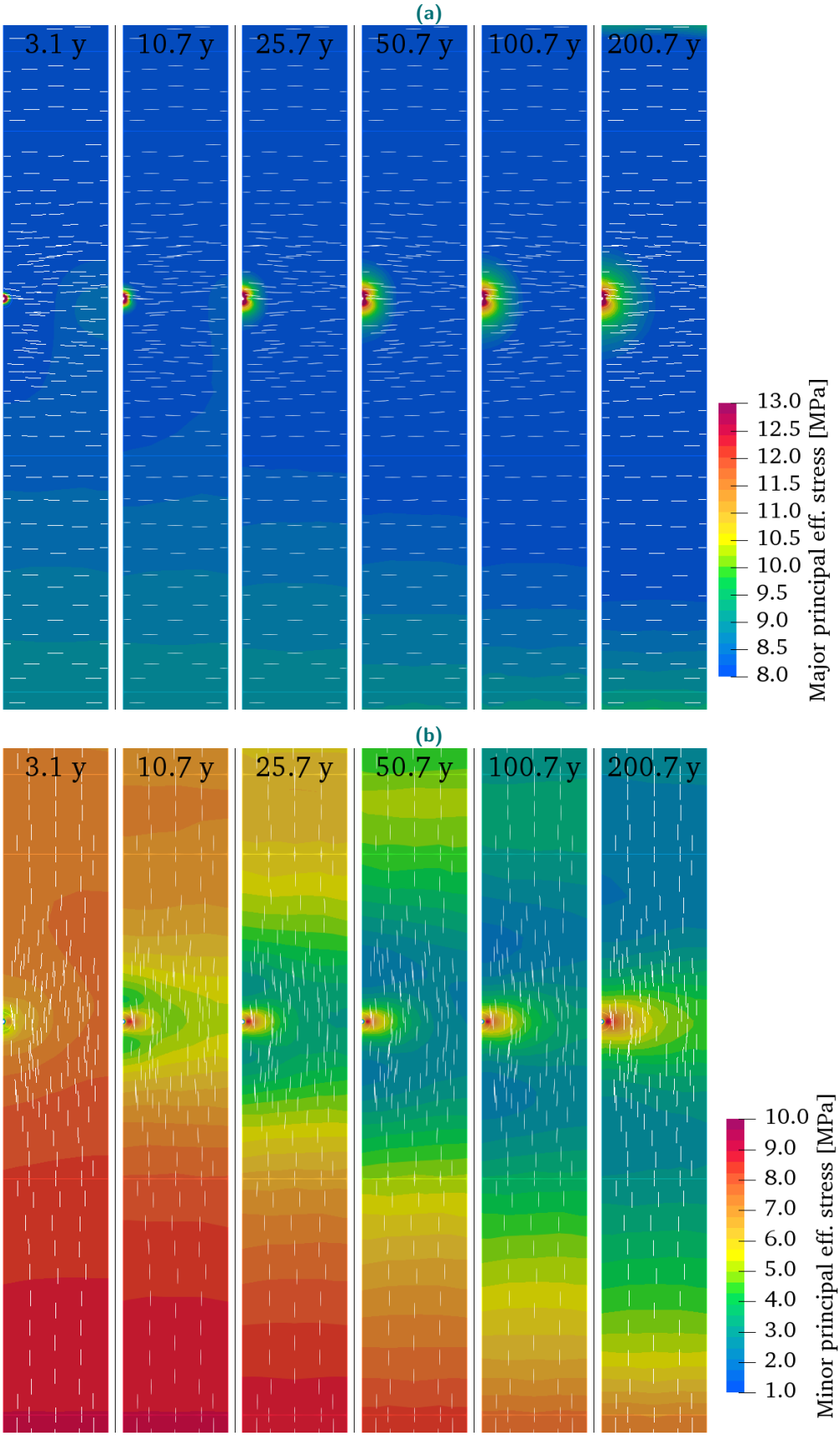


Fig. 4.24.: a) Major and b) minor principal effective stress parallel to the model plane. White dashes indicate the stress directions, which remained horizontal and vertical, respectively, apart from the zones close to the microtunnel. Note that stresses in the vicinity of the microtunnel can exceed the annotated scale, and are not detailed here

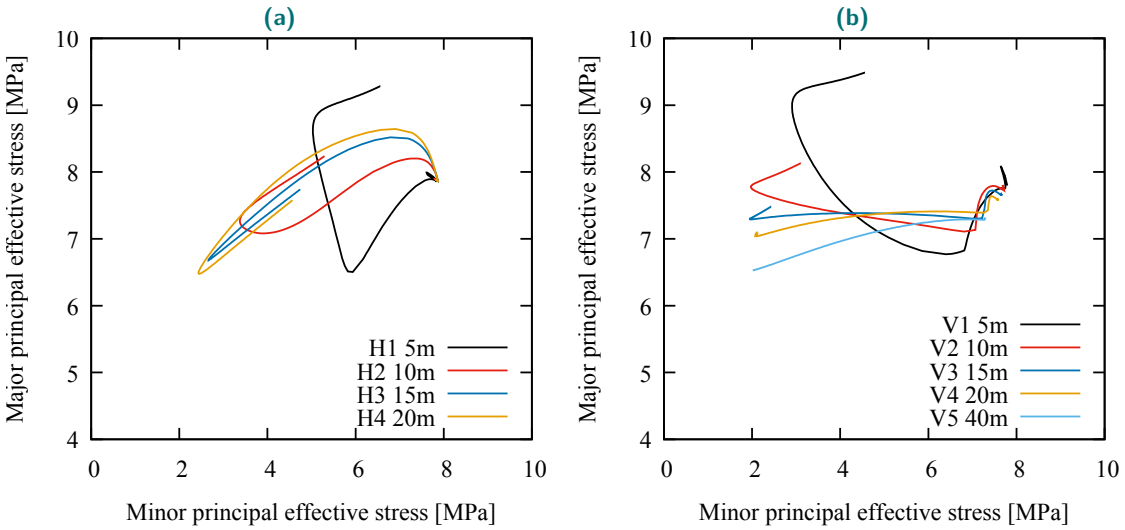


Fig. 4.25.: Principal effective stress paths for points in a) horizontal direction and b) vertical direction over the microtunnel

Tab. 4.7.: Transversely isotropic properties, used in the previous reference calculation, adapted to an equivalent isotropic poroelastic material, by taking the mean of anisotropic properties. In the third scenario the properties marked in bold were stress dependent

Scenario for UT+UA	E [GPa] z	h	ν_i [-] zh	hh	b_i [-] z	h	G [GPa]	K_s [GPa]	$\alpha_{d,i}$ [10^{-5}/K]	
transv. iso	2.81	5.95	0.09	0.29	0.93	0.87	1.7	22.5	0.21	0.51
equiv. iso	4.90		0.22		0.89		1.7	22.5	0.21	0.51
stress dependent	**2.81**	**5.95**	0.09	0.29	**0.93**	**0.87**	1.7	22.5	0.21	0.51

minor principal effective stress to -0.5 MPa. Governed by the geometry of the model, which limits horizontal volume changes, the dominant deformations which affect the amount of generated pressure are in vertical direction. Consequently, the vertical stiffness influences more importantly the thermal pressurization phenomenon. With the equivalent isotropic parameter set, the vertical stiffness was increased, which makes the rock less compliant, causing higher pore pressures.

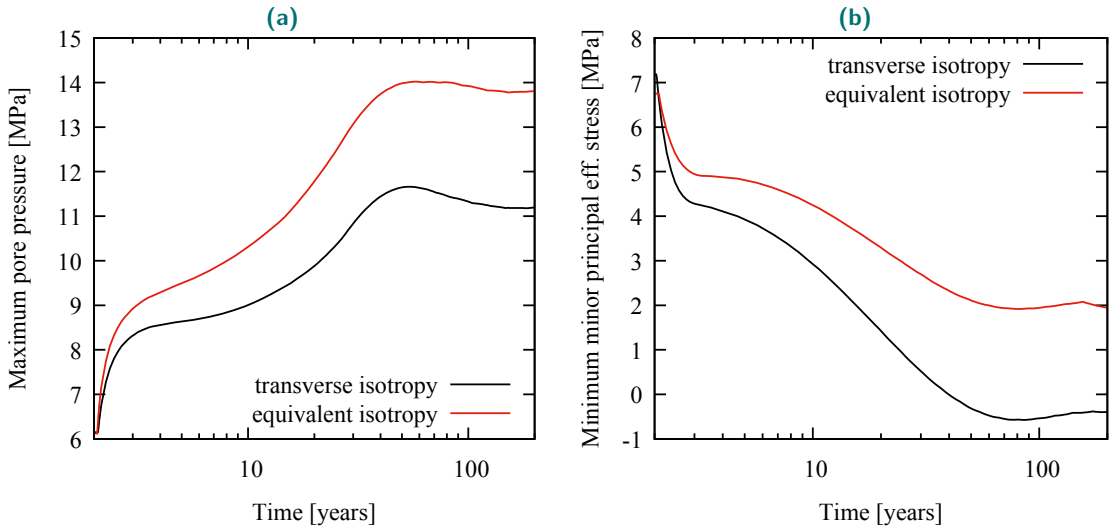


Fig. 4.26.: a) Calculated maximum pore pressure and b) minimum minor principal effective stress parallel to the model plane, calculated with the transversely isotropic hydromechanical properties and with an equivalent isotropic parameter set

4.4.5 Adoption of stress dependent anisotropic poroelasticity

Here we implemented the stress dependency of poroelastic properties, evaluated experimentally in Sec. 4 (Tab. 4.7). This involves Young's moduli, which decrease with decreasing effective mean stress, and Biot's coefficients, which increase with decreasing effective mean stress. From the numerical results (Fig. 4.27), comparing calculations under stress independent and stress dependent parameters, only a minor difference is notable. We showed before a decrease of vertical effective stress and an increase of horizontal effective stress in the formation. This increases deviatoric stresses with time, the mean effective stresses however remain fairly constant. For instance, at the microtunnel level, a decrease from the initial mean effective stress at 9.5 MPa to a minimum of around 7.0 MPa is observed in Fig. 4.28. The poromechanical stiffness decreases hence only slightly. Reducing the stiffness makes the material more compliant, which decreases thermal pressurization.

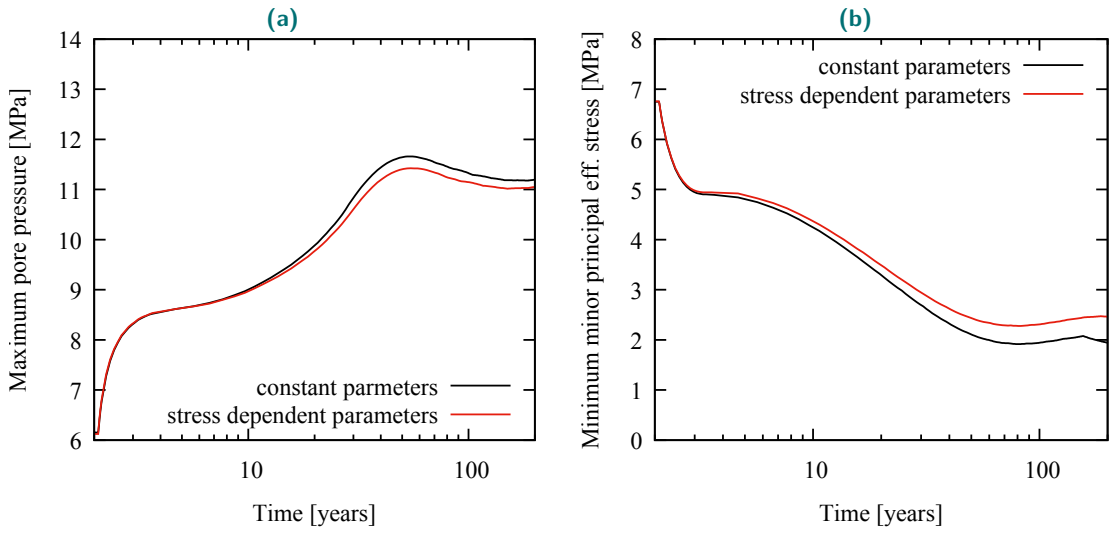


Fig. 4.27.: a) Calculated maximum pore pressure and b) minimum minor principal effective stress parallel to the model plane, calculated with and without stress dependent parameters

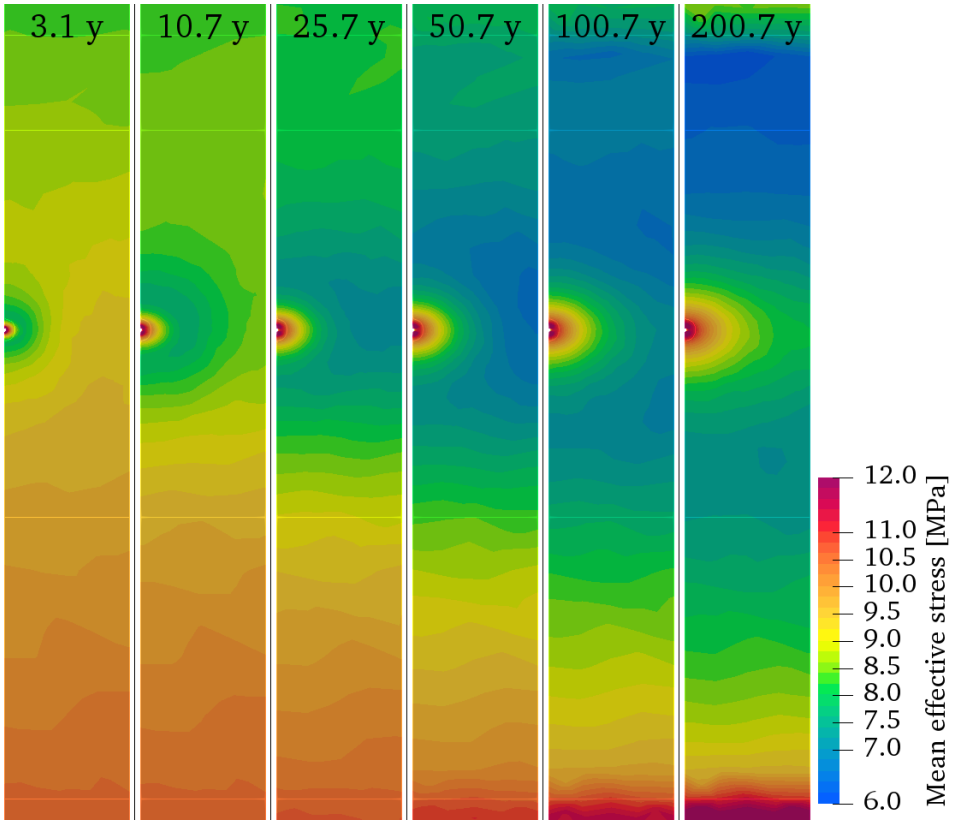


Fig. 4.28.: Mean effective stress with respect to time, calculated for a model with 20 m width. Note that values in the vicinity of the microtunnel might exceed the annotated scale

4.5 Conclusions

A laboratory study, using experimental equipment and testing procedures adopted for very low permeability materials, allowed us to conduct a large number of isotropic and deviatoric experiments on the COx claystone. Precise strain gage measurements were employed to investigate the transversely isotropic poromechanical properties and to determine a compatible set of poroelastic parameters.

- Tests on different samples from three cores provided consistent poromechanical coefficients, which confirms the reproducibility of the experiments, the same sample qualities and shows no noticeable natural variability between the two cores.

- The measurements show a clear stress dependency of the drained bulk moduli, the drained and undrained Young moduli and a less pronounced stress dependency of the undrained bulk modulus and the undrained Young modulus. The drained and undrained Poisson ratios perpendicular to the isotropy plane were observed to change very little with effective stress. The anisotropy ratios between strains perpendicular and parallel to the bedding plane, under drained isotropic loads, were observed to decrease slightly with increasing effective stress.

- The decrease of the drained bulk modulus with decreasing effective stress was observed to be reversible in isotropic tests. The reduction of moduli could probably be attributed to an elastic opening of microcracks.

- A back analysis of the unjacketed modulus, which is assumed to be isotropic at the micro-scale and constant with effective confining stress, gave a value $K_s = 22.5$ GPa. Also the parameters b and B were calculated, with values slightly decreasing with increasing effective stress, from close to 1.0 to around 0.85. The high values of the Biot coefficients close to 1.0 highlight the importance of hydromechanical couplings in this material.

- We carried out an optimization procedure, which aimed to match a stress dependent set of transversely isotropic poroelastic coefficients to the laboratory measurements. This framework, corresponding to the properties presented in Tab. 4.2, could well represent the measured parameters. Some compatibility issues were encountered, where the same elastic properties evaluated from deviatoric tests tend to be stiffer than those back-calculated from isotropic experiments. The fitted parameters indicated a negligible anisotropy of the calculated Biot's coefficients b_h and b_z. The calculated Skempton's coefficients, however, showed an important anisotropy, with higher values perpendicular to bedding and decreasing anisotropy with increasing effective stress.

Precise knowledge of the poromechanical properties of the COx claystone is important, not only for the hydromechanical modelling of the rock behaviour around excavated drifts (Guayacán-Carrillo et al., 2017), but also for the analysis of the deformations due to thermally induced pore pressures (Gens et al., 2007; Garitte et al., 2017). The parameters evaluated in this study give confidence due to their compatibility, evidencing a clear anisotropy. The effects of anisotropic poroelasticity and the dominant part of the stiffness perpendicular to bedding was illustrated in the numerical application. We observed a stress dependency of elastic properties on the mean effective stress, which could be considered in numerical modelling. The material was seen to become more compliant under decreasing effective stresses, which increases the elastic deformations in unloading paths. In the modelled THM behaviour around microtunnels, the dependency on the mean effective stress was seen to have minor effects, due to small changes in this value. Conversely, deviatoric stresses were observed to change more importantly. Further experimental investigations could help to identify a possible anisotropic stress dependency, which in application would result in larger stiffness changes.

5 Behaviour under thermal loads

In this section we characterized the THM response of the COx claystone to temperature changes through laboratory experiments. To this end, claystone samples were tested in a temperature controlled, high pressure isotropic loading cell, under stress conditions close to the *in situ* ones. We emphasize here the necessity of precise strain measurement devices, accounting for temperature induced errors (Sec. 3.3.3). Thermal loads were applied along different heating and cooling paths, following the protocols described in Sec. 3.6. Drained and undrained THM properties are determined and analysed for their compatibility. An overview of the testing program is given in Sec. 5.1. In Sec. 5.2 we show experimental results, analysed in Sec. 5.3. In Sec. 5.4, we show a simplified application example of these findings in a numerical model, followed by conclusions in Sec. 5.5.

The experimental findings of this chapter are included in the publication: Braun, P., Ghabezloo, S., Delage, P., Conil, N., and Sulem, J. (2019) "Thermo-poro-elastic behaviour of a transversely isotropic shale: Thermal expansion and pressurization". in preparation.

5.1 Testing programme

Before installing a specimen in the testing device, the drainage ducts were dried, in order to prevent material swelling. Four COx specimens were investigated, listed in Tab. 5.1. The COx specimens were mounted in the isotropic cell at a constant cell temperature close to ambient temperature. The specimens were consolidated at constant water content under isotropic stress with a loading rate of 0.1 MPa/min. All specimens were brought to a confining pressure close to the *in situ* effective stress (sample ISO1 to 10 MPa total stress and samples ISO2 - ISO4 to 8 MPa total stress, see Tab. 5.1) while monitoring deformations.

Tab. 5.1.: Characteristics of the four tested specimens ISO1 - ISO4, with the applied isotropic confining stress σ and measured volume change $\varepsilon_{\mathrm{hyd}}$ during saturation. The utilized testing procedure with imposed confining stress σ and pore pressure p_f, and the average measured thermo-elastic parameters are shown (note that thermo-plastic characteristics and temperature dependencies are not detailed here).

		Saturation		Test conditions			Average measured parameters					
#	Core EST	σ [MPa]	$\varepsilon_{\mathrm{hyd}}$ [%]	Type	σ [MPa]	p_f [MPa]	$\alpha_{d,z}{}^{(1)}$	$\alpha_{d,h}$	$\alpha_{u,z}{}^{(2)}$	$\alpha_{u,h}{}^{(2)}$	$\Lambda^{(2)}$	$H^{(2)}$
								$[10^{-5}\,^{\circ}\mathrm{C}^{-1}]$			[MPa/°C]	[GPa]
ISO1	57185	10	0.71	three-stage	14	4	-	0.53	4.82	2.30	0.19	2.32
ISO2	53650	8	0.86	two-stage	12	4	-	0.60	-	2.03	-	-
ISO3	53650	8	0.80	two-stage	12	4	0.18	0.30	4.63	1.86	-	-
ISO4	53650	8	0.72	three-stage	14	4	0.22	0.51	4.93	1.99	0.20	2.49

(1) only thermo-elastic values shown here
(2) temperature dependent

Once specimen deformations stabilized, vacuum was applied to the drainage ducts to evacuate the remaining air. The dry ducts were then filled with synthetic pore water (Tab. 3.2). The fluid pressure was chosen small enough in order to limit the change of effective stress. Some swelling strains were observed, that stabilized after about 5 days, with 0.71 % expansion for ISO1, 0.86 % expansion for ISO2, 0.80 % expansion for ISO3 and 0.72 % expansion for ISO4 (see Tab. 5.1). These values are comparable to the data of (Belmokhtar et al., 2017a), who found 0.97 and 0.85 % for samples saturated at 8 and 12 MPa effective stress, respectively.

After hydration, pore pressure and confining pressure were simultaneously increased under constant effective stress, until reaching a pore pressure close to the *in situ* one (4.0 MPa). Samples ISO1 and ISO4 were brought to 14 MPa total stress, and samples ISO2 - ISO3 to 12 MPa total stress. Note that an increment of 2 MPa confining pressure was finally applied to ISO4, resulting in higher effective stress than during saturation.

Two different step testing procedures, presented by Braun et al. (2019), Sec. 3.6, were utilized to determine the THM parameters of the material. Samples ISO1 and ISO4 were tested, following a three-stage protocol (Fig. 5.1a). This consists in rapidly increasing or decreasing the cell temperature (rate of 10 °C/h), while the drainage system is kept closed. In this phase, one can measure $\alpha_{u,z}$ and $\alpha_{u,h}$ as tangent parameters, with no need of correcting any effect of the drainage system. In the second phase, the temperature is kept constant until deformations and pore pressures stabilized. The corresponding pseudo-undrained conditions require the correction of the measured secant parameters $\alpha_{u,z}$, $\alpha_{u,h}$ and Λ, according to Eqs. (3.3) and (3.5). In the third stage, the drainage system is opened, imposing the initial pore pressure. The pore pressure gradually comes back to its initial distribution through a transient phase governed by pore pressure diffusion, and a drained state is finally reached. At final state, after strain stabilization, $\alpha_{d,z}$ and $\alpha_{d,h}$ can be determined. The change in pore pressure with respect to the change of strains during the third phase provides the moduli H_z and H_h.

Samples ISO2 and ISO3 were tested under a two-stage procedure (Fig. 5.1b). In this procedure, specimens are first rapidly heated or cooled under 10 °C/h and then kept at constant temperature. Even though the drainage system is always kept open, the temperature change is much faster than pore pressure diffusion, and one can measure $\alpha_{u,z}$ and $\alpha_{u,h}$. After reaching stable strains in a completely drained state, $\alpha_{d,z}$ and $\alpha_{d,h}$ can be measured.

The isotropic total stress was always kept constant during the tests, and the pore pressure at the bottom of the specimen was imposed constant by the PVC, by opening the connecting valve. Hence, at the end of the step tests, the induced pore pressure came to its initial value. Drained thermal strains were therefore always evaluated under a constant stress condition, while the stress state in the undrained phase changed according to $\mathrm{d}p_f = \Lambda \mathrm{d}T$.

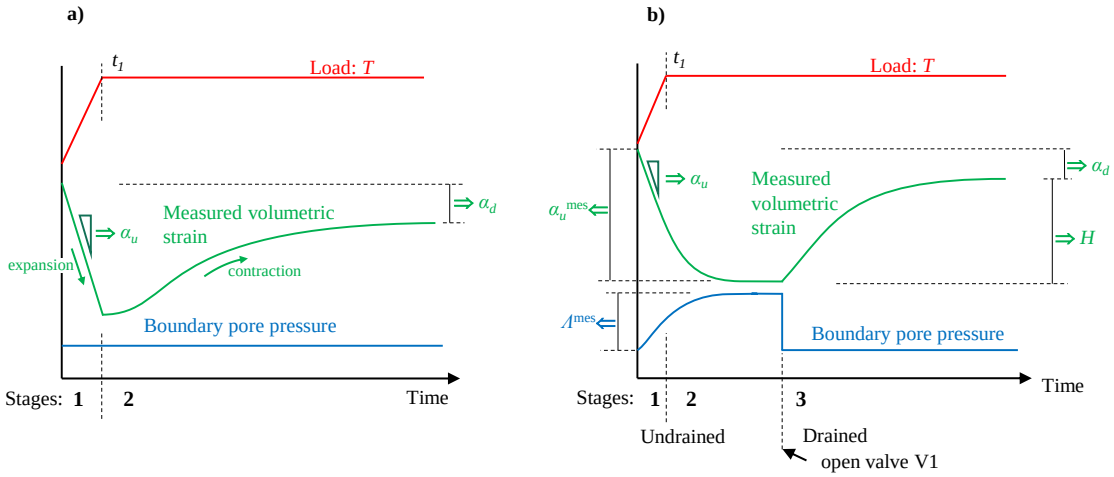


Fig. 5.1.: Schematic procedure of a) two-stage thermal test and b) three-stage thermal test

Depending on the increment of temperature applied in one step, this change in pore pressure might have a significant influence on the measured parameters, if the material properties are stress dependent. Also, a temperature dependency of the properties has to be taken into account, if the temperature increments are too large. The temperature at which the measured parameters are presented in the following, was chosen as the mean between initial and final temperatures during each step test. In subsequent steps, the specimens were heated until 90 °C (ISO1, ISO3), 80 °C (ISO4) and 75 °C (ISO2), and then cooled back, as presented in Fig. 5.2. The utilized testing procedures, as well as stress and pore pressure conditions and measured material parameters, are summarized in Tab. 5.1 (note that the axial strain gage on sample ISO2 failed after saturation, so that only radial strains could be recorded during this test).

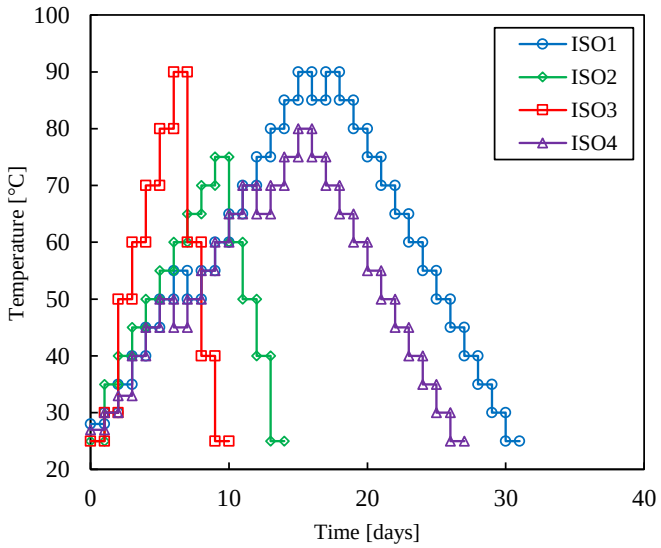


Fig. 5.2.: Applied heating and cooling paths on the four tested samples; in each step the temperature was changed rapidly with increments from 5 °C (ISO1, ISO4) up to 15 °C (ISO2, ISO3), followed by a constant temperature stage during one day

5.2 Experimental results

The data of a typical three-stage thermal test, run on specimen ISO4 between 50 to 45 °C, is presented in Fig. 5.3 and 5.4 in terms of pore pressure and strain changes, respectively. The target temperature was reached after about 1.5 h and then kept constant. Given that the drainage system was closed, a decrease in pore pressure due to thermal pressurization is observed, which stabilizes after 4 h. The peak at 1.5 h is due to the thermal pressurization coefficient of the drainage system Λ_L, which was found to be higher than that of the specimen. As also observed by Mohajerani et al. (2012), due to the rapid temperature change, there is initially no exchange between the fluid of the drainage system and the pore fluid of the specimen. One only detects the response due to the pressurization of the drainage system itself. After about 4 h, this pressure equilibrated with the specimen pore pressure. The measured thermal pressurization and expansion coefficients could then be corrected using Eq. (3.3) and (3.5), respectively. To reduce uncertainties, we preferred however to determine $\alpha_{u,i}$ from the initial slope of $\mathrm{d}\varepsilon/\mathrm{d}T$. This provides the undrained thermal expansion coefficients in both anisotropy directions. Once the equilibrium in undrained state was reached, we opened the drainage valve, so that the pore pressure in the drainage system and at the specimen bottom increased, back to their initial value, resulting in the dissipation of thermal excess pore pressures within the specimen. Such behaviour was also observed in thermal tests on Boom clay by Delage et al. (2000). The pore pressure dissipation observed in the present study caused transient deformations, that stabilized after about 20 h. This deformations can be seen in Fig. 5.4, presenting the changes in horizontal, vertical and volumetric strains with respect to time. Given that complete drainage was achieved, the drained thermal expansion coefficients were measured. The Biot modulus $H = \Delta p_f / \Delta \varepsilon_v$ could be computed from the volumetric deformations, under the pore pressure change of 1.3 MPa between the undrained and the drained phase. Once this temperature step completed, the drainage system was closed again and a subsequent similar three stage test was carried out.

In the two-stage tests on samples ISO2 and ISO3, we went directly from rapid thermal loading to a transient drained phase. The measured parameters and the characteristics of the transient deformations obtained in these phases are comparable to that from three-stage tests.

5.2.1 Drained thermal deformations

At the end of each step, a drained state was attained, when deformations stabilized. These strain changes with respect to temperature are presented in Fig. 5.5. The drained deformations in horizontal direction parallel to the bedding plane were recorded for all four samples. Specimens ISO1 and ISO2 showed some artefacts in vertical direction perpendicular to the

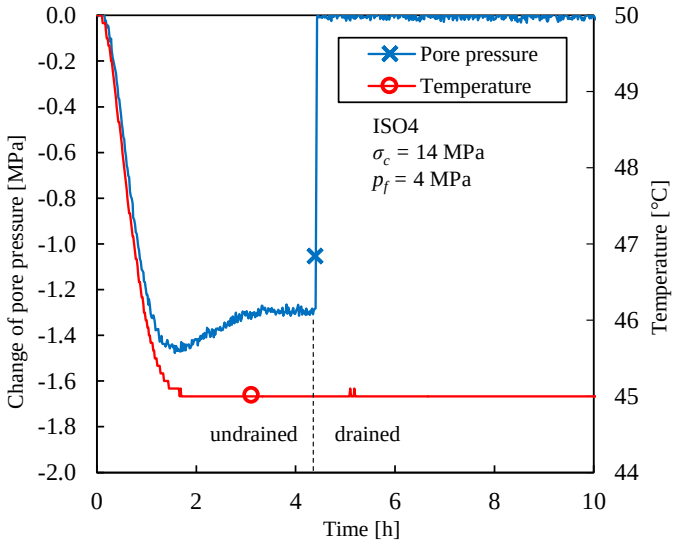


Fig. 5.3.: Typical three stage thermal test on ISO4: response in pore pressure resulting from an undrained decrease in temperature form 50 to 45 °C, followed by drainage opening and pore pressure dissipation

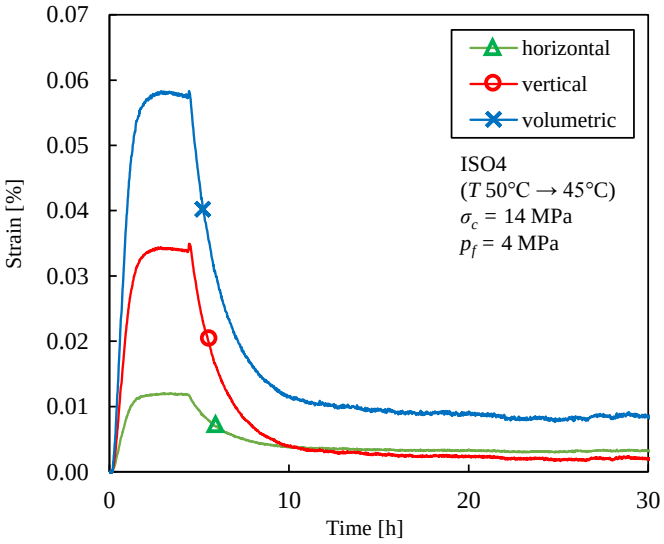


Fig. 5.4.: Measured strains parallel and perpendicular to the bedding plane during test ISO4, with an initial undrained thermal expansion stabilizing after 4 hours, followed by a transient deformation due to pore pressure dissipation, and stabilization at a drained state

bedding plane, probably due to the less precise correction of strain gages using calculated apparent strains, and data is not presented here.

Strains parallel to bedding were observed to be predominantly reversible and reasonably linear with temperature. In that direction, specimens expanded during heating and contracted during cooling, illustrating a thermo-elastic response with an average linear elastic thermal expansion coefficient $\alpha_{d,h} = 0.51 \times 10^{-5\circ}\mathrm{C}^{-1}$.

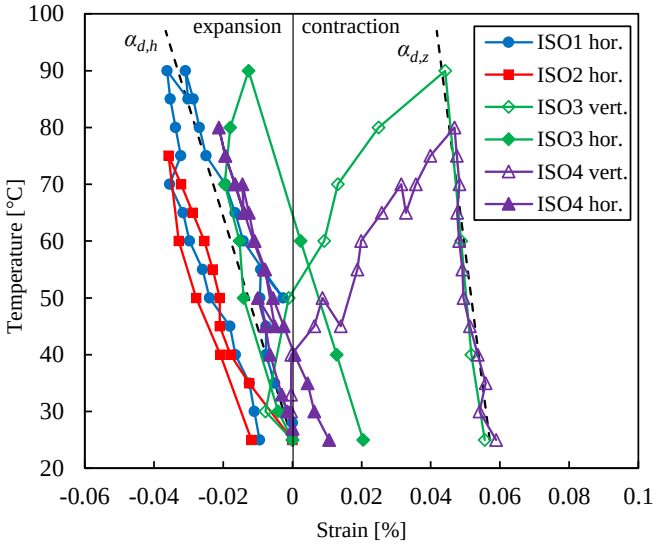


Fig. 5.5.: Drained strain changes (vertical = perpendicular and horizontal = parallel to bedding) with respect to temperature changes, under constant isotropic effective stress (10 MPa for ISO1 and ISO4 and 8 MPa for ISO2 and ISO3)

Perpendicular to bedding, the material first expanded with temperature up to 40 °C, followed by contraction at higher temperatures. During cooling, one can observe a linear contraction, providing a linear thermal expansion coefficient $\alpha_{d,z} = 0.21 \times 10^{-5\circ}\mathrm{C}^{-1}$ from tests ISO3 and ISO4. Note that this thermal expansion coefficient is about 2.4 times smaller than that measured parallel to bedding. This gives a bulk thermal expansion coefficient $\alpha_d = 1.23 \times 10^{-5\circ}\mathrm{C}^{-1}$.

To describe the observed contraction during heating, we use an elasto-plastic drained thermal expansion coefficient $\alpha^*_{d,z} = \alpha_{d,z} + \alpha^{irr}_{d,z}$, which includes reversible ($\alpha_{d,z}$) and irreversible ($\alpha^{irr}_{d,z}$) thermal strains (Sulem et al., 2007). We can adopt a linear relationship from the measurements on samples ISO3 and ISO4:

$$\alpha^*_{d,z} = (-0.035T + 1.238) \times 10^{-5\circ}\mathrm{C}^{-1}, \tag{5.1}$$

with T in °C, providing the value of the irreversible thermal expansion coefficient:

$$\alpha^{irr}_{d,z} = (-0.035T + 1.071) \times 10^{-5\circ}\mathrm{C}^{-1} \tag{5.2}$$

The contraction behaviour under heating was previously observed by Monfared et al. (2011a) on the Opalinus claystone and by Belmokhtar et al. (2017b) on the COx claystone. Belmokhtar et al. (2017b) determined $\alpha_d = 4.82 \times 10^{-5}°\mathrm{C}^{-1}$, by means of LVDTs, a value much larger than that observed here.

5.2.2 Undrained thermal deformations

During the first phase of each temperature step, the undrained thermal expansion coefficients were determined from the tangent of the strain-temperature curves. All four specimens showed a similar behaviour, with axial strains about 2.3 times higher than radial ones, and an average value $\alpha_{u,z} = 4.6 \times 10^{-5}°\mathrm{C}^{-1}$ (from 3 samples) and $\alpha_{u,h} = 2.0 \times 10^{-5}°\mathrm{C}^{-1}$ (from 4 samples). By carrying out step tests at different temperatures, we can present the changes in thermal expansion coefficients with respect to temperature, as seen in Fig. 5.6. Note that the values of the undrained thermal expansion coefficients are nearly one order of magnitude higher than the drained ones shown before. An increase of both vertical and horizontal thermal expansion coefficients with temperature was observed. A linear relationship between $\alpha_{u,z}$ and $\alpha_{u,h}$ with T is depicted in Fig. 5.6, and described with the following functions:

$$\alpha_{u,z} = (0.028T + 3.256) \times 10^{-5}°\mathrm{C}^{-1} \tag{5.3}$$

$$\alpha_{u,h} = (0.006T + 1.758) \times 10^{-5}°\mathrm{C}^{-1} \tag{5.4}$$

with T in °C.

This also provides an expression for the volumetric undrained thermal expansion coefficient:

$$\alpha_u = (0.040T + 6.772) \times 10^{-5}°\mathrm{C}^{-1} \tag{5.5}$$

This linear relationship is depicted in Fig. 5.7, together with the measured bulk thermal expansion coefficients. Note that due to the absence of radial measurements on ISO2, the volumetric response could not be displayed for this sample.

We could not detect any important difference between undrained thermal expansion coefficients during heating and cooling, showing that thermo-plastic deformations were not noticeable in undrained conditions. As shown before, the deformations of the solid matrix (α_d) contain some thermoplastic characteristics, but since α_d is about ten times smaller than α_u, its effects on the latter are not significant. We can conclude, that undrained thermal strains are mainly governed by the reversible thermal volume changes of the fluid phase.

Zhang et al. (2017) showed some data on the undrained bulk thermal expansion coefficient of a COx specimen under different confining stresses. Thermal strains were recorded by

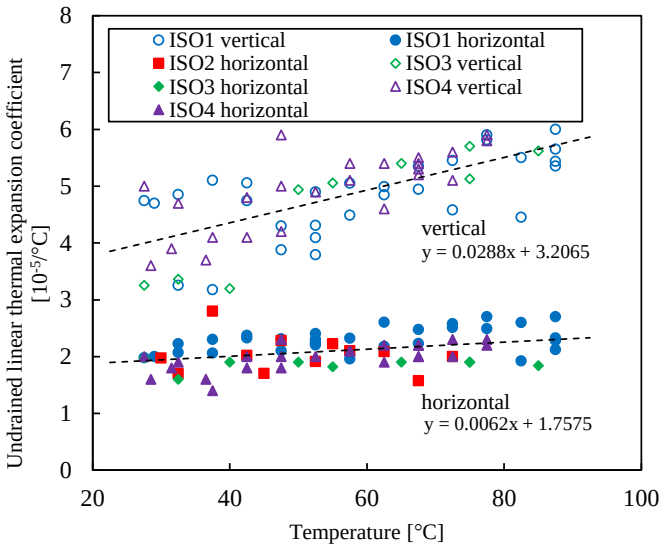


Fig. 5.6.: Linear undrained thermal expansion coefficient for heating and cooling, measured during the initial rapid temperature changes in each step test

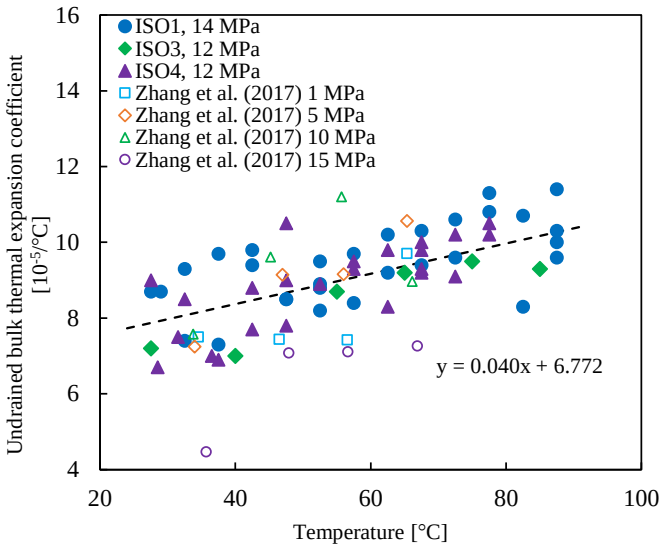


Fig. 5.7.: Bulk undrained thermal expansion coefficient for heating and cooling, measured during the initial rapid temperature changes in each step test. The data is compared with similar findings of Zhang et al. (2017)

means of LVDTs and extensometer chains. They pointed out, that under up to 10 MPa confining stress, α_u increased with temperature, from about $7.0 \times 10^{-5}°\mathrm{C}^{-1}$ at 30 °C to about $1.0 \times 10^{-4}°\mathrm{C}^{-1}$ at 65 °C. This confirms very well the findings of this work (Fig. 5.7). Under 15 MPa confining stress, they showed that α_u was lower with about $4.5 \times 10^{-5}°\mathrm{C}^{-1}$ at 30 °C and about $7.0 \times 10^{-5}°\mathrm{C}^{-1}$ at 65 °C. Mohajerani et al. (2012) investigated the undrained thermal behaviour of two COx samples in an isotropic cell. They did not record any specimen deformations, but they performed a back-calculation of α_u based on their measurements of thermally induced pore pressures. This theoretical α_u increased with temperature, with about $9.0 \times 10^{-5}°\mathrm{C}^{-1}$ at 30 °C and 8 MPa effective stress, up to about $1.6 \times 10^{-4}°\mathrm{C}^{-1}$ at 80 °C. The value at 80 °C, calculated at 3.4 MPa effective stress is higher than that measured in this study under 8 and 10 MPa effective stress. This might indicate some stress dependency of the undrained thermal expansion coefficient.

5.2.3 Strain response to pore pressure change

By changing the pore pressure under isostatic and isothermal conditions, one can measure the Biot modulus $H = \Delta p_f / \Delta \varepsilon_v$. This was done once the undrained equilibrium was reached in each three-stage step test, by opening the drainage system and bringing the thermally induced pore pressure back to initial value (see Fig. 5.3 and 5.3).

Note that due to the thermoplastic response observed above 40 °C we could not measure H along heating paths. Consequently, above 40 °C, H was determined from cooling paths, where thermoelasticity is supposed.

As one can observe in Fig. 5.8, the measured moduli appears to increase with temperature. The values at ambient temperature are corresponding with the findings of Sec. 4, where we determined a mean value of H around 2.15 GPa at 10 MPa effective stress and 25 °C. We observed a rather large variability of measured moduli at the same stress state, indicated in Fig. 5.8. The values evaluated in the present section lie almost all within this range, making it difficult to identify a material temperature dependency. However, for modelling the observed thermal pressurization test, a linear temperature relationship was considered in the further analysis.

5.2.4 Thermally induced pore pressure

Using the calibration presented in Sec. 3.3.3, we corrected the thermal pressurization coefficients, measured from the temperature steps applied on samples ISO1 and ISO4. This correction method is based on the assumption of a thermo-elastic response, which was not the case during heating over 40 °C. Therefore, we show in Fig. 5.9 the corrected results obtained along heating paths below 40 °C and along cooling paths, during which the

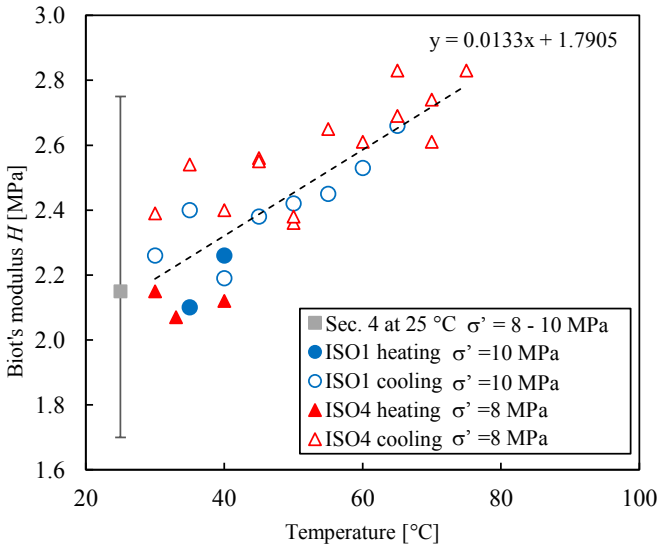


Fig. 5.8.: Measured modulus H with respect to temperature, compared with the data from Sec. 4 at 25 °C

response is considered as thermo-elastic. One can observe reasonable agreement between the data from heating below 40 °C and cooling phases.

We can see that the parameter Λ increases significantly with temperature, with values of around 0.12 MPa/°C at 25 °C and up to around 0.30 MPa/°C at 80 °C. Note that the stress conditions for these measurements remained nearly constant, close to the *in situ* ones. The total stress was kept constant, while the thermally induced pore pressures were released after each step.

In parallel, we use Eq. (2.39) to compute Λ for each step test carried out within the thermo-elastic regime, based on the measurements of α_u, α_d and H from each respective test. As seen in Fig. 5.10, these calculated values show good overall compatibility with the corrected measurements. Only the measured values for temperatures over 70 °C appear to be slightly higher than the calculated ones.

Mohajerani et al. (2012) measured thermal pressurization coefficients of two COx samples, heated under initially close to *in situ* stress ($\sigma' = 8$ MPa). During the experiment, Λ decreased slightly with temperature, with about 0.14 MPa/°C at 25 °C down to between 0.10 and 0.05 MPa/°C above 70 °C. As seen in Fig. 5.9, their results for ambient temperature correspond well with the findings of this study, however one can observe a large difference at higher temperatures. These observations will be discussed in more detail in Sec. 5.3.4.

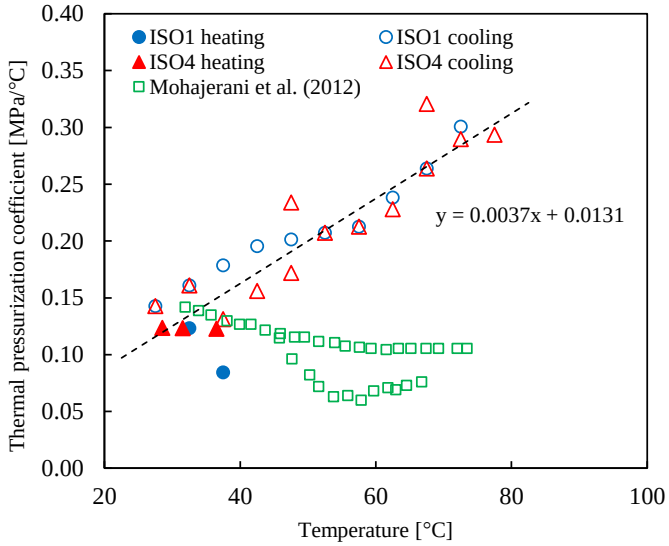


Fig. 5.9.: Corrected thermal pressurization coefficients obtained on samples ISO1 and ISO4 under heating up to 40 °C and during cooling paths, compared with the findings of Mohajerani et al. (2012)

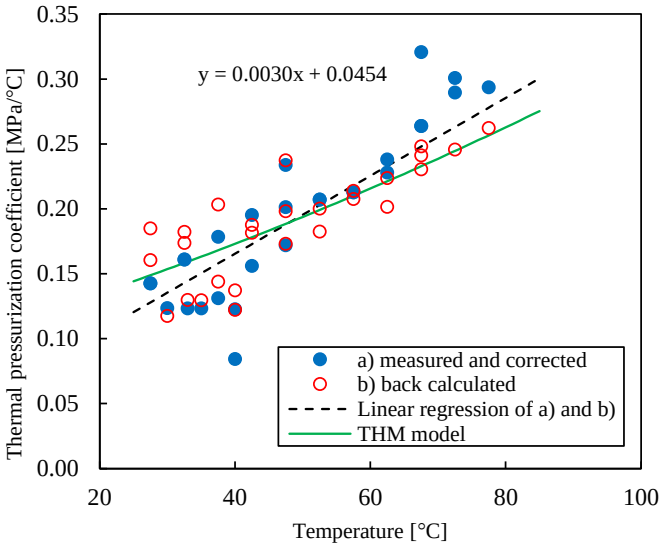


Fig. 5.10.: Comparison of the measured thermal pressurization coefficients (Fig. 5.9) with the back-calculated ones for each test using Eq. (2.39) and the THM calculation explained in Sec. 5.3.4 based on Eq. (2.34)

Tab. 5.2.: Thermal expansion coefficients of the bulk mineral composites and in directions perpendicular to the mineral layer ($\perp$) and parallel to the layer ($\parallel$), adapted from Belmokhtar et al. (2017b)

Mineral	Mass-%	α $[10^{-5\circ}\mathrm{C}^{-1}]$		
		bulk	linear ($\perp$)	linear ($\parallel$)
Clay (muscovite)	42	2.48	1.78 [1]	0.35 [1]
Quartz	25	3.3 [2]	1.1	
Calcite	30	1.4 [3]	0.5	
Feldspar	4	1.1 [3]	0.4	

[1]McKinstry (1965), [2]Palciauskas and Domenico (1982), [3]Fei (1995)

5.3 Discussion

5.3.1 Thermal strains of the solid matrix

Within a thermo-poromechanical framework, assuming micro-homogeneity, one can presume $\alpha_d = \alpha_\phi = \alpha_s$. The drained thermoelastic expansion coefficient of a specimen is therefore equal to the thermal volume changes of the solid matrix α_s. In the case of COx claystone, for which we measured $\alpha_{d,z} = 0.21 \times 10^{-5\circ}\mathrm{C}^{-1}$ (perpendicular to bedding) and $\alpha_{d,h} = 0.51 \times 10^{-5\circ}\mathrm{C}^{-1}$ (parallel to bedding), the solid phase is composed of around 42 % clay minerals, 30 % calcite, 25 % quartz and 4 % feldspar (Conil et al., 2018).

McKinstry (1965) measured the thermal expansion of clay minerals using a X-ray method. They provided mean values for muscovite, a mineral with the same molecular organisation as illite and smectite, of 1.78 $\times 10^{-5\circ}\mathrm{C}^{-1}$ perpendicular to the layer and of 0.35 $\times 10^{-5\circ}\mathrm{C}^{-1}$ parallel to the layer. Fei (1995) gave values for the volumetric thermal expansion of calcite and feldspar, and Palciauskas and Domenico (1982) for quartz (see Tab. 5.2).

Compared to the thermal expansion coefficients of the mineral constituents of the COx claystone, we can see that the drained thermal expansion coefficient parallel to bedding lies well within in the range of the values of elementary minerals. The reversible thermal expansion coefficient perpendicular to bedding is however smaller than that of the mineral constituents. This fact, together with the contraction observed perpendicular to bedding along heating paths, shows that strain in this direction are not only dependent on the thermo-elastic behaviour of the minerals. Given the preferred sub-horizontal orientation of the clay platelets, we presume that adsorbed water molecules, either within the platelets or in the inter-platelets porosity, could have an influence on thermal strains in this direction.

Tab. 5.3.: Reference parameters used for the sensitivity analysis at 25 °C, $\sigma = 14$ MPa, $p_f = 4$ MPa

α_d	$[°C^{-1}]$	1.23×10^{-5}	measured
α_f	$[°C^{-1}]$	2.60×10^{-4}	IAPWS-IF97 (2008), Spang (2002)
K_s	[GPa]	21.0	Belmokhtar et al. (2017a)
K_f	[GPa]	2.2	IAPWS-IF97 (2008), Spang (2002)
ϕ	[%]	18.0	measured
H	[GPa]	2.15	measured

Also in the literature one can find data on shales with rather low thermal expansion coefficients. Ross (1941) measured the thermal expansion of 139 building bricks, including different kinds of fire-clay, clay and shale type bricks. This author observed that in 87 % of the cases, the clay and shale bricks had a linear thermal expansion coefficient between 0.5 and 0.7 $\times10^{-5}°C^{-1}$. Thermal expansion coefficients of Marcellus shale, close to the ones observed in this study, were measured by Villamor Lora et al. (2016), with 0.26 $\times10^{-5}°C^{-1}$ perpendicular to bedding and 0.13 $\times10^{-5}°C^{-1}$ parallel to bedding. They note, that their specimens were quite desaturated, which indicates that the sample state was close to the drained one.

5.3.2 Parametric study of THM couplings

Looking at the thermoelastic expression of Λ given in Eq. (2.34), one observes that the parameter Λ is mainly depending on the difference between the thermal expansion of pore fluid α_f and of the solid matrix α_d. The unjacketed modulus K_s, the fluid bulk modulus K_f, the Biot modulus H and the porosity ϕ are also involved in the expression of Λ.

A sensitivity analysis was carried out by calculating Λ with Eq. (2.34), and α_u with Eq. (2.39), using the previously considered reference parameters presented in Tab. 5.3. The influences of separate variation of each input parameter on Λ and α_u are shown in Fig. 5.11 and 5.12, respectively. One observes little sensitivity of both parameters with respect to α_d, K_s and K_f. Conversely, the thermal pressurization coefficient is strongly dependent on the parameters α_f, ϕ and H, with the highest impact caused by α_f. We can also see that α_u is less sensitive to changes in ϕ and H. This identifies α_f as the single main parameter governing the changes in α_u.

5.3.3 Anomalous thermal behaviour of pore fluid

Baldi et al. (1988) observed on low porosity clays, that the experimentally measured undrained response could only be reproduced by utilizing a thermal expansion coefficient of the pore fluid, higher than that of free water. In the case of Opalinus clay, Monfared et al. (2011a) observed the same phenomenon and back-calculated a thermal expansion coefficient of the pore fluid about two times higher than that of free water. Valenza and Scherer (2005)

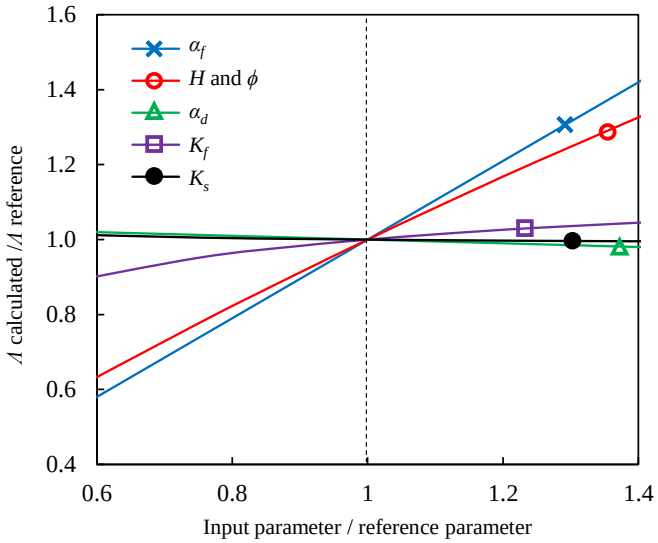


Fig. 5.11.: Variation of Λ with respect to a separate variation of the input parameters, listed in Tab. 5.3

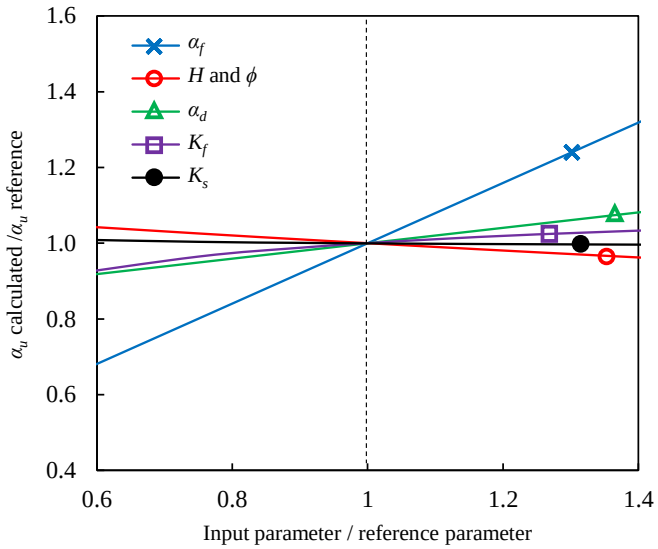


Fig. 5.12.: Variation of α_u with respect to a separate variation of the input parameters, listed in Tab. 5.3

reported an anomalous thermal expansion of water, confined in cement pores, based on their thermopermeametry and beam bending experiments. Ghabezloo et al. (2009b) confirmed such findings with measurements from undrained heating tests on hardened cement paste. In laboratory experiments on silica gel and silica glasses, respectively, Derjaguin et al. (1992) and Xu et al. (2009) could measure an elevated thermal expansion coefficient of the water contained in these small pores at nano-scale. Derjaguin et al. (1992) noted that, starting from 70 °C, the confined water lost its anomalous characteristics. Xu et al. (2009) were able to simulate their laboratory experiments by molecular dynamics calculations up to around 60 °C. Their model for higher temperatures, presented in Fig. 5.13, also show that the thermal expansion coefficient of confined water became equal to that of bulk water at around 70 °C.

To analyse the thermal expansion characteristics of COx pore fluid, we utilize the strong coupling between α_u and α_f (Fig. 5.12). This allows us to carry out a back-analysis of α_f, using other experimentally determined parameters and rewriting Eq. (2.39) and (2.34):

$$\alpha_f = \left[\frac{1}{\phi} + H\left(\frac{1}{K_f} - \frac{1}{K_s}\right)\right](\alpha_u - \alpha_d) + \alpha_d \tag{5.6}$$

Conversely, an adaptation of K_f in a reasonable range was not able to reproduce α_u, due the weak dependency between these parameters. We utilize Eq. (5.6) to calculate the thermal expansion coefficient of the pore fluid, under constant confining stress and pore pressure, as a function of temperature. The parameters of Tab. 5.3 are used here, taking into account the temperature and stress dependency of the water bulk modulus K_f (IAPWS-IF97, 2008; Spang, 2002). For H, we use the previously observed temperature dependency $H(\sigma' = 10\,\mathrm{MPa}, T) = 2.15 + 0.0133(T - 25)$, with H in GPa and T in °C. Also the experimentally determined undrained thermal expansion coefficient (Fig. 5.7) is inserted in Eq. (5.6). Doing so, we obtain a pore fluid thermal expansion coefficient α_f, which is highly temperature dependent, and differs from the thermal expansion coefficient of free water. We introduce a factor $\eta = \alpha_f/\alpha_w$ (depicted in Fig. 5.13), where α_w is the stress and temperature dependent thermal expansion coefficient of bulk water. For ambient temperatures, the pore fluid expands around 1.7 times more than bulk water. This ratio decreases with increasing temperature. For temperatures over 60 °C, the thermal expansion coefficient of the pore fluid is slightly lower than that of free water. A comparison with the values presented by Xu et al. (2009) shows a similar trend.

5.3.4 Stress and temperature dependent thermal pressurization

To investigate the stress and temperature dependency of the thermal pressurization coefficient, we insert in Eq. (2.34) the previously back-calculated elevated thermal expansion coefficient of the pore fluid (Fig. 5.13). Again, the temperature and stress dependency for

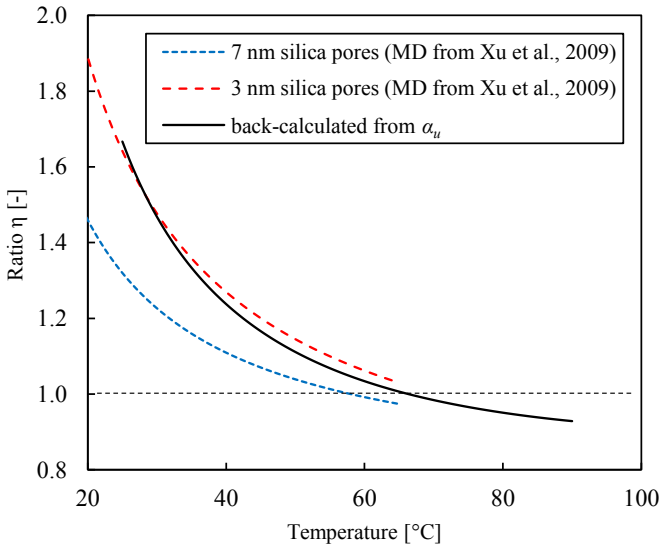


Fig. 5.13.: Back calculated ratio $\eta = \alpha_f/\alpha_w$ thermal expansion coefficient of the water confined in COx pores [Eq. (5.6)] with respect to that of bulk water, compared to molecular dynamics (MD) simulations of Xu et al. (2009)

K_f (IAPWS-IF97, 2008; Spang, 2002) was considered. For the Biot modulus H, we use the following stress-dependent relationship from Sec. 4:

$$H(\sigma') = \left[\frac{1}{H_\infty} + \left(\frac{1}{H_0} - \frac{1}{H_\infty}\right)\exp\left(-\beta_1\sigma'\right)\right]^{-1} \tag{5.7}$$

with $H_\infty = 3.38$ GPa, $H_\infty = 0.53$ GPa and $\beta_1 = 0.29$ MPa^{-1}. By assuming this stress dependency to be valid for all temperatures, we add the previously temperature dependent changes, observed in Fig. 5.8:

$$H(\sigma', T) = H(\sigma') + \beta_2\,(T - 25) \tag{5.8}$$

with $\beta_2 = 0.0133$ GPa and T in °C. Note that this relationship was assumed for modelling the presented experiments. Due to the scarcity of data and compared to the variability of H (Sec. 4), it has to be taken with caution. Other coefficients were taken from Tab. 5.3. A significant increase of Λ with temperature, due to an increasing α_f, can be noted in Fig. 5.10. We compare these values to the corrected measurements and calculated values from direct measurements using Eq. (2.39), also presented in Fig. 5.10. A good agreement between these values at temperatures up to 60 °C can be observed. For higher temperatures however, the back calculation underestimates slightly the measured thermal pressurization, but follows a similar trend.

Using the same model, but changing the stress conditions, according to the experiment carried out by Mohajerani et al. (2012), we are able to reproduce a similar nearly constant parameter (Fig. 5.14a). The changed stress conditions, which include a continuously increasing pore pressure (according to $\Delta p_f = \Lambda\Delta T$) reducing the effective stress, mainly

affect the parameter H. A decreasing H results in a thermal pressurization coefficient, which remains nearly constant, evidencing a strong stress dependency of Λ. Another calculation for a constant, but very low effective stress, is presented in Fig. 5.14a. Due to constant effective stress, we see again an increasing thermal pressurization coefficient, with however much lower values.

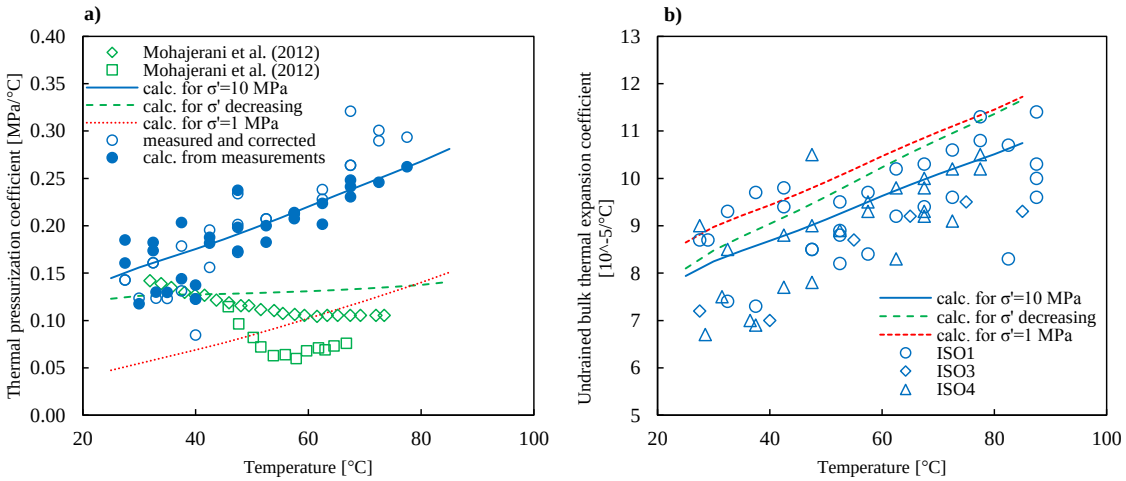


Fig. 5.14.: Back calculation using a value α_f obtained before (Fig. 5.13), of a) the thermal pressurization under different stress conditions, compared with the measurements presented in this study and by Mohajerani et al. (2012), and b) back calculation of the undrained bulk thermal expansion coefficient under different stress conditions, compared with the measurements presented in this study

The effect of stress on α_u was investigated by calculating α_u using Eq. (2.38) and (2.39), as shown in Fig. 5.14b. Unsurprisingly, since the measured mean values of α_u were used as input parameters for the model, we find a good agreement for the calculation at $\sigma' = 10$ MPa. More interestingly, we observe only a small stress dependency of α_u at $\sigma' = 1$ MPa, which lies within the range of variability of measured values. The plot for a decreasing effective stress represents, as also for the thermal pressurization coefficients in Fig. 5.14a, some transition between the limiting curves at 10 and 1 MPa effective stress. One can note, that the stress dependency of α_u is not significant compared to the variability of measured values.

5.4 Application of properties in a numerical model

5.4.1 Influence of the pore water thermal expansion coefficient

Here we adopted an anomalous thermal expansion coefficient α of pore water. The temperature and pressure dependent thermal expansion coefficient of bulk water was multiplied with a temperature dependent factor η, according to the back-calculated values depicted in

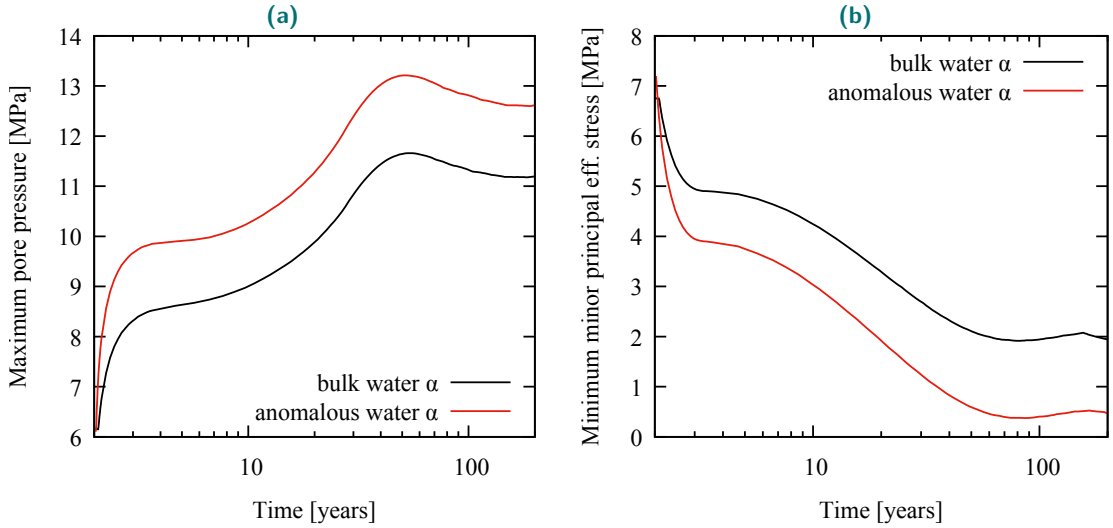


Fig. 5.15.: a) Calculated maximum pore pressure and b) minimum minor principal effective stress parallel to the model plane, calculated with properties of bulk water and with an anomalous thermal expansion coefficient α of water

Fig. 5.13. This is compared to the reference calculation, where temperature and pressure dependent properties corresponding to bulk water ($\eta = 1.0$) were used. A notable influence on the pore pressure and effective stress evolution can be observed in Fig. 5.15. Unsurprisingly, the higher thermal expansion coefficient of the pore fluid causes higher pore pressures and lower minor effective stresses. Interestingly, the two compared calculations indicate the same time evolution, but are shifted in magnitude.

5.4.2 Influence of the anisotropy of solid thermal expansion coefficients

To study the effect of the thermal expansion coefficients of the solid on THM processes in a large scale scenario, we adapted these parameters (Tab. 5.4). Similar to the parameter variation done on the poroelastic properties, we transformed the material to its equivalent isotropic characteristics. This was done by adopting an isotropic linear thermal expansion coefficient of the solid, equal to the mean $(2\alpha_{d,h} + \alpha_{d,z})/3$. The results, compared with the reference calculation, are presented in Fig. 5.16. Almost no difference can be detected between the two curves of maximum pore pressure and the two curves of minimum minor effective stress. This confirms the observations made in Sec. 5.3.2 on the elemental thermal pressurization coefficient. We can also observe, that variations of the rather small thermal expansion coefficients had negligible effects on the thermal pressurization phenomenon. The role of water thermal expansion is much more pronounced than that of the solid, and governs the THM behaviour.

Tab. 5.4.: Transversely isotropic properties, used in the previous reference calculation, adapted to equivalent isotropic thermal parameters, by taking the mean of anisotropic properties

Scenario for UT+UA	E [GPa] z	h	ν_i [-] zh	hh	b_i [-] z	h	G [GPa]	K_s [GPa]	$\alpha_{d,i}$ [10^{-5}/K]	
transv. iso	2.81	5.95	0.09	0.29	0.93	0.87	1.7	22.5	0.21	0.51
equiv. iso	2.81	5.95	0.09	0.29	0.93	0.87	1.7	22.5	0.41	

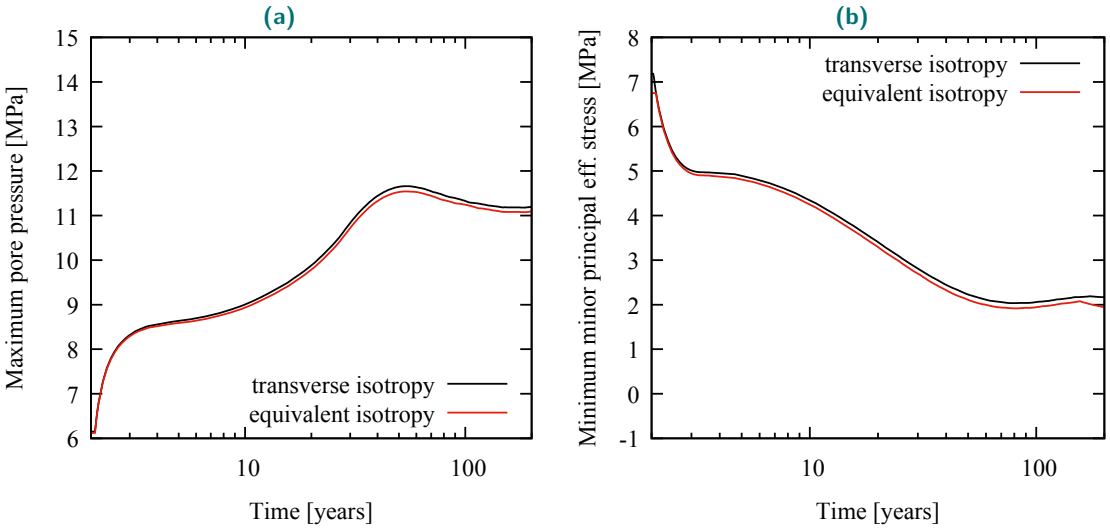


Fig. 5.16.: a) Calculated maximum pore pressure and b) minimum minor principal effective stress parallel to the model plane, comparing results with isotropic and anisotropic thermal expansion coefficients

5.5 Conclusions

Time saving testing protocols for thermal laboratory experiments, together with an optimized experimental device, allowed to efficiently determine the thermal properties of the COx claystone on four samples. A modified testing apparatus with a reduced drainage length permitted relatively fast specimen saturation and drainage times. The application of the protocols of Braun et al. (2019), Sec. 3.6, provided multiple material parameters in each experiment, rendering the laboratory study more time efficient. Strain gages were employed for measuring precise specimen deformations, where it was crucial to account for thermally induced measurement errors, especially due to the relatively small thermal strain response of the tested material.

Reversible drained thermal strains, parallel to the bedding plane, were detected during heating and cooling up to 90 °C. In perpendicular direction, we observed a thermal contraction upon heating, which appeared to be irreversible. During cooling, the material contracted in both directions, with strains parallel to bedding about 2.4 times higher than perpendicular to bedding. A relatively small reversible volumetric drained thermal expansion coefficient $\alpha_d = 1.23 \times 10^{-5} \mathrm{°C}^{-1}$ was found. The undrained thermal expansion coefficient during heating and cooling, under constant stress conditions, was determined, and found to increase with temperature. By conducting a back analysis, we showed that for reproducing the undrained thermal expansion coefficient and the thermal pressurization coefficient in a thermo-poroelastic framework, one could consider a thermal expansion coefficient of the pore water, greater than that of bulk water. Together with the measured Biot modulus H, and the measured drained thermal expansion coefficient α_d, the thermal pressurization coefficient Λ was calculated. The theoretical values reflect well the experimental results, and reproduce well previous observations made by Mohajerani et al. (2012). We obtain hence a thermal pressurization coefficient that increases significantly with temperature and increases with effective mean stress. By decreasing the effective stress during undrained heating, the material stiffness decreases, expressed through H, which results in a nearly constant thermal pressurization coefficient. One can also note that undrained characteristics (Λ, $\alpha_{u,i}$) were insensitive to $\alpha_{d,i}$, due to the relatively small values of $\alpha_{d,i}$. This emphasizes the decisive role of pore fluid in the undrained thermal behaviour of the COx claystone.

Similar observations were made when applying these findings in the numerical model. A variation of $\alpha_{d,i}$ had negligible effects. Conversely, an anomalous pore water thermal expansion coefficient caused notably higher pore pressures.

6 Extension behaviour and tensile failure

This chapter is devoted to the experimental investigation of the response of the COx claystone under extension paths. A novel triaxial device (Sec. 3.4) was utilized to submit specimens to stress paths expected *in situ* between microtunnels, in which exothermic waste has been placed. Thermally induced pore pressures generated effective tension within the samples, which led under constrained lateral deformations to axial extension. Eventually, the specimens reached their tensile resistance and failed. The testing program is summarized in Sec. 6.1, with its outcomes presented in Sec. 6.2. These observations are discussed and analysed in Sec. 6.3. In Sec. 6.4, we compare the findings with a numerical application. Conclusions of this chapter are given in Sec. 6.5.

The experimental findings of this chapter are included in the publication: Braun, P., Delage, P., Ghabezloo, S., Chabot, B., Conil, N., and Sulem, J. (2019) "Thermo-poro-elastic behaviour of a transversely isotropic shale: Tensile behaviour and failure in laterally constrained heating tests". in preparation.

6.1 Testing Procedure

We investigated the tensile behaviour of cylindrical specimens (20 mm diameter and around 30 - 40 mm height), listed in Tab. 6.1, in the specially designed extension apparatus. After having installed the rock samples in the cell, we brought the system to a constant initial temperature of around 25 °C. Only sample EXT3 was initially brought to 35 °C.

The specimens were consolidated by application of isotropic confining stress under a loading rate of 0.1 MPa/min, prior to be loaded up to different levels of confining pressure between 5 and 12 MPa (Tab. 6.1). Once the target confining pressure was reached and kept constant, the dry drainage lines were put under vacuum and saturated with synthetic pore fluid (Tab. 3.2).

Tab. 6.1.: Properties of the specimens tested during the experimental programme, where σ is the isotropic confining stress, $\varepsilon_{\mathrm{hyd}}$ is the swelling strain during hydration, γ_t the measured fracture angle with respect to the horizontal bedding plane

		Saturation		Initial state				Failure					
Sample	Core EST	σ [MPa]	$\varepsilon_{\mathrm{hyd}}$ [%]	T [°C]	σ'_z [MPa]	σ'_h [MPa]	p_f [MPa]	T [°C]	σ'_z [MPa]	σ'_h [MPa]	p_f [MPa]	ε_z [%]	γ_t [°]
EXT1	57185	8	0.2	25.0	7.7	6.9	4.9	61.9	-3.6	5.5	19	-0.36	2
EXT2	57185	5	0.21	25.0	2.7	3.5	2.1	53.4	-2.4	4.8	7.9	-0.20	18
EXT3	53650	12	0.64	35.0	3.2	8.4	4.0	63.5	-3.0	9.6	7.8	-0.33	7
EXT5	57185	-	-	25.0	5.7	0.0	0.2	25.0	-3.7	0.0	0.6	-0.09	0
EXT6	57185	-	-	25.0	0.1	0.0	2.0	25.0	-2.1	0.0	2.5	-0.07	4

The applied fluid pressure of 100 kPa was chosen small enough, to limit hydromechanical elastic strains due to the the corresponding decrease in effective stress. The swelling strains stabilized after about two days, with the values of strains given for each specimen in Tab. 6.1, comparable to that observed by Belmokhtar et al. (2017a). We noted that swelling decreases significantly under increased confining stress, confirming the necessity of saturating the specimens in confined state. Conversely, sample EXT2 showed surprisingly low swelling, given the relatively low confining stress applied.

After hydration, the piston was brought in contact with the specimen. We applied confining stress, axial stress and pore pressure, to bring the specimens to their respective initial states before thermal testing (Tab. 6.1). Hydraulic equilibrium was ensured after this phase by awaiting stable deformations. Thereupon, the extension tests were started by closing the drainage valve and heating the cells with a constant rate. Heating rates were set to 10 °C/h for samples EXT1 and EXT3, and to 5.0 °C/h for sample EXT2, with heating paths presented in Fig. 6.1. The servo-control of confining pressure was switched on, to maintain radial

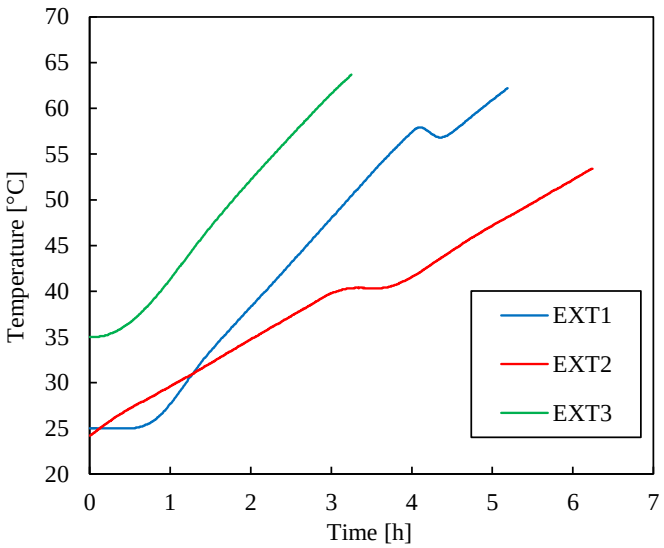


Fig. 6.1.: Imposed temperature changes with respect to time, applied during the extension tests

strains to zero, while the axial stress was kept constant. Leaks in the neoprene membrane of samples EXT5 and EXT6 made it impossible to create thermally induced pore pressures in these two tests. The leaks resulted in having the pore pressure becoming equal to the confining pressure. We chose to carry out isothermal hydromechanical extension tests on these samples. This involved increasing the confining stress, while the radial Terzaghi effective stress remained zero. Lateral strains were hence allowed. At the same time, the axial total stress was decreased, resulting in an axial extension. Note however, that the results of these tests have to be regarded with caution, as the infiltrating confining oil could have influenced the material behaviour.

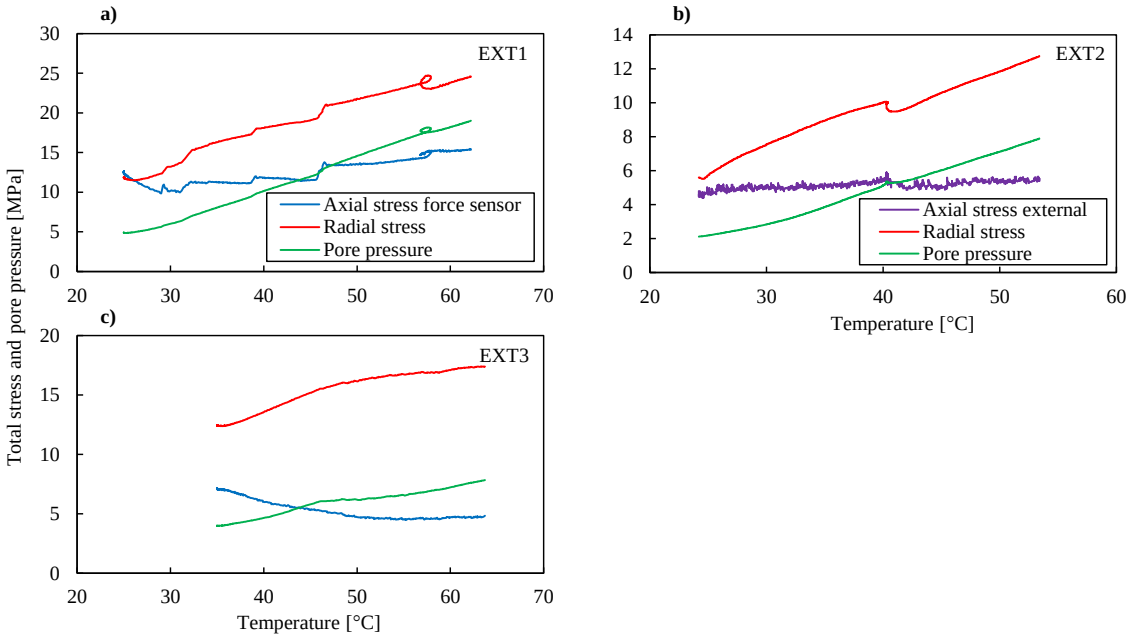


Fig. 6.2.: Stress and pore pressure conditions during the thermal extension tests; on specimen EXT2 the internal force sensor malfunctioned and we display stresses measured by the external transducer

It has to be noted, that different levels of radial effective stress were applied on the specimens, so as to investigate their effect on the stress-strain behaviour and the failure resistance of the claystone. Specimen EXT1 was tested starting from an isotropic stress state close to the *in situ* one, EXT2 started at a lower isotropic effective stress around 3.5 MPa, and EXT3 started at same radial effective stress as EXT1, but with reduced axial effective stress of 3.2 MPa. The isothermal tests EXT5 and EXT6 were carried out under zero radial effective stress.

6.2 Experimental results

Four heating tests under constrained lateral strains were carried out in this study. The imposed heating paths for these test are presented in Fig. 6.1, while the stress conditions with respect to temperature are shown in Fig. 6.2. The axial total stress, measured by the aluminium force sensor, remained more or less constant, with some variations due to the friction of the piston. On EXT2, we present the stresses measured externally by the PVC, as the internal force sensor malfunctioned. One can observe a continuous increase of measured pore pressures, generated through thermal pressurization. The pore pressure rises up to several MPa, with the most significant change of around 14 MPa in test EXT1. The values of induced pore pressures are presented in Tab. 6.1. Experimental measurements of stress, strain and temperature at initial state and at failure, which will be discussed in the following, are given. Conversely to the experiments in Sec. 5, we cannot evaluate the thermal pressurization coefficient Λ in this experiments, as it is defined for constant stress

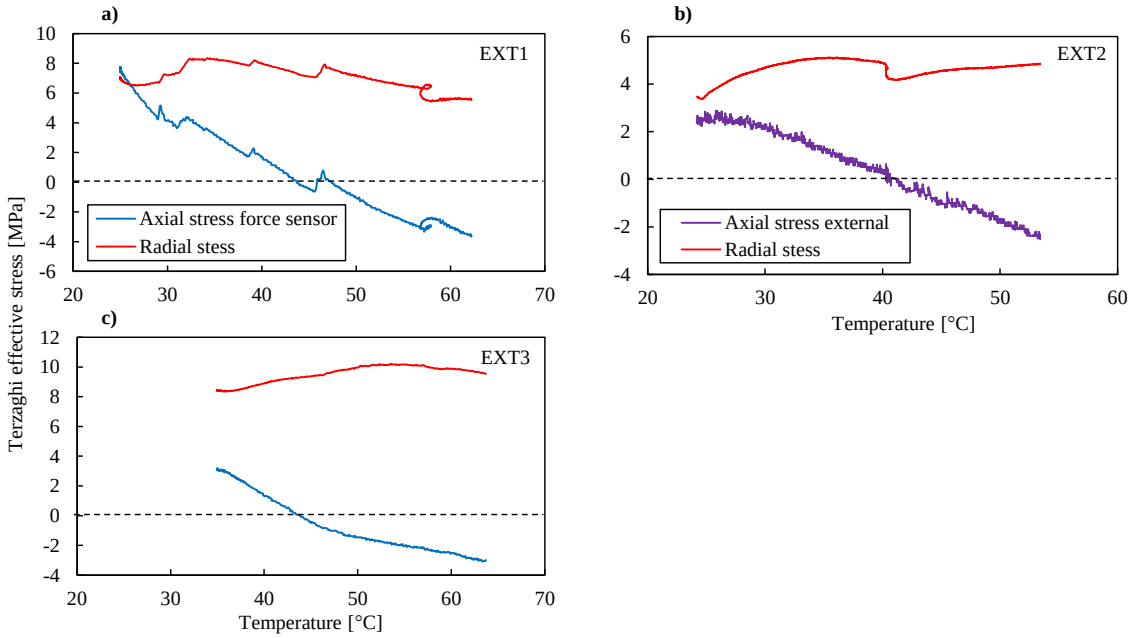


Fig. 6.3.: Terzaghi effective stresses during the heating test, where negative stresses represent effective tension; on specimen EXT2 the internal force sensor malfunctioned and we display stresses measured by the external transducer

conditions. The radial confining stress was controlled automatically, resulting in a steady stress increase, necessary to maintain radial deformations to zero.

Looking at the Terzaghi effective stresses plotted in Fig. 6.3, one can observe that the resulting radial effective stress, necessary to constrain lateral deformations, changed very little during the heating test. The axial effective stress however decreased significantly, due to the thermally induced pore pressure increase. Eventually, the axial effective stresses became negative, corresponding to effective tension. The specimens ultimately failed at effective stress values between -2.1 and -3.7 MPa. Together with the radial effective stress, we can plot the principal effective stress paths for each sample (Fig. 6.4). The axial effective failure stress appeared to be independent of the radial confining stress. A temperature dependency could not be observed in this study, due to the scarcity of results. Respective temperatures at failure are annotated in Fig. 6.4. These temperature values might however differ from the temperature under which failure is reached in perfectly undrained conditions. Due to some dead volume of the drainage system, the magnitude of induced pore pressure in the experiment can be different from those of an undrained REV. A correction of this effect is theoretically possible, but sensitive to uncertainties of both the testing device properties and the various transversely isotropic material properties involved. Axial and radial strains were recorded through the strain gages glued on the sample at mid-height (Fig. 6.5). In the tests EXT1 - EXT3 the strain readings show a constant zero value, confirming a successful lateral constraint. The stress strain path of EXT6, loaded under isothermal unconstrained conditions, is shown in Fig. 6.6. In this case, the radial strains are observed to be contracting. For EXT5, we cannot show sample strains, as the strain gage failed. Along

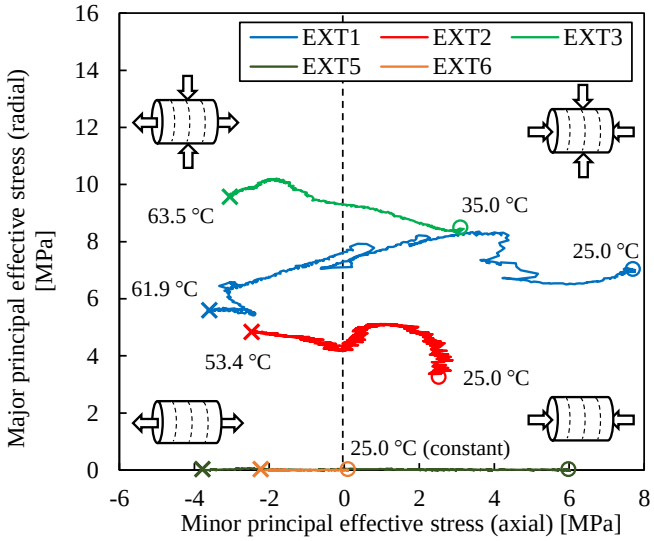


Fig. 6.4.: Principal (Terzaghi) effective stress paths for all specimens tested; circles indicate the initial stress state, while crosses mark the specimen failure with their respective temperature

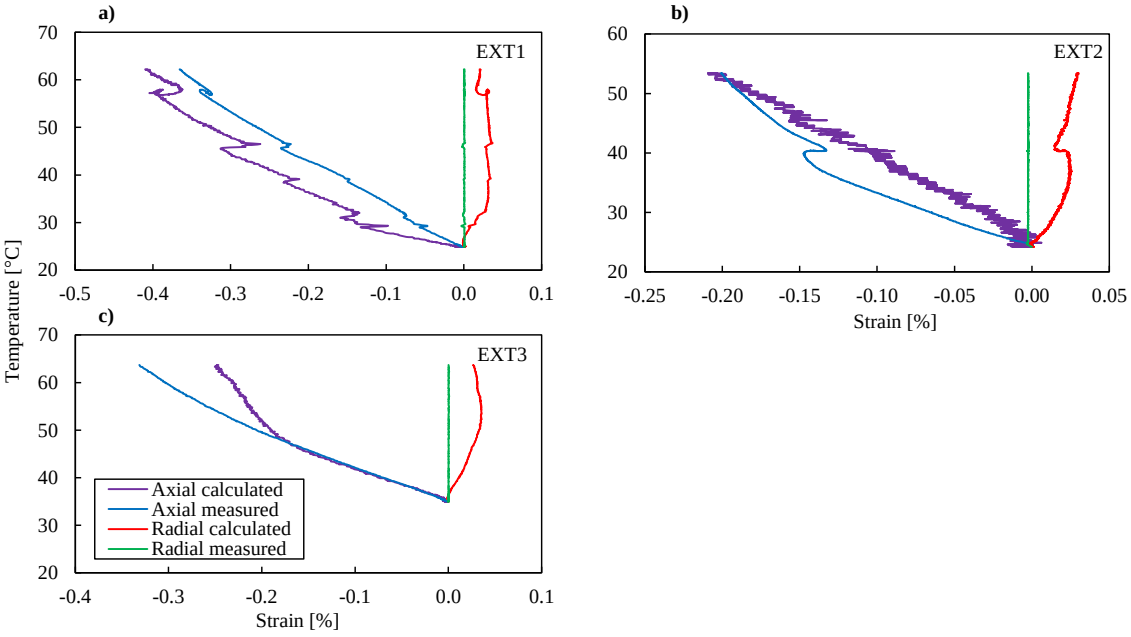


Fig. 6.5.: Temperature-strain measurements on the specimens during the heating tests, compared with calculated strains using a linear thermo-poroelastic model

the axial direction, we could observe extension strains up to -0.49 %, depending on the THM stress path. It is interesting to note, that a relatively brittle failure was observed, with fairly linear deformations before rupture. In Fig. 6.7a, we present the temperature-strain

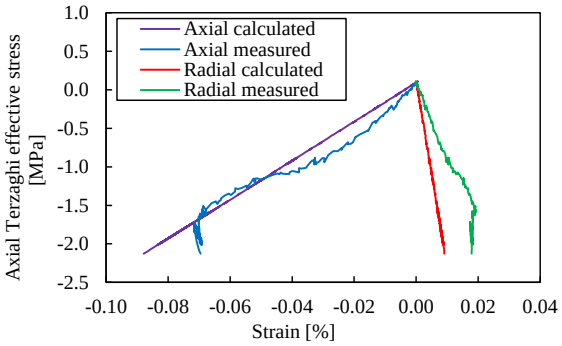


Fig. 6.6.: Stress-strain behaviour of specimen EXT6 tested under isothermal conditions

relationships for all thermally loaded specimens. The samples follow generally similar paths, which is also the case for strain changes with respect to effective axial stress (Fig. 6.7b).

The photos of Fig. 6.8 shows some examples of the failed specimens after unmounting from the triaxial apparatus. The fracture angles, with respect to the horizontal bedding planes (Fig. 6.8a), are listed in Tab. 6.1. Measured angles close to zero confirm the tensile failure mode of the generated fractures. We also note, that in three out of the five tested specimens we observed inclusions on the fracture surface, such as pyrite burrows or fossils (Fig. 6.8b). These heterogeneities could very probably correspond to locations for preferred fracture nucleation.

6.3 Discussion

Due to the complex nature of the transversely isotropic coupled THM behaviour, it is difficult to directly evaluate material parameters from the thermal extension test data. We could observe, that an increase of temperature in undrained conditions generated:

- An increase of pore pressure due to thermal pressurization
- An axial extension and an increase of radial stress due to constrained deformations
- An eventual failure, once the specimen reaches its tensile resistance

In the following, we use the measured behaviour to calibrate the parameters of a transversely isotropic THM model, adopting also values from previous chapters. The tensile failure is characterized with two different failure criteria and compared with the tensile properties of other weak rocks.

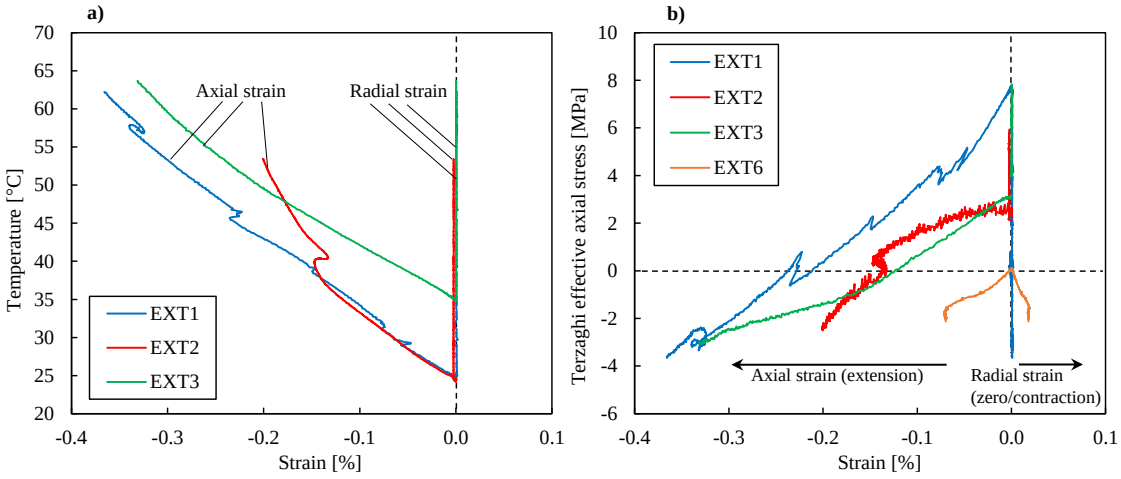


Fig. 6.7.: a) Temperature-strain relationship and b) axial effective stress-strain relationship compared for the tested specimens

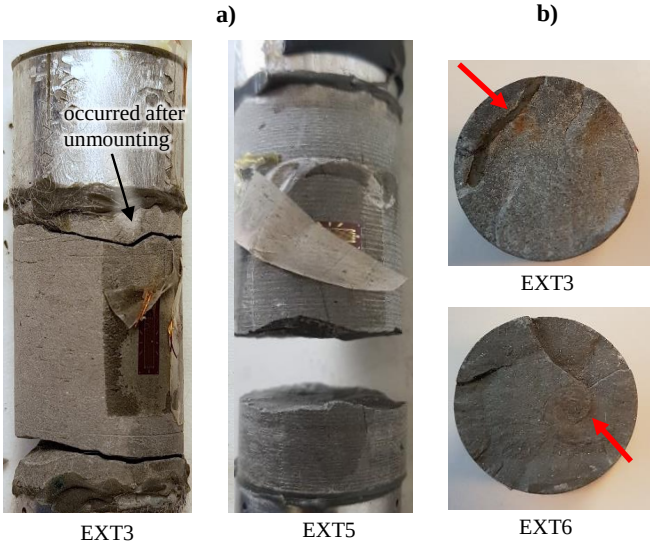


Fig. 6.8.: a) Samples after unmounting, with the induced tensile fractures; b) plan view of some fracture surfaces, showing natural heterogeneities in the material

Tab. 6.2.: Material properties adopted from Sec. 4 and Sec. 5, used to simulate measured strains in a coupled THM calculation

E_z [GPa]	E_h [GPa]	ν_{zh} [-]	ν_{hh} [-]	b_z [-]	b_h [-]	$\alpha_{d,z}$ $[10^{-5}\text{°C}^{-1}]$	$\alpha_{d,h}$ $[10^{-5}\text{°C}^{-1}]$	ϕ [-]
2.6	5.7	0.09	0.29	0.93	0.88	0.21	0.51	0.18

6.3.1 Thermo-poroelastic analysis

In this section, we described the observed claystone behaviour under extension within the thermo-poroelastic framework. To calibrate the model parameters, we can try to reproduce the measured strains in function of applied stresses, temperature and measured induced pore pressures. In Tab. 6.2 we show the adopted THM parameters.

Escoffier (2002) and Belmokhtar et al. (2017a) provided measurements for b close to 0.9, at effective stresses close to the *in situ* one (around 9 MPa). In Sec. 4, we estimated the Biot's coefficient also for lower effective levels, showing that b_z approaches 1.0 at effective stresses tending to zero. To analyse the experiments, carried out under mean effective stress conditions around 8 MPa, we chose therefore $b_z = 0.93$ and $b_h = 0.88$ (presented in Sec. 4 for this stress level). The Young's modulus E_z at 8 MPa mean effective stress was determined by Belmokhtar et al. (2018) with a value around 3 GPa, and at lower mean effective stress by Menaceur et al. (2015) and Zhang et al. (2012) with values around 1.0 and 1.5 GPa. For 8 MPa effective mean stress, we found a value $E_z = 2.6$ GPa (Sec. 4), which was adopted in this calculation. Less data was available for E_h and the Poisson ratios; we utilized $E_h = 5.7$ GPa and $\nu_{zh} = 0.09$ from Sec. 4 under 8 MPa effective stress. ν_{hh} was given by the Andra database (Guayacán-Carrillo et al., 2017) and confirmed in Sec. 4 as being equal to 0.29 (Tab. 6.2). We observed, that a variation of this parameter had minor effects on the calculated axial strains. Moreover, we assumed that all parameters are stress and temperature independent, which was sufficient for reproducing the measured strain response:

Using Eq. (2.2), one is able to calculate radial and axial strains, based on applied and measured stresses, pore pressure and temperature. The calculated strains for the thermal extension tests EXT1 - EXT3 and for the isothermal extension EXT6 are presented in Fig. 6.5 and 6.6. The calculations showed good results using the values reported from triaxial compression. We observe a good agreement between measurement and calculation of axial strains at the beginning of the loading paths for all tests. Close to failure, the calculations show a poorer agreement, but without distinctive over- or underestimation. Also, the simulated radial deformations show higher contraction in the case of EXT2 - EXT3 and lower contraction for EXT6, with respect to the measurements. This could be due to the natural variability of the specimens, to strain localization (measurements were done by local strain

gages), to induced damage or plastic deformations, which cannot be captured within the linear thermo-poroelastic model adopted in these calculations.

6.3.2 Failure criterion

Based on the stress state measured at tensile failure (Fig. 6.4), we extend an existing shear failure criterion of the COx claystone. A Mohr-Coulomb (MC) type failure criterion, constituted through uniaxial and triaxial compression tests on COx, is given by the Andra database (applied also by Guayacán-Carrillo et al., 2017). The criterion can be transformed to the principal effective stress domain, written as:

$$\sigma_1' = \frac{1+\sin\varphi}{1-\sin\varphi}\sigma_3' + \frac{2c\cos\varphi}{1-\sin\varphi} \tag{6.1}$$

where σ_1' and σ_3' are the major and minor principal effective stresses, respectively. Values for the cohesion $c = 5.9$ MPa and the friction angle $\varphi = 23°$ are taken from the Andra database, for the case of the minor effective stress perpendicular to the bedding plane. This shear failure criterion, displayed in Fig. 6.9, allows to determine an unconfined compressive strength $\sigma_c = \sigma_1'(\sigma_3' = 0) = 17.8$ MPa. One notes, that the Mohr-Coulomb criterion overestimates the measured strength in tension, and is therefore not applicable in this region.

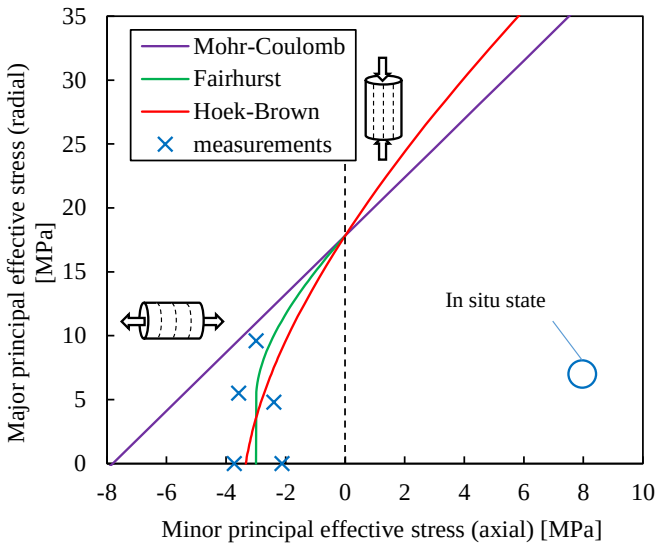


Fig. 6.9.: Hoek-Brown and Fairhurst's generalized Griffith criterion, adopted for measured tension failure with tension perpendicular to the bedding. The Mohr-Coulomb criterion is obtained from the Andra database, based on shear failure with a major principal stress parallel to bedding

Hoek and Brown (1980) and Hoek (1983) defined the Hoek-Brown failure criterion, proposed as an empirical relationship for rock shear failure under triaxial compressive stress, as follows:

$$\sigma_1' = \sigma_3' + \sigma_c\left(m_i\frac{\sigma_3'}{\sigma_c} + 1\right)^{0.5} \tag{6.2}$$

We fitted this criterion for the measured strength in tension. The shear failure region was not investigated here, however we adopt $\sigma_c = 17.8$ MPa from the Andra database. A single parameter m_i had to be fitted, carried out by minimising the sum of squared errors in terms of σ_3'. The best-fit, obtained with $m_i = 5.15$, is presented in Fig. 6.9.

As quoted by Hoek and Martin (2014), the Hoek-Brown can over-estimate the tensile strength of rocks with a low m_i value. Hoek and Martin (2014) suggested to utilize therefore the Fairhurst generalized Griffith fracture criterion (FG) (Fairhurst, 1964; Griffith, 1924) to predict tensile failure. This criterion can be applied in the form of a so-called "tension cutoff" under tensile stresses, combined with another criterion (e.g. Mohr-Coulomb or Hoek-Brown criterion) for shear stresses.

Fairhurst (1964) presented the FG criterion, which is here recalled according to Hoek and Martin (2014): If $w(w-2)\sigma_3' + \sigma_1' \leq 0$, failure occurs when:

$$\sigma_3' = \sigma_t \tag{6.3}$$

or when:

$$\sigma_1' = \frac{(2\sigma_3' - A\sigma_t)}{2} + \frac{\sqrt{(A\sigma_t - 2\sigma_3')^2 - 4\left(\sigma_3'^2 + A\sigma_t\sigma_3' + 2AB\sigma_t^2\right)}}{2} \tag{6.4}$$

where

$$\left.\begin{aligned} A &= 2(w-1)^2 \\ B &= \left[(w-1)/2\right]^2 - 1 \\ w &= \sqrt{\sigma_c/|\sigma_t| + 1} \end{aligned}\right\} \tag{6.5}$$

Combined with the MC or HB criterion described before, the major principal stress, where both criteria coincide at $\sigma_3' = 0$, is the unconfined compressive strength $\sigma_c = 17.8$ MPa. The remaining coefficient to be determined for the FG criterion is the tensile strength σ_t, that can be evaluated from laboratory measurements. Minimizing the least square error in terms of minor effective stress provided the best-fit value of σ_t = - 3.0 MPa (Fig. 6.9).

Both HB and FG criteria are able to satisfactorily characterize the tensile failure of the COx specimens. Both criteria can be adopted in combination with other criteria for shear failure, such as the MC criterion presented before. Note that the HB criterion, fitted for tensile failure, was observed to overestimate the shear failure characterized by a MC criterion from the Andra database.

6.3.3 Comparison with other shales

The behaviour of some soft rocks and shales has been investigated by various authors: Yang and Hsieh (1997) determined the tensile strength of a transversely isotropic claystone through direct tension tests. They evidenced a smaller tensile resistance for tension applied perpendicular to the plane of isotropy (~ -4 MPa) with respect to that measured on specimens loaded parallel to the plane of isotropy (~ -11.5 MPa). Interestingly, under tension loading, they found elastic material properties close to the values measured under compression (only the Young's modulus perpendicular to the plane of isotropy was detected to be higher in tension than in compression). They observed a quite linear stress-strain relationship under tension. Coviello et al. (2005) carried out various different types of tensile tests, to determine the strength of two types of weak rocks, Gasbeton and calcarenite. For calcarenite, they found the same tensile strength with both direct tensile test and brazilian test (~ -0.6 MPa). For Gasbeton, the strength measured with direct tension (~ -0.9 MPa) was higher than that measured in Brazilian tests (~ -0.5 MPa). They noted that for both materials, the Young moduli in tension and compression were about the same, with a very linear stress-strain behaviour until failure. In the work of Hansen and Vogt (1987), an overview of various shales is given with their unconfined compressive strength, elastic properties and tensile strength. These are compared in Tab. 6.3 with the data from Bossart and Thury (2008) on Opalinus clay and with the properties determined in this study on COx claystone.

Even though Perras and Diederichs (2014) concluded, that the estimation of the tensile strength σ_t from the unconfined compressive strength σ_c does not give accurate results, this ratio can be used to get a first estimation of the tensile resistance of brittle rocks. According to Diederichs (2007), one can estimate $-\sigma_t = \sigma_c/m_i$, where m_i is a material constant of the Hoek-Brown model. Hoek (2007) recommended an approximative value $m_i \sim 4.0 \pm 2$ for claystone. The calculated values $m_i = -\sigma_c/\sigma_t$ of some shales are presented in Tab. 6.3, confirming that calculated values are generally higher than the recommended value of 4.0 ± 2. For those clay rocks, the parameter m_i shows a rather large variability, with values between 6.5 and 13.6. One observes, that the fitted parameter m_i for COx claystone is found within the range of $m_i \sim 4.0 \pm 2$ (Hoek, 2007) and the estimated values for other shales. The measured tensile resistance of COx claystone is comparable to that of other shales, in the range of a few MPa.

The values obtained here by direct tension tests are somewhat higher than those presented by Auvray et al. (2015a), measured indirectly in Brazilian tests on COx. This could be due to the different testing methods adopted. The samples of Auvray et al. (2015a) were saturated under stress, but had to be deconfined for testing, which could result in some damage. Note also, that due to the small sample size adopted in this work, the specimens tested were prone to breakage during sample preparation. This could have caused an involuntarily reject

Tab. 6.3.: Shale characteristics adopted from the literature, with an estimation of the Hoek-Brown coefficient $m_i = -\sigma_c/\sigma_t$, compared with the experimental results of this study on COx claystone

Rock type	σ_c [MPa]	E [GPa]	ν [-]	σ_t [MPa]	m_i [-]
Pierre shale[1]	7.2	0.6	0.12	-0.5	13.6
Rhinestreet shale[1]	58.7	17.5	0.19	-8.4	7.0
Green river shale[1]	94.8	10.4	0.31	-11.9	8.0
Carlile shale[1]	22.8	3.3	0.16	-3.5	6.5
Colorado shale[2]	2.97	2.4	0.42	-0.4	6.9
Opalinus clay $\perp$ [3]	25.6	2.8	0.33	-2.0	12.8
Opalinus clay $\parallel$ [3]	10.5	7.2	0.24	-1.0	10.5
COx claystone $\parallel$	17.8[4]	5.7[5]	0.29[5]	-3.0[6]	5.15[6]

[1]Hansen and Vogt (1987),
[2]Mohamadi and Wan (2016), [3]Bossart and Thury (2008),
[4]Andra database, [5]this study, Sec. 4, [6]this study, Sec. 6

of less resistant or pre-fractured specimens, in such a way that predominantly resistant samples were tested.

Auvray et al. (2015a) did not note any significant change of tensile resistance on specimens tested at 90 °C temperature, neither could a temperature dependency be observed in this study, due to the scarcity of results.

6.4 Comparison with a numerical simulation

The significance and practicality of the thermal extension tests is demonstrated, by comparing the experimental stress paths with those from numerical simulation. Fig. 6.10 presents a compilation of the stress paths followed in the thermal extension device, the adopted failure criteria, and some selected stress paths from the numerical simulation. We chose here the reference calculation, with and without taking into account an anomalous thermal expansion coefficient of pore water. The stress paths are shown for a selected point at the symmetry boundary at the microtunnel level (point H4, see Fig. 4.19). We can observe, that the experimental stress paths followed well those that we obtained from numerical calculations. The paths show very little change in the major effective stress, together with a continuous decrease of the minor effective stress. The simulated stress paths stop at some point and revert, due to the combined effects of decreasing thermal load (the heating power of the exothermic waste decreases and the temperature stabilize around 60 °C, Sec. 4.4.2) and continuing pore pressure dissipation. We noted also before, that the value until which the simulated minor effective stress decreases, can be strongly dependent on some of the material parameters adopted. For instance, the minor effective stress decreases until around 1.0 MPa in the scenario with anomalous water expansion ($\eta\alpha_w$), compared to 2.5 MPa in the reference case. In both cases, we did not observe any tensile stresses. The test allowed

us to follow these stress paths, and to continue them, in order to explore the strength limit of the claystone.

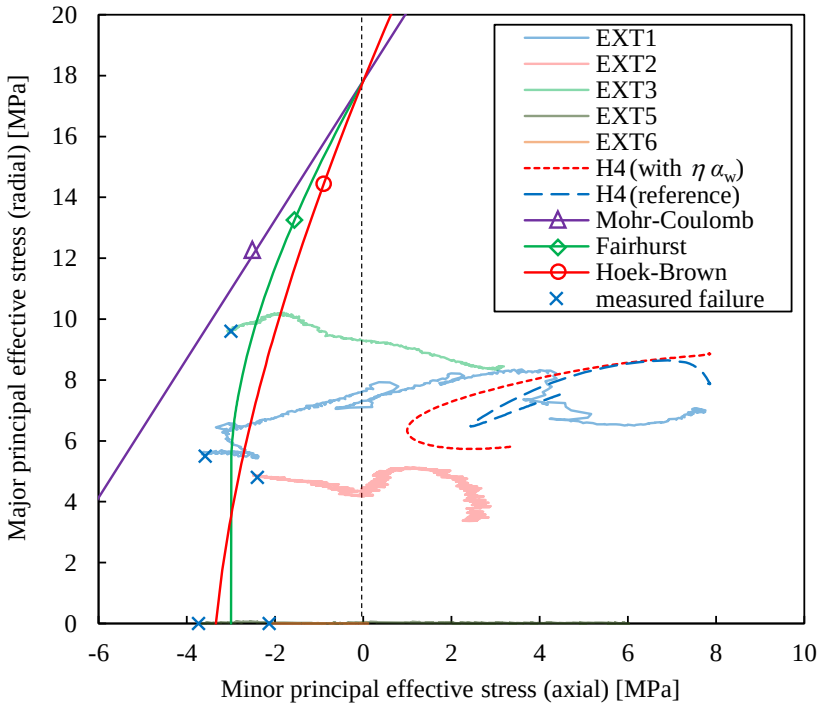


Fig. 6.10.: Compilation of the experimental stress paths and tensile failure, the fitted failure criteria, and the numerically simulated stress paths at point H4 (located 20 m horizontally from the microtunnel at the symmetry boundary). Numerical and experimental stress paths describe the same directions

6.5 Conclusions

The thermo-poro-mechanical response of the COx claystone was characterized in the laboratory, following specific *in situ* thermo-hydromechanic loading paths, expected in the COx formation between two microtunnels containing exothermic waste. These stress paths include an increase in pore pressure due to undrained heating, fairly constant axial overburden stress, and zero horizontal deformations due to the symmetric boundary conditions between two microtunnels. We used a novel triaxial apparatus, specially developed for these tension test, to generate axial effective tensile stresses on the specimens. During the tests we could control temperature, axial and radial stresses. Strains and induced pore pressures were recorded in parallel. Conditions of zero horizontal strain could be maintained by a servo-controlled confining pressure, which controlled automatically the lateral stress to control zero lateral strains.

Cylindrical specimens of 20 mm diameter and 30 - 40 mm height, cored perpendicular to the bedding plane, were tested in this device. We carried out undrained heating tests,

where the thermally induced pore pressures, combined with constant axial total stress, led eventually to effective axial tension and ultimately to failure. These tests were conducted under different lateral effective stresses. An average effective tensile strength of around - 3.0 MPa was observed. Additional specimens were submitted to pure hydro-mechanical loads without temperature changes, leading to a similar tensile material behaviour. We suggested a Hoek-Brown and a Fairhurst generalized Griffith criterion, fitted for the measured tensile resistance, which can be combined with other criteria established for shear failure.

During the laboratory tests, the induced pore pressures and generated strains were recorded. A linear thermo-poroelastic model for transversely isotropic materials was utilized to calculate the observed strains. We could show, that using previously measured parameters under compression (Sec. 4 and 5), we could satisfactorily reproduce the tensile behaviour. Using these THM parameters in the simplified repository model, we obtained the principal effective stress paths between two microtunnels. One could see, that the stress paths followed in the experiments mimicked well the numerical prediction.

7 Concluding remarks and perspectives

7.1 Conclusions

This work contributes to the extensive research carried out on the Callovo-Oxfordian claystone under the supervision of Andra. THM properties and failure criteria of the COx claystone are necessary parameters for the design of the high level waste repository, including the optimisation of the distance between the microtunnels containing the exothermic waste packages (Armand et al., 2017a).

COx claystone samples, extracted from the Bure Underground Research laboratory, were experimentally investigated to determine some material properties within the framework of transversely isotropic thermo-poro-elasticity. The measured properties were also used in a numerical model of simplified repository conditions. Thermal pressurization and stress changes between two heated microtunnels were simulated and analysed. Doing so, the significance of some model parameters was emphasized. More importantly, we simulated stress paths, corresponding to a decrease of minor effective stresses. For considering the potential failure under tensile effective stresses in a numerical model, a failure criterion had to be defined. This was achieved through the design and development of a novel triaxial extension apparatus. We were able to reproduce predicted *in situ* stress paths on samples in the laboratory, and to generate failure through thermally induced pore pressures.

The development of a novel triaxial apparatus was presented in detail. This device was specifically designed to carry out unconventional stress paths in the laboratory. Effective tension and failure can be generated through induced pore pressures (thermally or manually by a PVC). We can impose zero radial deformation by a servo-controlled confining pressure, while the axial stress is controlled and specimen strains recorded.

We proposed analytical solutions for the 1D pore pressure diffusion within a specimen under thermo-poro-mechanical loading. This provides a simple method for the evaluation of required experimental conditions, necessary to limit measurement errors. The effects of optimization of the loading rate, the loading level, the specimen geometry and the experimental device can be assessed. This aspect is particularly important for characterization of low permeability geomaterials, such as the COx claystone, for which THM experiments are generally very time consuming.

We presented new testing protocols, adapted for low permeable geomaterials. These are based on the fact, that true undrained conditions are generated under rapid loading, when pore pressure generation is much faster than dissipation. In these protocols, we apply a rapid loading, in the form of isotropic compression or heating, followed by a transient drainage phase until complete pore pressure dissipation. The procedure allows to determine multiple material parameters in one single test (4 directly measured material parameters a back-calculated permeability value). A correction of the initial undrained parameters is not required, and a completed drainage can be easily confirmed through the stabilization of deformations.

Hydromechanical experiments were carried out, to determine a large number of the coefficients required within a transversely isotropic material model. This includes isotropic compression tests, pore pressure tests, and deviatoric loading tests parallel and perpendicular to the bedding plane. We emphasized the adapted experimental devices and testing procedures, necessary to detect small strains under high pressures on a material which is sensitive to water and has a very low permeability. The performed experiments provided an overdetermined set of material parameters at different stress levels. Using all determined parameters in an optimization scheme, seven elastic coefficients and their effective mean stress dependency were characterized. In particular, we discovered a significant decrease of elastic stiffness with decreasing effective stress, which was observed to be reversible. In isotropic tests, the ratio between strains perpendicular and parallel to the bedding was found around 3.0. Under deviatoric loads, the Young modulus parallel to bedding was about 1.6 times higher than the one perpendicular to the bedding plane. A notably low Poisson ratio perpendicular to the bedding plane with values between 0.1 and 0.2 was evidenced. While the anisotropy of the back-calculated Biot coefficient was very low, an important anisotropy of the Skempton coefficient was computed. The importance of considering anisotropic properties has already been evidenced by Guayacán-Carrillo et al. (2017) in the response to drift excavation. Also for the THM behaviour around heated microtunnels, our numerical simulation indicated notable effects of the transversely isotropic stiffness. Under the considered geometry conditions, the stiffness perpendicular to bedding was observed to have more influence on the thermal pressurization. The experimentally determined decrease of elastic stiffness with decreasing mean effective stress can be considered in applications, where unloading is occurring. The material becomes more compliant generating larger deformations. For the scenario of heated microtunnels, this effect was however negligible, as the effective mean stress did not change significantly in the far field.

A second series of experiments was carried out to characterize the THM response to temperature changes. To this end, COx claystone samples were tested in a temperature controlled, high pressure isotropic loading cell, which allows to apply stress conditions close to the *in situ* ones. Thermal loads were exerted on the specimens along different heating and cooling paths. A temperature corrected strain gage system provided precise measurements of the anisotropic strain response of the specimens. Drained and undrained thermal expan-

sion coefficients in both transversely isotropic directions were determined. We detected reversible drained thermal strains parallel to the bedding plane, along heating and cooling paths up to 90 °C. Along perpendicular direction, thermal contraction was observed upon heating, which appeared to be irreversible. During cooling, the material contracted in both directions, with strains parallel to bedding about 2.4 times higher than perpendicular to bedding. A relatively small reversible volumetric drained thermal expansion coefficient $\alpha_d = 1.23 \times 10^{-5} \mathrm{°C}^{-1}$ was found. In a sensitivity analysis, as well as in the numerical simulation, it was shown that a variation of the drained thermal expansion coefficients had negligible effects on the induced pore pressures. The possibility of an anomalous thermal expansion coefficient of pore water in geomaterials has been discussed by various authors (Baldi et al., 1988 on low porosity clays, Derjaguin et al., 1992 on silica gel, Xu et al., 2009 on silica glasses, Valenza and Scherer, 2005 and Ghabezloo et al., 2009b on hardened cement paste and Monfared et al., 2011a on Opalinus clay). Using this assumption, we were able to reproduce the measured undrained thermal expansion coefficient and the measured thermal pressurization coefficient in a thermo-poroelastic framework. The measured and theoretically calculated thermal pressurization coefficient Λ was found to be stress and temperature dependent. Adopting these dependencies in a thermo-poroelastic framework, we were able to reproduce observations made by Mohajerani et al. (2012) under different effective stress conditions. This compatibility gives confidence in the evaluated THM properties. Moreover, we observed that utilizing an anomalous thermal expansion coefficient of pore water in the numerical model resulted in higher pore pressures and lower effective stresses, closer to tensile failure.

To characterise the behaviour of the COx claystone under effective tension, and to quantify the tensile failure criterion, a special triaxial system was developed. This apparatus allowed to control independently radial and axial stresses, as well as pore pressure and temperature of the claystone specimens. More importantly, the device allowed to maintain an axial effective tension on a specimen. Saturated cylindrical claystone specimens were heated in undrained conditions, under constrained null lateral deformation and constant axial stress. We recreated THM loading paths in the laboratory, which corresponded well to those obtained by numerical simulation. The specimens were heated, until thermally induced pore pressures created effective tensile stresses and ultimately fractured the material, at axial effective stresses around - 3.0 MPa. Fracturing under different lateral total stresses allowed to describe the failure with a Hoek-Brown or a Fairhurst's generalized Griffith criterion. Measured axial extension strains were analysed, based on our previously evaluated linear transversely isotropic thermo-poroelastic properties. This model was able to satisfactorily reproduce the observed behaviour, confirming the set of determined THM parameters and their validity under effective tension.

7.2 Perspectives

In this work we characterized the THM behaviour of COx claystone through element tests and unconventional stress paths until failure. Various questions arose during this work, indicating subjects for possible future studies:

We observed a mean effective stress dependency of elastic properties, which had however minor effects in the numerical application. This was due to small changes of mean effective stresses between the microtunnels. Deviatoric stresses were observed to change more significantly at this location. Further experimental investigations could help to characterize a potential dependency on deviatoric stress, as recently indicated by Zhang et al. (2019). Considering this dependency in the numerical application would most likely result in larger stiffness changes.

Even though the thermal volume changes of the solid skeleton were observed to be of minor influence in the numerical application, further studies could shed light on the observed thermoplastic and anisotropic thermal characteristics and on their microstructural origins. Moreover, specific experimental protocols could allow to describe the material within a thermoplastic material model (Hueckel and Baldi, 1990).

The presented experiments were conducted in timescales in the order of days and weeks, whereas one has to consider durations up to some thousands of years *in situ*. Possible time dependent effects involved in the thermal pressurization phenomenon could be further clarified in the laboratory.

Few permeability measurements were presented in this study, carried out through back analysis of hydromechanical and thermal tests. Further analysis of our experimental data will provide permeability values at different stress levels and at various temperatures. Moreover, we are currently involved in a benchmarking programme for permeability measurements, led by Andra. Different participating laboratories are measuring the permeability of COx claystone samples, following the same protocol. This aims to identify effects of measurement methods and sample variability on permeability estimations. Clarifying the reasons for the large difference between *in situ* and in the laboratory detected permeabilities is another perspective.

New insights on the THM fracturing behaviour will be provided by an *in situ* test (CRQ) at the Bure URL, planned to start in the following months (Conil et al., 2017). The aim of this experiment is to heat the rock until pore pressures exceed the vertical stress and eventually create fractures. It will be accompanied by pore pressure measurements, permeability tests and acoustic measurements. After the test, additional geomechanical tests will be carried out on the boreholes, characterizing deformations, created fractures, and extracting samples for

laboratory experiments. It becomes clear, that the CRQ test represents the *in situ* equivalent to the laboratory experiments presented in this work. Findings of both experimentations should be able to complement each other and give new information on the coupled THM behaviour under limit thermal loading. Moreover, the experimental methods developed in this study provide tools for possible future investigations on specimens extracted from the CRQ zone.

Further investigations on the fractured specimens are planned in form of a collaboration with L. Ponson and M. Abdulmajid from Institut Jean le Rond d'Alembert, UPMC, Paris. They use the method of Vernde and Ponson (2014), to conduct post-mortem analysis of the fracture surface at the micro-scale, giving information on the fracture process zone and its toughness. This data could be combined with the macro measurements, obtained in our study, to better understand the fracturing process at different scales.

To further study the fracture mechanisms, additional THM extension experiments can be conducted. This could help to capture the natural variability of samples, check possible temperature and stress dependencies, and investigate possible time dependent characteristics. Experiments on large specimens could help to identify size effects of the samples. It could be interesting to carry out classical tension tests, such as direct tension or Brazilian tests. The developed extension apparatus also permits to carry out isothermal hydraulic fracturing experiments. Comparing the resistance and behaviour under tensile stresses created through different mechanisms, this could contribute to the characterization of the material.

New adaptations and improvements of the experimental device could include the integration of acoustic emission sensors, or the measurement of wave velocities. Image analysis by the means of CT-scans before and after failure could give insights on the location of failure within the specimens, with the possible formation of extension bands (Rudnicki, 2002). This is difficult to carry out on claystone samples, which are prone to volume changes due to deconfining. Developing an adapted device, which permits to confine a specimen during scanning, could enable further studies in this regard.

Appendix

A

A.1 Calculation of time dependent pore pressure distribution

Assuming a fluid flow governed by Darcy's law, the pressure change in porous media can be described through Eq. (3.16). The pressure change is therefore dependent on the pressure gradient and a volumetric pressure source q:

$$q = B\frac{\mathrm{d}\sigma}{\mathrm{d}\theta} + \Lambda\frac{\mathrm{d}T}{\mathrm{d}\theta} = \tau_v \left(Bv_\sigma + \Lambda v_T\right) \tag{A.1}$$

Considering a domain of the length $2H_d$, the pore pressure diffusion problem can hence be described as a function of dimensionless time θ and dimensionless length Z:

$$\frac{\mathrm{d}p_f}{\mathrm{d}\theta} = \frac{\partial^2 p_f}{\partial Z^2} + q \tag{A.2}$$

$$p_f(0,\theta) = p_f(2,\theta) = v_p\tau_v\theta, \qquad \text{for} \quad \theta > 0 \tag{A.3}$$

$$p_f(Z,0) = 0, \text{for} \quad 0 < Z < 2 \tag{A.4}$$

The pore pressure is initially equal to zero over the specimen length, whereas it is controlled at the specimen ends is using a certain pore pressure loading rate v_p. In the following this problem is solved in the same way as it was described in detail for heat diffusion with sources by Hancock (2006), Guenther and Lee (1996), and Myint-U and Debnath (2007). We have to find an equilibrium solution $u_E(Z)$ that satisfies the PDE and the BCs:

$$0 = \frac{\partial^2 u_E}{\partial Z^2} + q \tag{A.5}$$

$$u_E(0) = 0, \qquad u_E(2) = 0, \qquad \text{for} \quad \theta > 0 \tag{A.6}$$

We define $u(Z,\theta)$ as:

$$u(Z,\theta) = p_f(Z,\theta) - u_E(Z) \tag{A.7}$$

Substituting $u_E(Z,\theta)$ from the above relation, we obtain:

$$\frac{\mathrm{d}u}{\mathrm{d}\theta} = \frac{\partial^2 u}{\partial Z^2} \tag{A.8}$$

$$u(0,\theta) = u(2,\theta) = v_p \tau_v \theta, \qquad \text{for} \quad \theta > 0 \tag{A.9}$$

$$u(Z,0) = -u_E(Z), \qquad \text{for} \quad 0 < Z < 2 \tag{A.10}$$

To solve a diffusion equation with time dependent boundary conditions, such as $u(Z,\theta)$, Carslaw and Jaeger (1959)(p. 103) propose the following analytical solution for u_c over the length $0 < x < L$, the time t (with $\frac{\mathrm{d}u_c}{\mathrm{d}t} = \kappa \frac{\partial^2 u_c}{\partial x^2}$, where κ is the diffusion coefficient, $\phi_1(t)$ and $\phi_2(t)$ are the boundary conditions for $u_c(0,t)$ and $u_c(L,t)$ respectively, and $f(x)$ is the initial distribution of $u_c(x,0)$):

$$u_c(x,t) = \frac{2}{L} \sum_{n=1}^{\infty} e^{-\kappa n^2 \pi^2 t / L^2} \sin\left(\frac{n\pi x}{L}\right) \times \left[\int_0^L f(x') \sin\left(\frac{n\pi x'}{L}\right) dx' + \frac{\kappa n \pi}{L} \int_0^t e^{\kappa n^2 \pi^2 \lambda / L^2} \left(\phi_1(\lambda) - (-1)^n \phi_2(\lambda)\right) d\lambda \right] \tag{A.11}$$

To obtain the solution for $u(Z,\theta)$, we insert $L = 2$, $\kappa = 1$ into Eq. (A.11) and replace t with θ and x with Z. For the boundary conditions we can insert $\phi_1(\lambda) = \phi_2(\lambda) = v_p \tau_v \lambda$ and $f(x') = -u_E(x')$.

$$u(Z,\theta) = \sum_{n=1}^{\infty} e^{-n^2 \pi^2 \theta / 4} \sin\left(\frac{n\pi Z}{2}\right) \times \left[\int_0^2 -u_E(x') \sin\left(\frac{n\pi x'}{2}\right) dx' + \frac{n\pi}{2} \int_0^\theta e^{n^2 \pi^2 \lambda / 4} v_p \tau_v \lambda \left(1 - (-1)^n\right) d\lambda \right] \tag{A.12}$$

The first integral in in Eq. (A.12) can be solved by partial integration:

$$\begin{aligned} &\int_0^2 -u_E(x') \sin\left(\tfrac{n\pi x'}{2}\right) dx' \\ &= \left[\tfrac{2}{n\pi} u_E(x') \cos\left(\tfrac{n\pi x'}{2}\right)\right]_0^2 - \int_0^2 \tfrac{2}{n\pi} \left(\tfrac{\partial^2 u_E(x')}{\partial x'^2}\right) \cos\left(\tfrac{n\pi x'}{2}\right) dx' \end{aligned} \tag{A.13}$$

The first term in the right hand side of Eq. (A.13) disappears because of the boundary conditions $u_E(0) = u_E(2) = 0$. Partial integration applied on the remaining second term gives:

$$\begin{aligned} &\int_0^2 -u_E(x') \sin\left(\tfrac{n\pi x'}{2}\right) dx' \\ &= -\left[\left(\tfrac{2}{n\pi}\right)^2 \left(\tfrac{\partial u_E(x')}{\partial x'}\right) \sin\left(\tfrac{n\pi x'}{2}\right)\right]_0^2 + \left(\tfrac{2}{n\pi}\right)^2 \int_0^2 \left(\tfrac{\partial^2 u_E(x')}{\partial x'^2}\right) \sin\left(\tfrac{n\pi x'}{2}\right) dx' \end{aligned} \tag{A.14}$$

Here the first term of Eq. (A.14) vanishes, as $sin(n\pi) = 0$. From Eq. (A.5) we can insert

$$\partial^2 u_E(x') \Big/ \partial x'^2 = -q$$

to obtain:

$$\int_0^2 -u_E(x') \sin\left(\frac{n\pi x'}{2}\right) dx' = q\left(\frac{2}{n\pi}\right)^3 \left[\cos(n\pi) - 1\right] \tag{A.15}$$

It can be seen that Eq. (A.15) becomes non-zero only for odd values of n. Note also that the second integral in Eq. (A.12) is non-zero only for odd values of n. For this reason the variable n is replaced by $(2n-1)$ and we introduce:

$$m = frac(2n-1)2\pi \tag{A.16}$$

Eq. (A.12) can then be rewritten to:

$$u(Z,\theta) = \sum_{n=1}^{\infty} e^{-m^2\theta} \sin(mZ) \left[-\frac{2q}{m^3} + 2v_p\tau_v m \int_0^{\theta} e^{m^2\lambda}\lambda d\lambda\right] \tag{A.17}$$

The remaining integral in Eq. (A.17) can be solved by partial integration. We also make use of the relationship $\sum_{n=1}^{\infty} \frac{1}{m} \sin(mZ) = \frac{1}{2}$, giving:

$$u(Z,\theta) = -2\sum_{n=1}^{\infty} e^{-m^2\theta} \sin(mZ)\, q\frac{1}{m^3} + 2\sum_{n=1}^{\infty} \left(e^{-m^2\theta} - 1\right) \sin(mZ)\, v_p\tau_v \frac{1}{m^3} + v_p\tau_v\theta \tag{A.18}$$

From the initial condition at $\theta = 0$ we know that:

$$u(Z,0) = -u_E(Z) = -2\sum_{n=1}^{\infty} \sin(mZ)\, \frac{q}{m^3} \tag{A.19}$$

This allows us to write down the final analytical solution for p_f, using Eq. (A.7), (A.18) and (A.19):

$$p_f(Z,\theta) = 2\left(Bv_\sigma + \Lambda v_T - v_p\right)\tau_v \sum_{n=1}^{\infty} \left[\left(1 - e^{-m^2\theta}\right)\frac{1}{m^3}\sin(mZ)\right] + v_p\tau_v\theta \tag{A.20}$$

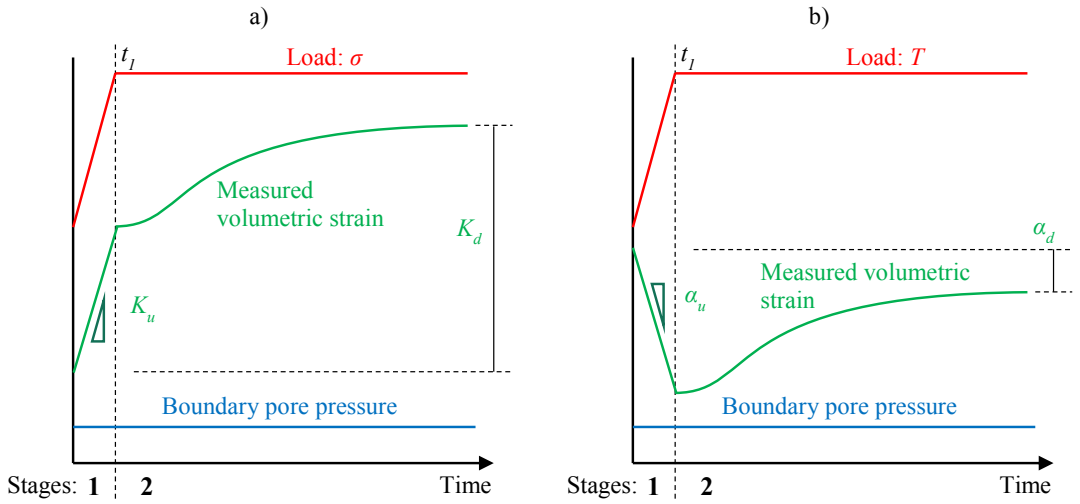


Fig. A.1.: Two-stage loading protocol and schematic volumetric response for a) mechanical tests and b) thermal test

A.2 Alternative two-stage loading protocol

An alternative loading protocol, similar to the three-stage protocol, but without the second stage, is presented in the following, together with two application examples. Rapid loading is applied in the first stage, where K_u or α_u are determined from the measured strains. The excess pore pressure starts then directly to dissipate. The specimen subsequently reaches hydraulic equilibrium once the monitored strains stabilise with time. From the strains measured at final equilibrated drained state, one can obtain the drained bulk compression modulus K_d or the drained volumetric thermal expansion coefficient α_d, respectively. The loading procedure is schematically presented in Fig. A.1, and the corresponding (undrained/drained) compression moduli and thermal expansion coefficients are also represented (note that the magnitude and directions of applied loading and resulting strains are indicative). A back analysis of the permeability based on observed transient deformations is carried out using the analytical diffusion solution [Eq. (3.51) - (3.59)]. The applied loading rates for the two-stage protocol are $v_{\sigma,0}$ in phase 1 and $v_{\sigma,1} = 0$ in phase 2 for a compression test ($v_{T,i} = v_{p,i} = 0$). In a thermal test ($v_{\sigma,i} = v_{p,i} = 0$) we apply $v_{T,0}$ in phase 1 and $v_{T,1} = 0$ in phase 2. The time t_1 at which monotonic loading is stopped is calculated with the applied load increment ($\Delta\sigma$ or ΔT) with $t_1 = \Delta\sigma/v_{\sigma,0}$ or $t_1 = \Delta T/v_{T,0}$ respectively.

The model parameters for the analytical description of the two-stage test are given in Tab. A.1. In addition to the parameters which are measured directly, K_s is required for simulating a mechanical test and K_d, H and K_u for simulating a thermal test. Having only k left as an unknown parameter, it can be back-calculated by fitting the calculated transient deformation to the experimental result.

Tab. A.1.: Input material parameters for the analytical simulation of two-stage THM tests

Load type:	Mechanical	Thermal
Measured parameters:	K_u K_d	α_u α_d
Unknown parameters for permeability back-analysis:	k K_s	k K_d K_u H

A.2.1 Two-stage compression test

In the compression experiment on the COx specimen 3, the confining pressure was increased from 12 to 13 MPa, with a loading rate of $v_{\sigma,0} = 6$ MPa/h, (Fig. A.2a,b). The drainage system was always opened with a imposed pore pressure of 4 MPa, effecting a progressive drainage, which was supposed to be completed when measured strains stabilized after 24 h. From the measured strains we obtain a tangent $K_u = 16.3$ GPa and a secant $K_d = 2.0$ GPa (Fig. A.2c). The analytical solutions presented before permit to simulate the step loading path carried out on the COx specimen (Figure 13). We can use a series of Heaviside functions [Eq. (3.57)] to calculate the pore pressure distribution generated through a loading sequence of different rates. We insert $p_{init} = 4$ MPa, $v_{\sigma,0} = 6$ MPa/h, $t_1 = 10$ min, $v_{\sigma,1} = 0$ MPa/h, $v_{T,i} = 0$, $H_d = 10$ mm and $z = h_g = 6$ mm. The calculated strains were then fitted to the experimental result with a minimum least square error. Two additional parameters are required, the permeability as the fitting parameter and the unjacketed modulus K_s, which was assumed with a value $K_s = 20$ GPa Belmokhtar et al. (2017a). The best fit shown in Fig. A.2 was then found with a permeability of $k = 1.56 \times 10^{-21}$ m^2 and a characteristic time $\tau_v = 8.2$ h.

A.2.2 Two-stage heating test

A drained heating experiment was carried out on COx specimen 4. The specimen had a height of 10 mm and the strain gages were fixed at a height of 6 mm. The applied pore pressure was always held constant with valve V1 open. The cell was heated up from 25 to 35 °C within one hour, which was the fastest applicable rate by the heating system (Fig. A.3a). The temperature-strain curve in Fig. A.3b provides the two thermal expansion coefficients. From the tangent of the strain in the rapid heating phase, $\alpha_u = 1.15 \times 10^{-4}$ °C^{-1} could be measured. The parameter $\alpha_d = 0.52 \times 10^{-4}$ °C^{-1} was determined as a secant on the strains after drained steady state was reached, after about 15 h. The isotropic heating test was then simulated in the thermo-poro-elastic framework. In contrary to the perfectly linear pressure control during mechanical tests, the temperature control cannot change its rate v_T abruptly. A series of several Heaviside functions with v_T changing gradually is necessary to describe the applied heating (Fig. A.3a). Using the two thermal expansion coefficients

measured, together with three poroelastic parameters measured in the three-stage test (K_d = 2.52 GPa, H = 2.65 GPa, K_u = 13.03 GPa), we can calculated specimen strains under thermal loading. The fitting parameter k = 1.43 $\times 10^{-21}$ m^2 was obtained by reducing the least square error between experimental results and the simulation (Fig. A.3b,c,d). A review of the obtained parameters in this thermal test is given in Tab. A.2.

Tab. A.2.: Best-fit results and input parameters

Input parameters		
H_d	[mm]	10.0
h_g	[mm]	6.0
K_d	[GPa]	2.52
H	[GPa]	2.65
K_u	[GPa]	13.03
α_u	[10^{-4} °C^{-1}]	1.15
$\alpha_d = \alpha_\phi$	[10^{-4} °C^{-1}]	0.52
Fitted parameter		
k	[10^{-21} m^2]	1.43

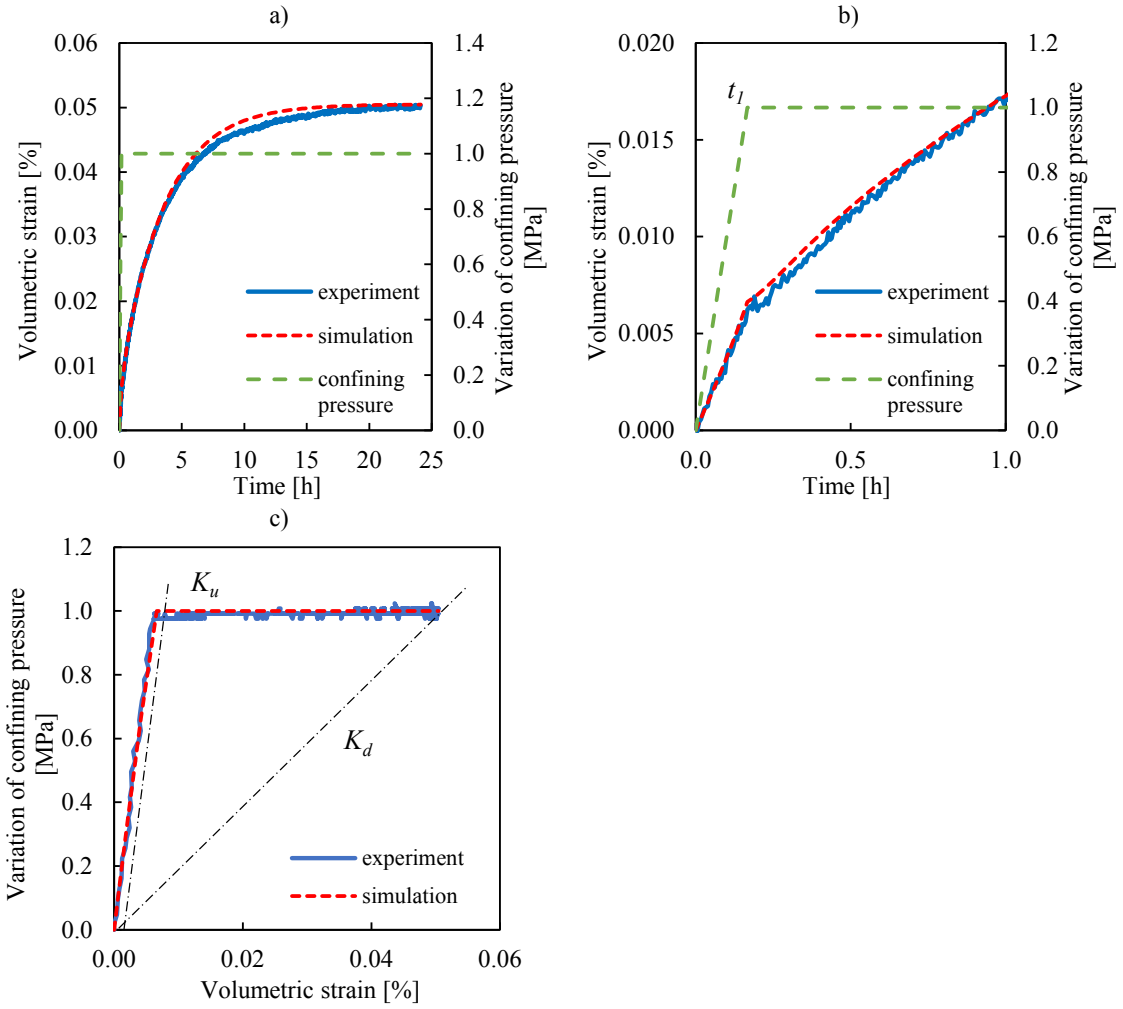


Fig. A.2.: Drained compression test and fitted simulation with a) applied load and specimen strains over time, b) zoom on a), c) stress-strain behaviour

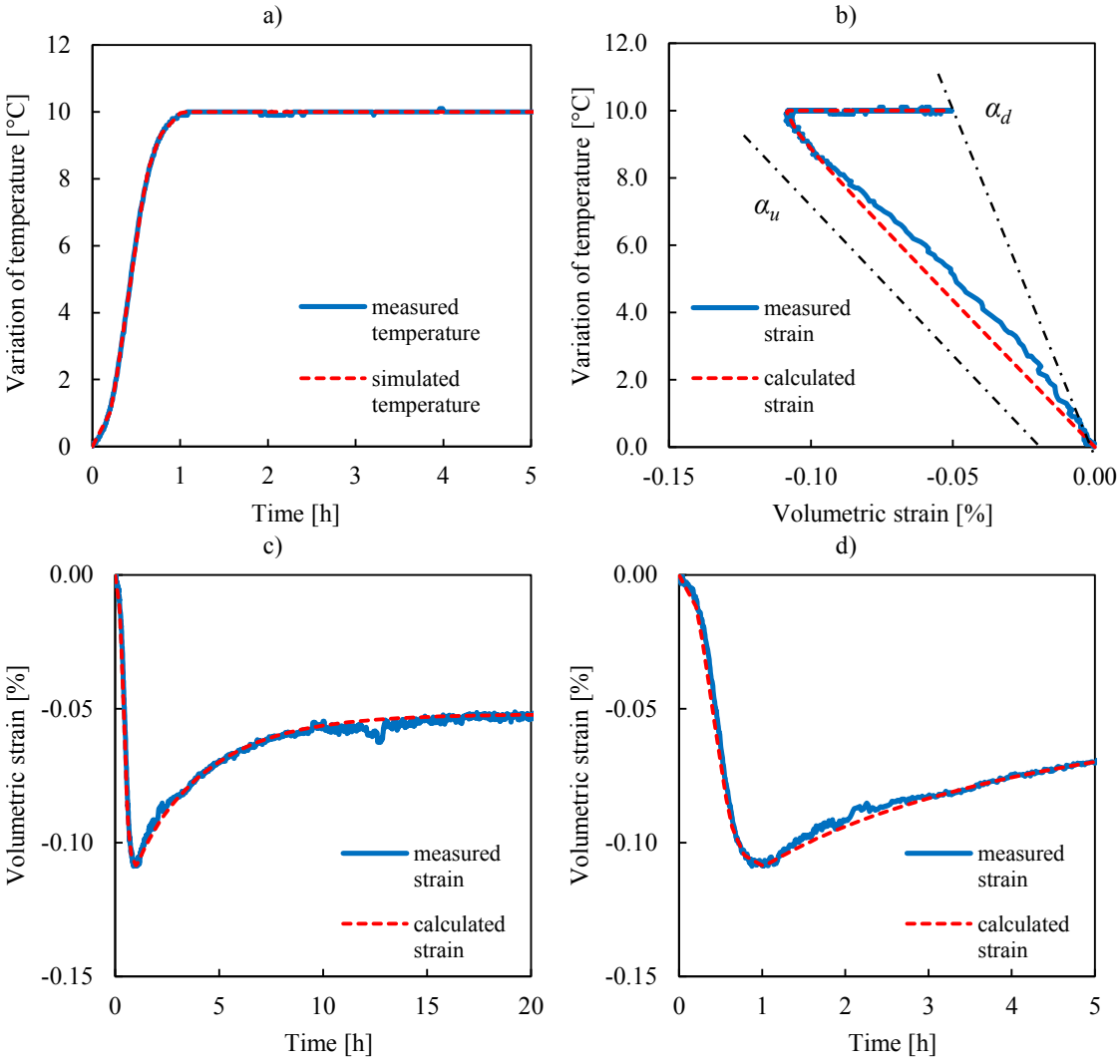


Fig. A.3.: Drained heating test and fitted simulation with a) applied load, b) temperature-strain curve, c) time evolution of strains, d) zoom on c)

Bibliography

Abuel-Naga, H. M., Bergado, D. T., and Bouazza, A. (2007). „Thermally induced volume change and excess pore water pressure of soft Bangkok clay“. In: *Engineering Geology* 89.1-2, pp. 144–154 (cit. on pp. 4, 30).

Aichi, M. and Tokunaga, T. (2012). „Material coefficients of multiphase thermoporoelasticity for anisotropic micro-heterogeneous porous media“. In: *International Journal of Solids and Structures* 49.23-24, pp. 3388–3396 (cit. on pp. 11, 12).

Andra (2005). *Dossier 2005 Argile: Evaluation of the feasibility of a geological repository in an argillaceous formation*. http://www.andra.fr/international/download/andra-international-en/document/editions/266va.pdf (cit. on pp. 1–4, 6, 18, 66, 114).

Armand, G., Dewonck, S., Bosgiraud, J.-M., and Richard-Panot, L. (2015). „Development and new research program in the Meuse Haute-Marne Underground Research Laboratory (France)“. In: *13th ISRM International Congress of Rock Mechanics*. Montreal (cit. on p. 3).

Armand, G., Bumbieler, F., Conil, N., de la Vaissière, R., Bosgiraud, J. M., and Vu, M. N. (2017a). „Main outcomes from in situ thermo-hydro-mechanical experiments programme to demonstrate feasibility of radioactive high-level waste disposal in the Callovo-Oxfordian claystone“. In: *Journal of Rock Mechanics and Geotechnical Engineering* 9.3, pp. 415–427 (cit. on pp. 5, 28, 165).

Armand, G., Conil, N., Talandier, J., and Seyedi, D. M. (2017b). „Fundamental aspects of the hydromechanical behaviour of Callovo-Oxfordian claystone: From experimental studies to model calibration and validation“. In: *Computers and Geotechnics* 85, pp. 277–286 (cit. on pp. 3, 18, 20).

Auvray, C., Grigc, D., and Homand, F. (2005). *Essais thermo-mecaniques ouvrage TER1301. Andra report C.RP.0ENG.05-0378*. Tech. rep. (cit. on p. 29).

Auvray, C., Giot, R., and Giraud, A. (2015a). *Caractérisation géomécanique sur échantillons - Essais de traction indirecte, Andra report*. Tech. rep., p. 49 (cit. on pp. 160, 161).

Auvray, C., Morlot, C., Fourreau, E, and Talandier, J (2015b). „X-Ray Tomography Applied to Self-Healing Experiments on Argillites“. In: *13th ISRM International Congress of Rock Mechanics* (cit. on p. 18).

Baldi, G., Hueckel, T., and Pellegrini, R. (1988). „Thermal volume changes of the mineral–water system in low-porosity clay soils“. In: *Canadian Geotechnical Journal* 25.4, pp. 807–825 (cit. on pp. 4, 5, 30, 32, 140, 167).

Bauer, C., Plas, F., Su, K., and Landais, P. (2004). *LA CHARGE THERMIQUE D'UN STOCKAGE - Site de Meuse / Haute-Marne, Andra report C.NT.ASIT.03.118*. Tech. rep. (cit. on p. 114).

Belmokhtar, M., Delage, P., Ghabezloo, S., Tang, A.-M., Menaceur, H., and Conil, N. (2017a). „Poroelasticity of the Callovo-Oxfordian Claystone“. In: *Rock Mechanics and Rock Engineering* 50.4, pp. 871–889 (cit. on pp. 13, 23–25, 36, 40, 51–53, 66, 81, 96, 99, 104, 108, 129, 140, 151, 157, 175).

Belmokhtar, M., Delage, P., Ghabezloo, S., and Conil, N. (2017b). „Thermal Volume Changes and Creep in the Callovo-Oxfordian Claystone“. In: *Rock Mechanics and Rock Engineering* 50.9, pp. 2297–2309 (cit. on pp. 4, 30, 40, 66, 73, 134, 139).

Belmokhtar, M., Delage, P., Ghabezloo, S., and Conil, N. (2018). „Drained Triaxial Tests in Low-Permeability Shales: Application to the Callovo-Oxfordian Claystone“. In: *Rock Mechanics and Rock Engineering* 51.7, pp. 1979–1993 (cit. on pp. 25–27, 104, 157).

Bemer, E., Longuemare, P., and Vincké, O. (2004). „Poroelastic parameters of Meuse/Haute Marne argillites: Effect of loading and saturation states“. In: *Applied Clay Science* 26, pp. 359–366 (cit. on pp. 22, 23).

Biot, M. A. and Willis, D. G. (1957). „The Elastic Coefficients of the Theory of Consolidation“. In: *Journal of Applied Mechanics* 24, pp. 594–601 (cit. on p. 9).

Bishop, A. W. (1976). „The influence of system compressibility on the observed pore-pressure response to an undrained change in stress in saturated rock“. In: *Géotechnique* 26.2, pp. 371–5 (cit. on pp. 42, 52, 63, 73, 76, 77, 83).

Blaise, T., Barbarand, J., Kars, M., et al. (2014). „Reconstruction of low temperature (<100 °C) burial in sedimentary basins: A comparison of geothermometer in the intracontinental Paris Basin“. In: *Marine and Petroleum Geology* 53, pp. 71 –87 (cit. on p. 30).

Bobich, J. K. (2005). „Experimental analysis of the extension to shear fracture transition in Berea sandstone“. PhD thesis (cit. on p. 48).

Bossart, P. and Thury, M. (2008). „Mont Terri Rock Laboratory. Project, programme 1996 to 2007 and results. Wabern: Reports of the Swiss Geological Survey“. In: *Mont Terri Project, Wabern Switzerland.* 3 (cit. on pp. 160, 161).

Brace, W. F. (1964). „Brittle fracture of rocks“. In: *State of stress in the Earths Crust*, pp. 111–174 (cit. on p. 46).

Braun, P., Ghabezloo, S., Delage, P., Sulem, J., and Conil, N. (2018). „Theoretical Analysis of Pore Pressure Diffusion in Some Basic Rock Mechanics Experiments“. In: *Rock Mechanics and Rock Engineering* 51.5, pp. 1361–1378 (cit. on pp. 51, 73, 74).

Braun, P., Ghabezloo, S., Delage, P., Sulem, J., and Conil, N. (2019). „Determination of Multiple Thermo-Hydro-Mechanical Rock Properties in a Single Transient Experiment: Application to Shales“. In: *Rock Mechanics and Rock Engineering*. in press (cit. on pp. 16, 73, 97, 129, 147).

Brown, R. J. and Korringa, J. (1975). „On the dependence of the elastic properties of a porous rock on the compressibility of the pore fluid“. In: *Geophysics* 40.4, pp. 608–616 (cit. on p. 9).

Cariou, S., Duan, Z., Davy, C., Skoczylas, F., and Dormieux, L. (2012). „Poromechanics of partially saturated COx argillite“. In: *Applied Clay Science* 56, pp. 36–47 (cit. on p. 110).

Carslaw, H. and Jaeger, J. C. (1959). *Conduction of heat in solids*. Second Edi. Oxford: Clarendon Press (cit. on p. 172).

Cheng, A. H.-D. (1997). „Material coefficients of anisotropic poroelasticity“. In: *International Journal of Rock Mechanics and Mining Sciences* 34.2, pp. 199–205 (cit. on pp. 10, 14).

Cheng, A. H.-D. (2016). *Poroelasticity*. Vol. 27. Theory and Applications of Transport in Porous Media. Cham: Springer International Publishing (cit. on pp. 60, 75).

Chiarelli, A. S. (2000). „Étude expérimentale et modélisation du comportement mécanique de l'argilite de l'Est, Influence de la profondeur et de la teneur en eau". PhD thesis. Université Lille I (cit. on pp. 25, 26).

Conil, N., Armand, G., Garitte, B., Jobmann, M., Jellouli, M., Filippi, M., De La Vaissière, R., and Morel, J. (2012). „In situ heating test in Callovo-Oxfordian claystone: measurement and interpretation". In: *Clays in natural and engineered barriers for radioactive waste confinement*. Montpellier (cit. on pp. 5, 114).

Conil, N., Talandier, J., Djizanne, H., de La Vaissière, R., Righini-Waz, C., Auvray, C., Morlot, C., and Armand, G. (2018). „How rock samples can be representative of in situ condition: A case study of Callovo-Oxfordian claystones". In: *Journal of Rock Mechanics and Geotechnical Engineering* 10.4, pp. 613–623 (cit. on pp. 18, 21, 28, 33, 34, 36, 38, 39, 112, 139).

Conil, N. (2012). *Expérimentation TED, Bilan de la deuxième anneé de chauffe. Report D.RP.AMFS.12.0031*. Tech. rep. (cit. on p. 29).

Conil, N. and Vitel, M. (2019). „TED in situ heating test in Callovo-Oxfordian claystone: concept, observations and interpretation". In: *Rock Mechanics and Rock Engineering*. submitted (cit. on pp. 29, 30).

Conil, N., Gatmiri, B., and Armand, G. (2010). *Premiers résultats de l'expérimentation TED. Andra report D.RP.AMFS.10.0067*. Tech. rep. (cit. on pp. 29, 54).

Conil, N., Djizanne, H., Guayacan Carillo, L., Leveau, F., and Armand, G. (2017). *SPÉCIFICATIONS DE L'EXPÉRIMENTATION CRQ, COMPORTEMENT THM REPRÉSENTATIF D'UN QUARTIER HA, Andra report*. Tech. rep. (cit. on p. 168).

Coussy, O. (2004). *Poromechanics*. New York: J. Wiley & Sons (cit. on p. 9).

Coviello, A, Lagioia, R, and Nova, R (2005). „On the Measurement of the Tensile Strength of Soft Rocks". In: *Rock Mechanics and Rock Engineering* 38.4, pp. 251–273 (cit. on p. 160).

Davy, C. A., Skoczylas, F., Barnichon, J. D., and Lebon, P. (2007). „Permeability of macro-cracked argillite under confinement: Gas and water testing". In: *Physics and Chemistry of the Earth* 32.8-14, pp. 667–680 (cit. on pp. 18, 28, 53).

De La Vaissière, R., Armand, G., and Talandier, J. (2015). „Gas and water flow in an excavation-induced fracture network around an underground drift : A case study for a radioactive waste repository in clay rock". In: 521, pp. 141–156 (cit. on p. 18).

De La Vaissière, R., Conil, N., and Talandier, J. (2017). *Synthèse des paramètres hydrogéologiques des argilites du Callovo-Oxfordien : perméabilité à l'eau et emmagasinement spécifique, Andra report*. Tech. rep. (cit. on p. 28).

Delage, P., Sultan, N., and Cui, Y. J. (2000). „On the thermal consolidation of Boom clay". In: *Canadian Geotechnical Journal* 37.2, pp. 343–354 (cit. on pp. 53, 131).

Delage, P., Menaceur, H., Tang, A.-M., and Talandier, J. (2014). „Suction effects in deep Callovo-Oxfordian claystone". In: *Géotechnique Letters* 4, pp. 267–271 (cit. on pp. 18, 20).

Derjaguin, B. V., Karasev, V. V., and Khromova, E. N. (1992). „Thermal expansion of water in fine pores". In: *Progress in Surface Science* 40.1-4, pp. 391–392 (cit. on pp. 32, 142, 167).

Detournay, E. and Cheng, A. H.-D. (1993). „Fundamentals of Poroelasticity“. In: *Analysis and Design Methods*. Ed. by C. Fairhurst. Oxford: Pergamon, pp. 113 –171 (cit. on p. 9).

Diederichs, M. S. (2007). „The 2003 Canadian Geotechnical Colloquium: Mechanistic interpretation and practical application of damage and spalling prediction criteria for deep tunnelling“. In: *Canadian Geotechnical Journal* 44.9, pp. 1082–1116 (cit. on p. 160).

Donaghe, R. T. and Chaney, R. C. (1988). *Advanced Triaxial Testing of Soil and Rock*. Vol. 977. ASTM International (cit. on pp. 45, 46).

Enssle, C. P., Cruchaudet, M., Croisé, J., and Brommundt, J. (2011). „Determination of the permeability of the Callovo-Oxfordian clay at the metre to decametre scale“. In: *Physics and Chemistry of the Earth* 36.17-18, pp. 1669–1678 (cit. on pp. 28, 112).

Escoffier, S., Homand, F., Giraud, A., Hoteit, N., and Su, K. (2005). „Under stress permeability determination of the Meuse / Haute-Marne mudstone“. In: *Engineering Geology* 81.3, pp. 329–340 (cit. on p. 51).

Escoffier, S. (2002). „Caractérisation expérimentale du comportement hydroméchanique des argilites de Meuse/Haute-Marne“. PhD thesis. Institut National Polytechnique de Lorraine (cit. on pp. 22–25, 51, 53, 99, 108, 157).

Ewy, R. T., Daniels, E. J., and Stankovich, R. J. (2001). „Behavior of a reactive shale from 12000 feet depth“. In: *DC Rocks 2001, The 38th U.S. Symposium on Rock Mechanics (USRMS)*. Washington, D.C., pp. 77–84 (cit. on p. 73).

Ewy, R. T. (2015). „Shale/claystone response to air and liquid exposure, and implications for handling, sampling and testing“. In: *International Journal of Rock Mechanics and Mining Sciences* 80, pp. 388–401 (cit. on pp. 21, 22, 33, 34, 39).

Fairhurst, C. (1961). „Laboratory measurement of some physical properties of rock“. In: *The 4th US symposium on rock mechanics (USRMS)*. American Rock Mechanics Association, pp. 105–118 (cit. on pp. 46, 47).

Fairhurst, C. (1964). „On the validity of the ‘Brazilian’test for brittle materials“. In: *International Journal of Rock Mechanics and Mining Sciences & Geomechanics Abstracts*. Vol. 1. 4. Elsevier, pp. 535–546 (cit. on p. 159).

Fei, Y. (1995). „Thermal Expansion“. In: *Mineral Physics & Crystallography: A Handbook of Physical Constants*. American Geophysical Union (AGU), pp. 29–44 (cit. on p. 139).

Garitte, B., Nguyen, T. S., Barnichon, J. D., et al. (2017). „Modelling the Mont Terri HE-D experiment for the Thermal–Hydraulic–Mechanical response of a bedded argillaceous formation to heating“. In: *Environmental Earth Sciences* 76.9, pp. 1–20 (cit. on pp. 30, 125).

Garitte, B., Gens, A., Vaunat, J., and Armand, G. (2014). „Thermal conductivity of argillaceous rocks: Determination methodology using in situ heating tests“. In: *Rock Mechanics and Rock Engineering* 47.1, pp. 111–129 (cit. on pp. 29, 53, 114).

Gaucher, E., Robelin, C., Matray, J. M., Négrel, G., Gros, Y., Heitz, J. F., Vinsot, A., Rebours, H., Cassagnabère, A., and Bouchet, A. (2004). „ANDRA underground research laboratory : interpretation of the mineralogical and geochemical data acquired in the Callovian – Oxfordian formation by investigative drilling“. In: *Physics and Chemistry of the Earth* 29, pp. 55–77 (cit. on pp. 18, 19).

Gens, A., Vaunat, J., Garitte, B., and Wileveau, Y. (2007). „In situ behaviour of a stiff layered clay subject to thermal loading: observations and interpretation“. In: *Géotechnique* 57.2, pp. 207–228 (cit. on pp. 5, 30, 86, 87, 114, 125).

Ghabezloo, S. (2015). „A micromechanical model for the effective compressibility of sandstones“. In: *European Journal of Mechanics - A/Solids* 51, pp. 140–153 (cit. on p. 107).

Ghabezloo, S. and Sulem, J. (2009). „Stress dependent thermal pressurization of a fluid-saturated rock“. In: *Rock Mechanics and Rock Engineering* 42.1, pp. 1–24 (cit. on pp. 4, 16, 30, 42, 52, 63, 67, 73, 74, 76, 77, 83).

Ghabezloo, S. and Sulem, J. (2010). „Effect of the volume of the drainage system on the measurement of undrained thermo-poro-elastic parameters“. In: *International Journal of Rock Mechanics and Mining Sciences* 47.1, pp. 60–68 (cit. on pp. 42–44, 52, 63, 73, 76, 77, 83).

Ghabezloo, S., Sulem, J., Guédon, S., Martineau, F., and Saint-Marc, J. (2008). „Poromechanical behaviour of hardened cement paste under isotropic loading“. In: *Cement and Concrete Research* 38, pp. 1424–1437 (cit. on p. 14).

Ghabezloo, S., Sulem, J., and Saint-Marc, J. (2009a). „Evaluation of a permeability-porosity relationship in a low-permeability creeping material using a single transient test“. In: *International Journal of Rock Mechanics and Mining Sciences* 46.4, pp. 761–768 (cit. on pp. 73, 74, 79, 80).

Ghabezloo, S., Sulem, J., and Saint-Marc, J. (2009b). „The effect of undrained heating on a fluid-saturated hardened cement paste“. In: *Cement and Concrete Research* 39.1, pp. 54–64 (cit. on pp. 5, 15, 16, 52–54, 73, 74, 142, 167).

Gibson, R. E. and Henkel, D. J. (1954). „Influence of duration of tests at constant rate of strain on measured “drained” strength“. In: *Géotechnique* 4.1, pp. 6–15 (cit. on pp. 52, 54).

Giger, S. B., Ewy, R. T., Favero, V., Stankovic, R., and Keller, L. M. (2018). „Consolidated-undrained triaxial testing of Opalinus Clay: Results and method validation“. In: *Geomechanics for Energy and the Environment* 14, pp. 16–28 (cit. on p. 73).

Giot, R., Auvray, C., Conil, N., and de La Vaissière, R. (2018). „Multi-stage water permeability measurements on claystone by steady and transient flow methods“. In: *Engineering Geology* 247, pp. 27–37 (cit. on pp. 18, 28).

Griffith, A. (1924). „The theory of rupture“. In: *Proceddings of the 1st international Congress of applied mechanics*. Delft: Tech. Boekhandel en Drukkerij J Walter Jr, pp. 55–63 (cit. on p. 159).

Guayacán-Carrillo, L.-M., Ghabezloo, S., Sulem, J., Seyedi, D. M., and Armand, G. (2017). „Effect of anisotropy and hydro-mechanical couplings on pore pressure evolution during tunnel excavation in low-permeability ground“. In: *International Journal of Rock Mechanics and Mining Sciences* 97, pp. 1–14 (cit. on pp. 66, 111, 112, 125, 157, 158, 166).

Guenther, R. B. and Lee, J. W. (1996). *Partial differential equations of mathematical physics and integral equations*. Courier Corporation (cit. on p. 171).

Hancock, M. (2006). „The 1-D Heat Equation“. In: *MIT Course 18.303 Linear Partial Differential Equations* (cit. on p. 171).

Hansen, F. D. and Vogt, T. J. (1987). *Thermo mechanical properties of selected shales, Oak Ridge National Laboratory Report ORNL/Sub/85-97343/2 (RSI-0305)*. Tech. rep. (cit. on pp. 160, 161).

Harrington, J. F., Cuss, R. J., and Talandier, J. (2017). „Gas transport properties through intact and fractured Callovo-Oxfordian mudstones“. In: *Geological Society, London, Special Publications* 454.1, pp. 131–154 (cit. on pp. 28, 112).

Hart, D. J. and Wang, H. F. (2001). „A single test method for determination of poroelastic constants and flow parameters in rocks with low hydraulic conductivities“. In: *International Journal of Rock Mechanics and Mining Sciences* 38.4, pp. 577–583 (cit. on p. 78).

Hart, D. J. and Wang, H. F. (1995). „Laboratory measurement of a complete set of poroelastic moduli for Berea sandstone and Indiana limestone“. In: *Journal of Geophysical Research* 100, pp. 741–751 (cit. on pp. 16, 73, 74).

Hassanzadegan, A., Blöcher, G., Milsch, H., Urpi, L., and Zimmermann, G. (2014). „The effects of temperature and pressure on the porosity evolution of flechtinger sandstone“. In: *Rock Mechanics and Rock Engineering* 47.2, pp. 421–434 (cit. on p. 107).

Hawkes, I. and Mellor, M. (1970). „Uniaxial testing in rock mechanics laboratories“. In: *Engineering Geology* 4, pp. 177–285 (cit. on pp. 46, 47).

Hecht, F. (2012). „New development in FreeFem++“. In: *J. Numer. Math.* 20.3-4, pp. 251–265 (cit. on p. 87).

Hoek, E (1964). „Fracture of Anisotropic Rock“. In: *Journal of the South African Institute of Mining and Metallurgy* 64.10, pp. 501–518 (cit. on p. 46).

Hoek, E. (1983). „Strength of jointed rock masses“. In: *Géotechnique* 33.3, pp. 187–223 (cit. on p. 159).

Hoek, E. (2007). *Practical Rock Engineering*, p. 196 (cit. on p. 160).

Hoek, E. and Brown, E. (1980). „Empirical strength criterion for rock masses.“ In: *Journal of the Geotechnical Engineering Division, ASCE* 106.GT9, pp. 1013–1035 (cit. on p. 159).

Hoek, E. and Martin, C. (2014). „Fracture initiation and propagation in intact rock – A review“. In: *Journal of Rock Mechanics and Geotechnical Engineering* 6.4, pp. 287–300 (cit. on p. 159).

Holt, R. M., Bakk, A, Stenebraten, J. F., Bauer, A, and Fjaer, E (2018). „Skempton's A – A key to man-induced subsurface pore pressure changes“. In: *52nd U.S. Rock Mechanics/Geomechanics Symposium*. Seattle: American Rock Mechanics Association (cit. on p. 111).

Homand, F., Giraud, A., Escoffier, S., Koriche, A., and Hoxha, D. (2004). „Permeability determination of a deep argillite in saturated and partially saturated conditions“. In: *International Journal of Heat and Mass Transfer* 47, pp. 3517–3531 (cit. on p. 51).

Homand, F. (2000). *Essais géomécaniques sondages EST204 et EST205, Rapport LAEGO LG-FH.GFE. PSI.RPRE.00.01 45/A*. Tech. rep. (cit. on p. 26).

Homand, F., Shao, J.-F., Giraud, A., Auvray, C., and Hoxha, D. (2006). „Pétrofabrique et propriétés mécaniques des argilites“. In: *C. R. Geoscience* 338, pp. 882–891 (cit. on p. 25).

Hu, D. W., Zhang, F., and Shao, J. F. (2014). „Experimental study of poromechanical behavior of saturated claystone under triaxial compression“. In: *Acta Geotechnica* 9.2, pp. 207–214 (cit. on pp. 26, 52).

Hueckel, T. and Baldi, G (Dec. 1990). „Thermoplasticity of Saturated Clays: Experimental Constitutive Study“. In: *Journal of Geotechnical Engineering* 116, pp. 1778–1796 (cit. on p. 168).

IAPWS-IF97 (2008). *IAPWS Industrial Formulation 1997 for the Thermodynamic Properties of Water and Steam*. Berlin, Heidelberg: Springer, pp. 7–150 (cit. on pp. 43, 53, 112, 140, 142, 143).

Jia, Y., Bian, H., Duveau, G., Su, K., and Shao, J. (2009). „Numerical modelling of in situ behaviour of the Callovo–Oxfordian argillite subjected to the thermal loading“. In: *Engineering Geology* 109.3-4, pp. 262–272 (cit. on p. 114).

Li, B. and Wong, R. C. (2018). „Creating tensile fractures in Colorado shale using an unconfined fast heating test“. In: *Geotechnical Testing Journal* 42.2 (cit. on p. 7).

Makhnenko, R. Y., Tarokh, A., and Podladchikov, Y. Y. (2017). „On the Unjacketed Moduli of Sedimentary Rock“. In: *Poromechanics VI*, pp. 897–904 (cit. on p. 52).

McKinstry, H. A. (1965). „Thermal Expansion of Clay Minerals“. In: *The American Mineralogist* 50 (cit. on p. 139).

Menaceur, H., Delage, P., Tang, A.-M., and Conil, N. (2015). „The thermo-mechanical behaviour of the Callovo-Oxfordian claystone“. In: *International Journal of Rock Mechanics and Mining Sciences* 78, pp. 290–303 (cit. on pp. 18, 26, 28, 34, 51, 53, 96, 157).

Menaceur, H., Delage, P., Tang, A.-M., and Talandier, J. (2016). „The Status of Water in Swelling Shales: An Insight from the Water Retention Properties of the Callovo-Oxfordian Claystone“. In: *Rock Mechanics and Rock Engineering* 49.12, pp. 4571–4586 (cit. on p. 20).

Menke, W. (1989). *Geophysical data analysis: Discrete inverse theory*. London: Academic Press Limited, p. 289 (cit. on pp. 16, 78).

M'Jahad, S., Davy, C. A., Skoczylas, F., and Talandier, J. (2016). „Characterization of transport and water retention properties of damaged Callovo-Oxfordian claystone“. In: *Geological Society, London, Special Publications* 443.1, pp. 159–177 (cit. on p. 28).

Mohajerani, M. (2011). „Etude experimentale du comportement thermo-hydro-mecanique de l'argilite du Callovo-Oxfordien“. PhD thesis. Université Paris-Est (cit. on pp. 23, 24, 96, 99, 108).

Mohajerani, M., Delage, P., Monfared, M., Tang, A.-M., Sulem, J., and Gatmiri, B. (2011). „Oedometric compression and swelling behaviour of the Callovo-Oxfordian argillite“. In: *International Journal of Rock Mechanics and Mining Sciences* 48.4, pp. 606–615 (cit. on pp. 18, 21–23, 28, 51).

Mohajerani, M., Delage, P., Sulem, J., Monfared, M., Tang, A.-M., and Gatmiri, B. (2012). „A laboratory investigation of thermally induced pore pressures in the Callovo-Oxfordian claystone“. In: *International Journal of Rock Mechanics and Mining Sciences* 52, pp. 112–121 (cit. on pp. 4, 31, 33, 40, 51, 52, 66, 67, 73, 108, 131, 136–138, 143, 144, 147, 167).

Mohajerani, M., Delage, P., Sulem, J., Monfared, M., Tang, A.-M., and Gatmiri, B. (2014). „The thermal volume changes of the Callovo-Oxfordian claystone“. In: *Rock Mechanics and Rock Engineering* 47.1, pp. 131–142 (cit. on pp. 4, 30, 51, 66, 67, 108).

Mohamadi, M. and Wan, R. G. (2016). „Strength and post-peak response of Colorado shale at high pressure and temperature“. In: *International Journal of Rock Mechanics and Mining Sciences* 84, pp. 34–46 (cit. on p. 161).

Monfared, M., Sulem, J., Delage, P., and Mohajerani, M. (2011a). „A Laboratory Investigation on Thermal Properties of the Opalinus Claystone“. In: *Rock Mechanics and Rock Engineering* 44.6, pp. 735–747 (cit. on pp. 4, 5, 30, 31, 134, 140, 167).

Monfared, M., Delage, P., Sulem, J., Mohajerani, M., Tang, A.-M., and De Laure, E. (2011b). „A new hollow cylinder triaxial cell to study the behavior of geo-materials with low permeability“. In: *International Journal of Rock Mechanics and Mining Sciences* 48.4, pp. 637–649 (cit. on pp. 21, 33, 39, 52).

Monfared, M. (2011). „Couplages température-endommagement-perméabilité dans les sols et les roches argileux“. PhD thesis. Université Paris-Est (cit. on p. 49).

Myint-U, T. and Debnath, L. (2007). *Linear partial differential equations for scientists and engineers*. Springer Science & Business Media (cit. on p. 171).

Palciauskas, V. V. and Domenico, P. A. (1982). „Characterization of drained and undrained response of thermally loaded repository rocks“. In: *Water Resources Research* 18.2, pp. 281–290 (cit. on p. 139).

Perras, M. A. and Diederichs, M. S. (2014). „A Review of the Tensile Strength of Rock: Concepts and Testing“. In: *Geotechnical and Geological Engineering* 32.2, pp. 525–546 (cit. on pp. 46, 160).

Pham, Q. T., Vales, F., Malinsky, L., Minh, D. N., and Gharbi, H. (2007). „Effects of desaturation – resaturation on mudstone“. In: *Physics and Chemistry of the Earth* 32, pp. 646–655 (cit. on pp. 21, 33).

Rice, J. R. and Cleary, M. P. (1976). „Some basic stress diffusion solutions for fluid-saturated elastic porous media with compressible constituents“. In: *Reviews of Geophysics and Space Physics* 14.2, pp. 227–241 (cit. on p. 9).

Robinet, J.-C. (2008). „Minéralogie, porosité et diffusion dans l'argilite du Callovo-Oxfordien de Bure (Meuse/Haute-Marne, France) de l'échelle centimétrique à micrométrique“. PhD thesis. Université de Poitiers (cit. on p. 18).

Robinet, J.-C., Sardini, P., Coelho, D., Parneix, J.-C., Pret, D., Sammartino, S., Boller, E., and Altmann, S. (2012). „Effects of mineral distribution at mesoscopic scale on solute diffusion in a clay- rich rock : Example of the Callovo-Oxfordian mudstone (Bure , France)“. In: *Water Resources Research* 48.May (cit. on p. 20).

Robinet, J.-C., Sardini, P., Siitari-Kauppi, M., Prêt, D., and Yven, B. (2015). „Upscaling the porosity of the Callovo-Oxfordian mudstone from the pore scale to the formation scale; insights from the 3H-PMMA autoradiography technique and SEM BSE imaging“. In: *Sedimentary Geology* 321 (cit. on p. 18).

Ross, C. W. (1941). „Thermal Expansion of Clay Building Bricks“. In: *Journal of Research of the National Bureau of Standards* 27, pp. 1–216 (cit. on p. 140).

Rudnicki, J. (2002). „Conditions for compaction and shear bands in a transversely isotropic material“. In: *International Journal of Solids and Structures* 39, pp. 3741–3756 (cit. on p. 169).

Seyedi, D., Armand, G., Conil, N., Vitel, M., and Vu, M.-N. (2017). „On the Thermo-Hydro-Mechanical Pressurization in Callovo-Oxfordian Claystone under Thermal Loading“. In: *Poromechanics 2017 - Proceedings of the 6th Biot Conference on Poromechanics*, pp. 754–761 (cit. on pp. 5, 30, 86).

Seyedi, D., Vitel, M., Vu, M.-N., and Armand, G. (2018). „Key parameters controlling thermo-hydro-mechanical pressurization in Callovo-Oxfordian claystone“. In: *International Symposium on Energy Geotechnics SEG-2018* (cit. on pp. 86, 112, 119).

Skempton, A. W. (1954). „The Pore-Pressure Coefficients A and B“. In: *Géotechnique* 4.4, pp. 143–147 (cit. on pp. 13, 111).

Skempton, A. W. (1961). „Effective stress in soils, concrete and rock“. In: *Pore Pressure and Suction in Soils*. London: Butterworths, pp. 3–28 (cit. on p. 34).

Skempton, A. and Sowa, V. (1963). „The behaviour of saturated clays during sampling and testing“. In: *Geotechnique* 13.4, pp. 269–290 (cit. on p. 34).

Song, Y., Davy, C., Troadec, D., Blanchenet, A.-M., Skoczylas, F., Talandier, J., and Robinet, J. (2015). „Multi-scale pore structure of COx claystone: Towards the prediction of fluid transport“. In: *Marine and Petroleum Geology* 65, pp. 63 –82 (cit. on p. 20).

Spang, B. (2002). *Excel add-in for properties of water and steam in SI-units*. http://www.cheresources.com/iapwsif97.shtml (cit. on pp. 53, 112, 140, 142, 143).

Sulem, J., Lazar, P., and Vardoulakis, I. (2007). „Thermo-poro-mechanical properties of clayey gouge and application to rapid fault shearing“. In: *International Journal for Numerical and Analytical Methods in Geomechanics* 31.3, pp. 523–540 (cit. on p. 133).

Sultan, N., Delage, P., and Cui, Y.-J. (2002). „Temperature effects on the volume change behaviour of Boom clay“. In: *Engineering Geology* 64.2-3, pp. 135–145 (cit. on pp. 4, 30).

Tang, A.-M., Cui, Y.-J., and Barnel, N. (2008). „Thermo-mechanical behaviour of a compacted swelling clay“. In: *Géotechnique* 58.1, pp. 45–54 (cit. on p. 40).

Tarantino, A. (2010). „Basic concepts in the mechanics and hydraulics of unsaturated geomaterials“. In: *Mechanics of Unsaturated Geomaterials*. Ed. by L Laloui. London: ISTE Ltd., pp. 3–28 (cit. on p. 34).

Thury, M. and Bossart, P. (1999). „The Mont Terri rock laboratory, a new international research project in a Mesozoic shale formation, in Switzerland“. In: *Engineering Geology* 52.3, pp. 347 –359 (cit. on p. 5).

Valenza, J. J. and Scherer, G. W. (2005). „Evidence of anomalous thermal expansion of water in cement paste“. In: *Cement and Concrete Research* 35.1, pp. 57–66 (cit. on pp. 140, 167).

Vardoulakis, I. and Sulem, J. (1995). *Bifurcation Analysis in Geomechanics*. Blackie Academic and Professional (cit. on p. 9).

Vernde, S. and Ponson, L. (2014). *Method for characterizing the cracking mechanism of a material from the fracture surface thereof, Patent WO2016050871A1* (cit. on p. 169).

Villamor Lora, R., Ghazanfari, E., and Asanza Izquierdo, E. (2016). „Geomechanical Characterization of Marcellus Shale“. In: *Rock Mechanics and Rock Engineering* 49.9, pp. 3403–3424 (cit. on p. 140).

Vincké, O., Longuemare, P., Boutéca, M., and Deflandre, J. P. (1998). „Investigation of the poromechanical behavior of shales in the elastic domain“. In: *SPE/ISRM Rock Mechanics in Petroleum Engineering*. Trondheim (cit. on pp. 22, 25).

Vinsot, A., Delay, J., de La Vaissière, R., and Cruchaudet, M. (2011). „Pumping tests in a low permeability rock: Results and interpretation of a four-year long monitoring of water production flow rates in the Callovo-Oxfordian argillaceous rock“. In: *Physics and Chemistry of the Earth* 36.17-18, pp. 1679–1687 (cit. on pp. 28, 112).

Wileveau, Y., Cornet, F. H., Desroches, J., and Blumling, P. (2007a). „Complete in situ stress determination in an argillite sedimentary formation“. In: *Physics and Chemistry of the Earth* 32.8-14, pp. 866–878 (cit. on p. 18).

Wileveau, Y., Su, K., and Ghoreychi, M. (2007b). „A heating experiment in the argillites in the Meuse/Haute-Marne underground research laboratory“. In: *The 11th International Conference on Environmental Remediation and Radioactive Waste Management*. American Society of Mechanical Engineers, pp. 939–944 (cit. on p. 5).

Wissa, A. E. Z. (1969). „Pore pressure measurement in saturated stiff soils“. In: *Journal of the Soil Mechanics and Foundations Division* 95.4, pp. 1063–1073 (cit. on pp. 42, 52, 63, 73, 76, 77, 83).

Xu, S., Scherer, G. W., Mahadevan, T. S., and Garofalini, S. H. (2009). „Thermal expansion of confined water“. In: *Langmuir* 25.9, pp. 5076–5083 (cit. on pp. 32, 142, 143, 167).

Yang, D., Billiotte, J., and Su, K. (2010). „Characterization of the hydromechanical behavior of argillaceous rocks with effective gas permeability under deviatoric stress“. In: *Engineering Geology* 114.3-4, pp. 116–122 (cit. on p. 28).

Yang, M.-T. and Hsieh, H.-Y. (1997). „Direct tensile behavior of a transversely isotropic rock“. In: *International Journal of Rock Mechanics and Mining Sciences* 34.5, pp. 837–849 (cit. on p. 160).

Yven, B., Sammartino, S., Geroud, Y., Homand, F., and Villieras, F. (2007). „Mineralogy, texture and porosity of Callovo-Oxfordian argillites of the Meuse/Haute-Marne region (eastern Paris Basin)“. In: *Mémoires de la Société géologique de France* 178, pp. 73–90 (cit. on p. 18).

Zhang, C. L. (2011). „Experimental evidence for self-sealing of fractures in claystone“. In: *Physics and Chemistry of the Earth* 36, pp. 1972–1980 (cit. on p. 53).

Zhang, C.-L. (2013). „Sealing of fractures in claystone“. In: *Journal of Rock Mechanics and Geotechnical Engineering* 5.3, pp. 214–220 (cit. on p. 18).

Zhang, C. L., Conil, N., and Armand, G. (2017). „Thermal effects on clay rocks for deep disposal of high-level radioactive waste“. In: *Journal of Rock Mechanics and Geotechnical Engineering* 9.3, pp. 463–478 (cit. on pp. 5, 134, 135).

Zhang, C. L., Armand, G., Conil, N., and Laurich, B. (2019). „Investigation on anisotropy of mechanical properties of Callovo-Oxfordian claystone“. In: *Engineering Geology* 251, pp. 128–145 (cit. on pp. 110, 168).

Zhang, F., Xie, S. Y., Hu, D. W., Shao, J. F., and Gatmiri, B. (2012). „Effect of water content and structural anisotropy on mechanical property of claystone“. In: *Applied Clay Science* 69, pp. 79–86 (cit. on pp. 26, 104, 157).

Zimmerman, R. W. (1991). *Compressibility of sandstones*. Amsterdam: Elsevier Sci. (cit. on p. 107).

Zimmerman, R. W., Somerton, W. H., and King, M. S. (1986). „Compressibility of Porous Rocks“. In: *Journal of Geophysical Research* 91.B12, pp. 12765–12777 (cit. on pp. 9, 99).

List of Figures

1.1 Geological map of the Meuse/Haute-Marne area in eastern France, where the Callovo-Oxfordian claystone is located in a layer at around 500 m depth. The Andra underground research laboratory is found near the village of Bure (Andra, 2005) 2

1.2 Concept of microtunnels, which incorporate high level radioactive waste packages (Andra, 2005) 4

1.3 a) Schematic layout of the microtunnels containing high-level radioactive waste (adopted from Andra, 2005), with b) a cross-section where we can assume plane strain and zero heat/ temperature flux perpendicular to the image plane, illustrating the heat radiation from periodically constructed microtunnels . . . 6

2.1 Strain gages and coordinate system oriented and attached with respect to the bedding plane of the COx specimens 12

2.2 Lithostratigraphy of the borehole EST205, taken from Gaucher et al. (2004) . 19

2.3 a) COx clay matrix obtained from synchrotron X-ray microtomography (Robinet et al., 2012), b) 3D reconstruction of the pore network from FIB/SEM images (Song et al., 2015), adopted from (Armand et al., 2017b) 20

2.4 Cumulative pore size distribution measured by mercury intrusion porosimetry on a freeze dried sample (Menaceur et al., 2016) 20

2.5 a) Oedometric modulus and b) Biot's coefficient under various effective axial stresses 23

2.6 a) Undrained bulk modulus and b) drained bulk modulus with respect to effective stress 24

2.7 Unjacketed bulk modulus with respect to effective stress 25

2.8 a) Young's modulus and b) Poisson's ratio with respect to effective stress, tested on specimen with different saturation degrees (Chiarelli, 2000) 26

2.9 a) Young's modulus and b) Poisson's ratio with respect to effective stress tested on saturated specimens 27

2.10 Comparison of the shear envelopes obtained from shear tests on saturated specimens, conducted by different authors, taken from Belmokhtar et al. (2018) 27

2.11 Thermal pressurization coefficient: experimental values and calculated values, assuming a constant drained compressibility (Mohajerani et al., 2012) 31

3.1 Site at the underground laboratory with drilling machine (on the left) 34

3.2 a) Extracted core section, b) core segment, c) core segment broken into fragments and placed in the WP4C tensiometer . . . 35
3.3 Suctions measured along the core, with measurements aborted before equilibrium in red . . . 35
3.4 Watercontent measured along the core, directly after extraction (this study), and and at the surface (taken from Conil et al., 2018) . . . 36
3.5 Porosity and saturation degree measured on extracted samples with a deviation caused by varying paraffin density . . . 37
3.6 Measured suction changes during different handling phases . . . 37
3.7 High pressure and temperature controlled isotropic cell . . . 40
3.8 High pressure and temperature controlled triaxial cell . . . 41
3.9 a) Apparent strains calculated in function of the cell temperature T, in function of the room temperature T_{room} and as total compared with the measured apparent strains during a thermal test; b) example horizontal strains in a thermal test, as measured by the strain gage on a COx specimen and after correction using apparent strains . . . 42
3.10 Linear thermal expansion of an aluminium 2011 specimen, heated from 26 °C 43
3.11 Schematic workflow of the controller loop . . . 45
3.12 Different cap connections which allow for triaxial extension tests (Donaghe and Chaney, 1988) . . . 46
3.13 a) Glued end surfaces with a so-called butt-joint (Fairhurst, 1961), b) glued lateral surfaces (Hawkes and Mellor, 1970) . . . 47
3.14 Dog-bone shaped sample (Bobich, 2005) . . . 48
3.15 a) Photo and b) schema of the novel extension device, permitting to maintain pore pressures larger than the axial total stress through glued connection, while saturation and drainage is achieved through lateral geotextiles . . . 48
3.16 Aluminium cylinder equipped with strain gages for axial force measurement . 49
3.17 a) Attaching the end platens to the specimen using epoxy adhesive, placed in a V-block to ensure axial alignment; b) schematic cut to illustrate the layout of two overlapping membranes to pass through strain gage wires . . . 50
3.18 Schematic set-up of an isotropic cell, dead volume of drainage system coloured in blue . . . 53
3.19 Geometry of model drainage conditions . . . 53
3.20 Applied pressure and temperature gradients during different test types, with confining stress in red solid lines, pore pressure in blue dashed lines and temperature in green dash dotted lines. a) Represents a drained compression test, b) an unjacketed test, c) a pore pressure test, d) a drained heating test, e) a undrained compression test and f) a undrained heating test . . . 55
3.21 a) F_1 [Eq. (3.18)] and F_2 [Eq. (3.24)] for $z = H_d$ as functions of dimensionless time, b) change of $F_1(z)$ with time . . . 58
3.22 Arbitrary loading sequence . . . 61

3.23 Numerical simulation of measured tangent parameter and pore pressure change in an undrained test 64
3.24 Zoom on F_2 [Eq. (32)] for $z = H_d$, used to evaluate θ, for example values of F_2 67
3.25 Error ϵ_β as a function of dimensionless time with a zoom indicating $\epsilon_\beta = 0.01$ under variation of the storage coefficient, for a) drained compression, b) unjacketed compression and c) pore pressure test. In c), the parameter variation has no effect on the result 68
3.26 Error on measurement of undrained pore pressure-related parameters with a) variation of reservoir coefficient R according to Tab. 3.8; b) variation of storage coefficient S according to Tab. 3.7; c) variation of the ratio Λ_L/Λ . . . 69
3.27 Cyclic drained loading paths with different rates 71
3.28 a) Calculated pore pressures in the specimen centre and b) measured volumetric strains for the fast loading path (red dotted line) and the slow loading path (blue solid line) 71
3.29 Three-stage loading protocol and schematic volumetric response for mechanical or thermal tests. Note that annotated parameters are only indicative and need always a pair of stress-strain, temperature-strain, pore pressure-temperature or pore pressure-stress values for their determination 77
3.30 Three-stage compression test with a) measured specimen strain and pore pressure over time, b) stress-strain curve 82
3.31 Drainage phase from Fig. 3.30a with measured and simulated strains 82
3.32 Three-stage thermal test with a) applied temperature change, b) specimen strains and pore pressure over time, c) temperature-strain curve 84
3.33 Drainage phase from Fig. 3.32b with measured and simulated strains 84
3.34 Schematic illustration of a) the geometry of the finite element model and b) the displacement, temperature and pore pressure boundary conditions applied to the finite element model. The dimensions are not to scale 88
3.35 Heat flux density through the microtunnel wall, exerted by the radioactive waste packages (from the Andra database) 90
3.36 Complete mesh displayed on the left, with zooms on the microtunnel. The mesh was generated using the FreeFem++ mesh builder, and utilized in the presented analysis 91

4.1 Measured swelling strains of specimens during hydration under various confining stresses, with a proposed power-law regression 97
4.2 Measured deformations during a deviatoric test on sample DEV2 loaded parallel to the bedding plane in a) function of time, with b) zoom on the first hour of a). One observes the time dependent deformations due to fluid dissipation, and the anisotropic radial strain response 98

4.3 Measured deformations during a deviatoric test on sample DEV2 loaded parallel to the bedding plane in a) function of deviatoric stress q highlighting the determination of the Young moduli, and in b) radial strains with respect to axial strains indicating the Poisson ratios 98

4.4 Measured stress dependent drained bulk modulus K_d for equivalent isotropy, with a fitted model based on isotropic tests (Tab. 4.3) and a fitting based on all isotropic and deviatoric test results (Tab. 4.5). 100

4.5 Measured stress dependent Biot's modulus H for equivalent isotropy, with a fitted model based on isotropic tests (Tab. 4.3) and a fitting based on all isotropic and deviatoric test results (Tab. 4.5). 100

4.6 Measured stress dependent drained bulk modulus K_d on samples ISO1, ISO6 and ISO10, illustrating the reversible reduction of stiffness with decreasing effective stress 101

4.7 Measured stress dependent undrained bulk modulus K_u for equivalent isotropy, with fitted linear relationship (Eq. (4.2), Tab. 4.3). 101

4.8 Measured anisotropic responses D_i during drained compression, with a fitted model based on isotropic tests (Tab. 4.3, 4.4) and a fitting based on all isotropic and deviatoric test results (Tab. 4.4, 4.5). 102

4.9 Measured anisotropic responses H_i during pore pressure tests, with a fitted model based on isotropic tests (Tab. 4.3, 4.4) and a fitting based on all isotropic and deviatoric test results (Tab. 4.4, 4.5). 102

4.10 Measured anisotropic responses U_i during undrained compression, with a fitted model based on isotropic tests (Tab. 4.3, 4.4) and a fitting based on all isotropic and deviatoric test results (Tab. 4.4, 4.5). 103

4.11 Measured ratio of anisotropic strain response R_i during drained and undrained compression and pore pressure tests, with a fitted model based on isotropic tests (Tab. 4.3, 4.4). 103

4.12 Measured stress dependent drained Young's modulus E_z perpendicular and E_h parallel to the bedding plane, with a fitted model using isotropic experimental results (Tab. 4.3) and a fitting based on all isotropic and deviatoric test results (Tab. 4.5) 104

4.13 Measured drained Poisson's ratio ν_{zh} perpendicular and ν_{hh} parallel to the bedding planes with respect to effective stress, with a fitted model using isotropic experimental results (Tab. 4.3) and a fitting based on all isotropic and deviatoric test results (Tab. 4.5) 105

4.14 Measured stress dependent undrained Young's modulus $E_{u,z}$ perpendicular and $E_{u,h}$ parallel to the bedding plane, with a fitted model using isotropic experimental results (Tab. 4.3) and a fitting based on all isotropic and deviatoric test results (Tab. 4.5) 105

4.15 Measured undrained Poisson's ratio $\nu_{u,zh}$ perpendicular and $\nu_{u,hh}$ parallel to the bedding planes with respect to effective stress, with a fitted model using isotropic experimental results (Tab. 4.3) and a fitting based on all isotropic and deviatoric test results (Tab. 4.5) 106
4.16 Biot's effective stress coefficient b for a) equivalent isotropy and b) transverse isotropy; calculated with Eq. (2.21) using the regression based on isotropic tests (Tab. 4.3, 4.4) and the regression based on isotropic and deviatoric tests (Tab. 4.4, 4.5). 108
4.17 Skempton's coefficient B for equivalent isotropy, calculated with Eq. (2.32) and (4.1) using the regression based on isotropic tests (Tab. 4.3, 4.4) and the regression based on isotropic and deviatoric tests (Tab. 4.4, 4.5). 109
4.18 Temperature field and its evolution with time, calculated for a model with 20 m width 115
4.19 Locations of the extracted point data, with their horizontal and vertical distance to the microtunnel center, respectively. The dimensions are not to scale 115
4.20 Time evolution of a) temperature and b) pore pressure at different horizontal distances form the microtunnel. Values for points in vertical distance are shown for c) temperature and d) pore pressure. The exact locations of these points are indicated in Fig. 4.19 116
4.21 Pore pressure with respect to distance from the tunnel wall, changing with time, in a) horizontal direction and b) vertical direction from the microtunnel 117
4.22 Pore pressure field with respect to time, calculated for a model with 20 m width. Blue circles indicate the location of maximum pore pressure 118
4.23 Maximum value of the pore pressure field and minimum value of the minor principal effective stress (disregarding the zone close to the tunnel wall), evaluated for a 20 m wide model 118
4.24 a) Major and b) minor principal effective stress parallel to the model plane. White dashes indicate the stress directions, which remained horizontal and vertical, respectively, apart from the zones close to the microtunnel. Note that stresses in the vicinity of the microtunnel can exceed the annotated scale, and are not detailed here 120
4.25 Principal effective stress paths for points in a) horizontal direction and b) vertical direction over the microtunnel 121
4.26 a) Calculated maximum pore pressure and b) minimum minor principal effective stress parallel to the model plane, calculated with the transversely isotropic hydromechanical properties and with an equivalent isotropic parameter set . . 122
4.27 a) Calculated maximum pore pressure and b) minimum minor principal effective stress parallel to the model plane, calculated with and without stress dependent parameters 123
4.28 Mean effective stress with respect to time, calculated for a model with 20 m width. Note that values in the vicinity of the microtunnel might exceed the annotated scale 123

5.1 Schematic procedure of a) two-stage thermal test and b) three-stage thermal test 130
5.2 Applied heating and cooling paths on the four tested samples; in each step the temperature was changed rapidly with increments from 5 °C (ISO1, ISO4) up to 15 °C (ISO2, ISO3), followed by a constant temperature stage during one day 130
5.3 Typical three stage thermal test on ISO4: response in pore pressure resulting from an undrained decrease in temperature form 50 to 45 °C, followed by drainage opening and pore pressure dissipation 132
5.4 Measured strains parallel and perpendicular to the bedding plane during test ISO4, with an initial undrained thermal expansion stabilizing after 4 hours, followed by a transient deformation due to pore pressure dissipation, and stabilization at a drained state 132
5.5 Drained strain changes (vertical = perpendicular and horizontal = parallel to bedding) with respect to temperature changes, under constant isotropic effective stress (10 MPa for ISO1 and ISO4 and 8 MPa for ISO2 and ISO3) . . 133
5.6 Linear undrained thermal expansion coefficient for heating and cooling, measured during the initial rapid temperature changes in each step test 135
5.7 Bulk undrained thermal expansion coefficient for heating and cooling, measured during the initial rapid temperature changes in each step test. The data is compared with similar findings of Zhang et al. (2017) 135
5.8 Measured modulus H with respect to temperature, compared with the data from Sec. 4 at 25 °C 137
5.9 Corrected thermal pressurization coefficients obtained on samples ISO1 and ISO4 under heating up to 40 °C and during cooling paths, compared with the findings of Mohajerani et al. (2012) 138
5.10 Comparison of the measured thermal pressurization coefficients (Fig. 5.9) with the back-calculated ones for each test using Eq. (2.39) and the THM calculation explained in Sec. 5.3.4 based on Eq. (2.34) 138
5.11 Variation of Λ with respect to a separate variation of the input parameters, listed in Tab. 5.3 141
5.12 Variation of α_u with respect to a separate variation of the input parameters, listed in Tab. 5.3 141
5.13 Back calculated ratio $\eta = \alpha_f/\alpha_w$ thermal expansion coefficient of the water confined in COx pores [Eq. (5.6)] with respect to that of bulk water, compared to molecular dynamics (MD) simulations of Xu et al. (2009) 143
5.14 Back calculation using a value α_f obtained before (Fig. 5.13), of a) the thermal pressurization under different stress conditions, compared with the measurements presented in this study and by Mohajerani et al. (2012), and b) back calculation of the undrained bulk thermal expansion coefficient under different stress conditions, compared with the measurements presented in this study 144

5.15 a) Calculated maximum pore pressure and b) minimum minor principal effective stress parallel to the model plane, calculated with properties of bulk water and with an anomalous thermal expansion coefficient α of water 145
5.16 a) Calculated maximum pore pressure and b) minimum minor principal effective stress parallel to the model plane, comparing results with isotropic and anisotropic thermal expansion coefficients 146

6.1 Imposed temperature changes with respect to time, applied during the extension tests 151
6.2 Stress and pore pressure conditions during the thermal extension tests; on specimen EXT2 the internal force sensor malfunctioned and we display stresses measured by the external transducer 152
6.3 Terzaghi effective stresses during the heating test, where negative stresses represent effective tension; on specimen EXT2 the internal force sensor malfunctioned and we display stresses measured by the external transducer . . . 153
6.4 Principal (Terzaghi) effective stress paths for all specimens tested; circles indicate the initial stress state, while crosses mark the specimen failure with their respective temperature 154
6.5 Temperature-strain measurements on the specimens during the heating tests, compared with calculated strains using a linear thermo-poroelastic model . . 154
6.6 Stress-strain behaviour of specimen EXT6 tested under isothermal conditions . 155
6.7 a) Temperature-strain relationship and b) axial effective stress-strain relationship compared for the tested specimens 156
6.8 a) Samples after unmounting, with the induced tensile fractures; b) plan view of some fracture surfaces, showing natural heterogeneities in the material . . 156
6.9 Hoek-Brown and Fairhurst's generalized Griffith criterion, adopted for measured tension failure with tension perpendicular to the bedding. The Mohr-Coulomb criterion is obtained from the Andra database, based on shear failure with a major principal stress parallel to bedding 158
6.10 Compilation of the experimental stress paths and tensile failure, the fitted failure criteria, and the numerically simulated stress paths at point H4 (located 20 m horizontally from the microtunnel at the symmetry boundary). Numerical and experimental stress paths describe the same directions 162

A.1 Two-stage loading protocol and schematic volumetric response for a) mechanical tests and b) thermal test 174
A.2 Drained compression test and fitted simulation with a) applied load and specimen strains over time, b) zoom on a), c) stress-strain behaviour 177
A.3 Drained heating test and fitted simulation with a) applied load, b) temperature-strain curve, c) time evolution of strains, d) zoom on c) 178

List of Tables

2.1 Laboratory data on the thermal conductivities λ (in W/m/K), provided by Conil et al. (2010) and Auvray et al. (2005) (table taken from Garitte et al., 2014) . 29

3.1 Mean and standard deviation (in brackets) of petrophysical measurements done on cuttings of three COx cores 39
3.2 Composition of synthetic pore fluid close to the *in situ* one, provided by Andra 39
3.3 Applied loading rates and measured tangent parameters for different tests . . 55
3.4 Measured tangent parameter according to Eq. (3.26) for different tests 60
3.5 Calculated time evolution of measurements during undrained tests. Parameters with an exponent "mes" correspond to the parameters defined by Ghabezloo and Sulem (2009) 63
3.6 Combinations of expected reservoir properties for parametric study 66
3.7 Expected elastic parameters for COx claystone 66
3.8 Expected thermal characteristics of tests on COx claystone 67
3.9 Influence of parameters on the characteristic time 70
3.10 Input material parameters for the analytical simulation of three-stage THM tests 80
3.11 Directly measured and optimized poroelastic parameters 81
3.12 Directly measured and optimized THM parameters 83

4.1 Overview of tested specimens with their initial saturation phase under stress and their respective subsequent loading paths; the inclined arrows ($\searrow$,$\nearrow$) indicate that several load steps were carried out between mentioned effective stresses. σ denotes the total isotopic confining stress, σ'_{ax} and σ'_{rad} the axial and radial effective stresses, respectively, while $\varepsilon_{\mathrm{hyd}}$ denotes the swelling strains observed during saturation 96
4.2 Summary of best-fit model parameters determined using a regression analysis, with some properties depending on the mean Terzaghi effective stress σ' (in MPa) 107
4.3 Best-fit model parameters resulting from a simultaneous fit of K_d and H and an independent linear fit for K_u. 108
4.4 Best-fit model parameters resulting from a simultaneous fit of D_i, H_i and U_i. . 109
4.5 Best-fit model parameters resulting from a simultaneous fit of E_i, ν_i and D_i. . 110
4.6 Material properties, taken from the Andra database, with modified values indicated in bold 113

4.7 Transversely isotropic properties, used in the previous reference calculation, adapted to an equivalent isotropic poroelastic material, by taking the mean of anisotropic properties. In the third scenario the properties marked in bold were stress dependent 121

5.1 Characteristics of the four tested specimens ISO1 - ISO4, with the applied isotropic confining stress σ and measured volume change $\varepsilon_{\mathrm{hyd}}$ during saturation. The utilized testing procedure with imposed confining stress σ and pore pressure p_f, and the average measured thermo-elastic parameters are shown (note that thermo-plastic characteristics and temperature dependencies are not detailed here). 128
5.2 Thermal expansion coefficients of the bulk mineral composites and in directions perpendicular to the mineral layer ($\perp$) and parallel to the layer ($\parallel$), adapted from Belmokhtar et al. (2017b) 139
5.3 Reference parameters used for the sensitivity analysis at 25 °C, $\sigma = 14$ MPa, $p_f = 4$ MPa 140
5.4 Transversely isotropic properties, used in the previous reference calculation, adapted to equivalent isotropic thermal parameters, by taking the mean of anisotropic properties 146

6.1 Properties of the specimens tested during the experimental programme, where σ is the isotropic confining stress, $\varepsilon_{\mathrm{hyd}}$ is the swelling strain during hydration, γ_t the measured fracture angle with respect to the horizontal bedding plane . 150
6.2 Material properties adopted from Sec. 4 and Sec. 5, used to simulate measured strains in a coupled THM calculation 157
6.3 Shale characteristics adopted from the literature, with an estimation of the Hoek-Brown coefficient $m_i = -\sigma_c/\sigma_t$, compared with the experimental results of this study on COx claystone 161

A.1 Input material parameters for the analytical simulation of two-stage THM tests 175
A.2 Best-fit results and input parameters 176